Spring 1-1-2017

Low Pressure Ratio Cascaded Joule-Thomson Cryogenic Coolers

Collin Jennings Coolidge
University of Colorado at Boulder, collin.coolidge@colorado.edu

LOW PRESSURE RATIO CASCADED JOULE-THOMSON CRYOGENIC COOLERS

by

COLLIN JENNINGS COOLIDGE

B.S., Mechanical Engineering, University of Colorado, 2011

M.S., Mechanical Engineering, University of Colorado, 2011

A thesis submitted to the

Faculty of the Graduate School of the

University of Colorado in partial fulfillment

of the requirement for the degree of

Doctorate of Philosophy

Department of Mechanical Engineering

2017

This thesis entitled:

Low Pressure Ratio Cascaded Joule-Thomson Cryogenic Coolers

written by Collin Jennings Coolidge

has been approved for the Department of Mechanical Engineering

_____

Y. C. Lee

_____

Ray Radebaugh

Date_____

The final copy of this thesis has been examined by the signatories, and we find that both the content and the form meet acceptable presentation standards of scholarly work in the above mentioned discipline.

Abstract

Coolidge, Collin Jennings (Ph.D., Mechanical Engineering)

Low Pressure Ratio Cascaded Joule-Thomson Cryogenic Coolers

Thesis directed by Professor Y. C. Lee

This thesis presents the design, fabrication, and characterization of several coldstages intended to investigate the feasibility of a low pressure ratio three stage cascaded Joule-Thomson (JT) based cryogenic cooler. The coldstages investigated use single component refrigerants operating at pressure ratios of less than 0.5:0.1 MPa. Low pressure ratio single component refrigerants offer an order of magnitude higher specific refrigeration capacity but a narrower temperature range of cooling when compared to mixed refrigerants. Cryogenic temperatures can be reached by cascading several self-contained JT refrigeration cycles. A micro-fabricated polyimide based single stage coldstage is built using micro-fabrication techniques developed in previous works. Several processing challenges are identified and recommended solutions and best practices are implemented. Control of the JT restriction is difficult as the polyimide micro-channels expand under high internal pressure. The coldstage is run in a high pressure environment to press the JT restriction into the correct geometry and cools to 280 K. To better control the JT restriction, a glass capillary based coldstage design is identified. The coldstage uses a glass capillary to form the JT restriction. The coldstage cools to 267 K and 283 K when run in a vacuum environment and atmosphere respectively as calculated. The coldstage is integrated with a mini-compressor and intermittently cools to 288 K in atmosphere. The glass capillary design is further developed to make a two stage cascaded coldstage with a Kapton tube-in-tube inter-stage heat exchanger. The coldstage cools to 228 K with a net refrigeration power of 150 mW. A three stage coldstage is demonstrated using the same design. The coldstage cools to 193 K with net refrigeration power of 15 mW. The coldstages presented demonstrate the feasibility of low pressure ratio cascaded JT cryogenic coolers. The efficiencies of the coldstages are low because of large natural heat leak into the

systems and inefficiencies of the inter-stage heat exchangers. Future work can improve efficiencies through design optimization of the inter-stage heat exchangers and implementation of more significant thermal insulation. An in-depth review of micro-fabrication techniques based on mechanical design, thermal design, and quality and ease of fabrication is needed for future scalability.

Dedication

To my friends and family who gave their unconditional support and encouragement during my graduate studies and to my wife without whom I would not be here.

Acknowledgments

I would like to thank my research advisor, Professor Y. C. Lee, for his support, insight, and advice throughout this study and my graduate career. I would also like to thank Dr. Ray Radebaugh, without his close collaboration and deep knowledge and insights of cryogenics this work would not be possible.

I would like to thank Professor Victor Bright, Professor Ronggui Yang, and Professor Bart Van Zeghbroeck for their support and serving on my dissertation committee. I would like to thank my colleagues and collaborators for their support, inputs, and discussion. In particular I would like to express my thanks to Dr. Ryan Lewis, Dr. Alex Yersak, Dr. Biddut Bhattacharjee, Dr. Nathan Eigenfeld, Ching-Yi Lin, Dr. Joseph Brown, Dr. Hsin-Ray Wu, and Paul Schroeder from the department of mechanical engineering at the University of Colorado Boulder, and Dr. Li-Anne Liew, Peter Bradley, Dr. John Nibarger, and Dr. Nicholas Barbosa from the National Institute of Standards and Technology (NIST) Boulder.

I would like to thank the Defense Advanced Research Projects Agency (DARPA) for providing funding for this work. This work was supported by the DARPA Micro-Cryogenic-Cooler program, contract no. W911NF-13-2-0029 (Wafer-Scale Integrated Micro Cryogenic Coolers).

Contents

Tables

Figures

Chapter 1: Introduction and Background

1.1 Thesis Motivation

Cryogenic coolers are used for a wide variety of applications including biological sample and food preservation, chemical liquefaction and separation processes, superconductivity, vacuum pumping, directed tissue ablation (cryosurgery), and electronic sensor cooling [1]. Cryogenic coolers used to cool low power sensors such as infrared sensors help minimize thermal noise, increase Q factor, and in some cases enable super conductivity [2]. Most cryogenic coolers operate through the use of vapor compression refrigeration cycles. In general, vapor compression refrigeration cycles use the energy of evaporation of a high pressure liquid refrigerant to a low pressure vapor state to provide heat lift at a low temperature. Most refrigeration cycles use a flow restriction such as a small orifice or capillary tube to generate a pressure drop in the refrigerant. The two major types of refrigeration cycles used to reach cryogenic temperatures are recuperative cycles and regenerative cycles. Recuperative cycles include the Joule-Thomson (JT) cycle and the Brayton cycle in which there is a continuous flow for refrigerant with constant high and low pressure conditions. A recuperative heat exchanger is used between the hot high pressure refrigerant and cold low pressure refrigerant to precool the refrigerant before expansion. Regenerative cycles have oscillating pressures analogous to AC voltage. Regenerative cycles include the Stirling cycle, the Pulse Tube cycle, and the Gifford McMmahon cycle in which the flow is oscillated with heating occurring during compression and cooling during expansion. Displacers are used to move the refrigerant to the hot side of the device during compression and to the cold side during expansion. Modern regenerative cryogenic coolers generally operate at frequencies of less than 60 Hz [1].

Successful miniaturization of cryogenic coolers will allow for compact portable cooling solutions to be integrated with sensors on a circuit board scale or even a wafer scale. However modern cryogenic coolers are large in size and not feasible for portable cooling solutions outside of high end applications and military applications. Vapor compression coolers are generally divided into two functional parts, the

portion where the refrigerant is expanded to provide cooling referred to the cold head, cold end, or coldstage, and the refrigerant compression mechanism such as a compressor or compressed gas cylinder. Significant research and development into the miniaturization of the cold head of cryogenic coolers has been accomplished over the past 30 to 40 years. However the major bottleneck is the miniaturization of the compression mechanism. Self-contained regenerative refrigeration cycle based devices have reached a size limit for the compression mechanism due to the low frequencies required for operation. Joule-Thomson cycles operate with a continuous flow and no moving parts outside the compression mechanism. This makes JT cycles the best candidate for miniaturization. Allowing the compressor to operate at high frequencies reduces the needed compression volume to maintain the same flow of refrigerant. However micro-compressor technology is in its infancy with the best performance wafer scale compressor only able to achieve low compression ratios of 1.2:1 [3]. Mini-compressors have been developed capable of compression ratios of 4:1 to 16:1 [4]–[6].

This thesis reports the development of low pressure ratio cascaded Joule-Thomson based coldstage. Through the use of a cascaded design the required compression ratio can be significantly reduced allowing a larger design space for future micro-compressor development. The details of the design, fabrication, and characterization of a cascaded Joule-Thomson cryogenic coldstage is presented and discussed in this thesis.

1.2 The Joule-Thomson (JT) Refrigeration Cycle

Figure 1.1 shows a basic thermodynamic system and a temperature-entropy diagram for a JT refrigeration cycle. The low pressure refrigerant is initially compressed to a high pressure (Figure 1.1, a-b), the heat of compression is rejected to ambient (Figure 1.1, b-b'), and the refrigerant is pre-cooled via a recuperative heat exchanger and liquefied at some lower temperature (Figure 1.1, b'-c). The liquid refrigerant then undergoes isenthalpic expansion when forced through a small restriction (Figure 1.1, c-

d) causing the refrigerant pressure to drop. The refrigerant boils and lifts heat from the cold end of the refrigeration device (Figure 1.1, d-e). The cold vapor refrigerant flows back to the compressor through the recuperative heat exchanger precooling the high pressure refrigerant (Figure 1.1, e-a).

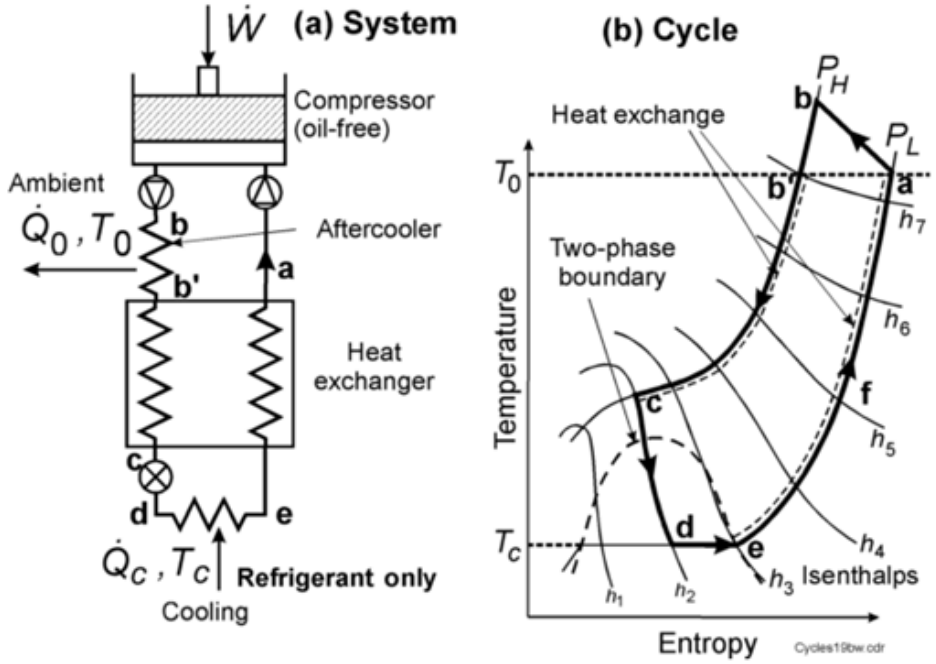

Figure 1.1: Basic JT (a) Thermodynamic System and (b) Temperature Entropy Diagram [7].

The ideal gross refrigeration power for a JT refrigeration cycle is [8]

$$\dot{Q}_r = \dot{m}(\Delta h|_T)_{min} \tag{1.1}$$

where $\dot{Q}_r$ is the ideal gross refrigeration power, $\dot{m}$ is the molar flow rate of the refrigerant, and $(\Delta h|_T)_{min}$ is the minimum enthalpy difference between the high and low pressure states of the refrigerant over the temperature range of cooling. The calculation of gross refrigeration power assumes ideal adiabatic expansion and perfect heat exchange. Any heat exchanger inefficiency or deviation from ideal adiabatic expansion decreases the gross refrigeration available.

JT refrigeration cycles are ideal for miniaturization because there are no moving parts outside the compression mechanism and the refrigerant flow is continuous. Having no moving parts in the cold

end of the device allows for simple micro-fluidic design of the heat exchanger and JT restriction. Continuous flow of the refrigerants allows for miniaturization of the compressor through high frequency operation of a micro scale compression volume. Modern Stirling cryogenic coolers are size limited because the refrigeration cycle operates at low frequencies demanding a relatively large minimum compression volume. Lewis et al. [2] highlight the unique design space afforded by the advantages of the JT refrigeration cycle in Figure 1.2. Indicating a size reduction of 10 times over modern Stirling coolers and an efficiency increase of 10 times higher than modern thermos-electric (TE) coolers is possible with proper miniaturization of the coldstage and compressor for JT based coolers.

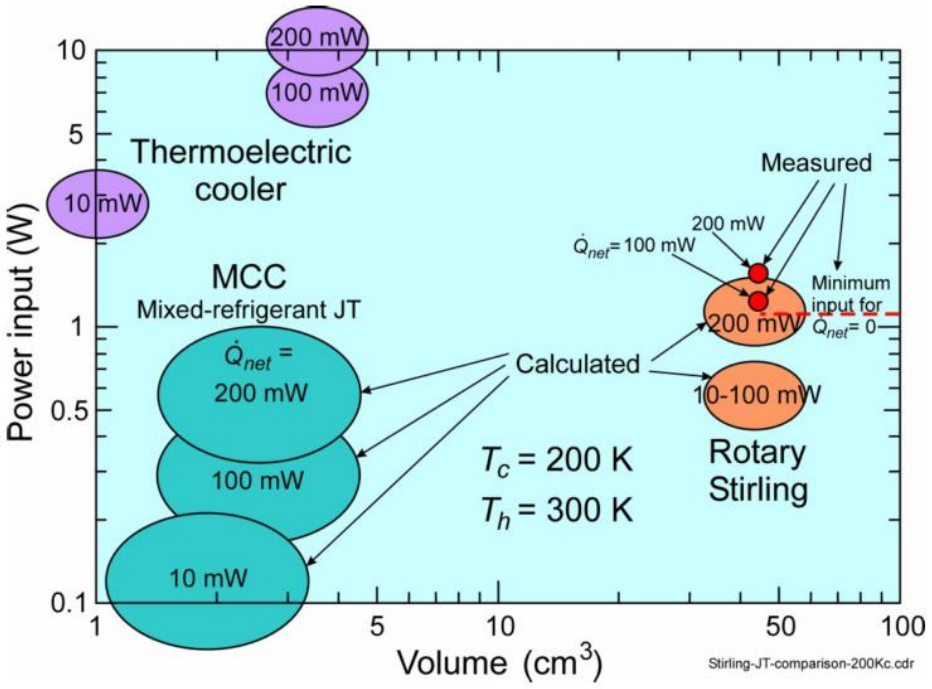

Figure 1.2: Comparison of device volume and input power for theoretical JT coolers, modern Stirling coolers, and thermos-electric coolers for net refrigeration powers of hundreds of milliwatts [2].

1.3 Previous Works on JT Coolers

Considerable research and development has been devoted to the miniaturization of the coldstage of JT coolers over the last several decades. However the major bottleneck for miniaturization

of JT coolers remains the compression mechanism. This section details the current state of development of miniature JT coolers and the importance of low pressure ratios for compressor miniaturization.

First the state of the art for modern vapor compressors is discussed to understand the importance of minimizing the pressure ratio required for JT cooler operation. Ideally oil free compressors are used for compression in JT coolers. If an oiled compressor is used an oil trap is needed to remove any contamination from the refrigerant to avoid clogging and poor performance. Table 1.1 summarizes a selection of state of the art compressors. In general pressures greater than 10 MPa are required for single refrigerant JT coolers using refrigerants such as N_2 and O_2. And pressures of 0.4 to 1.6 MPa are generally required for mixed refrigerant JT coolers. The best truly micro scale compressor is a wafer level fabricated three Si wafer stack compressor developed by Yoon et al. [3], [9]. However this compressor is not capable of delivering the pressure required for a JT refrigeration cycle. Modern compressor technology is not capable of providing the pressures needed for a JT cooler while maintaining a micro sized device volume. This highlights the importance of designing JT coldstages to operate with low pressures to expand the design space for future micro-compressor development.

Table 1.1: Summary of State of The Art Compressors

Compressor	Max Discharge Pressure at Opperational Flow Rate (MPa)	Opperational Flow Rate (sccm)	Volume (cm^3)	Source
Rix SA-6	31	3000	213000	[10]
Rix Microboost	15	7500	33000	[11]
FLIR w/ Rectifying Check Valves	1.6	50	252	[5]
Aspen Mini-Compressor	0.65	42	171	[6], [12]
PZT Driven Membrane Compressor	0.4	3	48	[4]
PZT Driven Membrane Compressor	0.2	2	61	[13]
Wafer-scale Compressor	0.12	3	1.8	[3], [9]

Micro-machined Joule-Thomson coolers have been studied over the last 30 years. In 1983 and 1984 Little [14] and Garevey et al. [15] proposed and demonstrated the first use of micro-machining techniques to make glass based micro-channels for a JT refrigeration cycle. The device developed is shown in Figure 1.3. The devices made were 0.5 x 2 x 15 mm in size and cooled to a temperature of 88 K with a cooling power of 25 mW. The devices used liquid nitrogen as the refrigerant operating at a high pressure of 13.6 MPa. Little goes on to explain the major bottleneck for miniaturization of closed loop JT coolers is not the cold head but the compressor. Noting the state of the art either runs in an open loop configuration with high pressure refrigerant running straight from a compressed bottle or in a closed loop configuration using small commercially available compressors designed for use in household refrigerators [16].

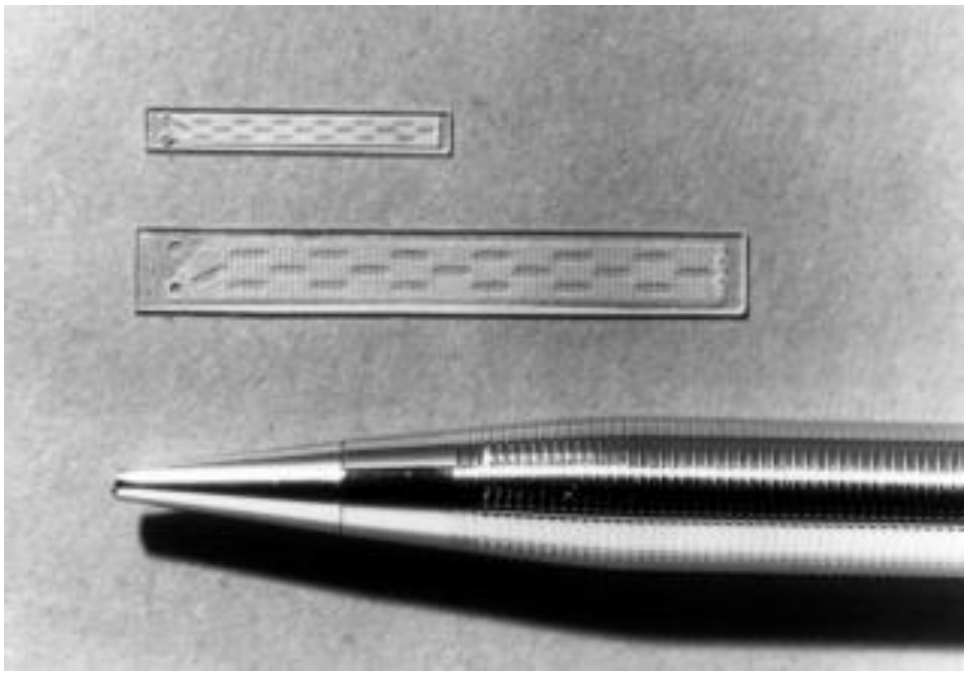

Figure 1.3: Micromachined coldstage presented by W. A. Little. The smallest device is a 25 mW 88 K cooler that is 15 mm long, 2 mm wide and 0.2 mm thick [14].

Little's work has been commercialized by MMR Technologies [17]. The coldstage is intended for laboratory use in a vacuum chamber with N_2 as the refrigerant supplied from a high pressure cylinder. The coldstage operates at a pressure ratio of 12.5:0.1 MPa and can provide a net refrigeration power of 250 mW at a cold end temperature of 85 K. Figure 1.4 shows the coldstage mounted to a vacuum flange.

Figure 1.4: MMR Technologies microminiature refrigerator mounted to a vacuum flange [17].

Kryoz Technologies [18] have developed a commercially available benchtop JT cryogenic cooling system. The full benchtop cooler is shown in Figure 1.5 and the coldstage is shown in Figure 1.6. The coldstage is run directly from a high pressure refrigerant cylinder. It is capable of coolign to 80 K with a available refrigeration power of 75 mW using N_2 as a refrigerant at a 9.5:0.1 MPa pressure ratio.

Figure 1.5: Kryoz Cryolab MSG 75 benchtop cryogenic cooler [18].

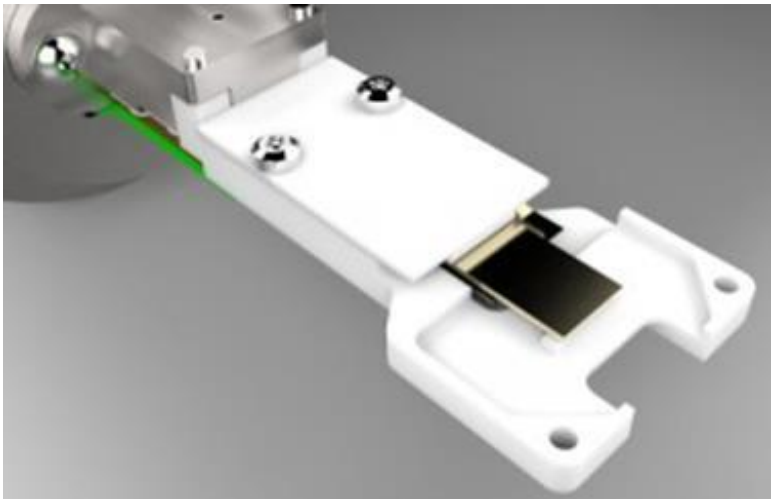

Figure 1.6 Kryoz Cryolab MSG 75 coldstage [18]*. Cold end is 1 cm x 1 cm.*

Brake et al. [19], [20] have improved on the glass micro-machined design and demonstrated coolers capable of cooling to 96K with a cooling power of 10 mW using nitrogen as the refrigerant at a pressure ratio of 8:0.6 MPa significantly reducing the pressure required for operation. Figure 1.7 shows the coldstage developed by Brake et al. [20] using a three glass wafer stack. The coldstage is run directly from a high pressure refrigerant cylinder.

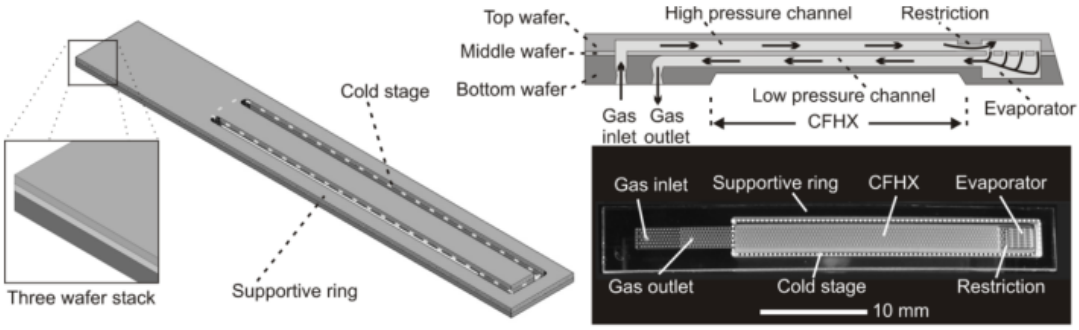

Figure 1.7: Basic design of 3 glass chip stack presented by Brake et al. [20]*. Showing the cold stage isolated from the supporting chip, the cross section, and fabricated coldstage.*

Macro-fabrication techniques such as tube in tube heat exchangers with capillary restrictions [21], [22] and coiled tube heat exchangers with small orifice restrictions [23], [24] have also shown promise with significant commercialization. Widyaparaga et al [21], [22] demonstarte a coldstage consisting of a long tube in tube heat exchanger with a small capillary restriction designed for cryo-

surgery shown in Figure 1.8. It is capable of coolign to 225 K with a available refrigeration power of 100 mW using CO_2 as a refrigerant at a 2:0.1 MPa pressure ratio. The coldstage is run directly from a high pressure refrigerant cylinder. LeTehnika [23], [24] manufactures coldstages with high pressure ratio and high flow rates for rapid cooling of missile guidance systems. A cross-section of one of LeTehnika's coldstages is shown in Figure 1.9. It is capable of coolign to 100 K with a available refrigeration power of 10 W using N_2 as a refrigerant at a 42:0.1 MPa pressure ratio. The coldstage is run directly from a high pressure refrigerant cylinder.

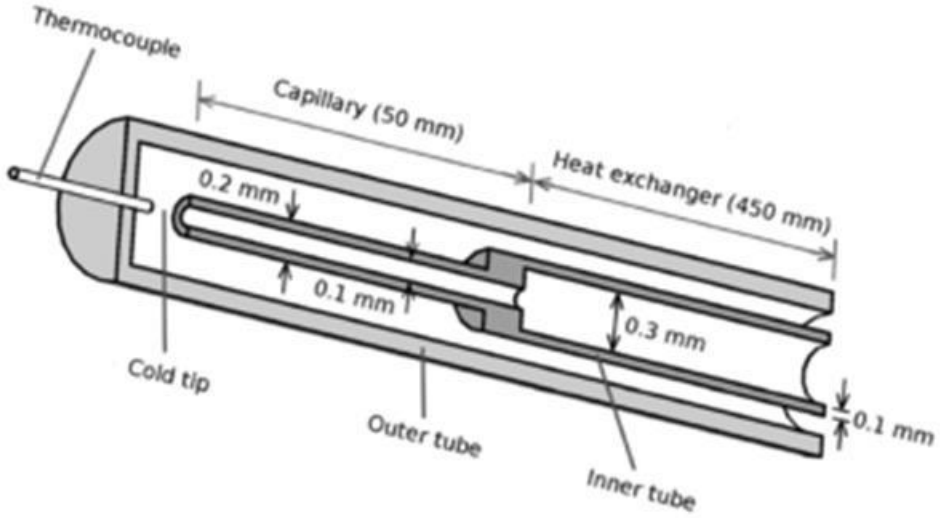

Figure 1.8: Coldstage presented by Widyaparaga et al. [21] *consisting of a long tube in tube heat exchanger and a small capillary restriction.*

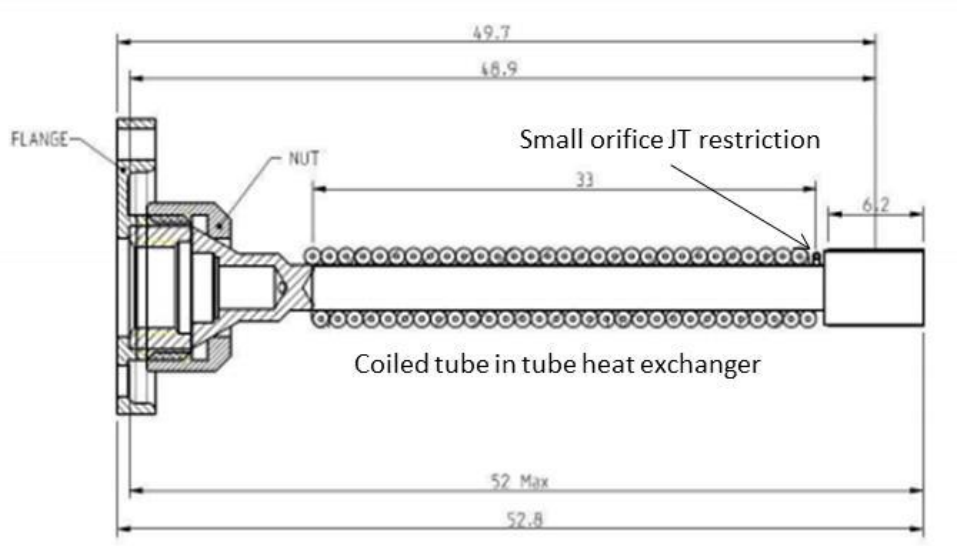

Figure 1.9: LeTehnika [23] *coldstage with coiled tube in tube heat exchanger and small orifice JT restriction.*

The previous coolers all use N_2 or CO_2 as a single component to achieve cryogenic cooling. Single component refrigerants require very high pressure ratios greater than 8:0.1 MPa for normal operation. These high pressures are not achievable through state of the art micro-compressor or mini-compressors. In an attempt to reduce the pressure required researchers have favored the use of custom mixed refrigerants. Mixed refrigerants generally consist of a selection of various hydrocarbons that liquefy at different temperatures within the range of cooling. Mixed refrigerants allow for much lower pressure ratios of around 0.4:0.1 MPa to 1.6:0.1 MPa with an order of magnitude higher specific refrigeration power when compared to single refrigerants operating at the same low pressure ratio [8]. Single refrigerant systems have a low specific refrigeration power when operated at low pressure ratios because no liquefaction occurs at these low pressures. Thus no phase change occurs across the JT restriction.

Lin et al. [25] used a custom mixed refrigerant to significantly reduce the pressures required for operation when compared to single refrigerants. Lin et al. [25] demonstrated a cooler using Si and glass micro-machining to form the JT restriction and hollow glass fibers to form the heat exchanger. The

cooler was able to cool to 140 K with a pressure ratio of 1.6:0.1 MPa. Figure 1.10 shows the coldstage developed by Lin et al.

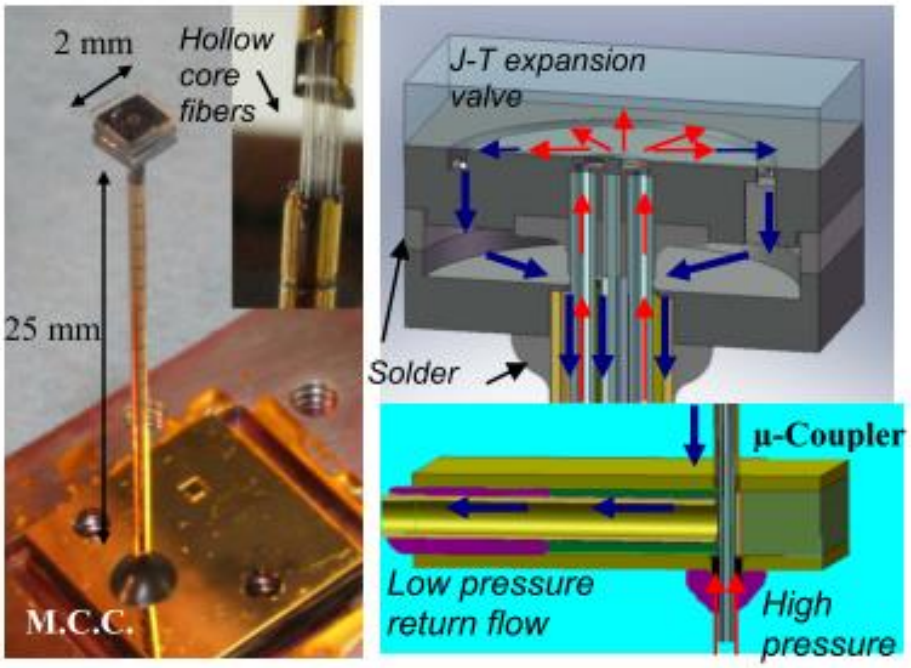

Figure 1.10: Coldstage developed by Lin et al. with 3D model cross section [25].

Wang et al. [26] improved on this work by fabricating the heat exchanger out of polyimide using micro-fabrication techniques. The micro-fabrication process uses alternating layers of structural polyimide and sacrificial copper. At the end of the micro-fabrication process all copper is removed via wet chemical etch and a polyimide structure containing micro-channels remains. The JT restriction is made using the same glass and silicon micromachining approach developed by Lin et al. [25]. This coldstage was able to cool to 233 K using a mixed refrigerant at a pressure ratio of 0.7:0.15 bar [27]. Figure 1.11 shows the coldstage fabricated by Wang et al. and Figure 1.12 shows a cross-sectional schematic of the coldstage.

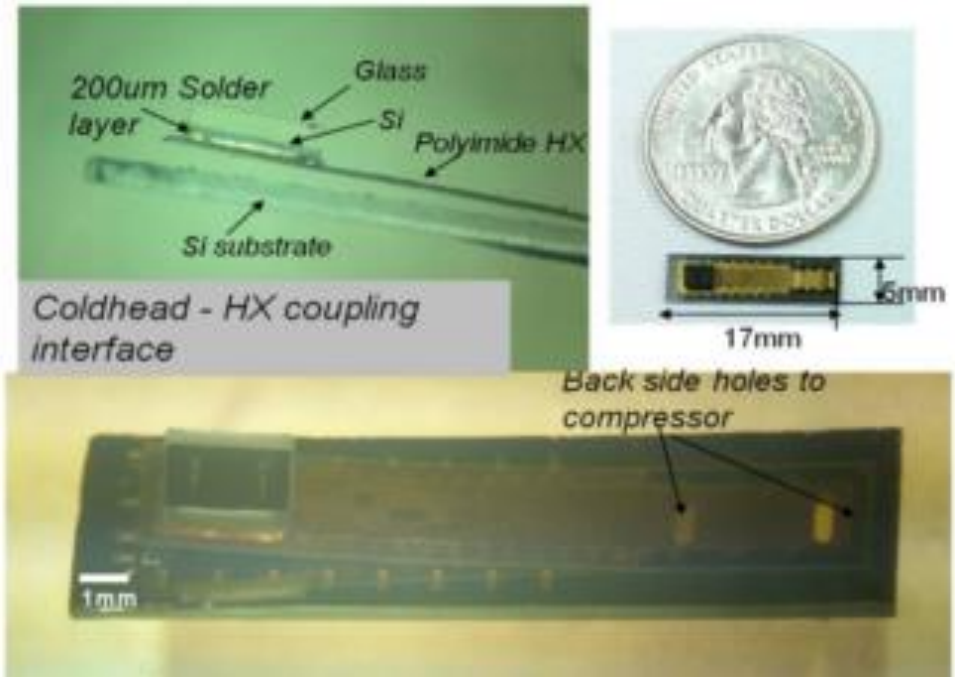

Figure 1.11: Coldstage presented by Wang et al. using a micro-fabricated polyimide based heat exchanger and a glass on silicon JT restriction [26].

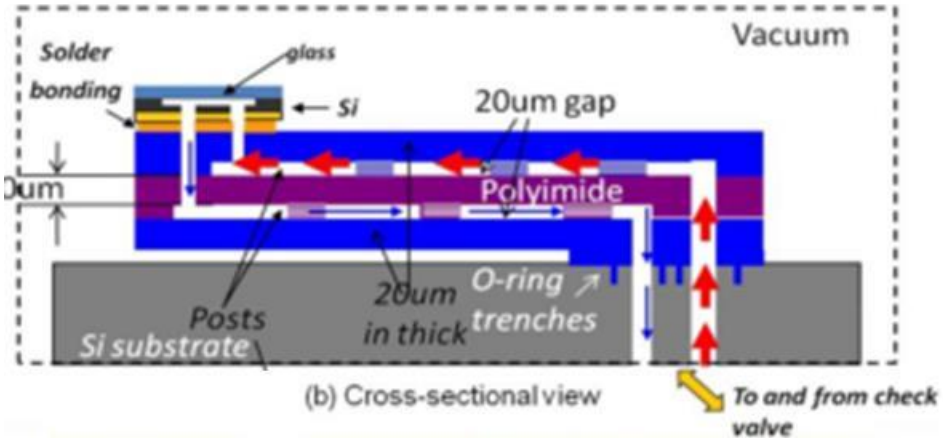

Figure 1.12: Cross-section of coldstage presented by Wang et al.[26].

Wang et al. [28] improved their design further by incorporating the JT restriction into the polyimide structure during the fabrication process. A thin 3 µm gap is defined by sacrificial copper at the end of the high pressure channel to create the JT restriction. Figure 1.13 shows a cross-section of the coldstage. This coldstage cooled to 200 K with a cooling power of 5 mW using a mixed refrigerant at a 0.55:0.1 MPa pressure ratio. Figure 1.14 shows the coldstage fabricated by Wang et al.

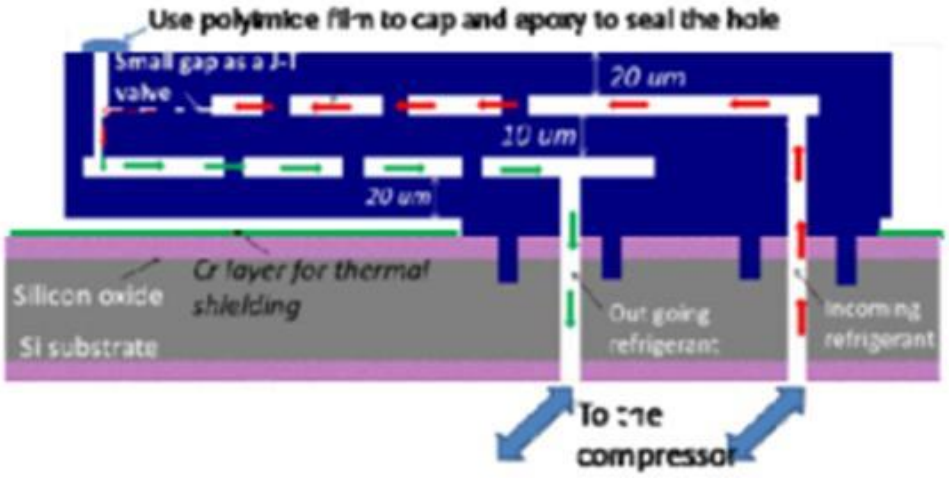

Figure 1.13: Cross-section of polyimide coldstage with integrated JT restriction developed by Wang et al. [28].

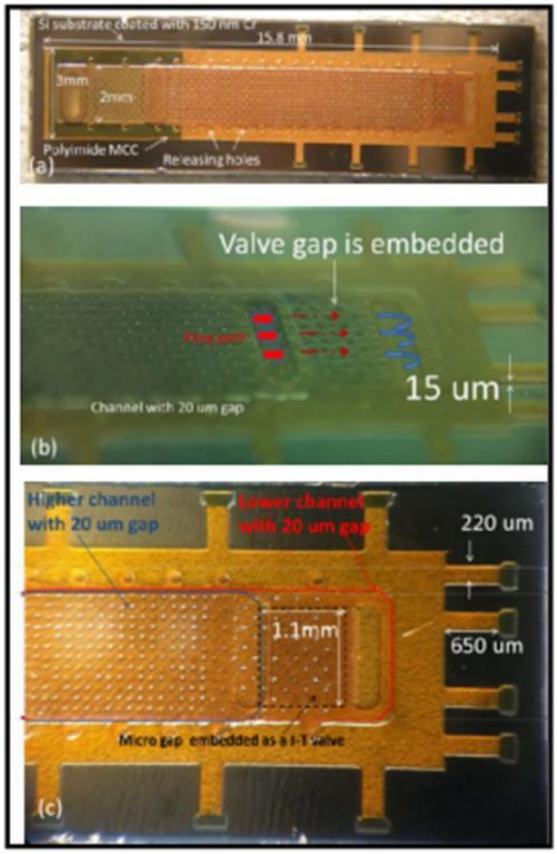

Figure 1.14: Monolithic polyimide coldstage presented by Wang et al. [28].

Gong et al. [6] present a macro-fabrication technique for a precision machined finned heat exchanger with small orifice restriction designed for use with a mixed refrigerant shown in Figure 1.15.

The coldstage is capable of coolign to 120 K with an available refrigeration power of 4 W using a custom mixed refrigerant at a 1.6:0.15 MPa pressure ratio.

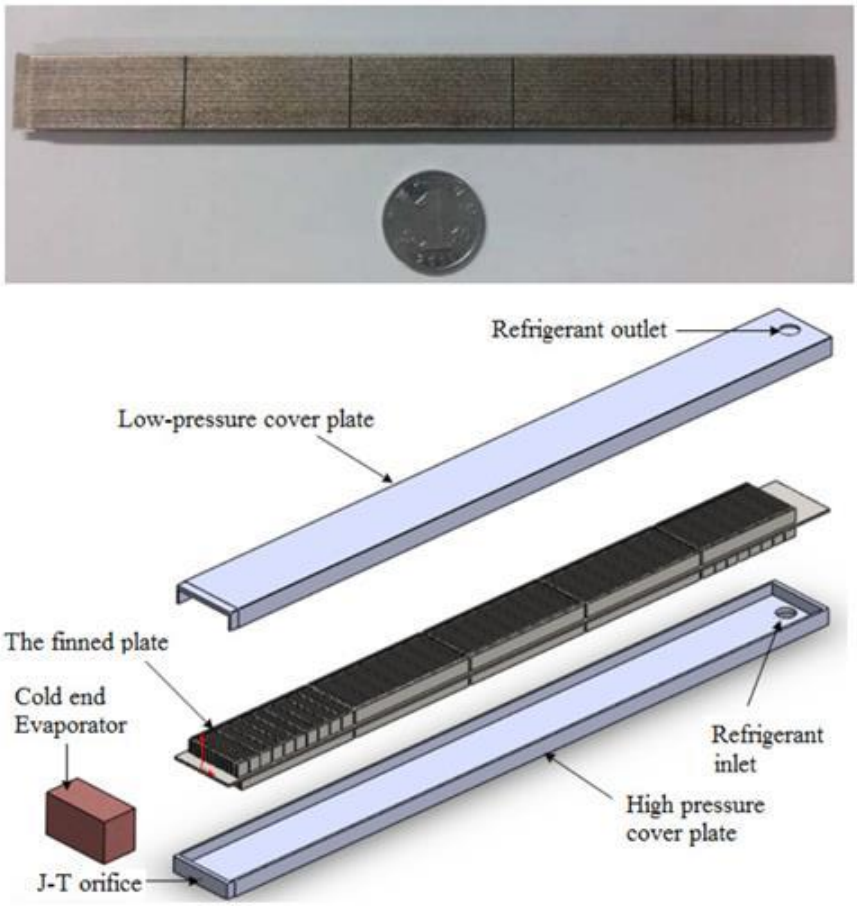

Figure 1.15: Coldstage presented by Gong et al. [6] *with precision machine heat exchanger and small orifice JT restriction.*

Mixed refrigerants have less than ideal behavior when practically implemented as reported by Lewis et al. [29]. It is shown that liquefaction of mixed refrigerants does not occur simultaneously for all components of the refrigerant. Instead the heavier components liquefy prior to the lighter components. The liquefied portion of the refrigerant collects on the side walls of the channels due to minimization of surface energy and remains motionless until a critical volume is reached where the liquid completely fills the channel cross section. At this critical volume a slug of liquid refrigerant is formed and flows through the cold stage. The stratification of the refrigerant causes pulses of pure liquid and pure vapor with

intermediate zones of two phase flow to move through the cold stage. The pulsed flow through the device leads to a nonhomogeneous refrigerant with lower refrigeration power than the theoretical homogeneous refrigerant. The pulsed flow also leads to unstable cooling due to both the vapor phase and liquid phase refrigerant having different specific refrigeration capacities. Lewis et al. [29]present a method to predict the stratification of mixed refrigerants as well as a method of minimizing the impact. However no solution to eliminate the stratification is presented.

1.4 Cascaded Opportunity

In an attempt to minimize required pressures and eliminate the use of mixed refrigerants a 5 stage cascaded cryogenic cooler design is proposed using a series of self-contained single refrigerant JT coldstages. In this design each single stage JT cycle is used to precool the following stage. This precooling allows the next stage refrigerant to liquefy at a low pressure and the low temperature of the cold end of the preceding stage. R. Radebaugh [30] performed the initial theoretical thermodynamic analysis of a 5 stage cascaded cooler. This analysis found cascading 5 stages together at a 0.4:0.1 MPa pressure ratio allows the final stage to reach a temperature of 150 K. Figure 1.16 shows the basic thermal resistance network for the 5 stage cascaded design. It incorporates intra-stage recuperative heat exchangers for basic JT cycle recuperation and inter-stage isothermal heat exchangers for precooling of each successive stage.

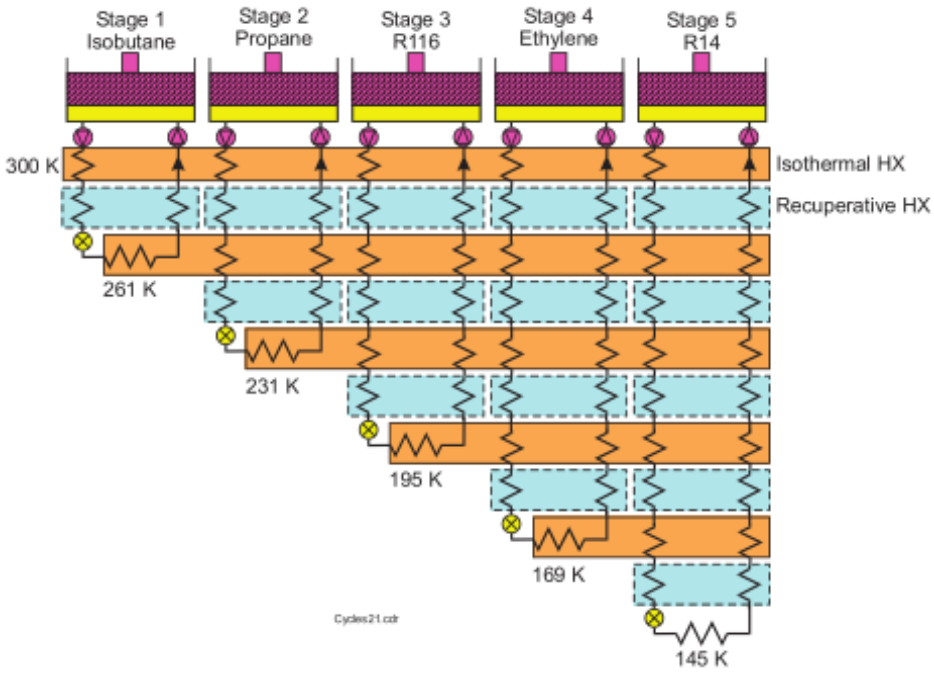

Figure 1.16: Basic thermodynamic model of a 5 stage cascaded JT cryogenic cooler [30].

This cascaded design incorporates the benefits of refrigerant stability of single refrigerant devices with the low pressures of mixed refrigerant devices. Another advantage to the cascaded coolers is the relatively high specific refrigeration capacity. The design presented by Radebaugh et al. [8] has an order of magnitude higher specific refrigeration capacity when compared to a 5 component mixed refrigerant optimized for the same 300 – 150 K temperature range as shown in Figure 1.17. This allows the cascaded cooler to be run at lower flow rates to achieve the same net refrigeration power.

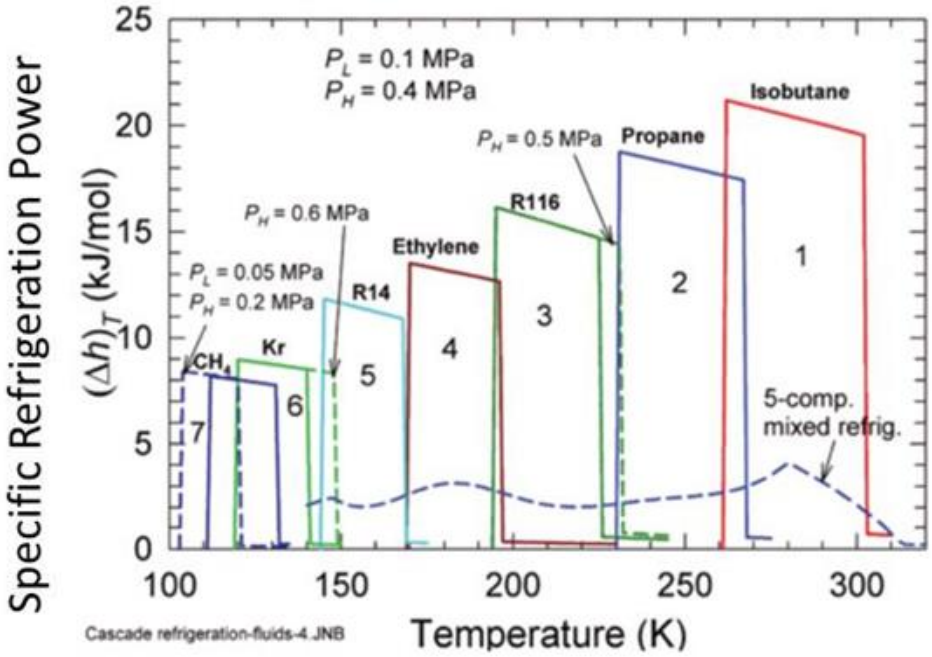

Figure 1.17: Specific refrigeration power for a selection of single component refrigerants and a 5 component mixed refrigerant operating at a 0.4:0.1 MPa pressure ratio over the temperature range of 300 – 150 K [8].

Because each stage in this cascaded design is operating over a small temperature range there is no need for recuperative heat exchangers within each cascaded stage [8]. The only requirement is the efficient exchange of heat between each stage in order to properly liquefy the refrigerant in each succeeding stage [8]. Recuperative heat exchangers can be added to increase efficiency [8]. In contrast the 5 component mixed refrigerant single stage coldstage presented by Wang et al. [27] needs a 90% effective recuperative heat exchanger in order to not lose all refrigeration power to heat exchange ineffectiveness [8].

The basic layout for a polyimide based 3 stage cooler based on the fabrication techniques developed by Wang et al. [27], [28] was developed. The layout presented follows the basic thermal model designed by R. Radebaugh [30] shown in Figure 1.16 but with modified isothermal heat exchangers. In designing a practical layout we found only the isothermal heat exchange between immediately adjacent stages is critical. Modifying the isothermal heat exchangers as shown in Figure

1.18b leads to only a small loss in overall device efficiency, increasing the ideal input power from 0.218 W to 0.226 W for a net refrigeration power of 0.35 W. Figure 1.19 shows the theoretical layout of a 3 stage coldstage. The high pressure channels are placed on the bottom layer and connected to a JT restrictions on the top layer via a vertical interconnect then the low pressure channels return to the warm end of the coldstage on the top layer. This design provides efficient isothermal heat exchange between each immediately adjacent stage as well as efficient intra-stage recuperative heat exchange.

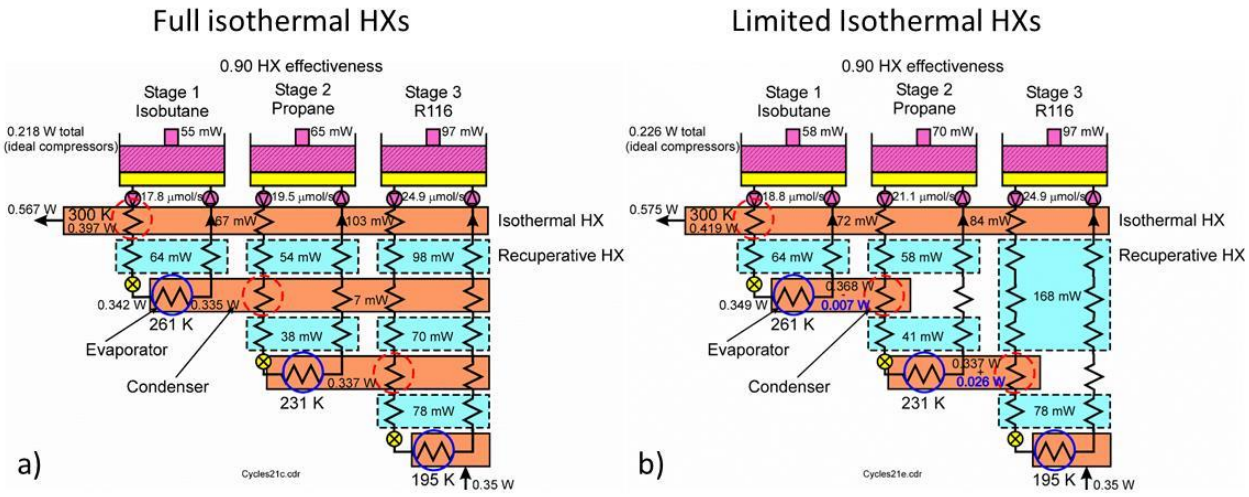

Figure 1.18: Comparison of a) ideal isothermal heat exchangers to b) modified isothermal heat exchangers for ease of coldstage layout and fabrication (figure developed by R. Radebaugh).

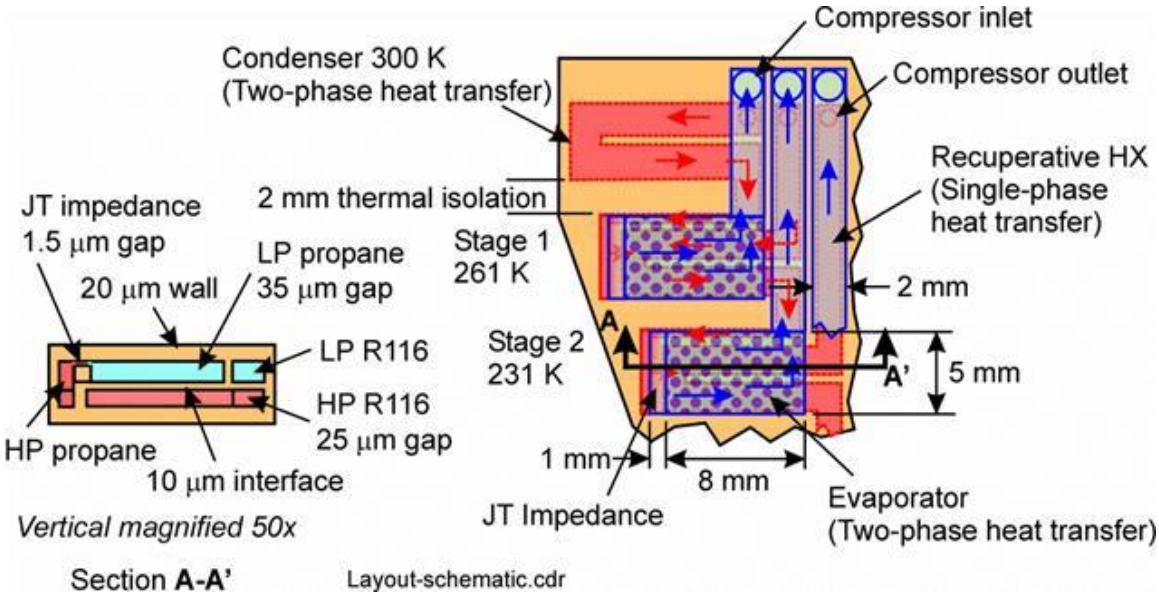

Figure 1.19: Initial layout for a micro-fabricated 3 stage cascaded JT cryogenic coldstage [8].

In reviewing this design we found having all stages utilize both channel layers each requiring a separate fabrication step and requiring the use of vertical channel connections introduced significant challenges to practical fabrication. In an attempt to eliminate these fabrication challenges we investigated the possibility of having each stage be self-contained on a single device layer. A new layout was found that eliminates the use of any vertical connection between separate channel layers. Furthermore we found with proper device spacing only two micro channel layers are required where stages 1, and 3 are on the first (bottom) channel layer and stage 2 is on the second (top) channel layer. This layout provides efficient isothermal heat exchange between immediately adjacent stages (eg. Stage 1-2, stage 2-3) but sacrifices the use of intra-stage recuperative heat exchangers. However with proper channel overlap we can introduce inter-stage recuperative heat exchangers to slightly increase our efficiency when compared to a design without any recuperative heat exchange. This design increase our ideal input power from 0.228 W to 0.355 W for a net refrigeration power of 0.35 W. Figure 1.20 shows the thermodynamic resistance model and Figure 1.21 shows a 3D model of a proposed 3 stage device fabricated using the same polyimide micromachining techniques developed by Wang et al. [27], [28]. This design is studied by the coldstages investigated in this work.

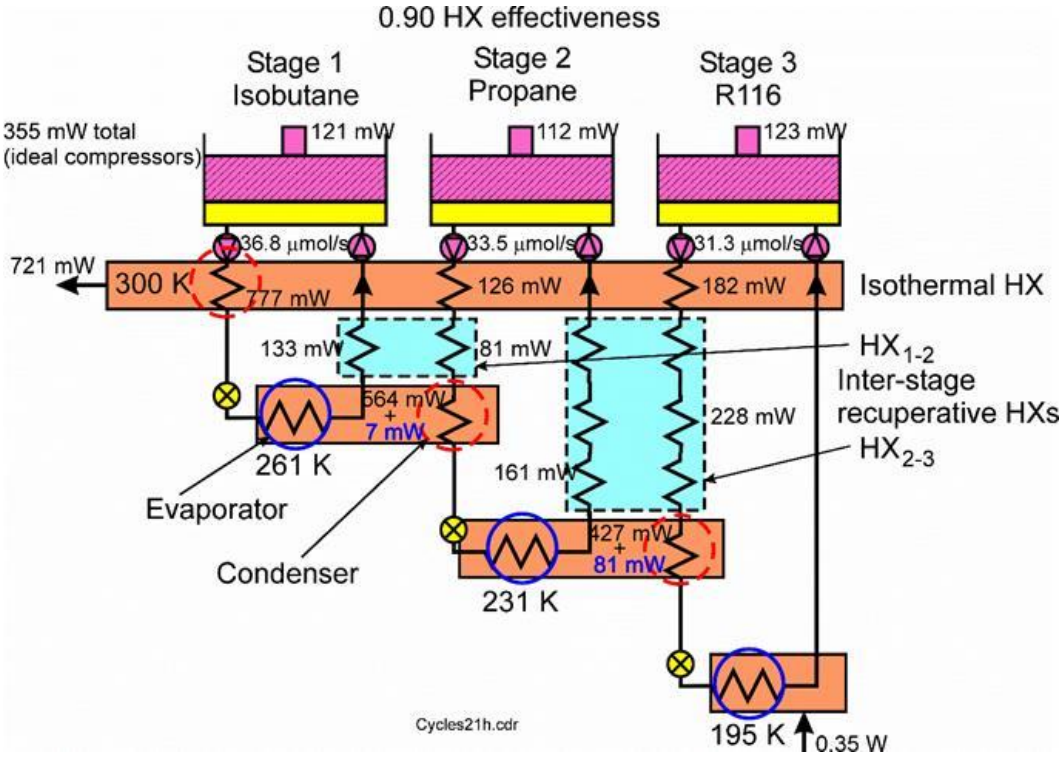

Figure 1.20: Thermodynamic resistance model for a three stage cascaded JT cryogenic coldstage without intra-stage recuperative heat exchangers. Inter-stage recuperative heat exchangers are used to increase efficiency (figure by R. Radebaugh).

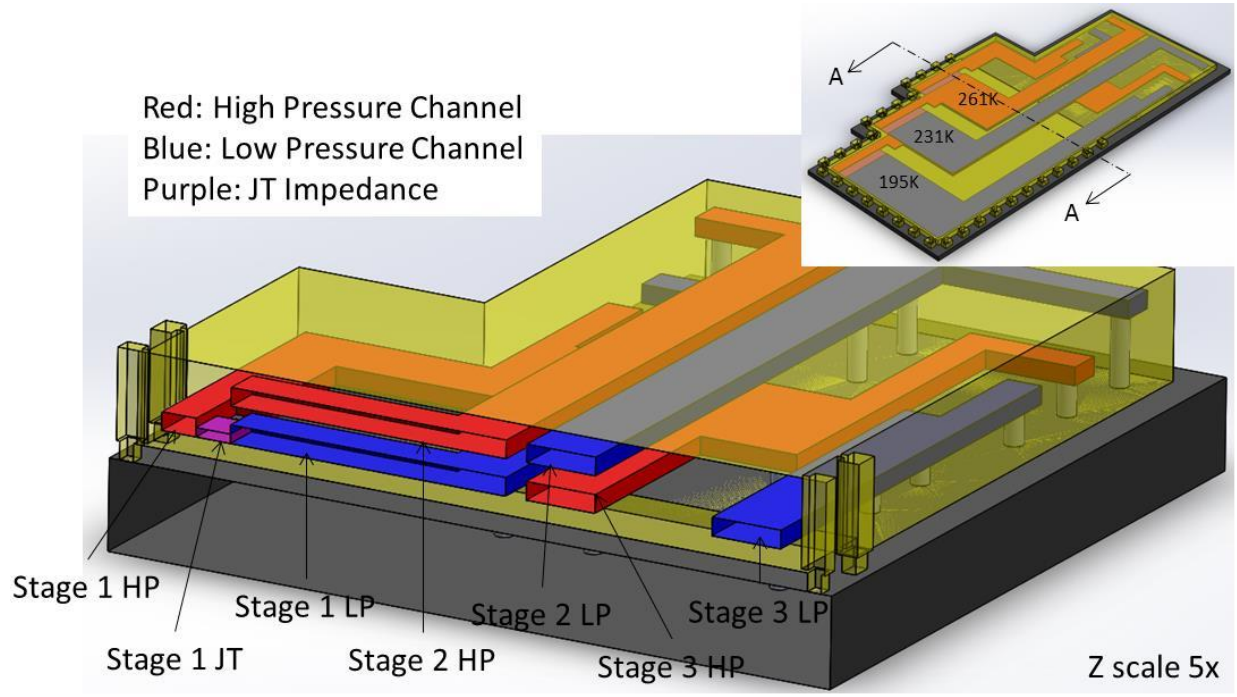

Figure 1.21: Basic 3D model of initial design for a three stage cascaded cryogenic coldstage without intra-stage recuperative heat exchangers. Stages 1 and 3 are on the bottom channel layer and stage 2 is on the top channel layer.

1.5 Previous Cascaded Joule-Thomson Coolers

Continuing the research based on three glass wafer stacks by Brake et al. [19], [20] Cao et al. [31], [32] designed and developed a two stage cascaded cooler using N_2 as the refrigerant for the first stage operating at a pressure ratio of 8.5:0.1 MPa to pre cool the second stage to 95 K. The second stage uses H_2 as a refrigerant operating at a pressure ratio of 6:0.6 MPa to provide 30 mW of net cooling power at 30K. Figure 1.22 shows the coldstage developed by Cao et al. [32]. The coldstage follows the ideal thermodynamic circuit for two stages cascaded together where there is full use of intra-stage recuperative heat exchangers. Each stage of the coldstage uses both top and bottom channel layers with a vertical connection similar to the design presented by Brake et al. [20] in Figure 1.7.

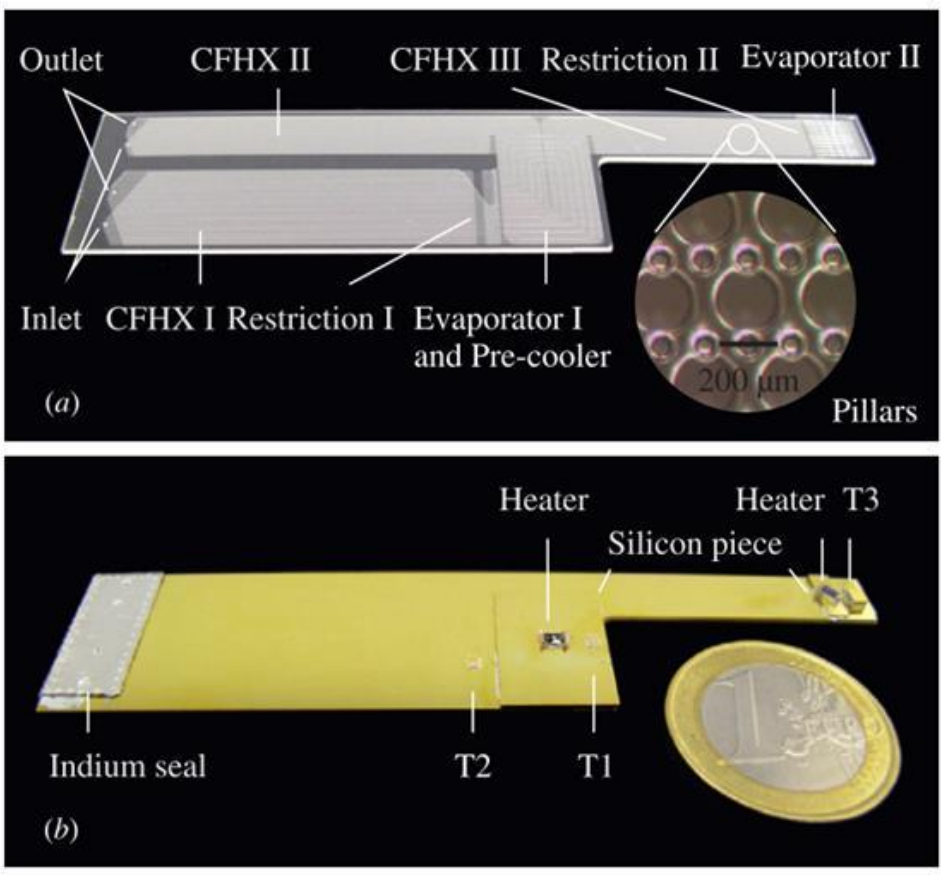

Figure 1.22: 2 stage cascaded JT cryogenic coldstage presented by Cao et al. [32].

1.6 Summary of State of The Art JT Coolers and Work Presented In This Thesis

Table 1.2 summarizes the state of the art JT coolers discussed previously and the two cascaded coldstages presented in this work in chapters 4 and 5. The Efficiency is calculated assuming 100% efficient compression as no compressors are used to run these coldstages. For a practical closed loop system with a coldstage integrated with a micro-compressor the compressor efficiency and size will need to be accounted for. Figure 1.23 plots the device size and efficiency versus coldstage size for the JT coolers presented in Table 1.2 along with several commercial Stirling and thermo-electric coolers. Figure 1.23 highlights the unique design space afforded by JT based cryogenic coolers. The opportunity exists for JT based micro-coolers to be orders of magnitude smaller than Stirling coolers with higher efficiencies than thermos-electric coolers with proper compressor miniaturization.

Table 1.2: Summary of State of the Art JT Coldstages

Coldstage Description	Temperature Range of Cooling (K)	Pressure Ratio (MPa)	Coldstage Size (cm^3)	Efficiency (% Carnot Assuming 100% Efficient Compression)
Single Refrigerant Coolers				
Glass Capillary Restriction w/ Tube in Tube HX [22]	300 – 225	2:0.1	0.5	0.7%
MEMS Glass on Glass Planar Coldstage [20]	300 – 96	8:0.6	0.06	18.8%
1st Micro-machined Coldstage (Glass on Si) [14]	300 – 88	12:0.1	0.03	6.2%
MEMS Glass on Glass w/ 2 Expansion Valves In Parallel [33]	300 – 83	8.5:0.1	0.57	40.7%
MEMS Glass on Glass w/ TE Precooling [34]	300 – 100	8.5:0.1	0.57	13.6%
MMR Technologies Off the Shelf JT Cooler [17]	300 – 70	12.5:0.1	3.5	6.5%
Kryoz CryoLab MSG 75 SQUID Benchtop Cooler [18]	300 – 80	9.5:0.1	1	6.0%
Le Tehnika Self-Regulated Cooler [23]	300 – 78	42:0.1	2.7	22.2%
Le Tehnika Dual Flow Cooler [24]	300 – 80	42:0.1	1.5	22.2%
Mixed Refrigerant Coolers				
MEMS Glass on Si Restriction w/ Glass Capillary Based HX [35]	275 - 200	1.6:0.1	0.1	12.5%
MEMS Polyimide Based Monolithic Coldstage [27], [28]	300 - 200	0.55:0.11	0.05	1.5%
Macro-machined Stainless Steel HX w/ Machined Restriction [6]	300 - 120	1.6:0.15	2.63	42.0%
Single Refrigerant Cascaded Coolers				
MEMS Glass on Glass 2 Stage Nitrogen and Hydrogen [32]	300 - 30	8.5:0.11 N_2 6:0.57 H_2	1.8	1.8%
Two Stage Low Pressure Ratio Glass Capillary Restriction w/ Kapton Tube in Tube HX (Chapter 4)	300 - 228	0.4:0.1 CH_4 & C_3H_8	4.5	26.6%
Three Stage Low Pressure Ratio Glass Capillary Restriction w/ Kapton Tube in Tube HX (Chapter 5)	300 - 193	0.4:0.1 CH_4 & C_3H_8 0.5:0.1 R116	4.5	3.2%
Theoretical design of Low Pressure Ratio 5 Stage Cascaded Cooler [8]	300 - 145	0.4:0.1	0.6	72.4%

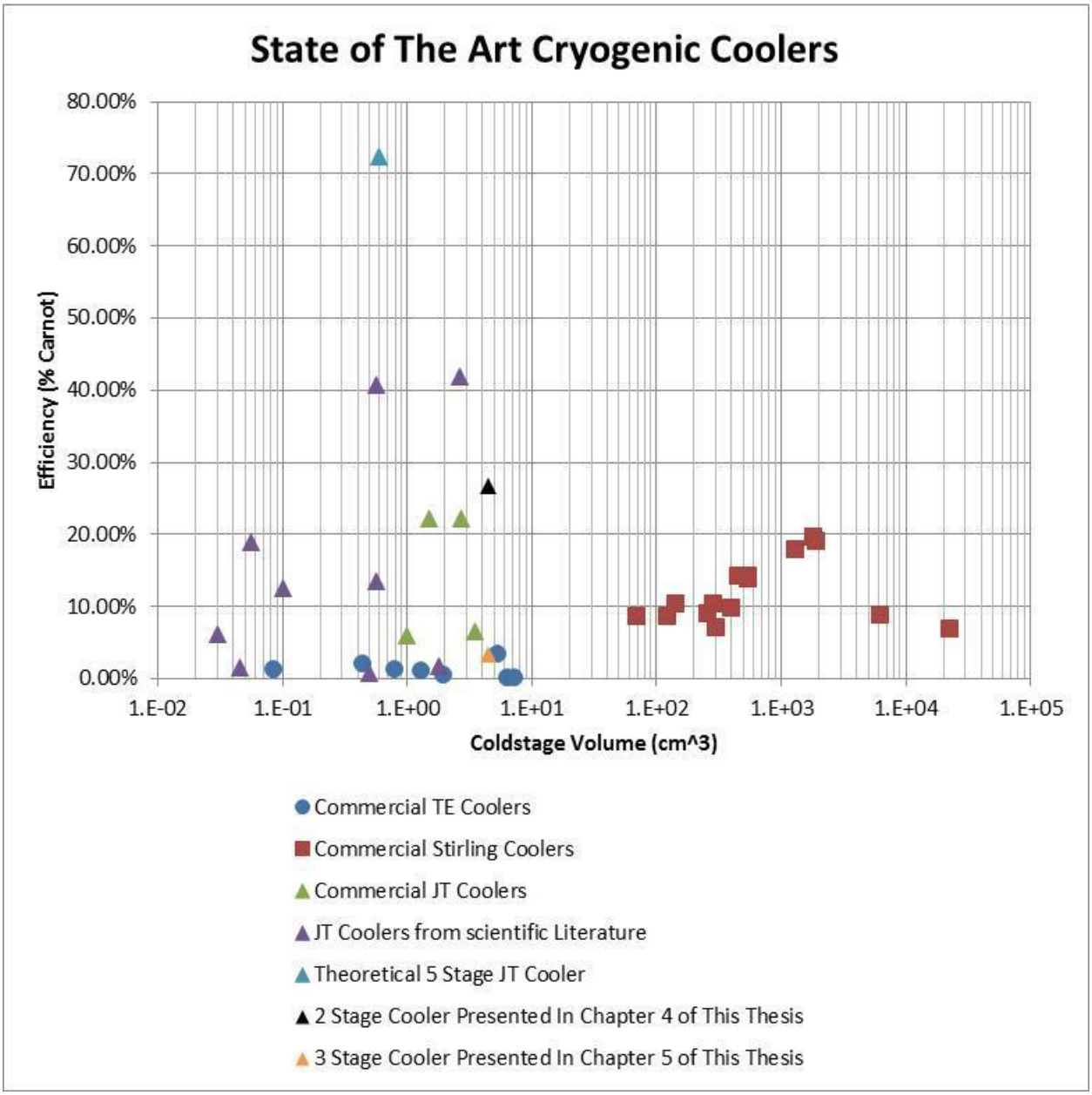

Figure 1.23: State of The Art Cryogenic Cooler comparison of cooler size and efficiency (% Carnot). Commercial Thermo-Electric coolers are blue circle. Commercial Stirling Coolers are red squares. JT coolers are triangles where green are commercial coolers, Purple are coolers published in research literature, Teal is the theoretical 5 stage cooler developed by R. Radebaugh, and black and orange are the cascaded coolers presented in this work (Chapters 4 and 5). JT cooler efficiency assumes 100% efficient compression.

1.7 Thesis Outline

This thesis will present the design, fabrication, and characterization of several coldstages used to investigate the three stage cascaded design proposed in chapter 1.4 with the thermodynamic resistance model presented in Figure 1.20. The cascaded coldstage design is intended to minimize operational pressure ratios to widen the design space available for future micro and miniature compressors. Miniaturization of the compressor is critical to the development of a closed system micro cryogenic cooler, but is outside the scope of this work.

This thesis consists of the following chapters:

(1) An introduction including the project motivation, previous works on micro cryogenic coldstages, the opportunities of cascaded Joule-Thomson coldstages, and a summary of state of the art Joule-Thomson coldstages.

(2) The design, fabrication, and characterization of a polyimide based micro-fabricated single stage coldstage, including major fabrication challenges and solutions with recommended best practices.

(3) The design, fabrication, and characterization of a single stage low pressure ratio low flow rate glass capillary based coldstage, including testing from a high pressure cylinder both in a vacuum environment and in atmospheric conditions and an integration test with a silicon chip based mini-compressor.

(4) The design, fabrication, and characterization of a low pressure ratio glass capillary based two stage cascaded coldstage, including a study of the natural heat leak, net refrigeration power, gross refrigeration power, coefficient of performance, coldstage efficiency, and an investigation of deviation from design.

(5) The design, fabrication, and characterization of a low pressure ratio glass capillary based three stage coldstage for cryogenic temperatures, including a study of natural heat leak, net refrigeration power, gross refrigeration power, coefficient of performance, coldstage efficiency, an investigation of deviation from design, and confirmation of heat exchanger ineffectiveness.

(6) A summary of conclusions of this work and recommendations for future work.

Chapter 2: Single Stage Polyimide Based Micro-Fabricated Coldstage

2.1 Motivation and Summary

The goal of this study is to design, fabricate, and demonstrate the first stage of the proposed three stage cooler introduced in chapter 1.4 with the thermodynamic resistance model presented in Figure 1.20. The coldstage is designed to investigate the feasibility of the fabrication techniques when applied to the relative large device size of the first stage of a cascaded coldstage when compared to previous works [26]–[28], [36], [37]. The large size of the coldstage is driven by the size of the cold end required for efficient heat exchange to a theoretical second stage. The coldstage is fabricated via a monolithic process using polyimide as a structural material and copper as a sacrificial material. The coldstage is designed to use isobutane as the refrigerant operating at a pressure ratio of 0.4:0.1 MPa and a flow rate of 5 sccm to provide 100 mW of net refrigeration power. The coldstage is expected to cool to 261 K when properly insulated in a vacuum environment. Due to low process yield the coldstage was run in a 0.4 MPa environment in order to maintain proper micro channel geometry under 0.4 MPa internal pressure. The coldstage cooled to 280 K when run in a high pressure environment. Significant convective heat leak due to the high pressure environment is believed to cause the coldstage to reach thermodynamic equilibrium at 280 K. Major fabrication challenges include negative copper-polyimide interactions and poor definition of the JT restriction. Future development of the process presented here will allow for the development of low pressure ratio cascaded JT based micro-cryogenic-coldstages.

2.2 Initial Stacked Channel Design

The coldstage presented here is fabricated using microfabrication techniques developed by Wang et al. [26]–[28], [36], [37]. The process uses polyimide as a structural material and copper as a sacrificial material. At the end of the process the copper is removed via a wet chemical etching process to leave behind micro-channels in a polyimide structure. The original single stage coldstage design used a two stacked channel structure where the low pressure channel is on the bottom layer and the high

pressure channel is on the top layer. The stacked channel construction is similar to the design presented by Wang et al. [26]–[28], [36], [37]. Figure 2.1 shows the basic refrigerant flow path, the top down layout of the coldstage, and a cross-section of the recuperative heat exchanger. The design connects the top channel to the bottom channel by etching vertically through the polyimide where the two channels overlap. The etch hole is then capped with Kapton film and epoxy. By stacking the channels a recuperative heat exchanger can be incorporated to pre-cool the incoming high pressure refrigerant. The design incorporates “drumhead” supports to provide mechanical connection of the suspended cold end of the coldstage to the silicon substrate while minimizing thermal conduction. A four hole pattern of through wafer vias is used to make backside connection to match a micro compressor that was designed in parallel. Two other through wafer vias are used to allow refrigerant charging when the coldstage is coupled to the micro compressor. A “tooth” design is used to create an area of isolation for the charging lines as shown in Figure 2.2. These areas can be temporarily sealed by mechanical pressing or permanently sealed by injecting the channel with epoxy. Trenches are etched in the front side silicon around the through wafer vias to provide effective sealing of the polyimide structure to the substrate. Release holes are etched from the top side and back side to allow efficient removal of the sacrificial copper at the end of the process.

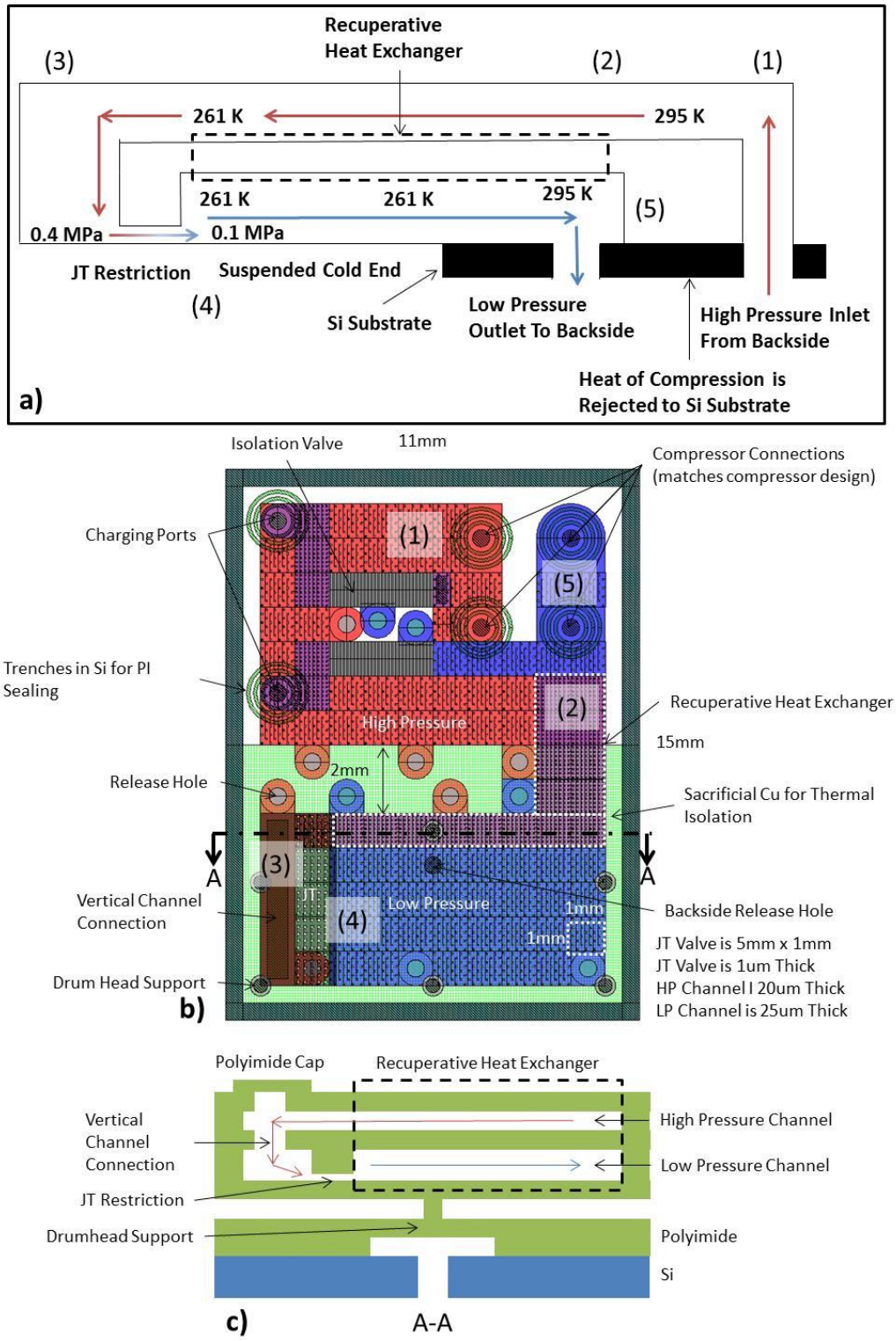

Figure 2.1: a) The general refrigerant flow path with key points marked (1-5). b) A top view of the proposed layout with key points marked. c) A cross-section of the recuperative heat exchanger. In (a) the high pressure refrigerant enters from the backside of the coldstage (1), the heat of compression is rejected to the silicon substrate (1-2), the high pressure refrigerant is pre-cooled via the recuperative

heat exchanger (2-3), the refrigerant is expanded across the JT restriction (3-4), the cold low pressure refrigerant flows through the recuperative heat exchanger (4-5), and exits the coldstage through the backside (5).

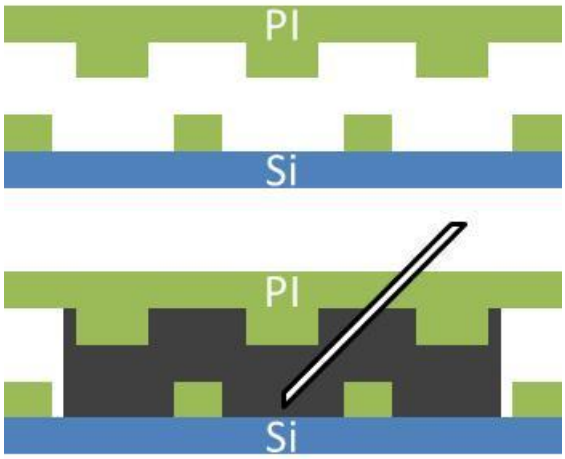

Figure 2.2: Cross-section of the "tooth" design intended to provide temporary and permanent sealing of the refrigerant charging lines.

The initial estimate for the fabrication of this design uses 11 photo masks, 20 major processing steps, and is estimated to take ~6 months to complete. This design can be simplified significantly by removing some minor features and removing the stacked channel aspect of the design without significantly hindering coldstage performance. The "drumhead" support design is changed to a tether design developed by Wang et al. [27], [28] shown in Figure 1.14 and a cartoon presented in Figure 2.3. This eliminates 1 photo mask and 2 major processing steps. The "tooth" design is removed from the charging line isolation areas eliminating 2 photo masks and 2 major fabrication processes. The most significant design change is moving from a stacked channel structure to a single channel layer where the high and low pressure channels are defined on the same layer and connected by the JT restriction. This design removes the recuperative heat exchanger and reduces the thermodynamic efficiency of the JT cycle from 94.6% with perfect recuperative heat exchange to 81% with no recuperative heat exchange [8]. Utilizing only one channel layer removes 2 photo masks and 3 major processing steps. The estimated fabrication time for the new single channel layer design is ~3 months. The single channel layer design is

the final design for the single stage coldstage. The design and fabrication process for this final design are detailed in chapters 2.3 – 2.5.

Figure 2.3: Basic cross-section of the tether design developed by Wang et al. [27], [28] and shown in Figure 1.14

2.3 Mechanical Design of the Single Channel Layer Coldstage

The coldstage presented here is fabricated using microfabrication techniques developed by Wang et al. [26]–[28], [36], [37]. The process uses polyimide as a structural material and copper as a sacrificial material. At the end of the process the copper is removed via a wet chemical etching process to leave behind micro-channels in a polyimide structure. Figure 2.4 shows the refrigerant flow cross-section, a basic 3D model of the coldstage, and a fully fabricated coldstage. The coldstage consists of a high pressure and low pressure channel on the same plane joined by the JT restriction. This design scheme simplifies the fabrication of previous designs developed by Wang et al. [27], [28]. It removes the stacked channel layers by placing both channels on the same device layer. This eliminates the need for extra process steps to fabricate a second channel layer and make a vertical connection between the two channels. This design however removes the heat exchanger and reduces the thermodynamic efficiency of the JT cycle from 94.6% with perfect recuperative heat exchange to 81% with no recuperative heat exchange [8]. The micro channels are 20 µm tall and vary in width from 1 mm to 5 mm. All channels are supported by 60 µm diameter intra-channel posts with a pitch of 250 µm. This post design has been shown to withstand internal pressures up to 1 MPa [28].On the cold end of the coldstage a JT restriction of 1 mm x 5 mm x 1 µm (length, width, thickness) joins the two channels. The

JT restriction also has 60 µm diameter intra-channel posts with a pitch of 250 µm. On the warm end of the coldstage the channels are connected to a compressor or other macro scale fluidic connections with through wafer vias. The cold end of the device is suspended off of the Si substrate for thermal insulation and mechanically held in place by polyimide tethers. The overall size of the coldstage is 16 x 13 mm x 480 µm. The Si substrate is 380 µm thick and the polyimide structure is 100 µm in total thickness.

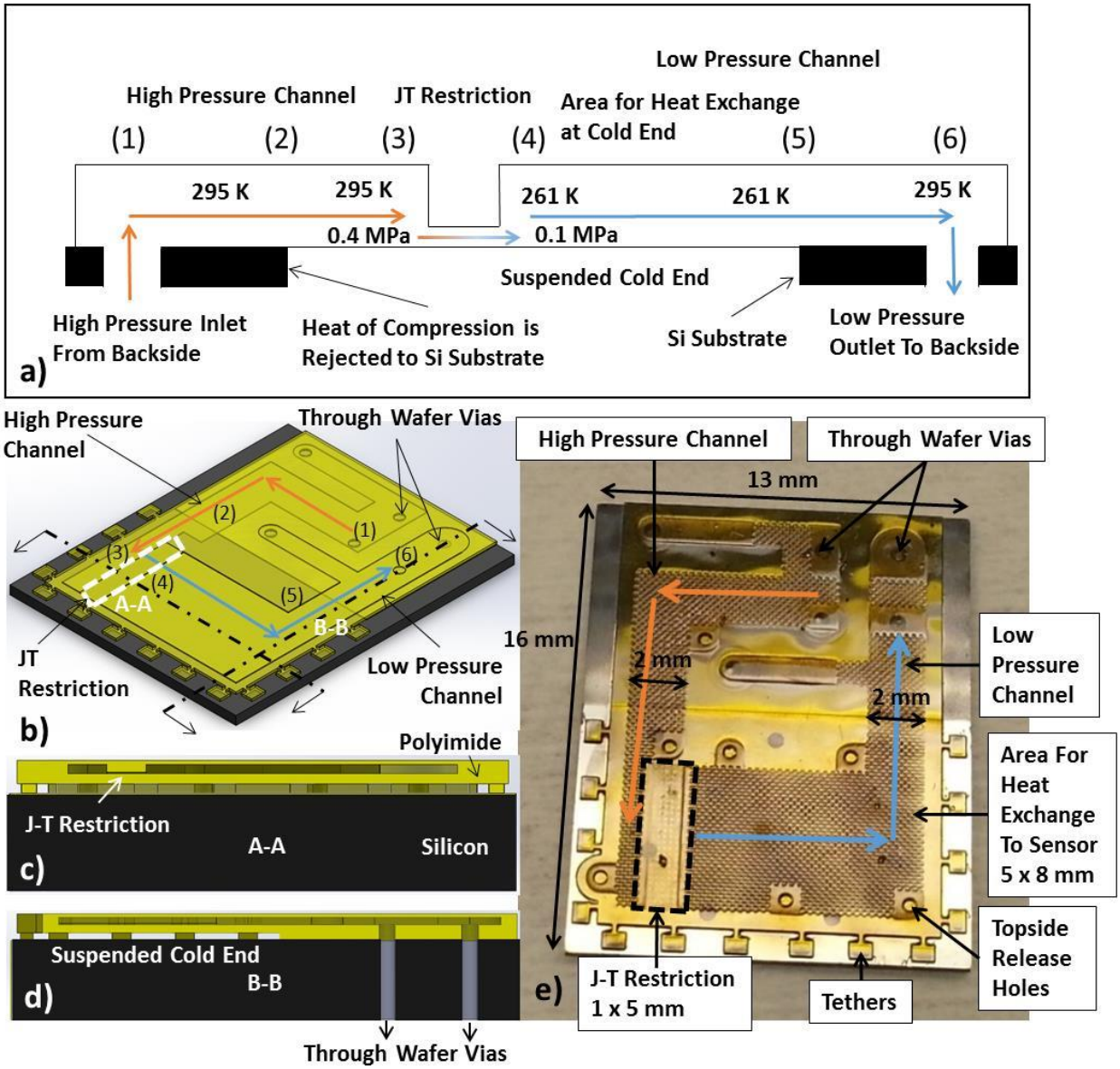

Figure 2.4: a) A cross-section of the refrigerant flow path with key points 1-6 marked. b) A 3D model of coldstage with key points marked. c-d) Cross sections of the flow path. d) The coldstage after all micro-machining with key features marked. In (a) the refrigerant enters the coldstage from the backside (1).

From (1)-(2) the heat of compression is rejected to the Si substrate. From (2)-(3) the high pressure 0.4 MPa liquid refrigerant moves to the entrance of the JT restriction. From (3)-(4) the refrigerant is expanded to 0.1 MPa across the JT restriction. From (4)-(5) the low pressure refrigerant boils and heat is lifted from the cold end. From (5)-(6) the vapor refrigerant moves to the coldstage outlet. At (6) the vapor refrigerant exits the coldstage though the backside.

Figure 2.5 shows the layout of the single stage cold stage with major design features indicated. These features include: 4 through wafer connections in a square pattern designed to couple to a micro compressor; 2 other through wafer connections to facilitate charging of refrigerant to both high and low pressure channels; etched trenches in the Si substrate around the through wafer vias to enhance polyimide bonding to the substrate; 14 polyimide tethers designed to anchor the suspended cold end to the substrate with a minimal heat conduction path; both topside and backside release holes to allow efficient removal of the sacrificial copper; a 5 mm wide by 1 mm long by 1 µm thick JT restriction; a 8 mm by 5 mm cold end area for heat exchange at the cold end temperature; the fluid channels are 20 µm thick with a width of 1 mm to 5 mm and are reinforced with 120 um diameter polyimide posts with 250 um pitch.

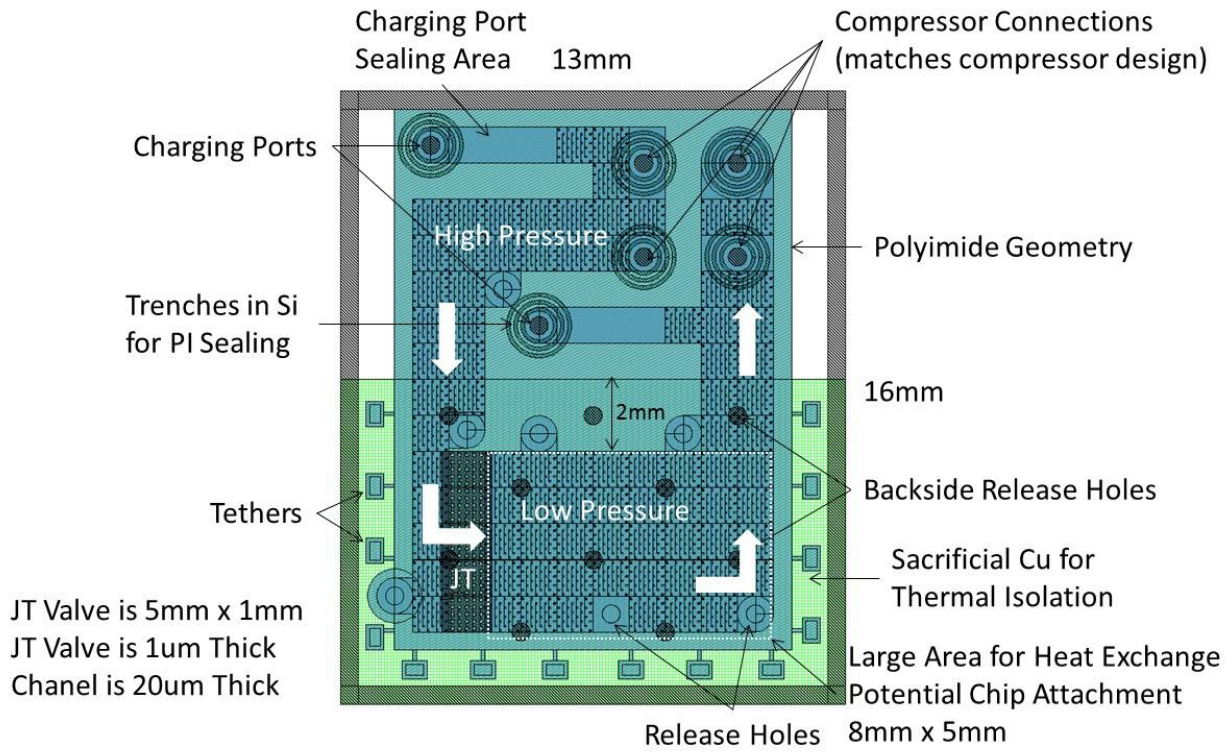

Figure 2.5: Layout of coldstage with key features indicated.

2.4 Thermal and Fluidic Design of the Single Channel Layer Coldstage

The net refrigeration power available at the cold end of the coldstage is

$$\dot{Q}_{net} = \dot{Q}_r - \dot{Q}_{cond} - \dot{Q}_{conv} - \dot{Q}_{rad} - \dot{Q}_{\Delta P} \tag{2.1}$$

where $\dot{Q}_{net}$ is the net refrigeration power, $\dot{Q}_r$ is the gross refrigeration power available from the JT expansion of the refrigerant, $\dot{Q}_{\Delta P}$ is any loss from pressure drop through the micro-channels outside the JT restriction, and $\dot{Q}_{cond}$, $\dot{Q}_{conv}$, and $\dot{Q}_{rad}$ are the heat leak into the cold end of the coldstage by conduction, convection, and radiation respectively. The coldstage is designed to operate in a vacuum environment and convective losses are assumed to be negligible.

Both the high pressure and low pressure channels before and after the JT restriction must not introduce significant pressure drops for the coldstage to function properly. We assume negligible pressure losses when the pressure drop outside the JT restriction is less than5% of the designed 0.4:0.1

MPa pressure drop across the JT restriction. The pressure drop for laminar single phase flow without significant change in fluid density and viscosity through a rectangular channel is [8]

$$\Delta P = \frac{12\,\dot{m}\,\mu\,L}{D_m\,w\,t_g^3} \tag{2.2}$$

Where ΔP is the pressure drop, $\dot{m}$ is the molar flow rate of the refrigerant, μ is the viscosity, L is the length, and D_m is the molar density. The high pressure channel is assumed to be filled 100% liquid isobutane and the low pressure channel is assumed to have 100% vapor isobutane. For less than 5% of the total 0.4 MPa to 0.1 MPa pressure drop to occur outside the JT restriction a minimum channel thickness of 20 µm is required.

There are two major sources or conductive losses. The first is the suspended body of the coldstage provides a conduction path from the cold end to the warm end. The second is the conduction path is along the tethers anchoring the cold end to the warm Si substrate. For this analysis it is assumed the entire cold end is at a constant 261 K and the substrate is at 300 K. Figure 2.6 shows the locations of the major conduction paths. Basic solid conduction is described by Fourier's law of heat conduction. For rectangular cross sections the Fourier's law can be simplified to [38]

$$\dot{Q}_{cond} = \frac{k\,A\,(T_{warm} - T_{cold})}{L} \tag{2.3}$$

where k is the thermal conductivity of the material, A is the cross sectional area of the conduction path, T_{warm} and T_{cold} are the temperatures of the warm and cold end respectively, and L is the length of the conduction path.

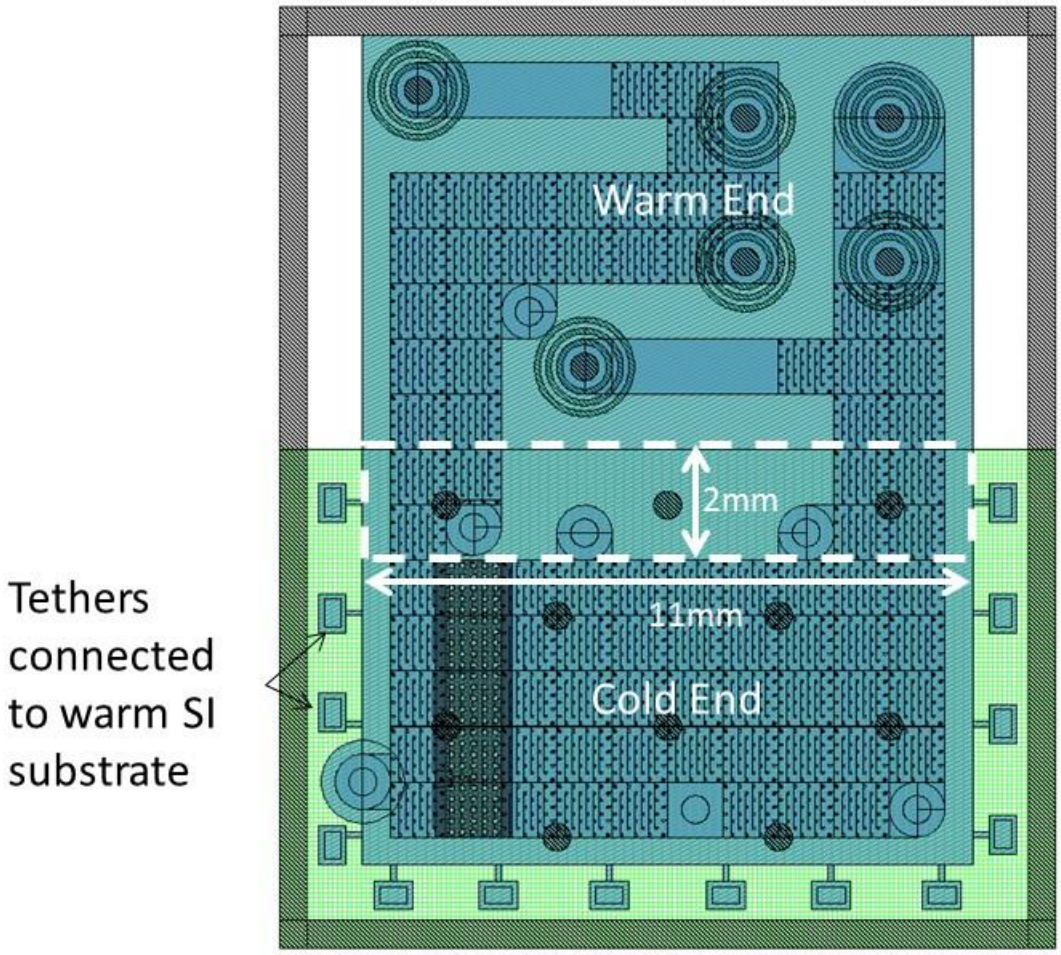

Figure 2.6: Locations of major conduction paths.

The structural material of the coldstage is polyimide 2611 from HD MicroSystems. PI 2611 has a thermal conductivity of 0.105 W/m/K. The total thickness of the polyimide structure is 80 µm. The cold end is connected to the warm end of the cold stage by a 2 mm long by 11 mm wide section of structural polyimide. The cold end is anchored to the substrate with 14 tethers with a length of 300 µm and width of 60 µm. Using equation 2.3 a total conductive heat loss of 3 mW is estimated.

Heat transfer from an ideal radiator or black body is given by the Stefan-Boltzmann law of thermal radiation. For radiation between a surface and its surrounding at steady temperatures the Stefan-Boltzmann law simplifies to [38]

$$\dot{Q}_{rad} = \varepsilon_{eq}\, \sigma\, A_1\, (T_2^4 - T_1^4) \text{ for } T_2 \geq T_1 \tag{2.4}$$

where T_1 is the temperature of the cold end of the cold stage (261 K), T_2 is the temperature of the surrounding (300 K), A_1 is the surface area of the cold end of the cold stage, ε_{eq} is the equivalent emissivity factor for the two radiators, and σ is the Stefan-Boltzmann constant with a value of 5.669E-8 W/m^{2}K. There are two major areas of radiation losses for the cold end. The first is from the top side of the cold end to the surrounding environment. The second is from the bottom side of the cold end to the Si substrate. For the first case where A_2 >> A_1 ε_{eq}=ε_1. For the second case it is considered an infinite parallel plate structure where $\varepsilon_{eq} = 1/(1/\varepsilon_1 + 1/\varepsilon_2 - 1)$. For the second case chromium (a low emissivity material) is deposited on the Si surface to act as a radiation shield. Chromium has an emissivity of 0.05 and PI 2611 has an emissivity of 0.95. Considering a cold end area of 11 mm by 5.5 mm the radiation heat loss is calculated. The radiation loss from the cold end to the Cr coated Si substrate is 0.5 mW. The radiation loss from the cold end to the surrounding environment is 11 mW. This heat loss can be significantly reduced by coating the top surface of the cold stage with a thin layer of Cr to act as a radiation shield. Applying this coating reduces the radiation heat loss from 11 mW to 0.05 mW with negligible conduction losses added.

From chapter 1.2 the ideal gross refrigeration power for a JT refrigeration cycle is [8]

$$\dot{Q}_r = \dot{m}(\Delta h|_T)_{min} \tag{1.1}$$

where $\dot{Q}_r$ is the ideal refrigeration power, $\dot{m}$ is the molar flow rate of the refrigerant, and $(\Delta h|_T)_{min}$ is the minimum enthalpy difference between the high and low pressure states of the refrigerant over the temperature range of cooling. This design eliminates the recuperative heat exchanger and is expected to operate at 81% of ideal [8]. Considering negligible convective losses when the coldstage is run in a vacuum environment and negligible pressure losses the net refrigeration power simplifies to

$$\dot{Q}_{net} = 0.81\dot{Q}_r - \dot{Q}_{cond} - \dot{Q}_{rad} \tag{2.5}$$

where $\dot{Q}_{net}$ is the net refrigeration power, and $\dot{Q}_{cond}$ and $\dot{Q}_{rad}$ are the heat leak into the cold end of the coldstage by conduction and radiation respectively. The conduction losses are estimated to be 3 mW. The radiation heat leak is estimated to be 11.05 mW without any radiation shielding and 0.55 mW when proper radiation shielding is applied via thin-film deposited Cr. The target net cooling power is 100 mW. A desired flow rate of 5.63 µmol/s (7.51 sccm) is estimated for a net refrigeration power of 100 mW given the estimated heat leaks, the absence of a recuperative heat exchanger, and a $(\Delta h|_T)_{min}$ of 19.54 kJ/mol over the desired cooling range for isobutane as the refrigerant.

The flow rate for a fluid undergoing laminar adiabatic expansion through a rectangular restriction is the integral form of equation 2.2 [8]

$$\dot{m} = \frac{w\ t_g^3}{12\ L}\int_{P_l}^{P_h} \frac{D_{m,avg}}{\mu_{avg}} dP \tag{2.6}$$

where $\dot{m}$ is the molar flow rate of the refrigerant, w, L, t_g are the JT restriction width, length, and thickness respectively, P_h, P_l are the high and low pressure conditions across the restriction, and $D_{m,avg}$ and μ_{avg} are the Dukler averages of density and viscosity for a homogeneous model of two phase flow where [39]

$$D_{m,avg} = \frac{1}{\frac{x}{D_{m,v}} + \frac{1-x}{D_{m,l}}} \tag{2.7}$$

$$\mu_{avg} = D_{m,avg}\left(\frac{x\mu_v}{D_{m,v}} + \frac{(1-x)\mu_l}{D_{m,l}}\right) \tag{2.8}$$

where x is the quality of the fluid at a given pressure, $D_{m,v}$ and $D_{m,l}$ are the molar densities of the vapor and liquid portions of the fluid respectively, and μ_v and μ_l are the viscosities of the vapor and liquid portions of the fluid respectively. The integral is evaluated via tabular integration using fluid properties for isobutane from the NIST REFPROP v. 9.1 program [40]. The properties used are tabulated in

Appendix B. Given the desired flow rate of 5.63 µmol/s (8 sccm), the JT gap is designed to be 1 mm x 5 mm x 1 µm (length, width, thickness). The flow rate of the refrigerant is highly dependent on the gap thickness of the JT restriction. Any small variation in the gap thickness of the JT restriction significantly alters the performance of the coldstage. Table 2.1 provides the estimated flow rate for isobutane undergoing a 0.4:0.1 MPa pressure drop across a 1 mm long and 5 mm wide JT restriction for various JT restriction gap thicknesses. It is important to note that a gap variation of only 100 nm can cause significant impact to device performance.

Table 2.1: Effect of the JT restriction gap thickness on coldstage flow rate. The JT restriction has a length of 1 mm and width of 5 mm. The refrigerant is isobutane undergoing a 0.4:0.1 MPa pressure drop across the JT restriction.

Gap Thickness (µm)	Flow Rate (sccm)	Deviation From Desired 8 sccm
0.5	1	88%
0.75	3.4	58%
0.9	5.8	28%
0.99	7.7	4%
1	8	0%
1.01	8.2	2%
1.1	10.6	33%
1.25	15.6	95%
1.5	26.9	236%

2.5 Fabrication Process for the Single Channel Layer Coldstage

The fabrication process for the coldstage is based on the fabrication process for the monolithic coldstage presented by Wang et al. [26]–[28], [36], [37]. The fabrication process uses polyimide (HD Micro Systems PI2611) as a structural material and copper as a sacrificial material. Alternating layers of copper and polyimide are deposited on a Si substrate and the copper is released in a final step to create a suspended polyimide structure with internal micro-channels. Figure 2.7 shows the fabrication process flow for the coldstage. The detailed processing parameters and step by step breakdown of the process are presented in Appendix D. The fabrication process starts with (Figure 2.7, a) a double side polished

380 µm thick Si wafer with 2 µm of thermally grown SiO_2 on both sides. (Figure 2.7, b) The front side (Figure 2.9 & Figure 2.10) and backside (Figure 2.22) oxide are patterned and etched with buffered oxide etchant (BOE) and the front side Si exposed under the oxide is etched an additional 5 µm with reactive ion etching (RIE) (Figure 2.11). (Figure 2.7, c) A 100 nm chromium layer is deposited via e-beam evaporation and patterned via lift-off. (Figure 2.7, d) A 500 nm copper seed layer is deposited via e-beam evaporation and a 15 µm copper layer is electroplated on the seed layer. The copper layer is patterned via a wet chemical etch (Figure 2.12 & Figure 2.13). This copper layer is used to suspend the cold end of the cold stage off of the Si substrate. (Figure 2.7, e) A 40 µm polyimide layer is deposited via spin coating. Four spins of 10 µm each are required to form the 40 µm layer. (Figure 2.7, f) A 500 µm copper seed layer is deposited via e-beam evaporation. A 20 µm copper layer is electroplated on the seed layer. The copper layer is then patterned and etched via a wet chemical etch (Figure 2.14 & Figure 2.15). This copper layer defines both the high and low pressure channels. (Figure 2.7, g) A 1 µm copper layer is deposited via e-beam evaporation and patterned via lift-off. This copper pattern forms the JT restriction and bridges the high and low pressure channels (Figure 2.16 & Figure 2.17). (Figure 2.7, h) A 40 µm polyimide layer is deposited via spin coating. This layer fully encapsulates the copper layers. (Figure 2.7, i) A 500 nm copper layer is deposited and patterned via lift-off (Figure 2.18, Figure 2.19, & Figure 2.20). This layer acts as a hard etch mask for the RIE of the polyimide from the topside (Figure 2.7, j). These steps define the overall geometry of the cold stage and expose portions of the copper channel structure for future releasing. (Figure 2.7, k) From the backside deep reactive ion etching (DRIE) is used to etch the through wafer vias to expose the first copper layer and the first polyimide layer (Figure 2.21, Figure 2.22, & Figure 2.23). The DRIE step also dices the wafer into individual device chips. Processing continues on an individual chip bases. From the backside the first polyimide layer is etched via RIE to expose the second copper layer. This creates backside vias used for fluidic connection to the high and low pressure channels and provides access for the release etchant. (Figure 2.7, l) The copper layers are

released via a wet chemical etch to form the free standing polyimide structure with internal micro-fluidic channels (Figure 2.24 & Figure 2.25). (Figure 2.7, m) Finally the topside release holes are sealed with epoxy.

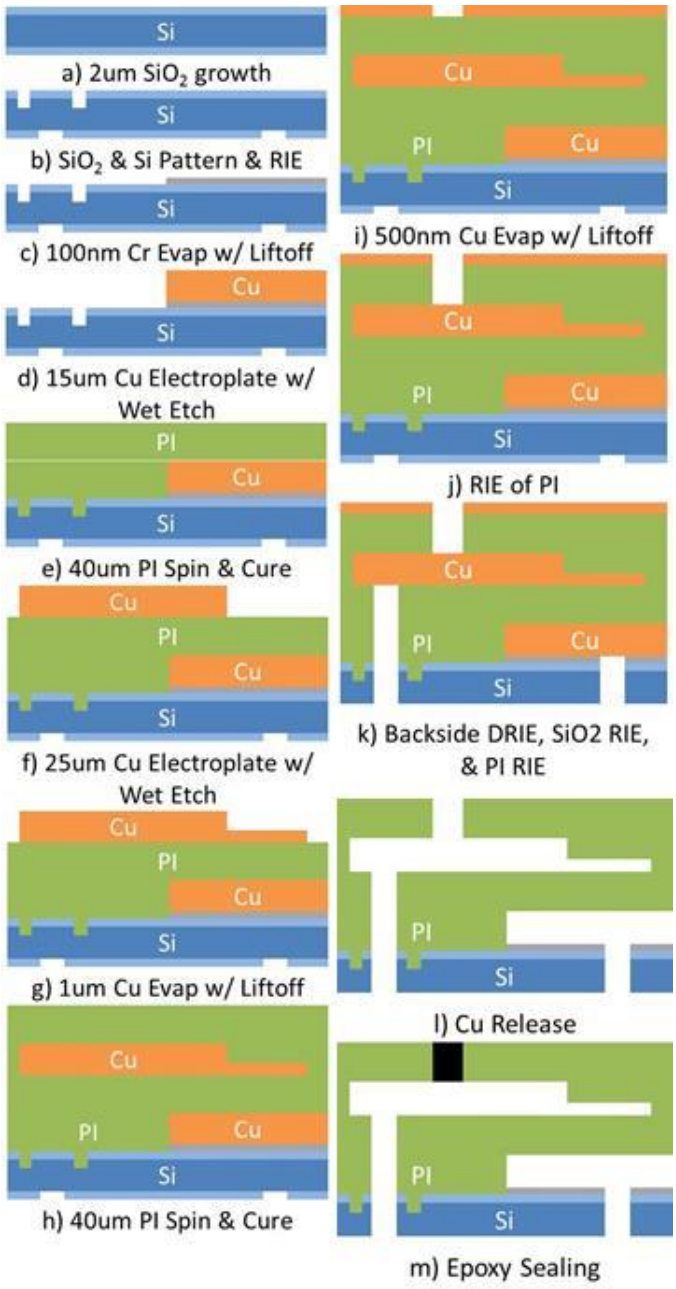

Figure 2.7 Fabrication process flow

2.5.1 : Select Photos of the Fabrication Process

This section contains select photos representative of the fabrication process including measurements of critical step heights of select patterns and photo mask patterns used.

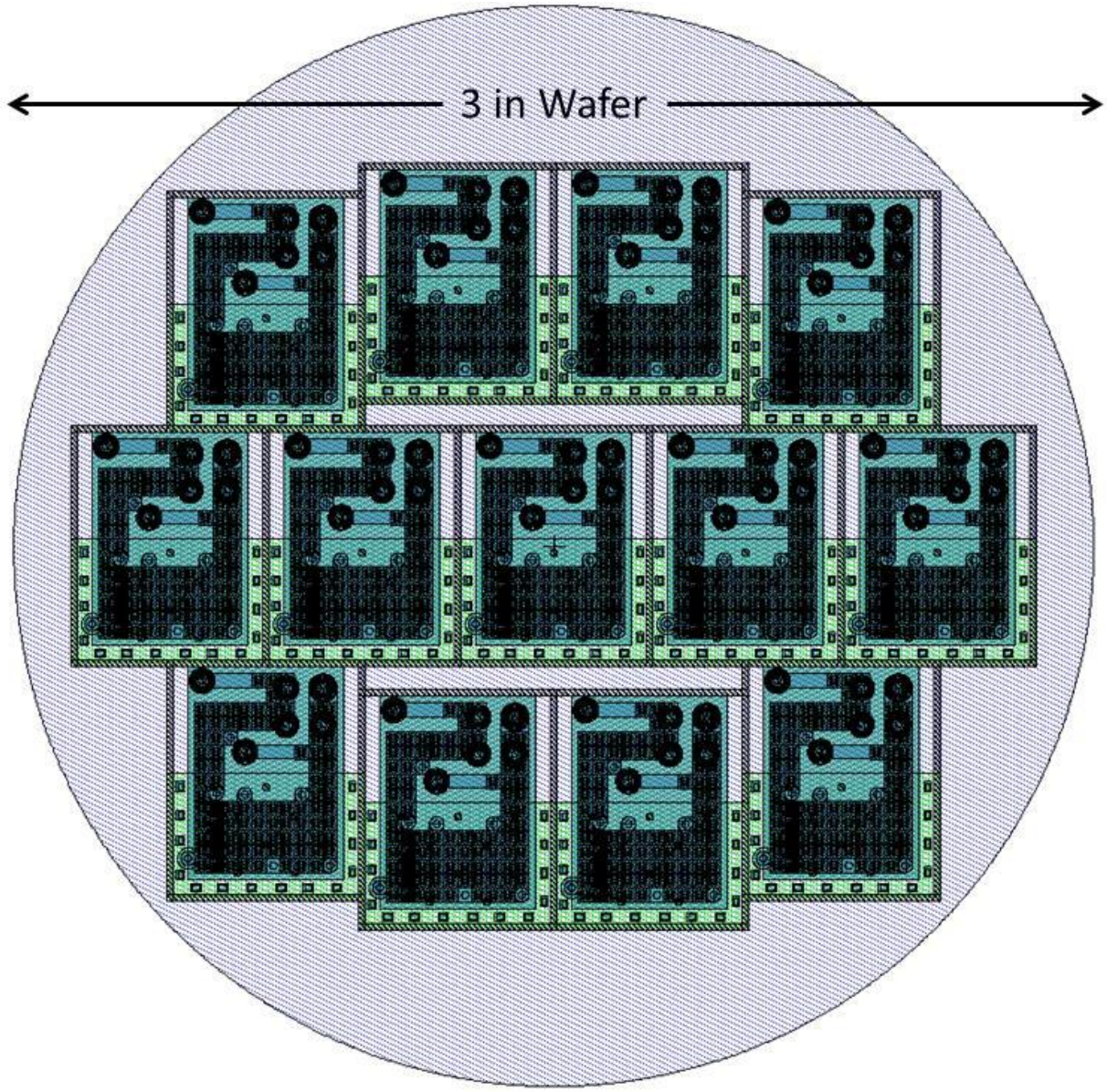

Figure 2.8

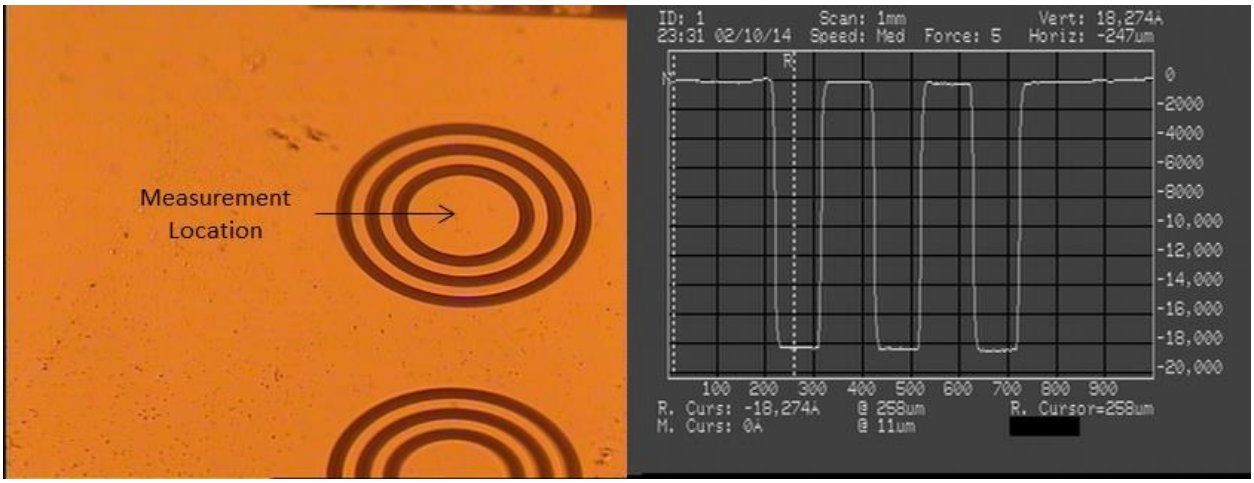

Figure 2.9: Front side oxide etch and profilometer measurement.

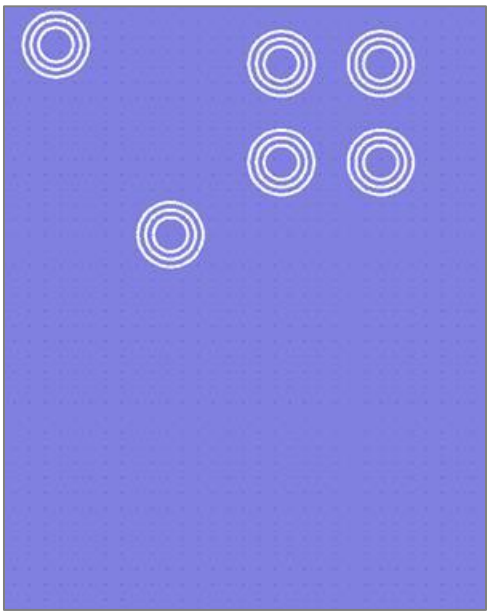

Figure 2.10: Photo mask pattern for front side oxide etch.

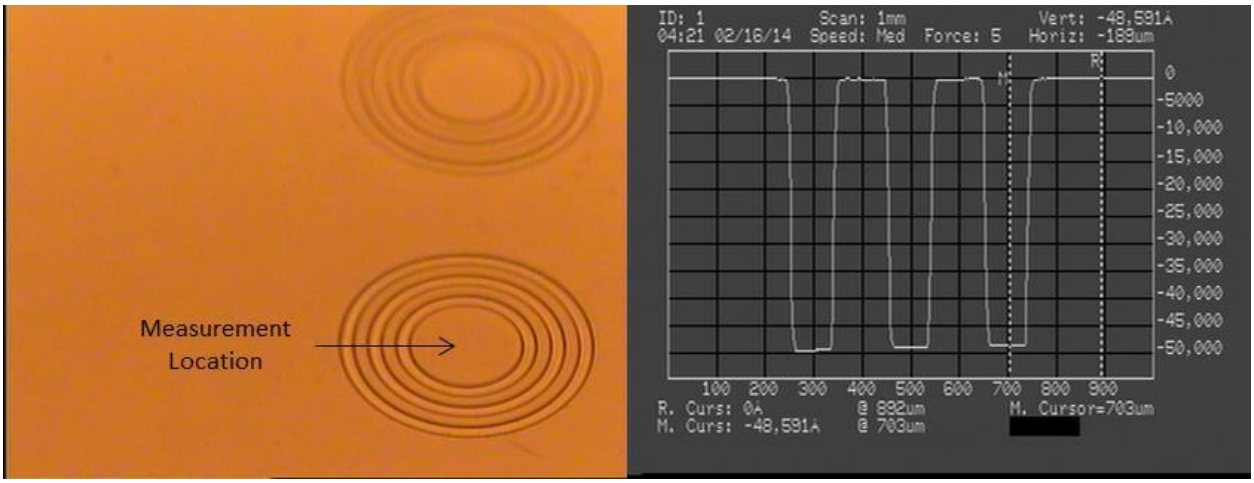

Figure 2.11: Front side Si RIE and profilometer measurement.

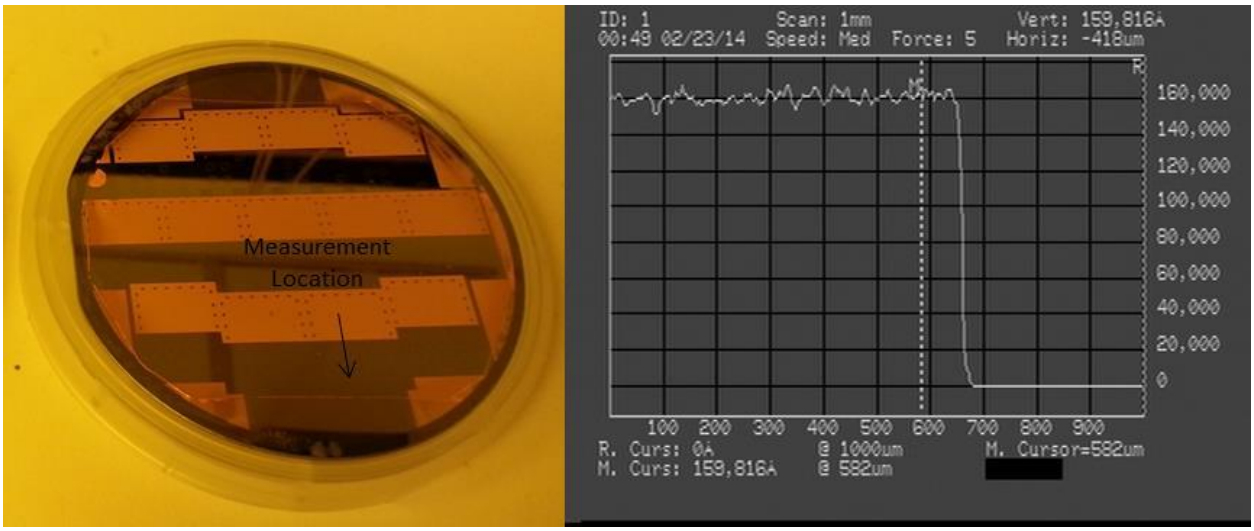

Figure 2.12: First sacrificial copper pattern used to suspend the cold end of the coldstage off of the Si substrate with profilometer measurement.

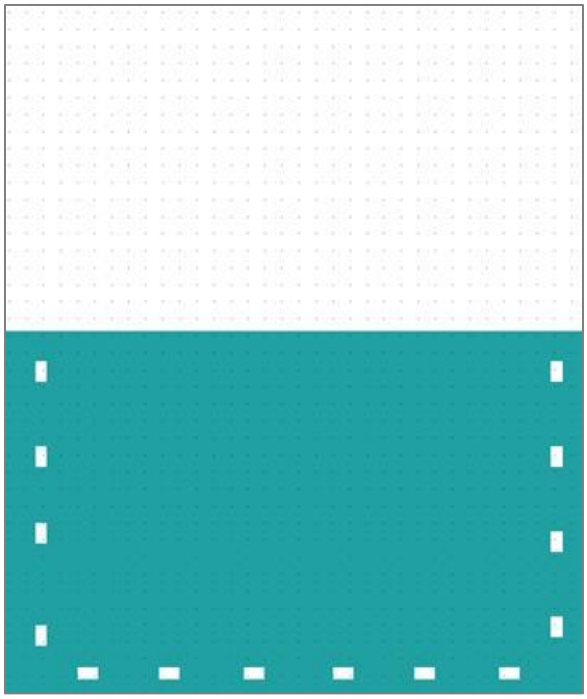

Figure 2.13: Photo mask Pattern for first sacrificial copper layer used to suspend the cold end of the coldstage off of the silicon substrate.

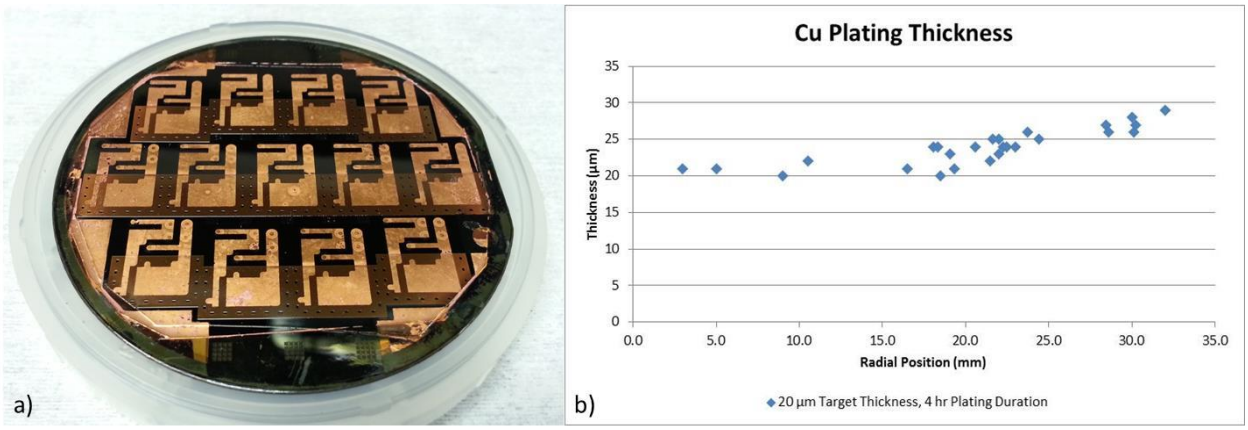

Figure 2.14: a) Second sacrificial copper layer used to define the high and low pressure channels. b) Measurements of the channel thickness at various positions on the wafer.

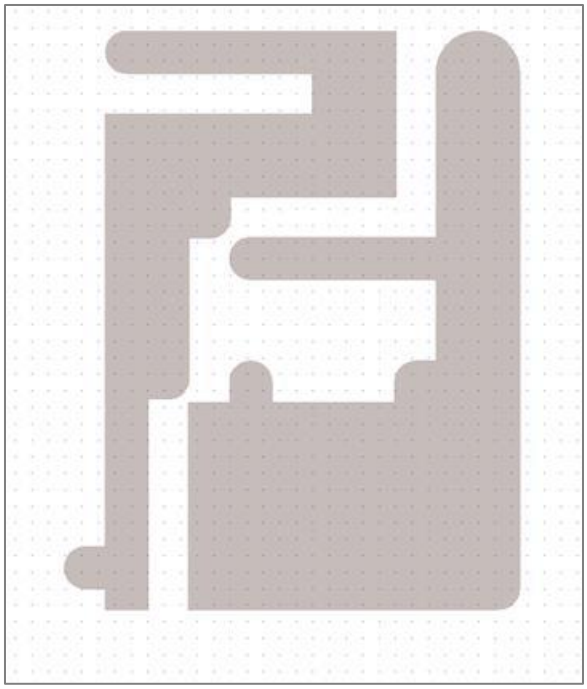

Figure 2.15: Photo mask pattern for the second sacrificial copper layer used to define the high and low pressure channel geometry. The post pattern is not rendered in this image.

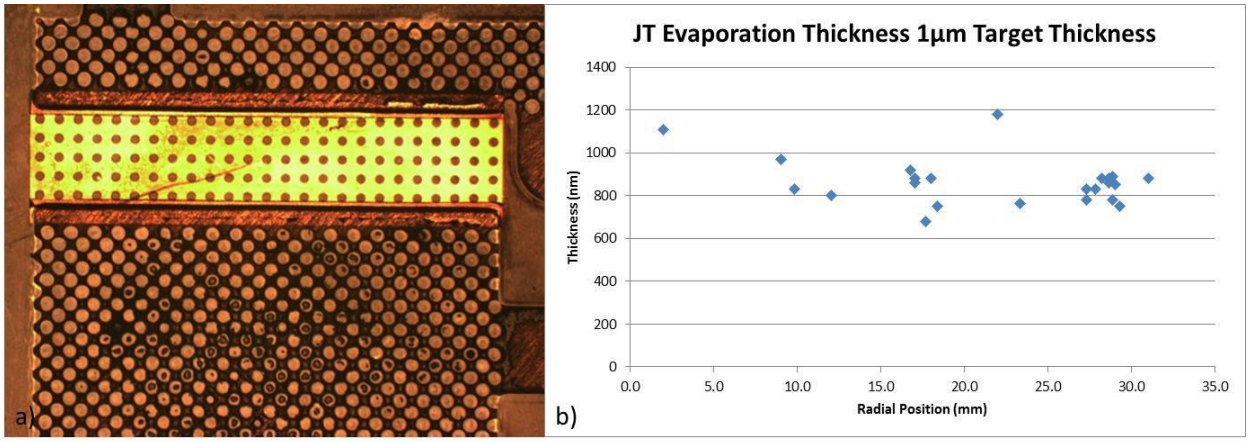

Figure 2.16: a) JT restriction deposited connecting the high and low pressure channels. b) Measurements of the JT restriction thickness at various positions on the wafer.

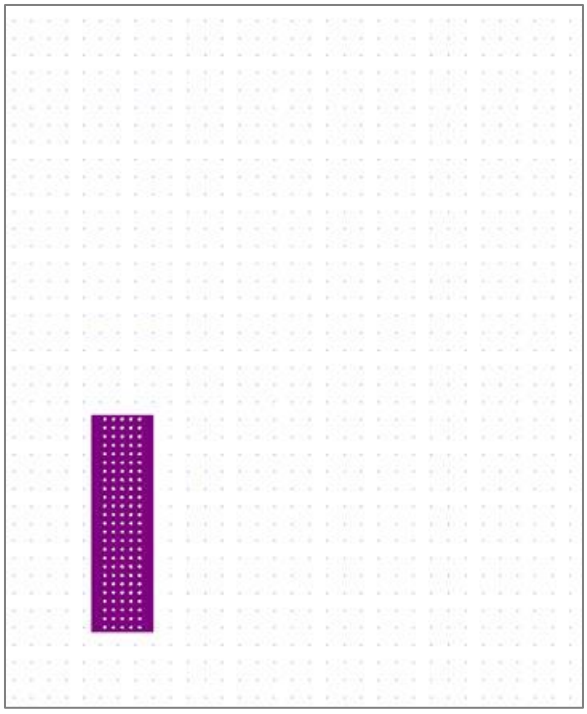

Figure 2.17: Photo mask pattern used to define the JT restriction and connect the high and low pressure channels.

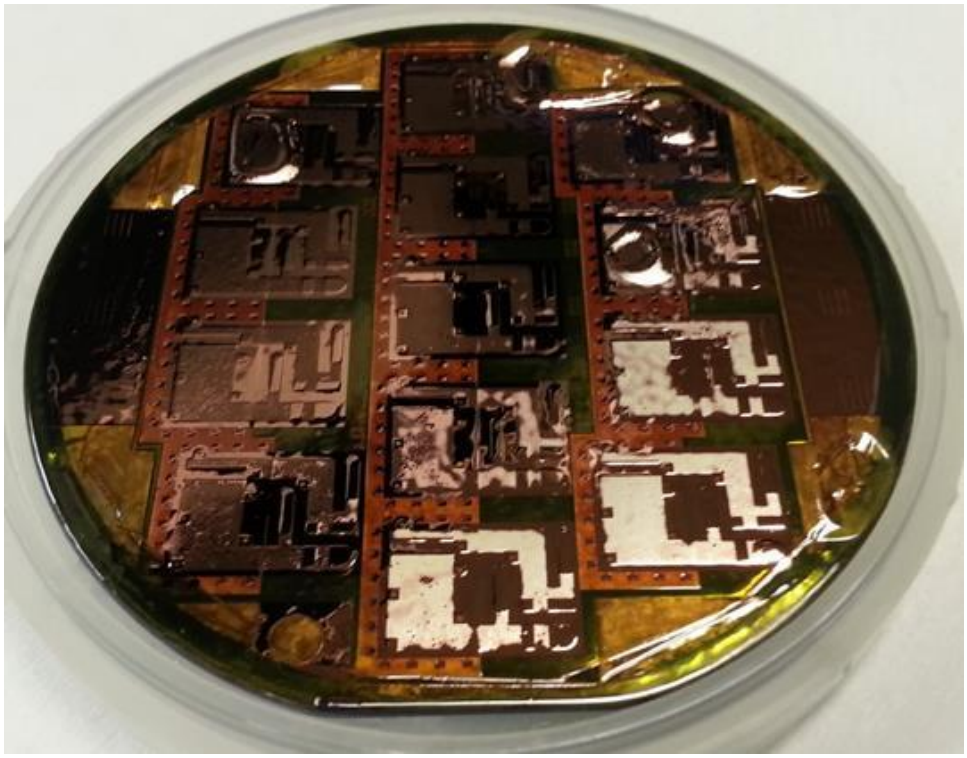

Figure 2.18: Copper hard mask for polyimide RIE after the liftoff definition process.

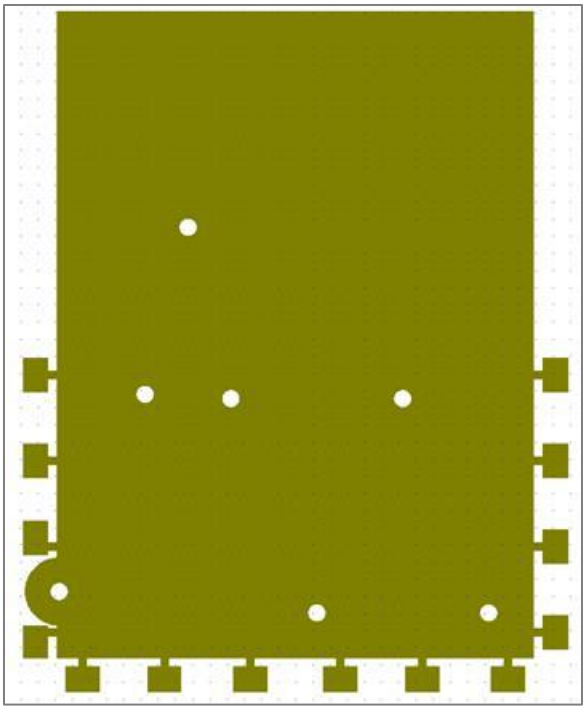

Figure 2.19: Photo mask pattern to define the polyimide coldstage geometry.

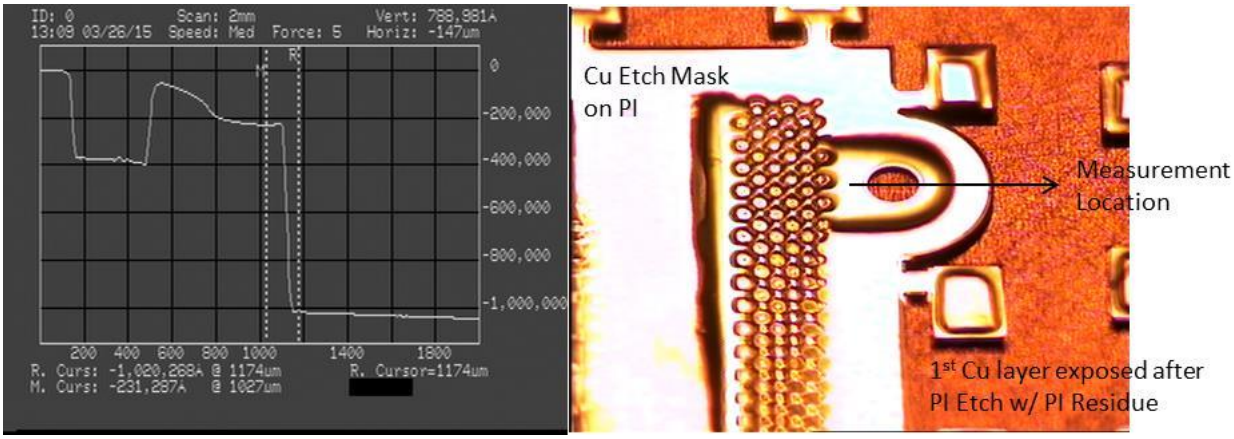

Figure 2.20: Profile measurement after the polyimide RIE step.

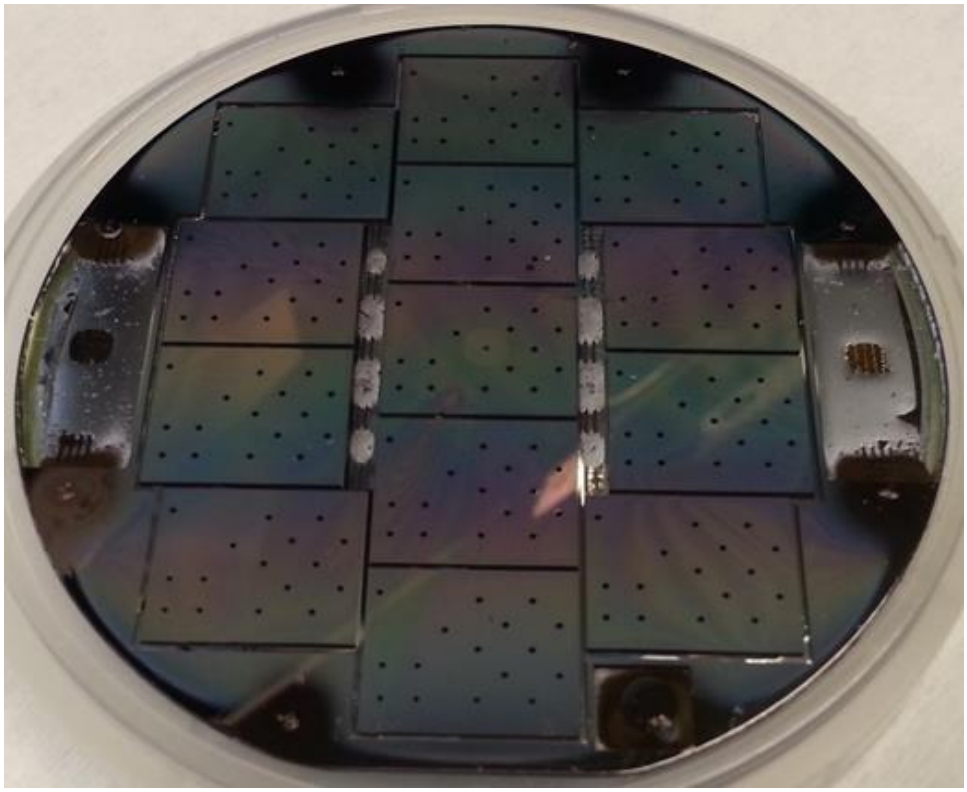

Figure 2.21: Backside of the coldstage wafer after the DRIE Process.

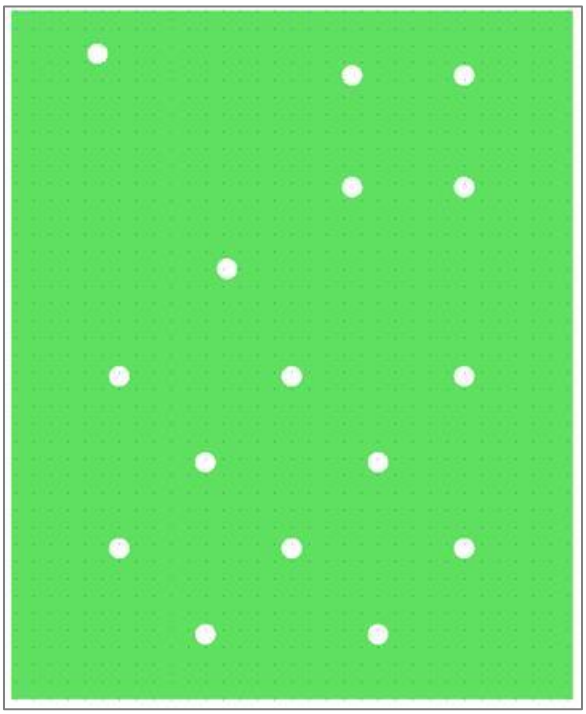

Figure 2.22: Photo mask used to define the backside oxide layer for DRIE through wafer via etching and chip dicing.

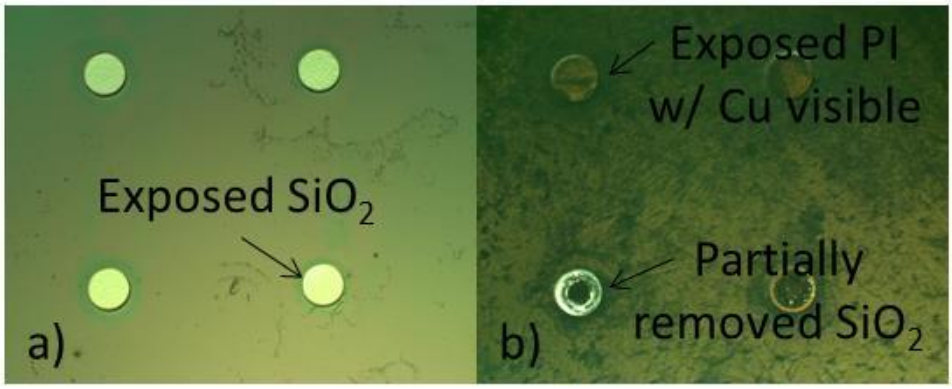

Figure 2.23: Backside view of the through wafer vias a) before and b) after the backside RIE of the front side oxide.

Figure 2.24: Two coldstage chips during the release process. One is fully released after 10 days and the other still has copper remaining inside the channel structure after 8 days.

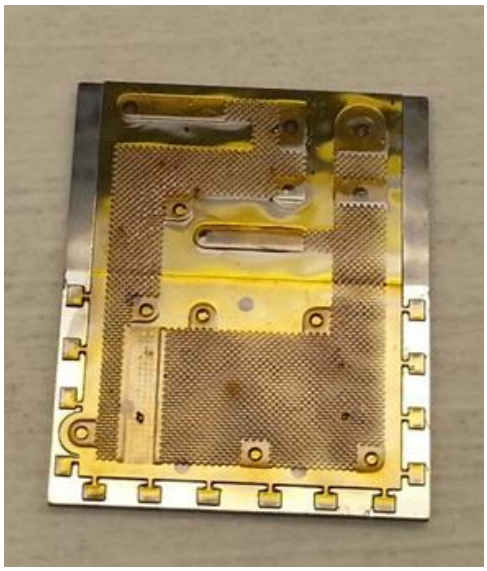

Figure 2.25: A fully released and rinsed coldstage chip before release hole sealing.

2.6 Fabrication Challenges

2.6.1 Polyimide Blistering

One major fabrication issue observed was the appearance of polyimide blisters. These polyimide blisters were most often observed between the second copper layer and the second polyimide layer. The blisters appeared during the curing process of the second polyimide layer. Figure 2.26 shows one example of a wafer experiencing blistering during polyimide curing. The blisters are most evident when the wafer is above 200 ^{o}C.

Figure 2.26: Wafer during second polyimide layer curing. Polyimide blisters formed when the wafer exceeded 200 ^{o}C

Polyimide and copper interactions are well documented but not well understood in the literature [41]. Two interactions between polyimide and copper are believed to cause polyimide blisters to form. Figure 2.27 shows an illustration of the two major blister formation mechanisms. The first is the interaction between the polyamic acid present is the spin-on polyimide solution and local areas of copper oxide. This causes the formation of copper carboxylate which inhibits the imidization of the polyimide layer [41]. This reaction causes outgassing leading to the formation of a blister. The second major cause of blistering is poor adhesion of the underlying copper layer to the first polyimide layer. Adhesion of metals to polyimide is discussed at length and copper is known to have poor adhesion to polyimide [41]. When poor adhesion is present the thermal expansion mismatch between copper and polyimide causes the copper layer to blister up before the polyimide layer is fully cured.

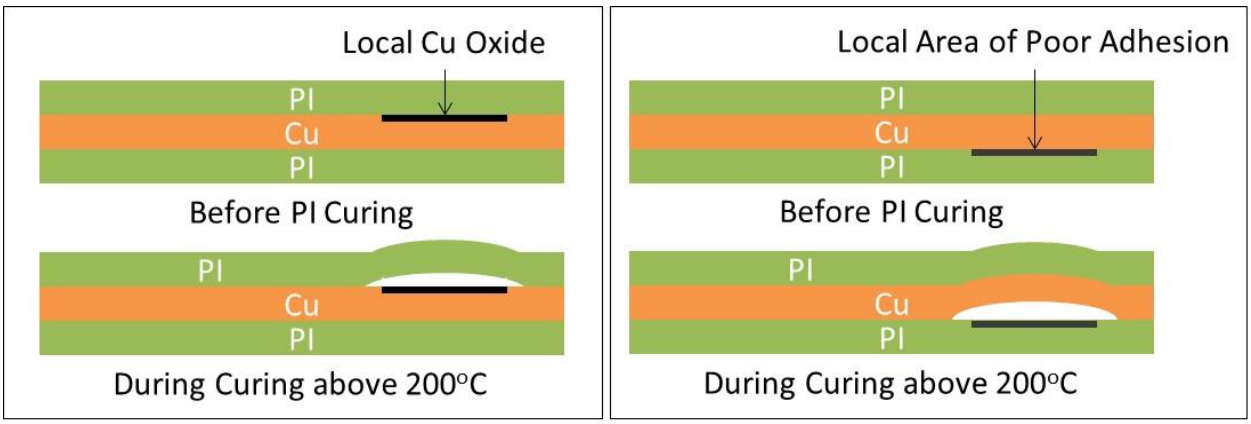

Figure 2.27: Two major causes of PI blistering. Left: chemical interaction between polyamic acid of spin-on polyimide and copper oxide, Right: poor adhesion of underlying copper layer to first polyimide layer.

To solve the polyimide blister issue several best practices have been developed. First the removal of copper oxide from the copper surface is critical. A cleaning process was developed where the wafer is exposed to a formic acid vapor. A hotplate hood shown in Figure 2.28 was developed to run this process. In this process the wafer is heated on the hooded hotplate to 200 ^{o}C in a nitrogen environment. The nitrogen environment avoids further oxidization of the copper. A nitrogen flow of 50 sccm is used to create the nitrogen environment while the hotplate with the wafer on it is heated from room temperature to 200 ^{o}C. Formic acid vapor is flowed into the heated chamber via a bubbler setup using liquid formic acid and nitrogen as a carrier gas. The flow of pure nitrogen is decreased to 20 sccm and the formic acid bubbler flow is increased to 30 sccm. The wafer remains at temperature in the acid environment until all visibly oxidized copper is removed. After cleaning, the formic acid flow is stopped and the pure nitrogen flow is increased back to 50 sccm. The hotplate heater is turned off and the wafer is allowed to naturally cool to room temperature in a nitrogen environment. The polyimide spinning process is run immediately following the acid cleaning to minimize contact with atmospheric oxygen. Figure 2.29 shows a coldstage wafer both before and after formic acid cleaning.

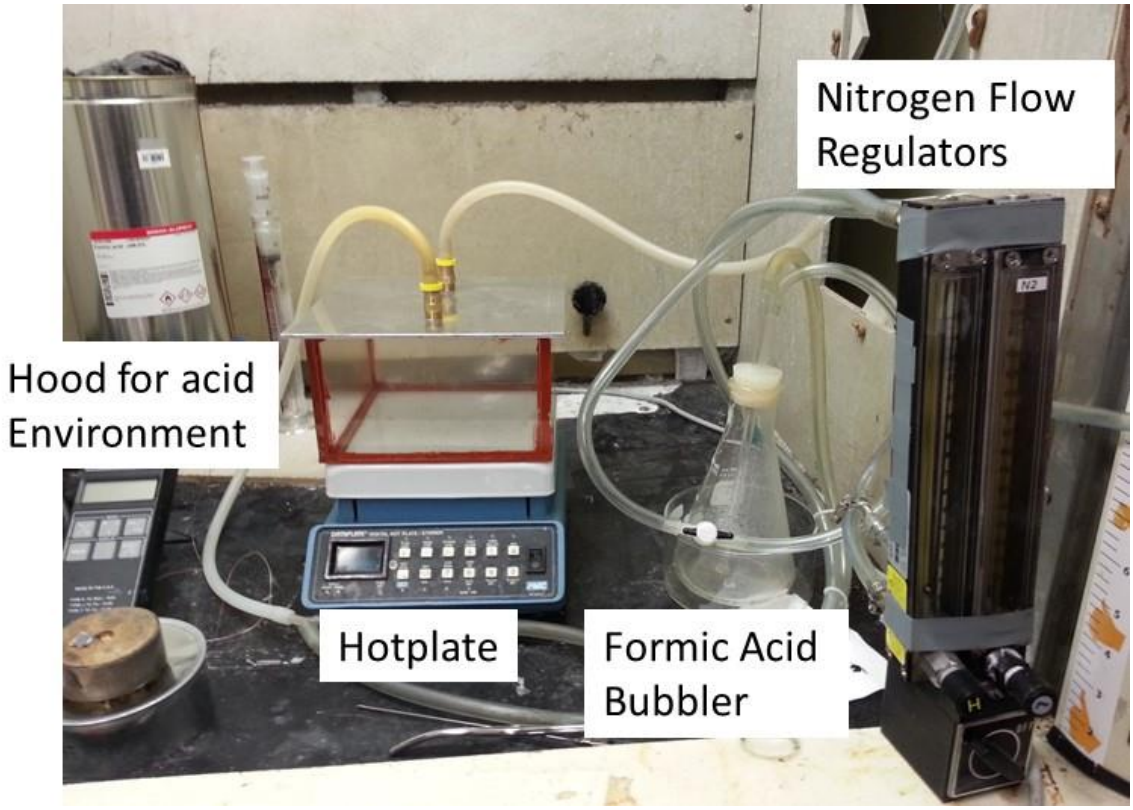

Figure 2.28: Formic acid vapor hood and hotplate with nitrogen flow regulators and acid bubbler.

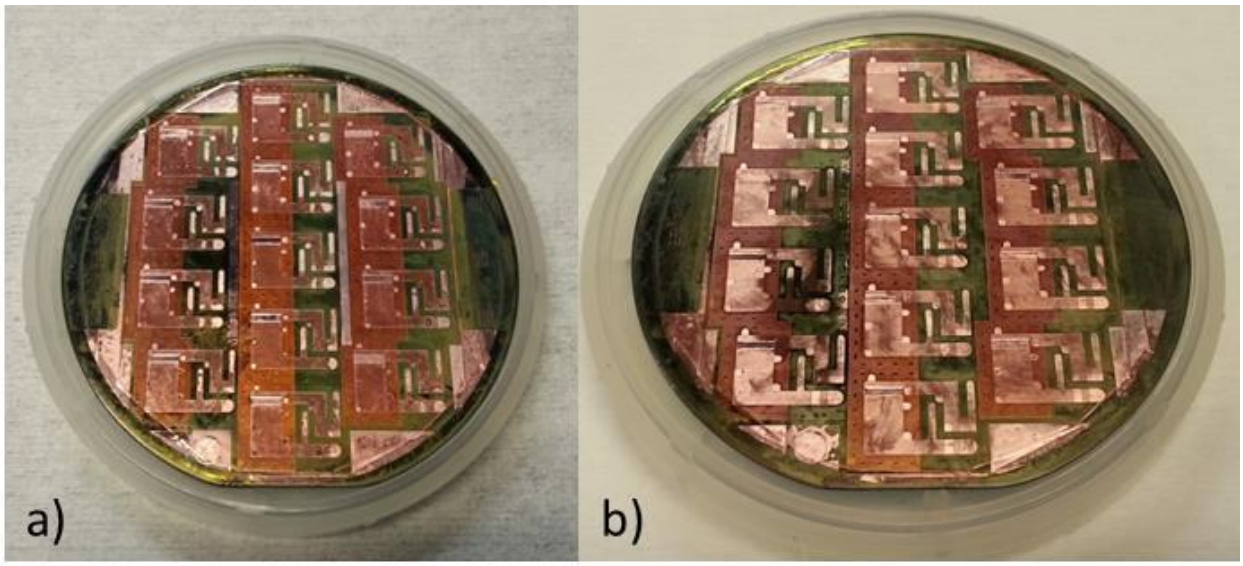

Figure 2.29: Second copper layer a) before and b) after formic acid cleaning. Dark regions in (a) indicate copper oxide, light areas indicate clean copper. Dark regions in (b) are due to poor reflection off of a rough copper surface and are not oxide.

Several best practices have been developed to improve adhesion of the second copper layer to the first polyimide layer. First a standard acetone and IPA spin cleaning is run followed by an automatic

spin-rinse-dry cycle. This removes any particulate contamination from the surface of the wafer. Next a dehydration bake at 130 ^{o}C on a vacuum hotplate is performed to drive out any moisture adsorbed by the polyimide layer. Finally an oxygen plasma cleaning is run to both roughen up the polyimide surface and partially activate the surface before entering the e-beam evaporator for the copper seed layer deposition. A titanium or chromium adhesion layer is recommended for the seed layer evaporation. A 50 nm titanium adhesion layer is found to be sufficient for good adhesion. Maintaining these practices has improved the repeatability and reliability of copper adhesion to polyimide.

2.6.2 Joule-Thomson Restriction Definition and Continuity

The definition of the JT restriction (Figure 2.7g) required extensive rework during the fabrication process. The first issue with the JT restriction definition was caused by expired photoresist. The photoresist would appear fully developed but leave behind a relatively thick layer or residue where the resist should have been removed. During the lift-off process the entire copper layer used to define the JT restriction would be removed. New photoresist was ordered and the photolithography process was fine-tuned. The second issue was the quality of the connection between the 20 µm copper channels and the 1 µm copper layer used to define the JT restriction. Figure 2.30 highlights the discontinuity in the separately defined copper patterns. These two patterns need to overlap to ensure a continuous flow path after the copper is released to form the micro-channel structure. The discontinuity is believed to be caused by shadowing during the JT restriction copper evaporation caused by the tall 20 µm copper channel pattern.

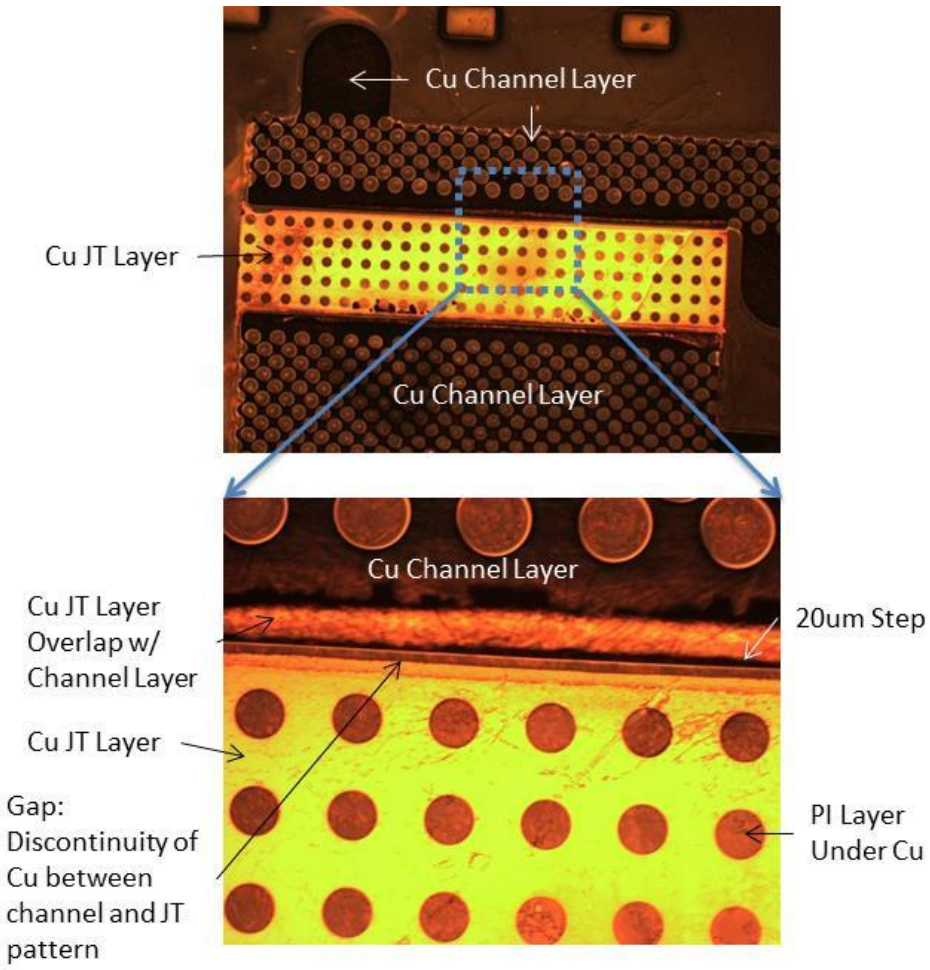

Figure 2.30: Disconnect between copper channel definition and JT restriction definition.

To fill the gap between the channel definition and the JT restriction definition a 1 µm thick patch was applied at the interfaces of the JT restriction to the high and low pressure channels. The patch was applied using e-beam evaporation of copper. To ensure good sidewall coverage the wafer was mounted to an angled stage at 45^{o}. The axis of rotation of the wafer is out of line with the direction of evaporation to ensure all surfaces are directly exposed to the evaporated copper. Figure 2.31 shows a schematic of the angled evaporation stage and Figure 2.32 shows the repair of the interface between the channel definition layer and the JT restriction layer. It is recommended to use angled evaporation for the JT restriction definition step in the future to ensure good side wall coverage and avoid the need for a separate patching step.

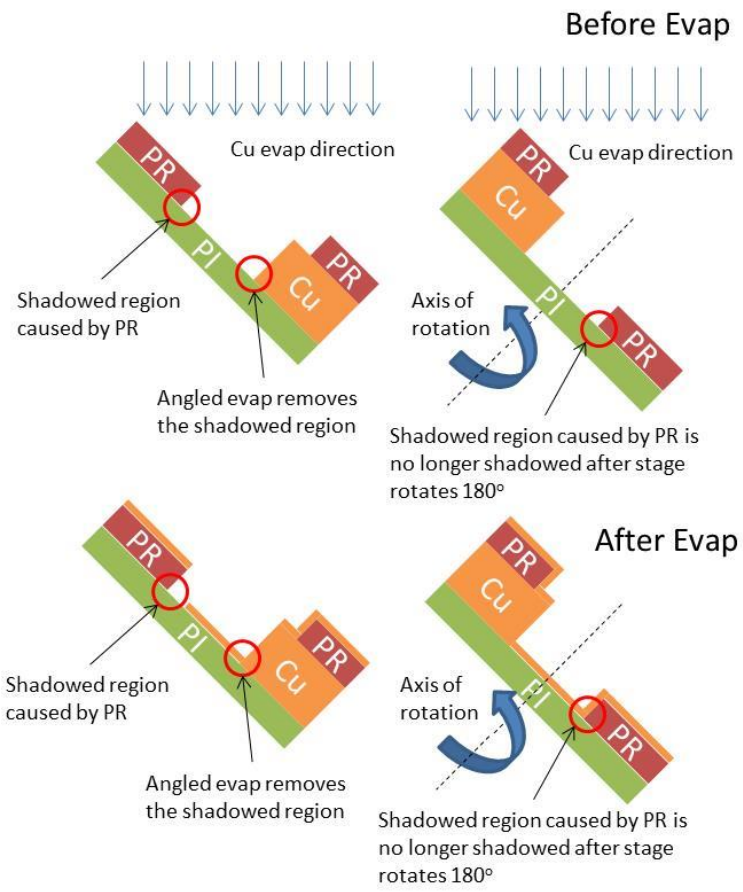

Figure 2.31: Basic schematic of angled evaporation stage.PR identifies a photo resist pattern defining the JT restriction, Cu is the large copper step and PI is the polyimide layer the JT pattern is deposited on.

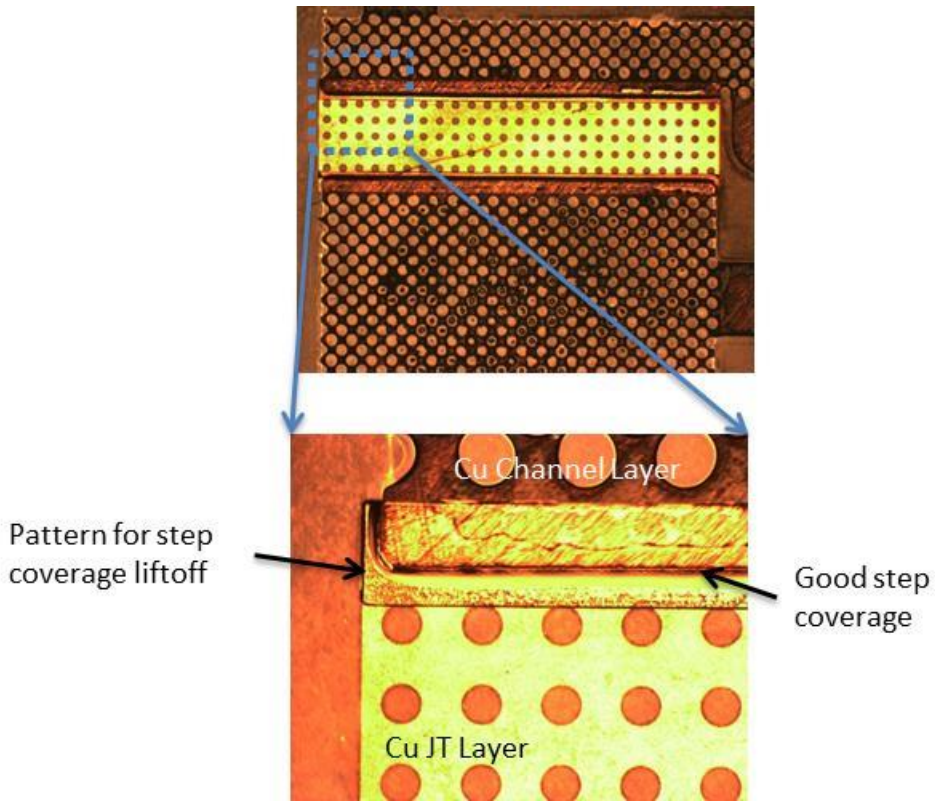

Figure 2.32: Channel definition to JT definition repair.

2.6.3 Polyimide to Polyimide Adhesion

If there is poor adhesion between the polyimide layers, the posts designed to hold the channel structure together under high internal pressure will delaminate. If a post has delaminated the stress on the surrounding posts will increase when the coldstage is pressurized. If enough posts delaminate locally, the stress on the surrounding posts will be high enough to cause failure. In this scenario the posts will experience a cascading failure and the entirety of the channel structure will balloon as shown in Figure 2.33. The JT restriction posts require 100% good adhesion. If one post is delaminated cascaded failure may not happen but the thickness of the JT restriction will be significantly increased at the location of the delaminated post. Because the JT restriction is dependent on the gap thickness to the third power (from equation 2.6), any increase in gap thickness will significantly reduce the restrictiveness of the JT restriction and not provide the required pressure drop. To solve this issue the spin cleaning process described previously to help copper adhesion to polyimide was implemented.

Additionally an adhesion promoter developed by HD MicroSystems (VM-651) was also used. The standard recipe for the adhesion promoter was used with the recommended spin on parameters. The only modification to the process was a three minute dwell after the adhesion promoter was applied to the wafer before the spin process is run to ensure the adhesion promoter wet to all surfaces.

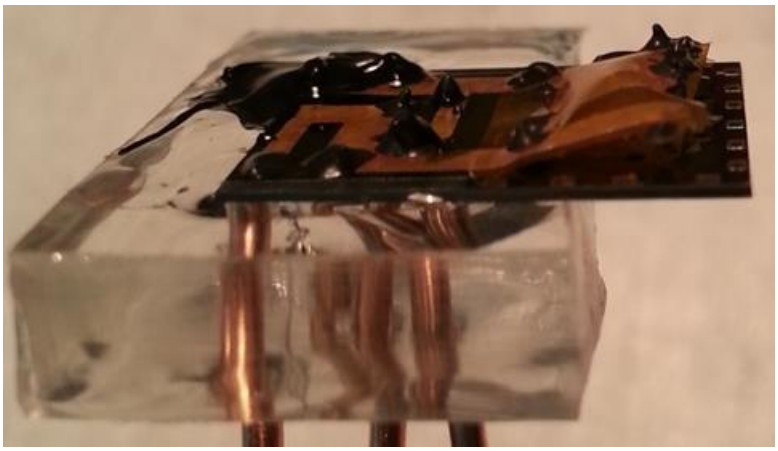

Figure 2.33: A coldstage experiencing cascaded failure of the intra channel support posts causing ballooning of the channel structure.

2.6.4 Electroplating Uniformity

Maintaining a uniform copper thickness during electroplating was a significant issue. The electroplating is done in a 5 gal plating tank with Copper U Bath RTU from Technic Inc. as the electrolyte solution and solid copper anodes. A current density of 5 mA/cm^2 is known to give a plating rate of ~5 µm/hr for the entire exposed front side of a 3 in wafer. The original design of the coldstage had 25 µm thick channels defined by the electroplated copper. The first plating process yielded significantly non-uniform plating thicknesses across the surface of the wafer. The plating increases at the edge of the wafer as shown in Figure 2.34. Profilometer measurements of the channel thickness were taken after etching the electroplated copper layer in to the channel geometry. Having significant variation in plating thickness causes significant issues when etching the copper layer with a wet etch. Because ~40 µm of copper must be etched at the edge of the wafer there is significant over etching of the 20 µm thick copper at the center of the wafer. The suspected cause of the extreme plating rate near the edge of the

wafer is a significant current concentration near the edge of the wafer. Plating rate is dependent on the local current density. If a region of the wafer has a significant current concentration in one location the plating rate will be higher in that region. To compound this issue, as a region has a higher plating rate and thus thicker plated thickness the electrical resistance to the region will decrease thus increasing the plating rate further. This positive feedback mechanism is suspected to cause the edge of the wafer to plate much faster. Because the plating rate is directly proportional to the plated thickness it is suspected that the non-uniformity of the plating will be exaggerated for longer plating times. Previous research conducted with the plating tank used showed uniform plating up to 15 – 20 μm across a 3 in wafer. The plating thickness is reduced to 20 μm with a plating time of 4 hours. The new plated thickness is shown in Figure 2.35. Reducing the plating time and thickness reduces the plating non-uniformity from ~200% to less than 50% across the wafer. Channel thicknesses of 20 – 25 μm are sufficient for successful coldstage fabrication and operation. Future process optimization and plating techniques should be investigated for plating thicknesses greater than 20 μm.

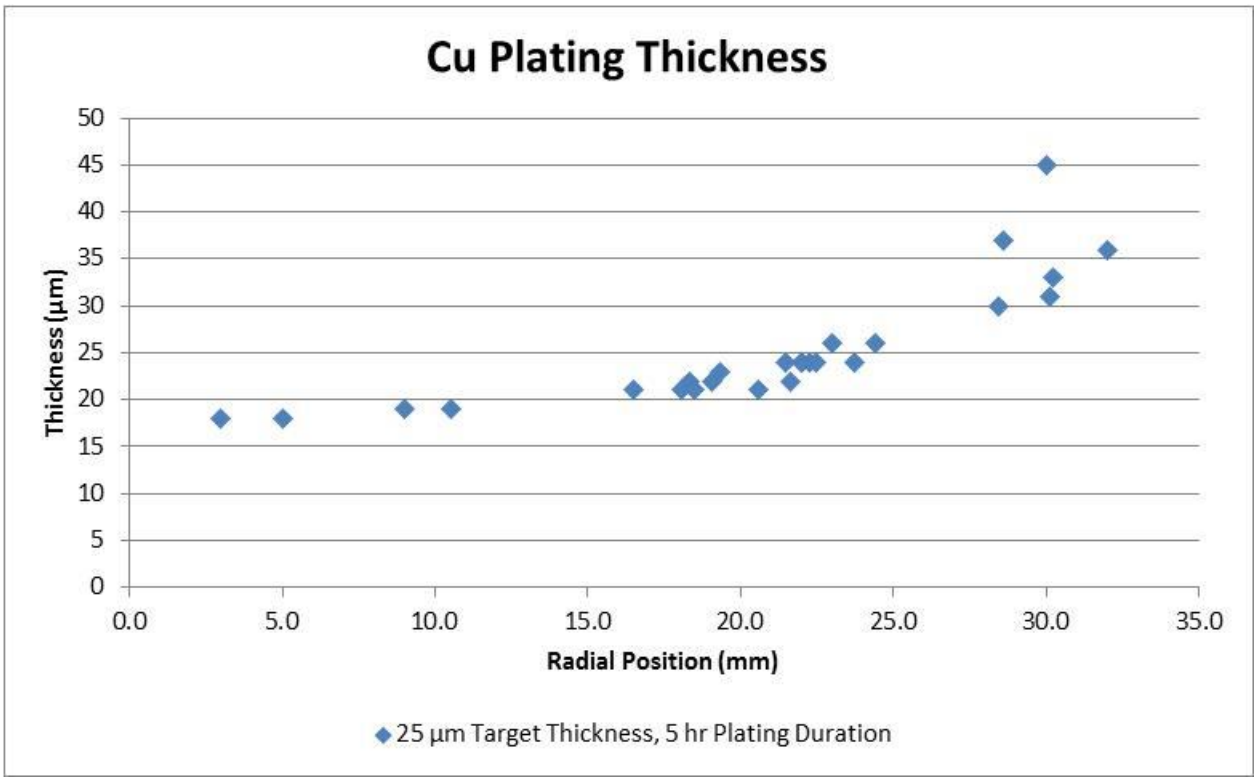

Figure 2.34: Thickness of electroplated copper after 5 hours of plating targeting a thickness of 25 µm.

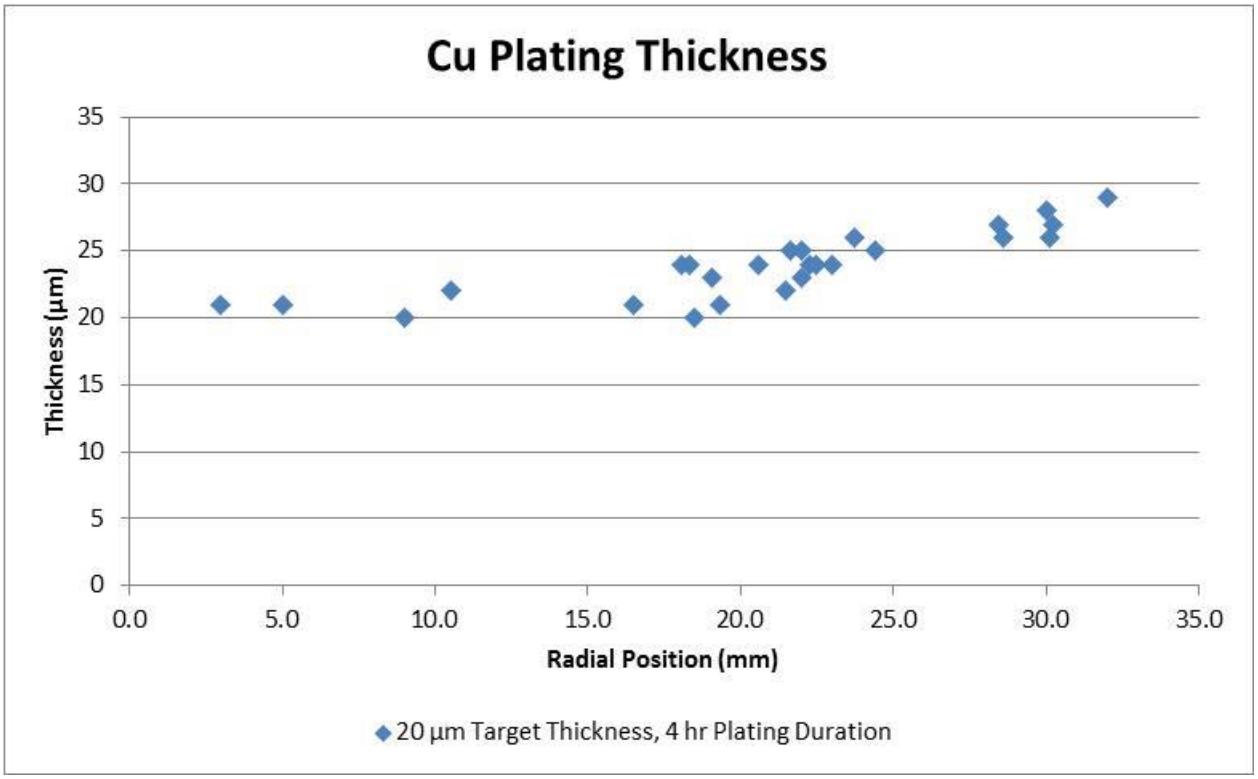

Figure 2.35: Thickness of electroplated copper after 4 hours of plating targeting a thickness of 20 µm.

2.6.5 Chemical Compatibility of Tygon Tubing

Although not a fabrication issue a major chemical compatibility issue was discovered during testing of the coldstages. The “Ultra Chemical Resistant Tygon 2375” laboratory tubing used for some fluidic connections was found to react with high pressure liquid isobutane. The specifications of the Tygon tubing indicate compatibility with hydro-carbons. However when exposed to liquid isobutane an oily residue is produced as shown in Figure 2.36. When exposed to atmospheric pressure any liquid isobutane will evaporate indicating the residue is not the refrigerant. A test was performed with hexane to confirm the residue generation. Hexane is liquid at atmospheric pressure and used as a facsimile to isobutane. A section of Tygon tubing was placed in a beaker of hexane overnight and then the hexane was allowed to evaporate in a fume hood the following morning. When all the hexane evaporated there was an oily residue remaining in the beaker as shown in Figure 2.37. The oily residue causes a significant problem when generated in the high pressure lines of the test setup. The residue is carried through the high pressure lines by the liquid isobutane. When the isobutane expands and evaporates across the JT restriction the residue precipitates and is deposited in the JT restriction. Eventually enough residue is deposited in the JT restriction to clog the coldstage causing device failure. To solve this issue all polymer tubing was replaced with copper tubing. It is recommended for chemical compatibility to be considered for any future test setup and coldstage design.

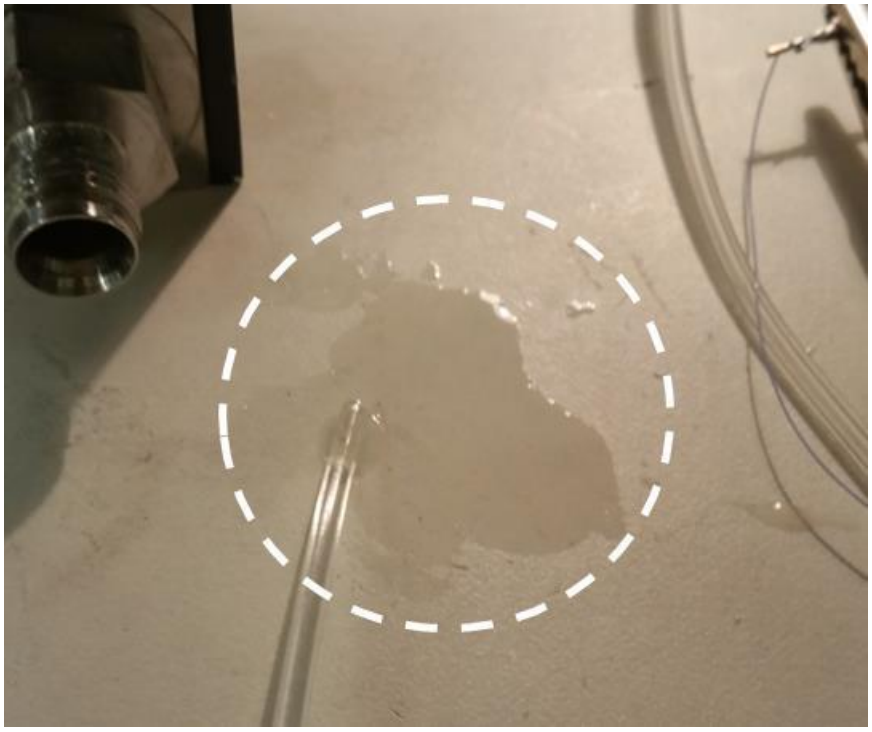

Figure 2.36: Oily residue caused by reaction of liquid isobutane and Tygon tubing.

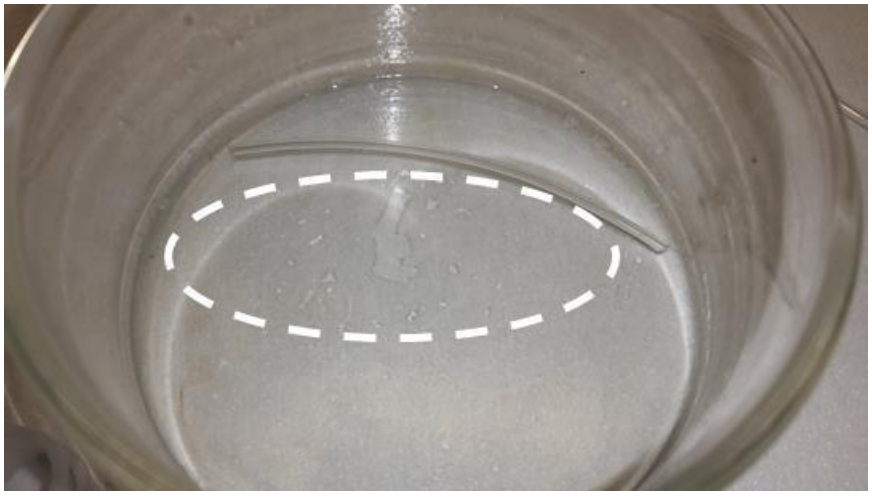

Figure 2.37: Oily residue remaining after soaking a section of Tygon tubing in hexane overnight and allowing the hexane to evaporate in a fume hood.

2.7 Fabrication Results

2.7.1 First Fabrication Run

After fabrication and assembly the first set of coldstages are tested in a qualification test where the channels are exposed to high internal pressure. The chips failed the qualification. At 0.23 MPa (20 psig) internal pressure the channel structure ballooned as shown in Figure 2.38. This is a much lower

pressure than the expected maximum of 0.4 MPa required to liquefy isobutane at room temperature. The assumed cause of the channel failure was the strength of the polyimide posts used to hold the channel together under high internal pressure. The posts were suspected as the point of failure due to low yield of the post patterning during processing. Figure 2.39 shows an example of the yield of the posts in the pattern of the sacrificial copper layer used to define the channels. Light areas are voids in the copper used to define the posts and the dark area is the sacrificial copper. To address this issue for future wafers the post diameter was increased from 60 µm to 120 µm. Increasing the post diameter both increases the strength of the individual posts by four times and increases the yield by making the pattern wider and easier to photo define and wet etch. Figure 2.40 shows a chip from the second wafer to go through the fabrication process. This wafer has the copper channel pattern changed to increase the post diameter to 120 µm. The chips on the second wafer experienced 100% yield of the post pattern except for 3 chips located close to the edge of the wafer.

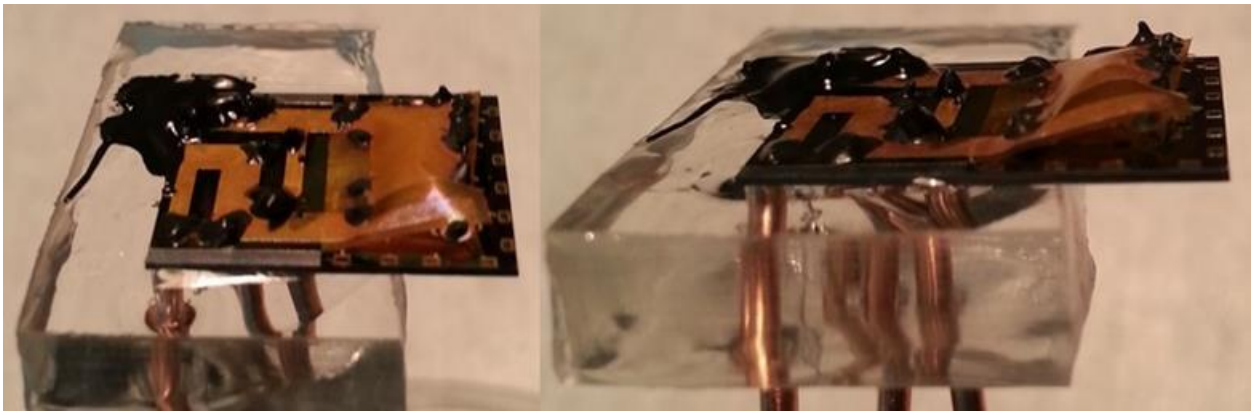

Figure 2.38: Ballooned channels from first set of fabricated chips.

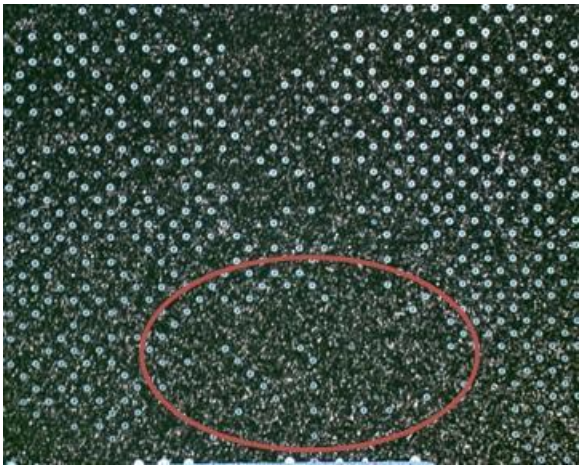

Figure 2.39: Low yield of post pattern. Dark area is the copper pattern used to define the channels; light circles are voids in the copper used to define the post pattern. Area circled in red is an area with very low yield. The post pattern should be a uniform grid of light circles.

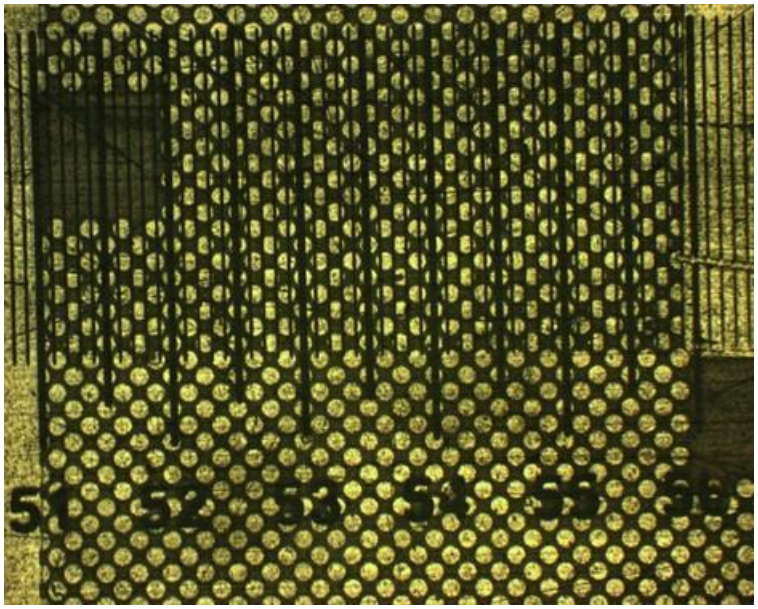

Figure 2.40: Channel and post pattern on second wafer to go through the fabrication process. Dark area is sacrificial copper, light circles are the 120 µm posts. A transparent ruler with 100 um minor ticks is overlaid.

2.7.2 Second Fabrication Run

A second fabrication run was completed with the larger 120 µm post design. The post strength was tested by applying high internal pressure. The JT restriction ballooned and failed at a pressure of 0.31 MPa (35 psig) as shown in Figure 2.41. The 120 µm post design is stronger than the 60 µm post design (failed at .23 MPa) but is still not strong enough to withstand the expected maximum internal

pressure of 0.4 MPa. In contrast to the 60 µm post design the ballooning 120 µm design does not cascade through the entire cold end of the coldstage. The larger post design is strong enough to withstand cascading failure indicating there should be no initial failure. To investigate the cause of failure a through design rev review was performed. During the design review a critical design error was discovered. A small area without posts was discovered where the JT pattern was intended to overlap with the high and low pressure channel patterns. Figure 2.42 shows a schematic view of the JT restriction with a 200 µm by 5 mm strip on either side of the JT restriction where there are no posts. To study the region of suspected failure a COMSOL multi-physics model was developed.

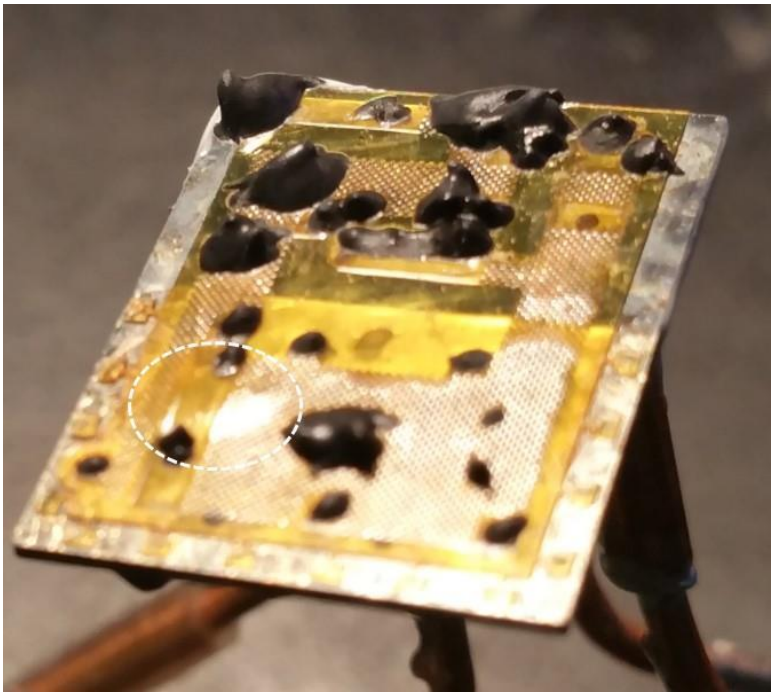

Figure 2.41: Ballooning of cold stage with 120 um posts. JT restriction is completely destroyed by the balloon. Balloon is outlined in white dashes.

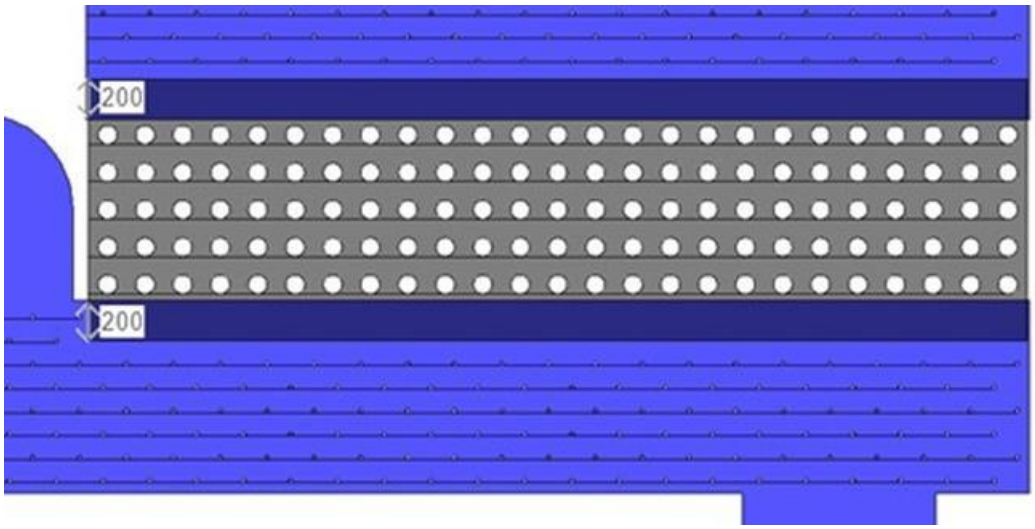

Figure 2.42: 200 µm by 5 mm strip between the high pressure channel and JT restriction, and between the JT restriction and the low pressure channel.

2.7.3 Qualitative Model using COMSOL Multi-Physics

To study and redesign the suspected area of failure a steady state model of the basic geometry was conducted using COMSOL multi-physics. A simplified geometry was used in the model for ease of computation. The modeled geometry ignores the 1 µm thick JT restriction and only considers 20 µm thick channel regions with a gap in the post pattern. Figure 2.43 shows the top down and cross sectional geometry for both the model and actual cold stage chips. Figure 2.44 shows the actual geometry constructed in COMSOL. The geometry utilizes the presence of three axis symmetry to minimize the computing time.

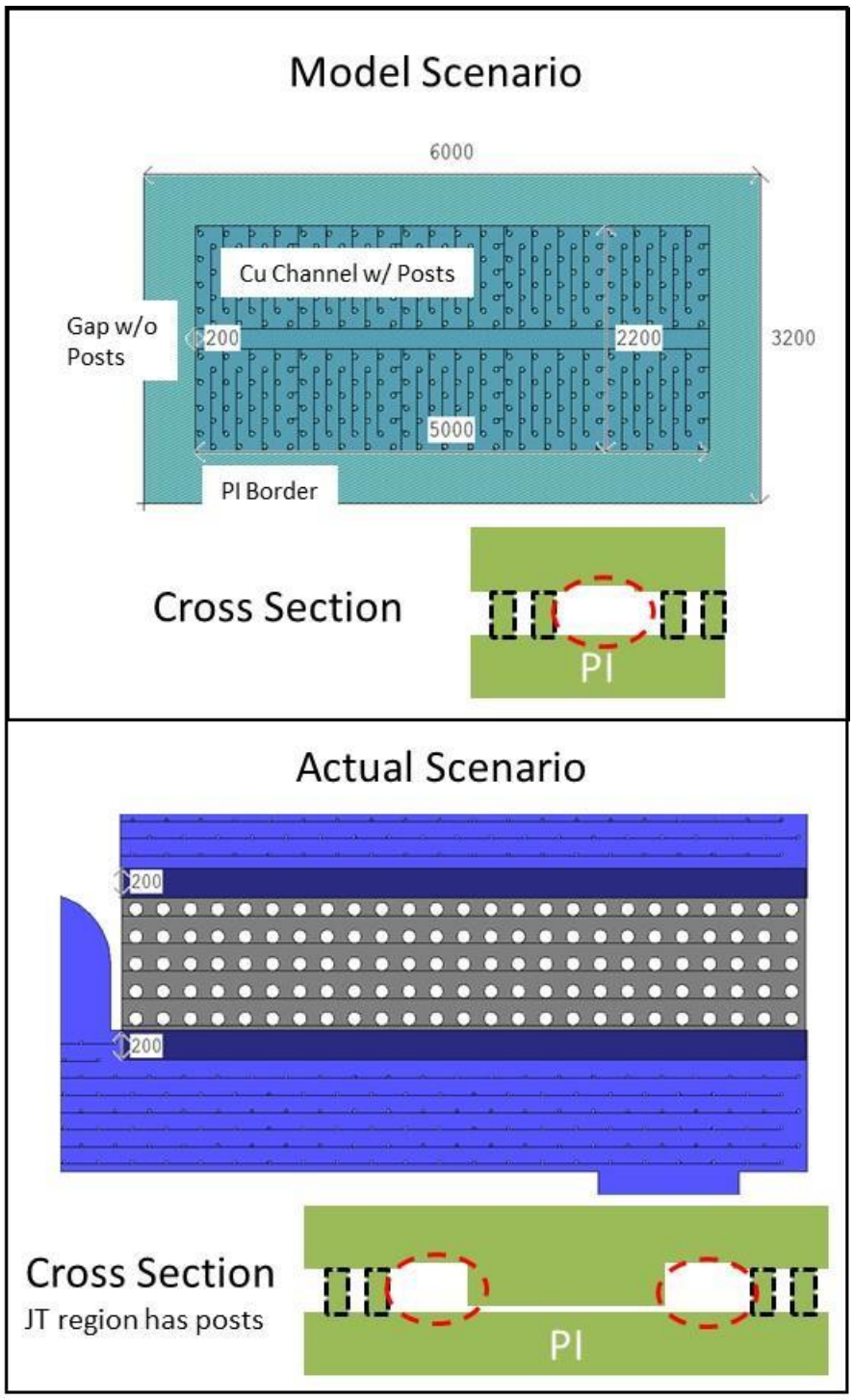

Figure 2.43: Top down schematic and cross section of both the modeled and actual geometry.

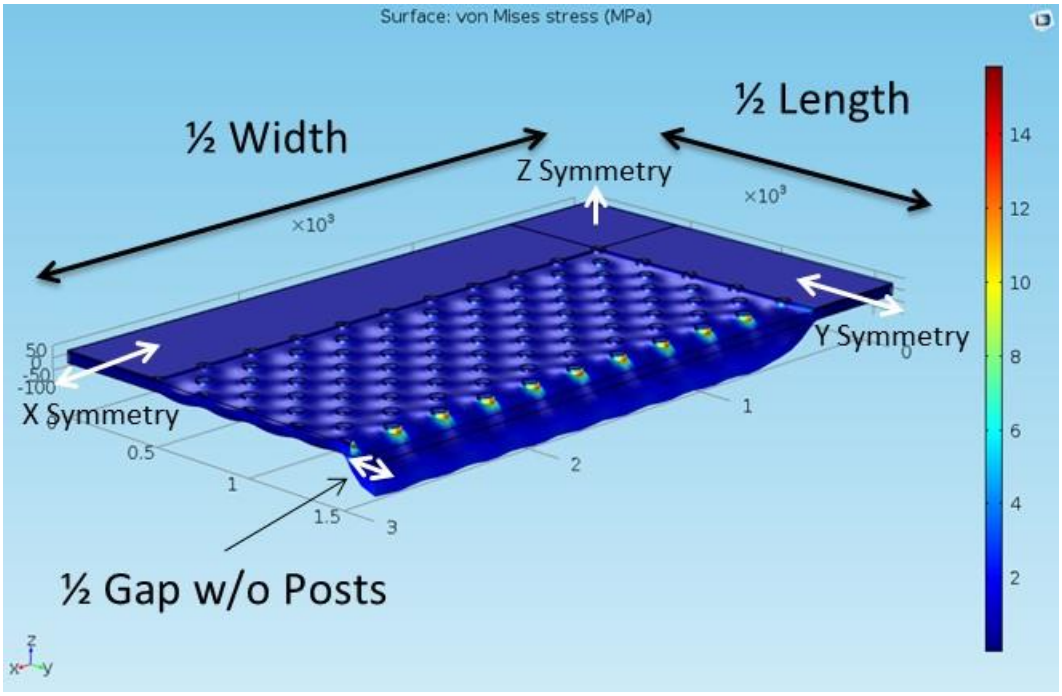

Figure 2.44: Geometry used to run the COMSOL model. The model uses three axis symmetry conditions to minimize computation.

The two known failure cases and a proposed new design are simulated and qualitatively compared. The first failure case uses an internal pressure of 0.23 MPa, post diameter of 60 µm, and a gap without posts of 200 µm as shown in Figure 2.45. A maximum simulated von Mises stress of 20 MPa is found. The maximum von Mises stress is used as a qualitative measure of failure criteria rather than a quantitative measure because the failure mode is most likely mode 1 peeling fracture. Modeling of fracture mechanics is a very difficult and lengthy process and is beyond the scope of this work. The second failure case uses an internal pressure of 0.31 MPa, a post diameter of 120 µm and a gap without posts of 200 µm as shown in Figure 2.46. A maximum simulated von Mises stress of 11 MPa is found. With the two failure cases modeled a failure criteria of 11 MPa von Mises stress is estimated.

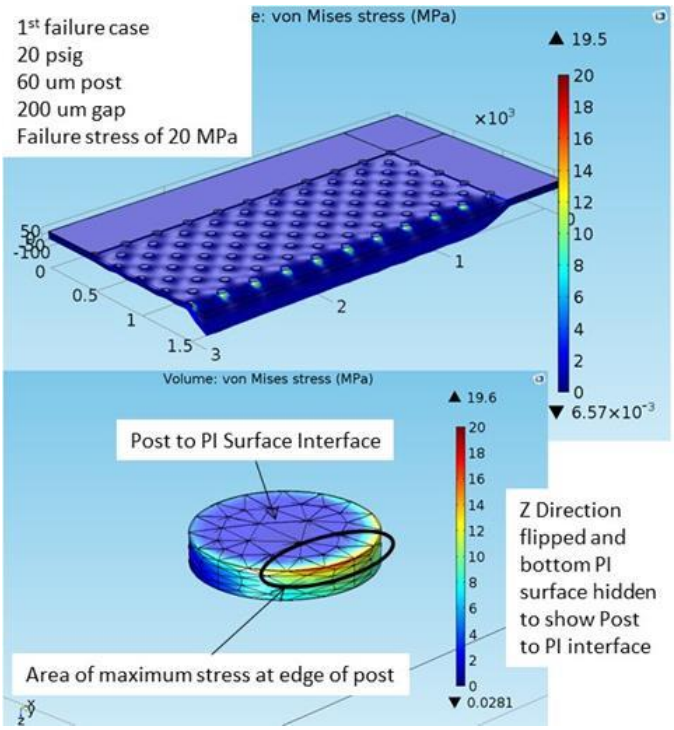

Figure 2.45: 1st failure case with 60 µm posts, 200 µm gap without posts, and 0.23 MPa internal pressure.

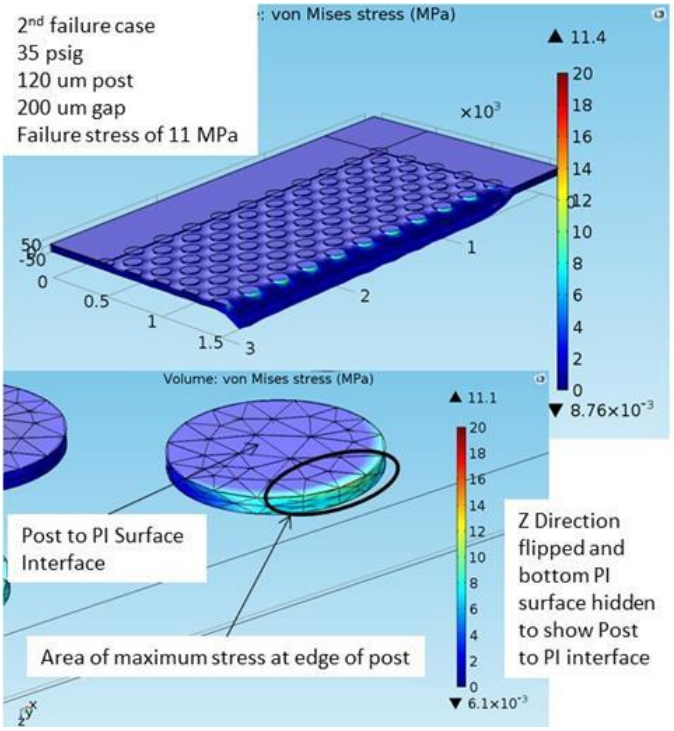

Figure 2.46: 2nd failure case with 120 µm posts, 200 µm gap without posts, and 0.31 MPa internal pressure.

Using the failure criteria of 11 MPa von Mises stress as an upper limit a proposed new design was simulated. The new design has 120 µm posts, a 50 µm gap without posts, and an internal pressure of 0.4 MPa (the maximum expected pressure when using isobutane as a refrigerant). Figure 2.47 shows a maximum von Mises stress of 5 MPa. This is an order of magnitude below the failure criteria estimated for the two known failure cases. Table 2.2 summarizes the results of the COMSOL modeling.

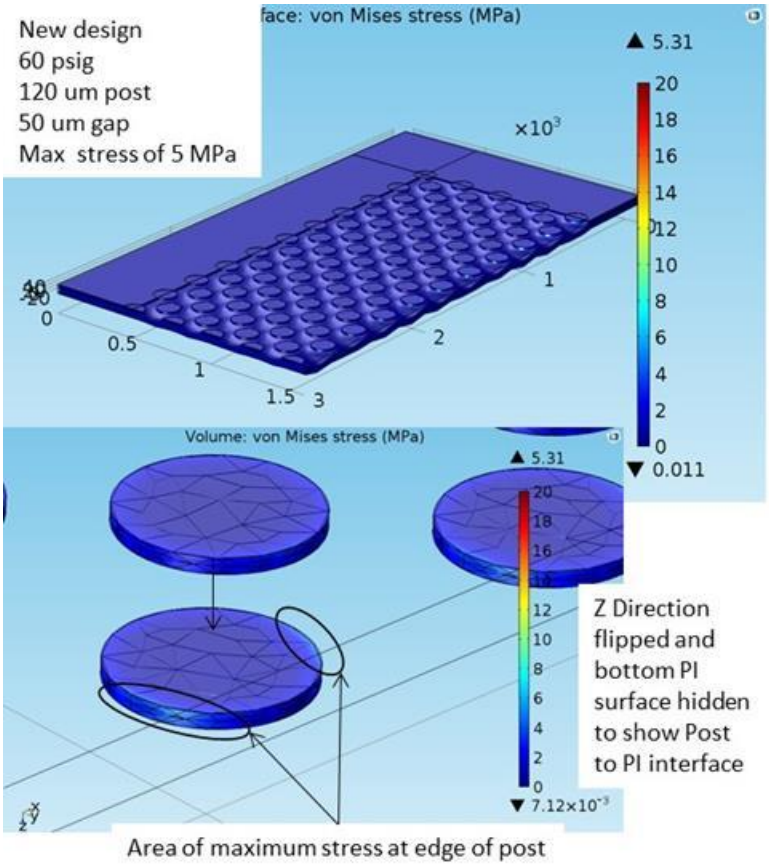

Figure 2.47: Simulation of new design with 120 µm posts, 50 µm gap without posts, and 0.4 MPa internal pressure.

Table 2.2: Summary of the cases modeled in COMSOL.

Case	Post Diameter (μm)	Gap w/o Posts (μm)	Internal Pressure of Failure or Maximum Internal Pressure Expected (Mpa)	Maximum von Mises Stress (Modeled) (Mpa)
1st Failure	60	200	0.23	20
2nd Failure	120	200	0.31	11
Proposed New Design	120	50	0.4	5

2.7.4 Third Fabrication Run

Due to extensive rework of the JT definition process step (Figure 2.7g) for reasons mentioned in chapter 2.6 the total process yield was very low and the best coldstage made had partial delamination of the posts supporting the JT restriction. This delamination occurred during processing and was not caused by high internal pressure. The partial delamination of the JT restriction will lead to ballooning if pressurized with high pressure isobutane. When the JT restriction expands it will not cause the required pressure drop. Due to this the coldstage was tested in a hyperbaric chamber at 0.4 MPa external pressure to ensure the JT restriction is squeezed into the correct geometry. Figure 2.48 shows the delaminated posts inside the JT restriction of the best coldstage fabricated during the third fabrication run. The posts circled in red are delaminated. Delamination is identified by the presence of optical fringes characteristic of sub-micron gaps.

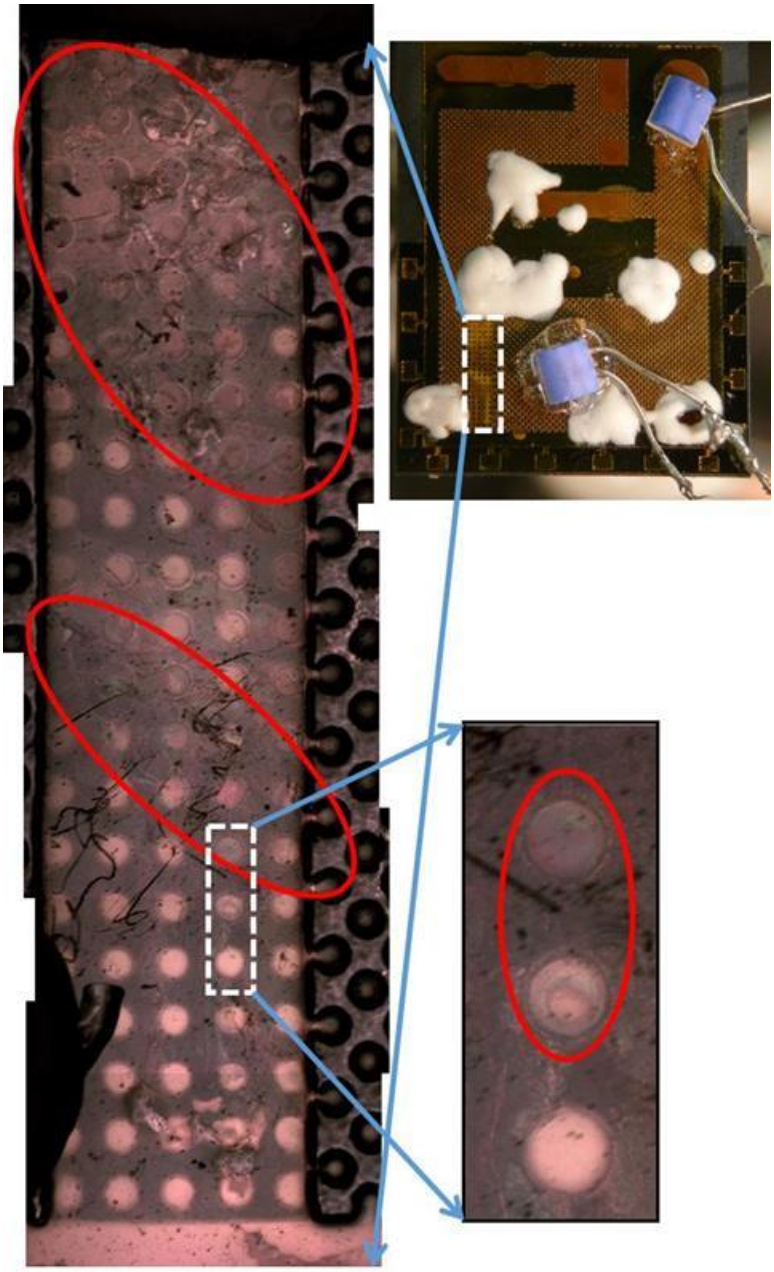

Figure 2.48: Partially delaminated JT restriction. Posts circled in red are delaminated indicated by fringe patterns characteristic of sub-micron gaps.

2.8 Coldstage Test Setup in Hyperbaric Chamber

Macro-scale fluidic connections are made to the coldstage by epoxying copper tubes too the backside of the coldstage around the through wafer vias. The coldstage is mounted to a liquid feedthrough to allow mounting into a hyperbaric chamber. Two temperature sensors are mounted to the coldstage one on the cold end after the J-T restriction and the other on the warm end on top of the

low pressure channel outlet. If the JT restriction is working properly the cold end temperature sensor will show cooling and the warm end temperature will read room temperature. If the JT restriction is not restrictive enough the refrigerant expansion will happen at the low pressure channel outlet and the cold end temperature sensor will read room temperature and the warm end temperature sensor will show cooling.

Figure 2.49 shows a schematic of the test set up. The coldstage is run in an open loop configuration where high pressure liquid isobutane is supplied by a cylinder with a liquid syphon tube. The syphon tube ensures liquid isobutane is being delivered to the coldstage. The isobutane flows through the coldstage and is vented to atmosphere after exiting the coldstage. A high pressure nitrogen cylinder is used to pressurize the hyperbaric chamber the coldstage is tested in to 0.4 MPa. The high pressure line pressure is measured with a pressure transducer connected to the refrigerant lines at the inlet of the hyperbaric chamber. The low pressure refrigerant is vented to atmosphere after passing through a mass flow meter. The low pressure line is operated at atmospheric conditions (0.082 MPa) and is monitored with a digital pressure gauge. The chamber pressure is measured with an analog gauge connected to the nitrogen line. A 0.5 µm pore size particulate filter is placed in between the isobutane tank and the hyperbaric chamber to eliminate any particulate contamination. Due to data acquisition limitations only the two temperature sensors, high side pressure, and flow rate are recorded. The chamber pressure and low side pressure are manually monitored.

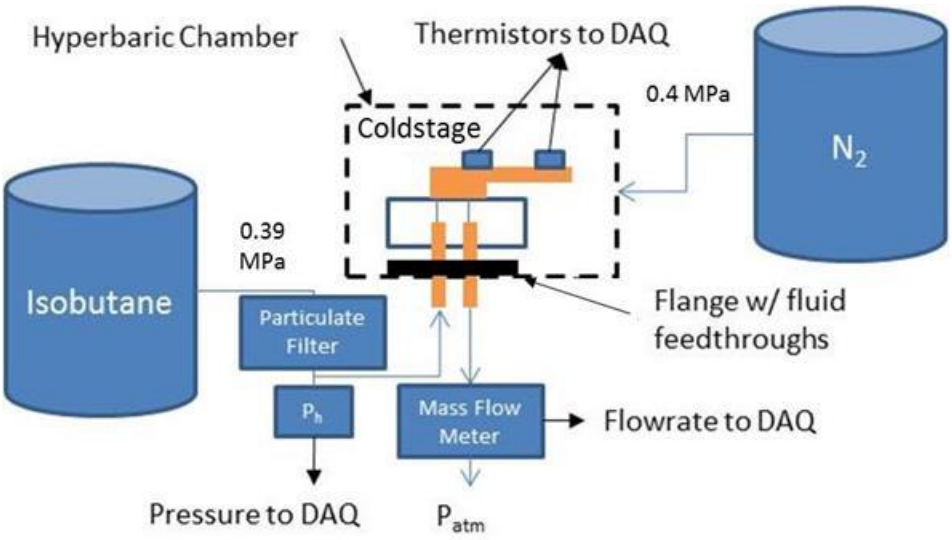

Figure 2.49: Test setup schematic for testing of coldstage in a hyperbaric chamber.

Figure 2.50a shows a fully fabricated chip mounted on to the liquid feedthrough flange. Copper tubes are epoxied to the backside of the device around the through wafer vias to make macroscale fluidic connection. The high pressure copper tube is soldered to the liquid feedthrough. The low pressure copper tube is connected to the liquid feedthrough with a short length of flexible Tygon 2375 Ultra Chemical Resistant tubing. After the coldstage is mounted to the liquid feedthrough the device is sealed into a vacuum cube repurposed to act as a hyperbaric chamber. Figure 2.50b shows the coldstage fully mounted into the hyperbaric chamber with the electrical feedthrough removed.

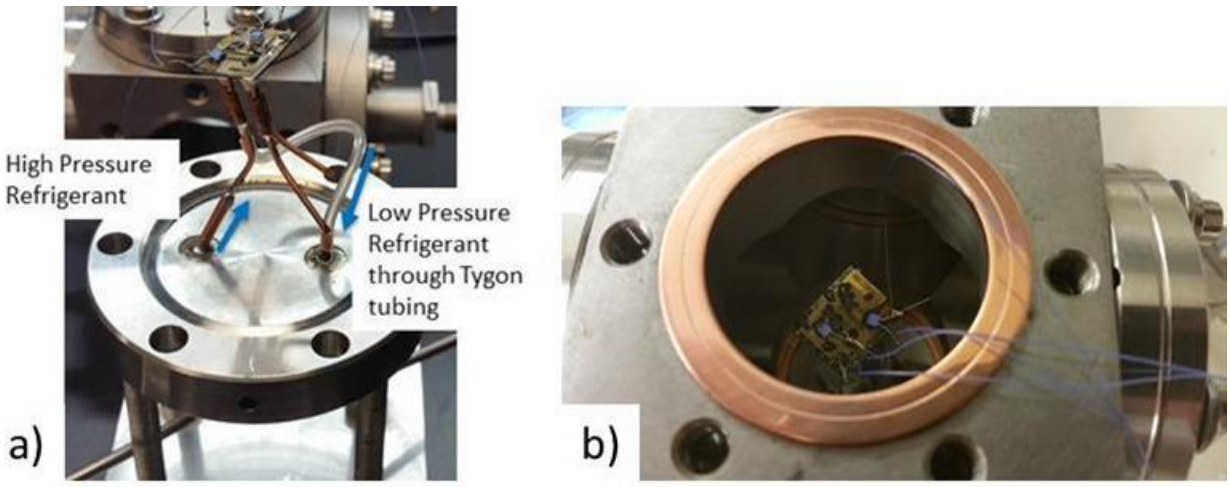

Figure 2.50: a) Coldstage mounted to liquid feedthrough and b) hyperbaric chamber mounted around coldstage with electrical feedthrough removed.

2.9 Coldstage Test Results in Hyperbaric Chamber

Before the refrigeration test is run vacuum is pulled on the refrigerant lines to attempt to eliminate any air and water contamination in the lines. The refrigerant lines maintain 5 x 10^{-5} torr for 1 hour. To start the test the vacuum pump is isolated from the refrigerant lines and the hyperbaric chamber is pressurized to 0.41 MPa. The isobutane tank is then opened to allow 0.1 MPa isobutane to fill the high pressure lines. The low pressure lines are opened to vent to atmosphere 0.082 MPa. Slowly the isobutane is increased to 0.39 MPa. In region 1 of Figure 2.51 the hyperbaric chamber is at 0.41 MPa and no flow or cooling is seen. This is due to a 0.02 MPa external pressure difference pinching shut the JT restriction. In region 2 of Figure 2.51 the hyperbaric chamber pressure is reduced to 0.4 MPa and cooling and flow is seen. The flow starts slow and then quickly increases to 6 sccm. This is indicative of a small air bubble trapped in the high pressure lines. Air moves slower through the JT restriction than liquid and two phase isobutane leading to an initially slow flow rate as the air passes through the JT restriction followed by a jump in flow rate as isobutane passes through the JT restriction. The flow rate then slowly decreases to 5 sccm. This is believed to be due to the increase in the refrigerant viscosity as the entirety of the cold end of the device cools to 281 K. In region 3 of Figure 2.51 the hyperbaric chamber pressure is reduced to 0.39 MPa and the flow rate increases to 10 sccm with the same slow

decrease in flow as the cold end continues to cool to 280 K. The dramatic increase in flow rate is due to the slight expansion of the JT restriction. Using equation 2.6 a flow rate of 6 sccm indicates a theoretical JT restriction thickness of 0.9 µm and a flow rate of 10 sccm indicates a theoretical JT restriction thickness of 1.1 µm. In region 4 of Figure 2.51 the hyperbaric chamber is pressurized back to 0.41 MPa to confirm the pinching of the J-T restriction. At the end of the test all refrigerant lines and the hyperbaric chamber are vented.

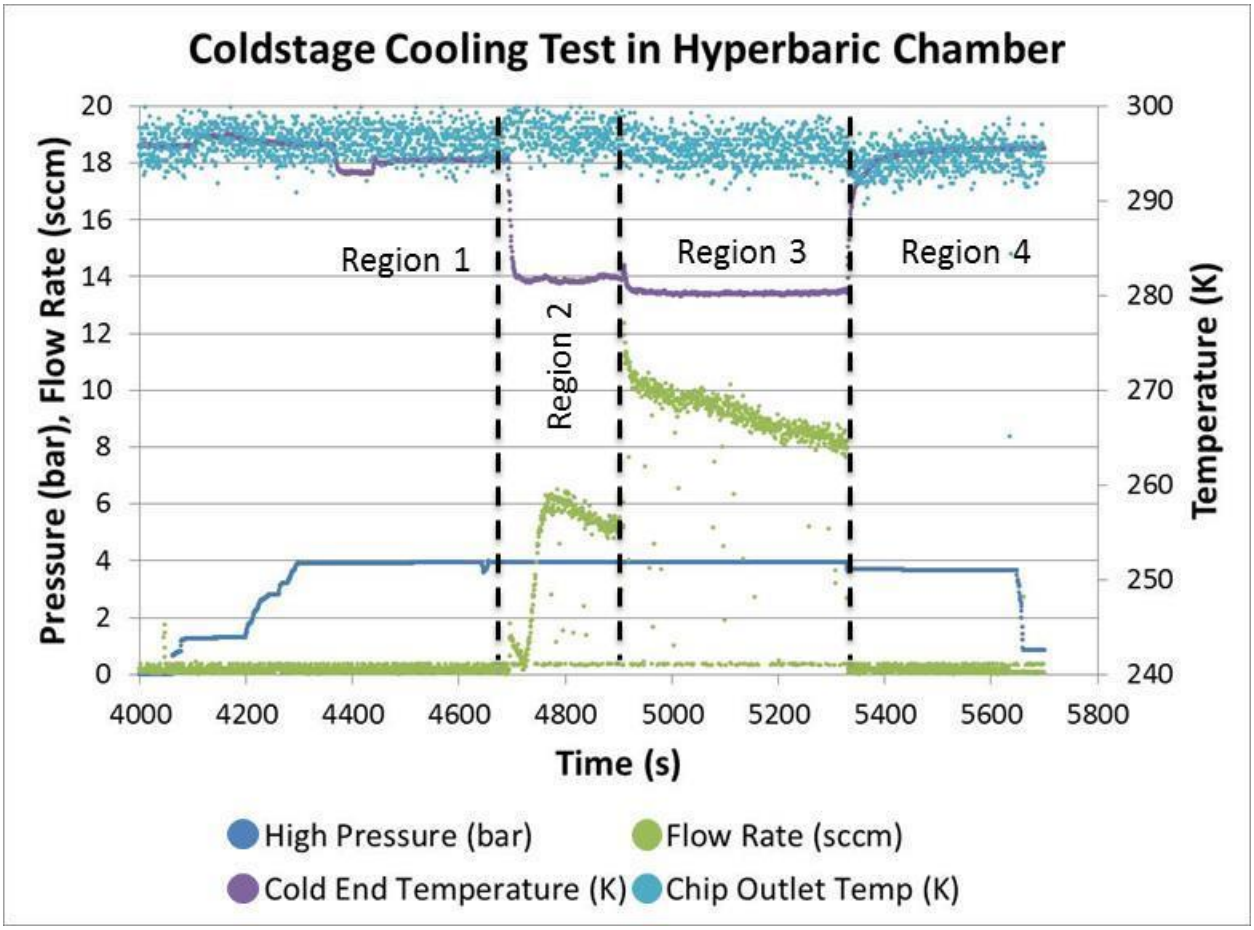

Figure 2.51: Coldstage cooling test in hyperbaric chamber, Region 1: hyperbaric chamber is at 0.41 MPa, Region 2: hyperbaric chamber is at 0.4 MPa, Region 3: hyperbaric chamber is at 0.39 MPa, Region 4: hyperbaric chamber is at 0.41 MPa followed by shutoff behavior.

2.10 Discussion

The ultimate cooling temperature of the coldstage is 280 K. This is 19 K higher than the expected temperature of 261 K. The temperature difference is due to the device being run in a 0.39 MPa nitrogen

environment. This environment adds significant natural convection heat leaks that were not designed for. The convective heat leak is assumed to be zero when run in a vacuum environment. When run in a high pressure environment the convective heat leak must be accounted for. The temperature is at equilibrium at 280 K meaning all heat leak into the cold end is equal to the gross refrigeration power of the JT cycle. The designed gross refrigeration power is 110 mW.

The heat leak from natural convection is [38]

$$\dot{Q}_{conv} = hA\Delta T \tag{2.9}$$

where $\dot{Q}_{conv}$ is the convective heat leak, h is the convective heat transfer coefficient, A is the surface area of the cold end of the device, and ΔT is the temperature difference between the cold end of the device and ambient. The convective heat transfer coefficient is based on geometry and fluid properties. Calculating the exact convective heat transfer coefficient for the microscale geometry presented is beyond the scope of this study. Instead an order of magnitude analysis is run with an assumed coefficient of 100 W/m^2/K. looking at both the top and bottom surfaces of the cold end of the device, a cold temperature of 280 K, and ambient temperature of 295 K the convective heat leak is approximated to be on the order of 100 mW. This is reasonable considering a gross refrigeration capacity of 110 mW. A convective heat leak on the order of 100 mW is sufficient to cause the coldstage to reach thermodynamic equilibrium at a cold end temperature of 280 K.

A more refined and more controlled fabrication process will greatly increase process yield. A successfully fabricated coldstage without any fabrication errors will be able to withstand internal pressures of up to 1 MPa without failure [28]. This will allow the coldstage to be run in a vacuum environment and eliminate convective heat leak. Future development of this fabrication process will enable MEMS fabricated low pressure ratio cascades JT coolers as described in chapter 1.4.

While micro-fabrication of wafer scale coldstages is the best method of miniaturization and most cost-effective method for producing large quantities, it has significant drawbacks for university level research and development. Developing a new micro-fabrication process flow is a long process requiring development time f each specific process step. Once the process is refined, completing one wafer run takes 3 to 6 months. Compound this with unforeseen processing errors, low yield, and the need for multiple device design iterations after testing, micro-fabrication leads to a significantly long design cycle. This long design cycle limits design iteration and does not allow for quick changes to device operating parameters like pressure ratio and flow rate. Because of the need for rapid prototyping of coldstages to work with different refrigerants at different pressure ratios and flow rates and to eventually work with a mini-compressor capable of producing unknown but low pressure and flow rate a faster coldstage fabrication approach is needed.

A different coldstage fabrication approach was identified. Chapter 3 presents the development of a micro-capillary based coldstage designed to work with low pressure ratios and low flow rates using a single refrigerant. Switching to a micro capillary based construction using hand assembly from a micro-fabrication based approach reduces device fabrication time from months to weeks, significantly improved device yield, and allows for rapid prototyping for specific pressure and flow rate design criteria.

2.11 Summary

This chapter presents the design, fabrication, and characterization of a low pressure ratio polyimide based micro-fabricated coldstage. The coldstage is designed to investigate the feasibility of the polyimide based fabrication techniques when applied to the relative large device size of the first stage of a cascaded coldstage presented in chapter 1.4 and Figure 1.20. The large size of the coldstage is driven by the size of the cold end required for efficient heat exchange to a theoretical second stage. The

coldstage is designed to operate with isobutane as a single component refrigerant at a pressure ratio of 0.4:0.1 MPa and to cool to 261 K. A gross refrigeration power of 110 mW is estimated for a net refrigeration power of 100 mW when considering lack of a recuperative heat exchanger, and expected heat leak form conduction and radiation when run in a vacuum environment. Major fabrication issues include copper-polyimide interactions, step coverage of evaporated copper, and polyimide-polyimide adhesion. Several solutions and best practices are presented. However the best coldstage fabricated had partial delamination of the posts supporting the JT restriction. Because the JT restriction was not fully supported it could not provide the required pressure drop. To solve this, the coldstage was run in a high pressure environment to squeeze the JT restriction into the correct shape. When tested in the hyperbaric chamber the coldstage cooled to a temperature of 280 K with a flow rate of 10 sccm at a 0.4:0.082 MPa pressure ratio. Due to increased convective heat leak form running the coldstage in a high pressure environment the coldstage reaches thermodynamic equilibrium at 280 K higher than the designed target of 261 K. The benefits of micro-fabrication are important for coldstage miniaturization and mass production. However the long design cycle and low process yield are not conducive to rapid prototyping. A faster and more reliable fabrication technique using glass capillaries and hand assembly is investigated in chapter 3.

Chapter 3: Single Stage Glass Capillary Based Coldstage for Low Pressure Ratio and Low Flow Rate

3.1 Motivation and Summary

The goal of this study is to develop a macro-scale coldstage fabrication process. The process developed needs to have a faster design cycle when compared to the 3 to 6 month design cycle of the micro-fabrication process detailed in chapter 2. This chapter describes the design, fabrication and characterization of a coldstage using this new fabrication process. The coldstage is fabricated from commercially available glass capillaries and a machined copper evaporator block reducing the design cycle to the order of weeks. The glass capillaries available have inner diameters ranging from 15 µm to 75 µm, and lengths of 10s of mm for ease of fabrication. The coldstage is designed to use n-butane as a single-component refrigerant with pressure ratio of 0.2:0.1 MPa and flow rate of 2 sccm, so as to be compatible with the miniature silicon-based compressors developed in parallel by Liew et al [13]. This study describes the design and fabrication of a single-stage coldstage, its expected performance, and shows cooling from 295 K to 268 K when insulated in a vacuum environment and 295 K to 285 K when run in atmosphere as predicted. The coldstage is integrated with a mini-compressor and run in atmosphere. The coldstage experiences pulsatile flow due to a flow rate mismatch between the coldstage and the mini-compressor. The coldstage is able to intermittently cool to 288 K when liquid butane flows through the JT restriction. No stable steady state temperature is reached during the integration test. The ease and speed of this fabrication technique is ideal for study of low pressure ratio single refrigerant multi-stage cascaded coolers as presented in chapter 1.4.

3.2 Design and Fabrication

The coldstage presented here is designed to work with a mini-compressor developed in parallel by Liew et al. [13]. The compressor is capable of producing a sustained flow rate of 2 sccm at a pressure ratio of 0.2:0.1 MPa. At this low pressure ratio n-butane is an ideal single refrigerant as it liquefies at

room temperature and 0.22 MPa. In practical application with the mini-compressor minor precooling to 291 K will be required to liquefy the butane at 0.2 MPa. When the high pressure butane is expanded to 0.082 MPa (atmospheric pressure in Boulder, CO) the coldstage is expected to reach 267 K when properly thermally isolated.

Figure 3.1 shows a cross-sectional schematic of the coldstage. Figure 3.2 shows a fully fabricated coldstage. The coldstage consists of a glass capillary sheathed in Kapton as the JT restriction. The glass capillary is 32 mm long and has an inner diameter (ID) of 25 um and an outer diameter (OD) of 150 um. The capillary inlet is epoxied into copper tubes of increasing diameter to couple it to a 3.175 mm (0.125 in) OD copper tube on the high pressure side which ultimately connects to a high pressure n-butane cylinder or the mini-compressor. On the low pressure side the capillary outlet is epoxied to an evaporator block (shown in Figure 3.3) consisting of a bored out copper block (of dimensions 5 mm x 5 mm x 7 mm) with #100 copper mesh packed into the cavity and diffusion bonded in place. The large surface area created by the mesh inside the evaporator block ensures all evaporation takes place at the evaporator block providing a consistent cold zone. The evaporator block is capped with a small copper disc and copper tube to accept the capillary fiber. The copper evaporator block is thermally isolated from the remainder of the low pressure lines by a 20 mm length of 3.175 mm (0.125 in) OD Kapton tubing. The Kapton tube is coupled to a 3.175 mm (0.125 in) OD copper tube through an intermediate 6.35 mm (0.25 in) OD coper tube. The coldstage does not utilize a recuperative heat exchanger to pre-cool the incoming refrigerant. Both the high and low pressure 3.175 mm (0.125 in) OD copper tubing are mounted to a vacuum liquid feedthrough for operation in a vacuum environment. All joints are made using a commercial (TorrSeal) vacuum epoxy.

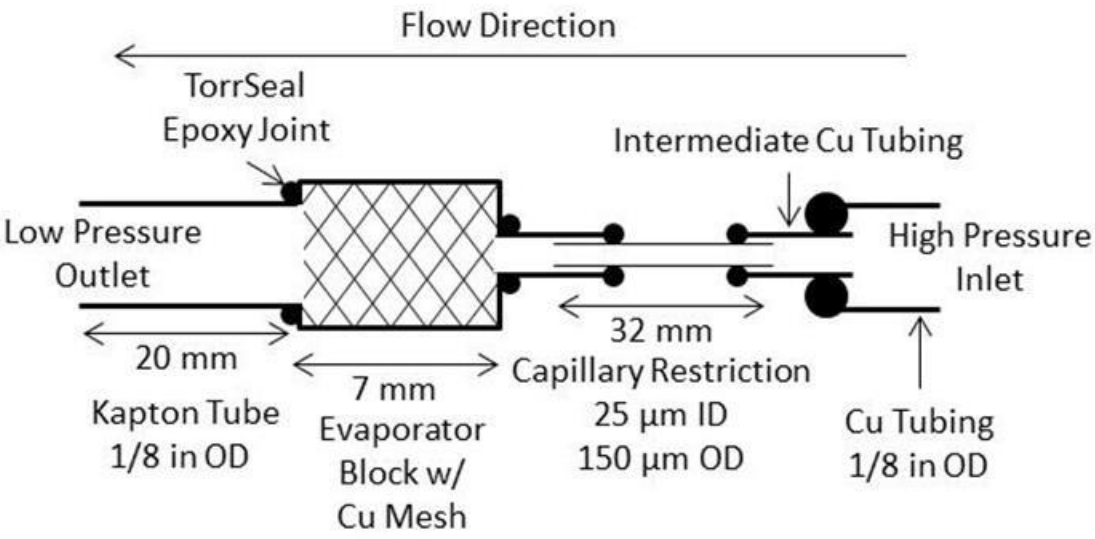

Figure 3.1: Cross-sectional schematic of coldstage (not to scale).

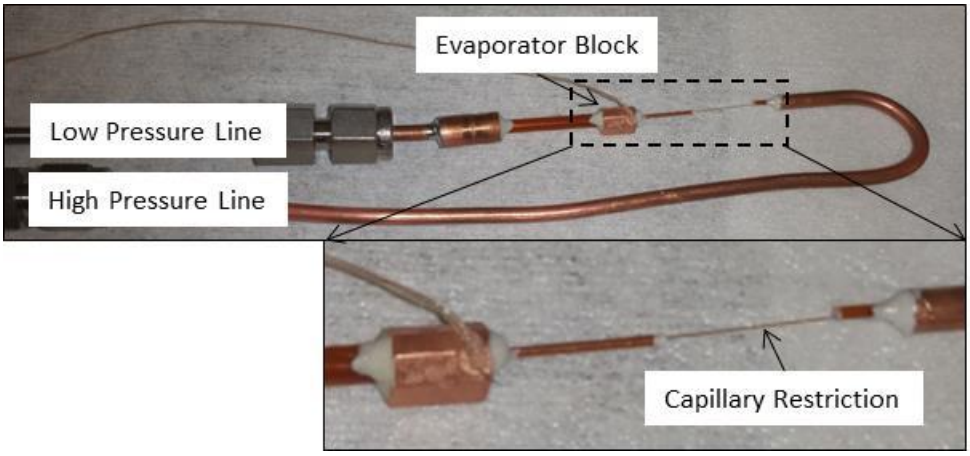

Figure 3.2: Fully assembled coldstage.

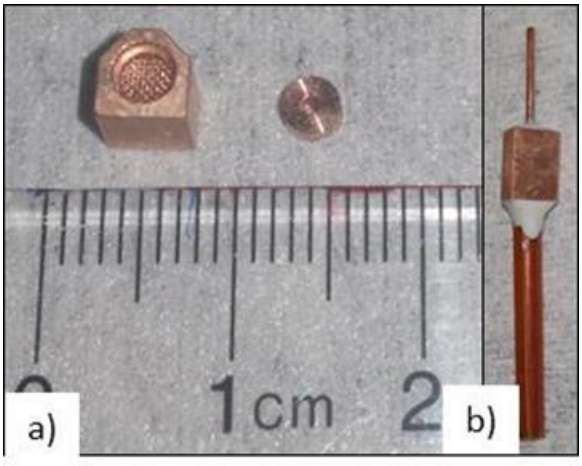

Figure 3.3: Copper evaporator block with copper mesh diffusion bonded in place next to a copper cap. b) Fully assembled evaporator block and Kapton tube for thermal standoff.

The length and inner diameter of the capillary is determined by consideration of the laminar two phase flow undergoing adiabatic expansion through a circular tube as expressed by equation 2.7 [8] rearranged for length and a circular cross-section

$$L = \frac{\pi d^4}{128\dot{n}} \frac{1}{\int \frac{D_{m,avg}}{\mu_{avg}} dP} \tag{3.1}$$

where L is the length of the capillary, d is the inner diameter of the capillary, $\dot{n}$ is the mass flow rate of the refrigerant, P is the pressure of the fluid ,and from chapter 2.4 the Dukler averages of density and viscosity for two phase flow are [39]

$$D_{m,avg} = \frac{1}{\frac{x}{D_{m,v}} + \frac{1-x}{D_{m,l}}} \tag{2.7}$$

$$\mu_{avg} = D_{m,avg}\left(\frac{x\mu_v}{D_{m,v}} + \frac{(1-x)\mu_l}{D_{m,l}}\right) \tag{2.8}$$

where x is the quality of the two phase fluid at a given pressure, $D_{m,v}$ and $D_{m,l}$are the molar densities of the vapor and liquid portions of the fluid respectively, and μ_v and μ_l are the viscosities of the vapor and liquid portions of the fluid respectively. The integral is evaluated via tabular integration using fluid properties from the NIST REFPROP v. 9.1 program [40]. The properties used are tabulated in Appendix B.

A capillary length of 32 mm and ID of 25 µm is calculated to produce the desired flow rate of 2 sccm of n-butane at a 0.2:0.1 MPa pressure ratio. Table 3.1 lists the JT capillary restriction lengths for all available capillary inner diameters required to provide a 0.2:0.1 MPa pressure drop at a flow rate of 2 sccm of n-butane. The restrictiveness of the JT capillary is dependent on the inner diameter to the forth power. Increasing the inner diameter leads to a significant increase in capillary length to maintain the same pressure drop and flow rate.

Table 3.1: JT restriction capillary lengths for various available capillary inner diameters. Capillaries are designed to operate with a 0.2:0.1 MPa pressure ratio and a flow rate of 2 sccm of n-butane.

Diameter (µm)	Length (mm)
15	4
20	13
25	32
30	66
40	210
50	512
75	2591

From chapter 1.2 the gross refrigeration power of a JT refrigeration cycle is [8]

$$\dot{Q}_r = \dot{m}(\Delta h|_T)_{min} \tag{1.1}$$

where $\dot{Q}_r$ is the ideal gross refrigeration power, $\dot{m}$ is the molar flow rate of the refrigerant, and $(\Delta h|_T)_{min}$ is the minimum enthalpy difference between the high and low pressure states of the refrigerant over the temperature range of cooling. The coldstage design eliminates the recuperative heat exchanger and is expected to operate at ~80% of the ideal when calculated using the method of heat exchanger ineffectiveness detailed in [8], [30]. Butane has a $(\Delta h|_T)_{min}$ of 21.5 kJ/mol for the expected operating conditions. The coldstage is expected to have a gross refrigeration power of ~35 mW. When operating the coldstage in a vacuum environment we expect to see a total heat leak into the cold end of the coldstage from conduction and radiation to be less than10 mW due to radiation and conduction. This leads to an expected available refrigeration power of ~25 mW.

3.3 Testing the Coldstage from a High Pressure Cylinder

Figure 3.4 shows a schematic of the test setup used. The coldstage is run in an open loop configuration where high pressure butane is supplied by a compressed gas cylinder with a liquid syphon tube. The syphon tube ensures liquid butane is being supplied to the high pressure inlet of the coldstage. The outlet of the coldstage is connected to a mass flow meter to measure the outflow of the butane at ambient atmospheric conditions. An inline particulate filter is placed upstream of the coldstage to ensure particles larger than 25 um diameter do not clog the capillary restriction. Figure 3.5 shows the coldstage mounted into the vacuum chamber for thermal isolation.

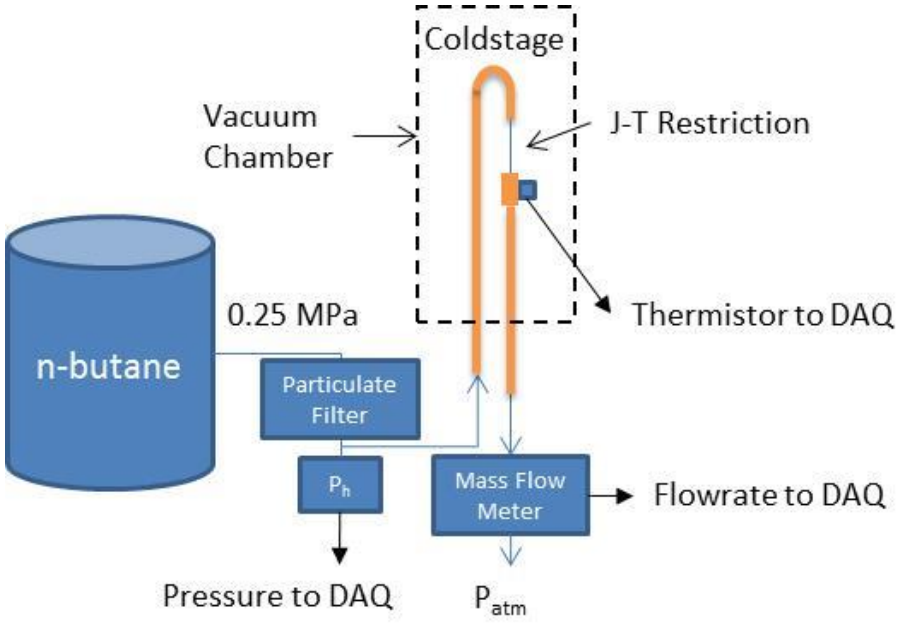

Figure 3.4: Schematic of test setup with high pressure refrigerant cylinder.

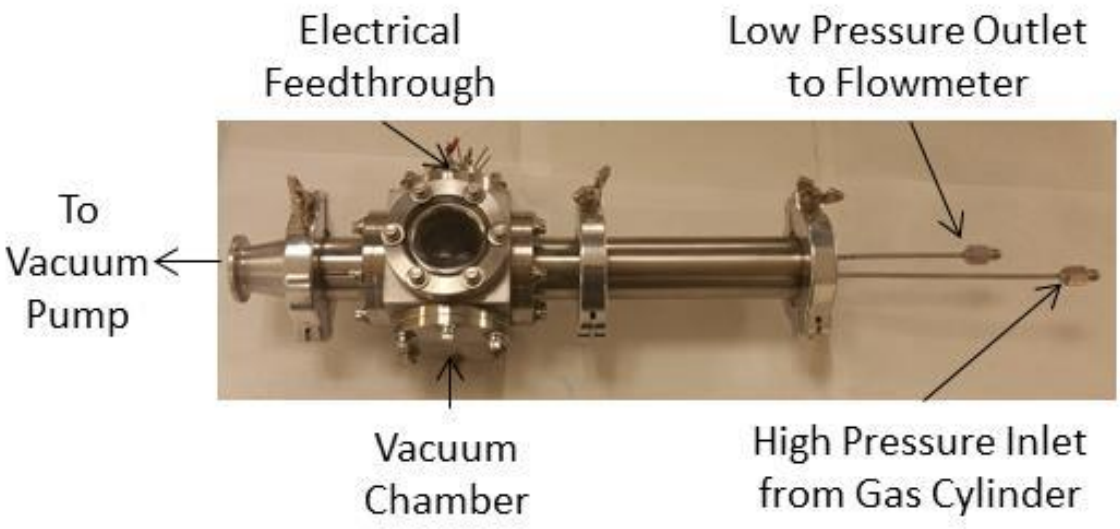

Figure 3.5: Vacuum chamber with coldstage mounted to liquid feedthrough.

Before the refrigeration test is run vacuum is pulled on the refrigerant lines to attempt to eliminate any air and water contamination in the lines. The refrigerant lines maintain 5 x 10^{-5} torr for 1 hour. Test results are shown for the coldstage operating in a vacuum environment in Figure 3.6 and in atmosphere in Figure 3.7. In both plots time zero is when the high pressure lines are pressurized with 0.25 MPa liquid butane. In the vacuum test (Figure 3.6) there is a brief delay as liquid builds in the high pressure lines and any remaining air bleeds through the JT restriction. Eventually liquid is present at the inlet to the capillary restriction. At this point there is an increase in flow rate and the evaporator begins to cool down. Once the evaporator reaches the saturation temperature (268 K) of butane at 0.084 MPa there is a slight drop in flow rate. It is believed because we are measuring the outflow of the coldstage small droplets of liquid butane are condensing in the evaporator's small mesh crevices. This leads to a net drop in mass outflow until all available crevices are filled. Once steady state is reached (around 1700 s) a steady state flow rate of 3 sccm and temperature of 268 K are measured.

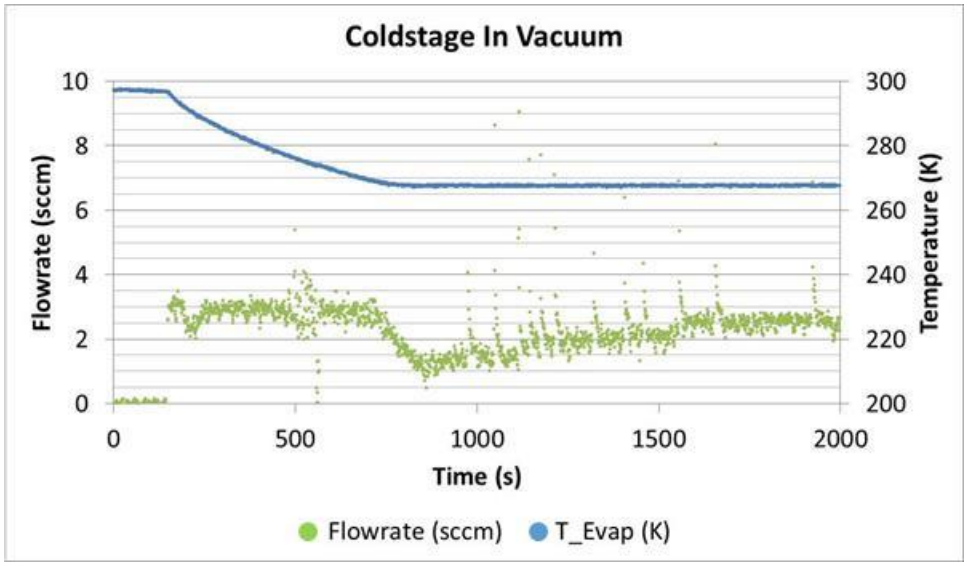

Figure 3.6: Refrigeration test in vacuum chamber. Vacuum of 5 x 10^{-5} torr is maintained in the chamber. High pressure lines pressurized with 0.25 MPa butane at time zero.

When the coldstage is run in atmosphere (Figure 3.7), i.e. without thermal insulation, there is a longer delay before cooling starts. This is believed to be caused by a larger amount of air in the high pressure lines than the vacuum environment test. This air must move through the capillary restriction before the liquid butane reaches the capillary inlet. The momentary spikes in cooling seen before steady state is reached is believed to be caused by small slugs of liquid butane flowing through the coldstage followed by more air. Eventually steady state is reached (around 2000 s) and steady state flow rate of 3 sccm and temperature of 285 K are reached.

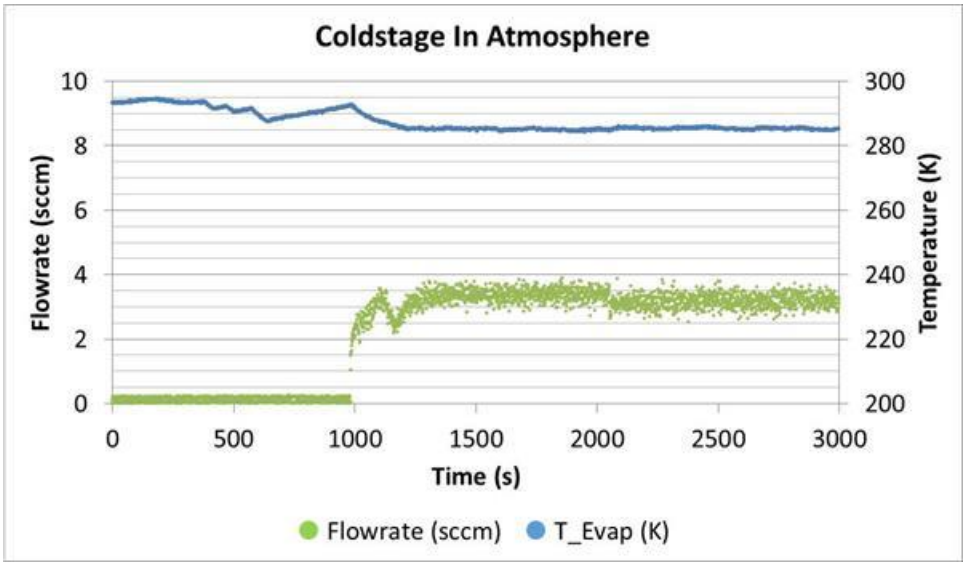

Figure 3.7: Refrigeration test in atmosphere. High pressure lines pressurized with 0.25 MPa butane at time zero.

The steady state temperature of 285 K when run in atmosphere is reasonable due to the introduction of significant convective heat losses. From chapter 2.10 the heat leak from natural convection is [38]

$$\dot{Q}_{conv} = hA\Delta T \tag{2.9}$$

where $\dot{Q}_{conv}$ is the convective heat leak, h is the convective heat transfer coefficient, A is the surface area of the cold end of the device, and ΔT is the temperature difference between the cold end of the device and ambient. The convective heat transfer coefficient is based on geometry and fluid properties. Calculating the exact convective heat transfer coefficient for the coldstage presented is beyond the scope of this study. Instead an order of magnitude analysis was run where we assume the convective heat transfer coefficient is on the order of 10 – 100 W/m^2/K. The convective heat leak is expected to be on the order of 10 – 100 mW. It is therefore reasonable to expect to see thermodynamic equilibrium at 285 K (Figure 3.7) when the estimated available refrigeration power is ~25 mW.

The coldstage is tested in vacuum to ensure it is operating as designed. The coldstage is tested in atmosphere because when integrated with the mini-compressor there is no access to the vacuum

chamber or vacuum pump. The test in atmosphere establishes a baseline to judge the results of integrating the coldstage to the mini-compressor. The next section of this chapter discusses the integration of this coldstage with the mini-compressor developed by Liew et al. [13].

3.4 Coldstage Integration with Mini-Compressor

The coldstage is qualified in atmosphere with a flow rate of 3 sccm, an ultimate cooling temperature of 285 K, and a pressure ratio of 0.25:0.1 MPa. Butane liquefies at 295 K and 0.22 MPa. The compressor developed by Liew et al. [13] is capable of providing a 0.2:0.1 MPa pressure ratio at a flow rate of 2 sccm. Icepack precooling is needed to liquefy the butane at 0.2 MPa and 290 K. The flow rate mismatch between the compressor and coldstage causes pulsatile flow and intermittent cooling. Figure 3.8 shows the schematic of the test setup used to integrate the Mini-compressor and coldstage. Butane is supplied to the low pressure inlet of the compressor slightly above atmospheric pressure at 0.11 MPa. The n-butane is compressed to a high pressure measured by a pressure transducer with a target pressure of 0.2 MPa. The high pressure butane is liquefied before the JT restriction via icepack precooling. The liquid butane expands across the JT restriction and provides cooling at the evaporator. The butane is vented to atmosphere through a mass flow meter. Figure 3.9 shows a photograph of the integration test setup and a close up of the coldstage with icepack precooling applied.

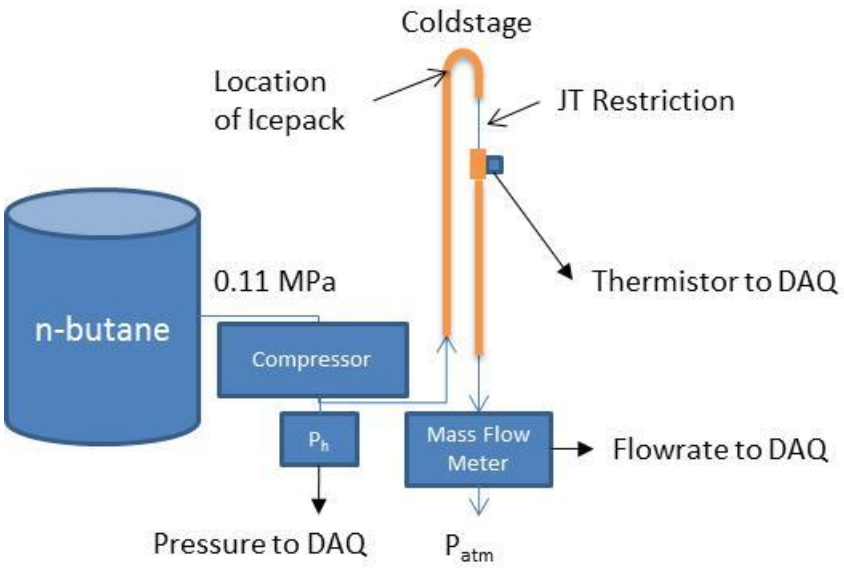

Figure 3.8: Schematic of mini-compressor – coldstage integration test setup.

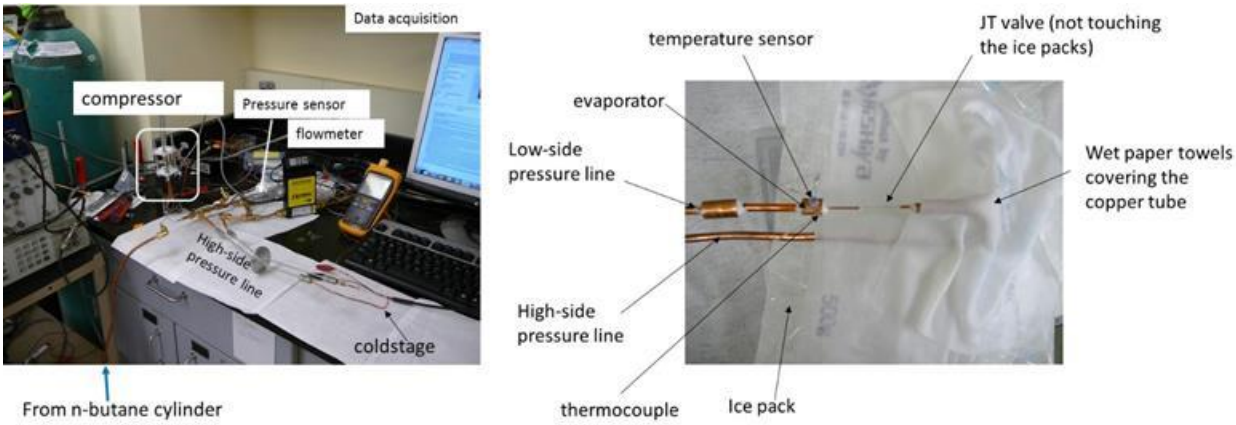

Figure 3.9: (Left) Photograph of compressor and coldstage in the experimental set-up. (Right) Close up photograph of the coldstage with icepack.

Figure 3.10 shows the evaporator temperature of the coldstage over time along with the compressor's outlet pressure and the coldstage flow rate when tested as in Figure 3.8 and Figure 3.9. During the first 3000 seconds of the test, the butane is gradually displacing the ambient air that was initially inside the high pressure lines, thus the flow rate is minimal despite the increasing pressure. After about 3000 seconds, all the air has been removed and the JT expansion can be seen as the drop in evaporator temperature and increase in butane flow rate. The pressure ratio is 0.2:0.1 MPa and the maximum flow rate is 3 sccm. The compressor's delivered flow rate of about 2 sccm is not sufficient to

maintain a steady flow of the refrigerant, thus there is a time lag from when the high-pressure liquid butane expands and vaporizes inside the high pressure line and new liquid builds up enough pressure to re-liquefy, leading pulsatile flow. This can be seen in the pulsing flow rate and temperature and is explained by the variation in the high side pressure around the saturation pressure (0.2 MPa or ~13 psig). As the high side pressure drops below the saturation pressure all liquid butane in the high pressure line vaporizes causing the flow rate to drop and the evaporator temperature rises. Because the flow rate is now below what the compressor can supply the pressure builds back up and the butane liquefies again. The liquid butane then reaches critical volume to cover the JT restriction inlet and a flow rate of 3 sccm is measured as liquid butane expands across the JT restriction. Because the compressor can only supply butane at 2 sccm there is a net mass loss of butane in the high pressure lines causing a decrease in pressure. As the pressure drops below the saturation pressure all liquid butane in the high pressure line vaporizes and the flow rate drops back below 2 sccm allowing the compressor to increase the high pressure line back to saturation pressure. During these periods of low flow of about 10 seconds, the ambient air warms up the coldstage, leading to the periodic change in temperature. A periodic minimum temperature of 288 K was measured with a flow rate of 3 sccm. This is reasonable considering the evaporator could not be cooled for a long enough time to reach a steady temperature. Application of thermal insulation would reduce the ambient heat load and result in a lower steady-state evaporator temperature. Redesigning the JT restriction to be slightly more restrictive and have a steady flow rate of less than2 sccm world remove the pulsatile behavior of the system. Due to project schedule limitations a follow-up study was not conducted.

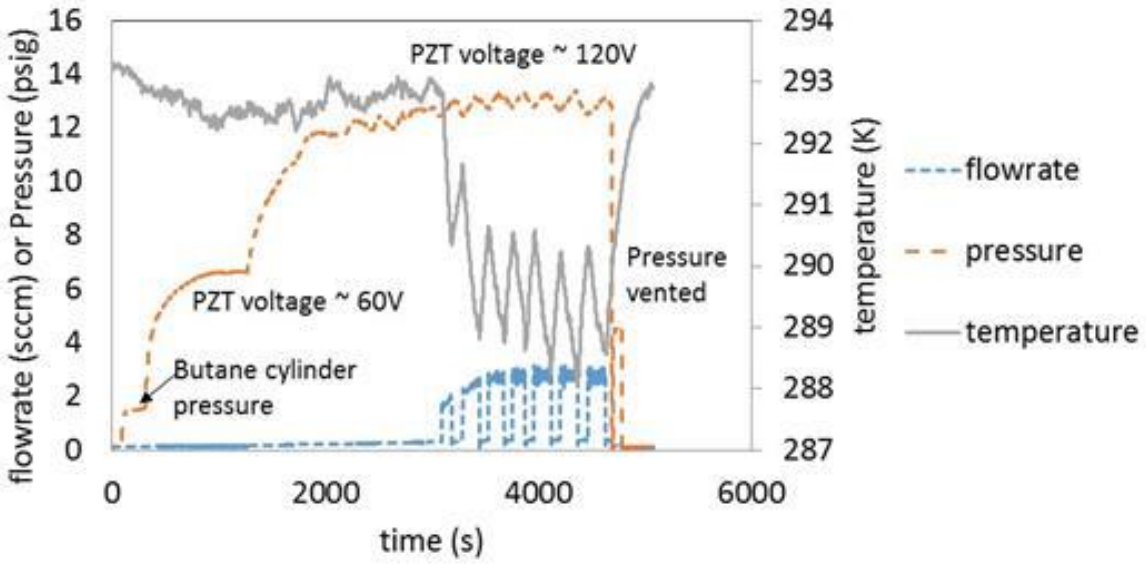

Figure 3.10: Mini-compressor – coldstage integration test results.

3.5 Summary

This study describes a coldstage consisting of a 32 mm long 25 um ID 150 um OD glass capillary restriction and copper mesh based evaporator for use in a JT refrigeration cycle. The coldstage is capable of running with low pressure (0.25 MPa) and low flow rate (3 sccm) when connected directly to a high pressure n-butane cylinder. Evaporator temperatures of 268 K and 283 K are reached when the coldstage is run vacuum and atmosphere respectively. The coldstage was integrated with a mini-compressor and able to cool to 288 K in atmospheric conditions with pulsatile flow. The fabrication process presented significantly reduces design cycle time when compared to the microfabrication approach discussed in chapter 2. This fabrication process is ideal for rapid prototyping of future cascaded coldstage designs. The next two chapters will discuss the use of this fabrication approach to investigate a two stage and three stage cascaded coldstage based on the design presented in chapter 1.4.

Chapter 4: Low Pressure Ratio Two Stage Cascaded Glass Capillary Coldstage

4.1 Motivation and Summary

The goal of this study is to show the feasibility of the macro-scale glass capillary fabrication process presented in the previous chapter when applied to a 2 stage cascaded design. The coldstage presented here is based on the theoretical design presented by Radebaugh et al. [8], [30] and elaborated on in chapter 1.4. The thermal resistance model of a three stage coldstage is shown in Figure 1.20. This chapter demonstrates the development of the first two stages of this model. The coldstage is designed to work at a 0.4:0.1 MPa pressure ratio using isobutane as the first stage refrigerant with flow rate of 51 sccm. The first stage pre-cools the second stage to 261 K with a designed heat lift of 700 mW across the stage 1-2 heat exchanger. The second stage uses propane as the refrigerant to cool to 231 K with a designed heat lift of 500 mW and a flow rate of 48 sccm. The JT restrictions are made using the glass capillary design developed in the previous chapter. The heat exchange between the two stages is a Kapton based tube-in-tube heat exchanger. The second stage evaporator consists of a copper block packed with copper mesh as developed in the previous chapter. The coldstage presented here successfully cools to 228 K with a net refrigeration capacity of 150 mW. The discrepancy in net refrigeration power from design is due to a larger heat leak into the cold end than expected and a significant decrease in the second stage flow rate due to ineffective heat exchange between the two stages. The coldstage has a coefficient of performance (COP) of 1.06 when considering ideal reversible compression of the refrigerants. The coldstage operates at 26.6% of the ideal Carnot COP. The efficiency of the JT cycle will decrease when the coldstage is practically integrated with compressors to form a closed system. The efficiency will increase when measures are taken to reduce natural heat leak and the heat exchanger design is optimized. The coldstage design presented here is improved and further studied to make a three stage cascaded coldstage discussed in chapter 5.

4.2 Design and Fabrication

The two stage coldstage presented here is based on the thermodynamic design presented in chapter 1.4 and Figure 1.20. The coldstage is designed to demonstrate the feasibility of the glass capillary fabrication approach when applied to the first two stages of the three stage design. The coldstage consists of two single component JT refrigeration cycles. The first stage is used to pre-cool and liquefy the high pressure refrigerant of the second stage. The pre-cooling is accomplished via a tube-in-tube heat exchanger. A top view and cross-section of the coldstage is shown in Figure 4.1. The first stage JT restriction is a glass capillary sheathed in Kapton. The capillary is 56 mm long with a 50 µm inner diameter (ID) and 150 µm outer diameter (OD). The high pressure inlet of the capillary restriction is epoxied to a 21 mm long 0.813 mm (0.032 in) ID 1.32 mm (0.052 in) OD copper tube. The copper tube maintains room temperature and allows the high pressure isobutane to liquefy at 0.35 MPa and 295 K. The copper tube is mounted to an aluminum fixture designed to accept all components of the coldstage and provide simple fluidic connection on the backside. The first stage glass capillary JT restriction is bent 180^{o} and the low pressure outlet is epoxied to the inlet to the first stage channel of the tube-in-tube heat exchanger. The tube-in-tube heat exchanger is also mounted to the aluminum fixture. The second stage of the coldstage uses a 74 mm long 50 µm ID 150 µm OD glass capillary sheathed in Kapton as the JT restriction. The high pressure inlet of the capillary restriction is epoxied to the outlet of the second stage channel of the tube-in-tube heat exchanger. The second stage glass capillary JT restriction is bent 180^{o} and the low pressure outlet is epoxied to the inlet of the copper evaporator block. The copper evaporator block consists of a bored out copper block packed with #100 copper mesh. The mesh is diffusion bonded in place. The copper block is caped with a small copper disk and copper tube to accept the second stage capillary fiber. The evaporator block is thermally isolated from the aluminum mounting fixture with a 20 mm length of 2.8 mm OD Kapton tubing.

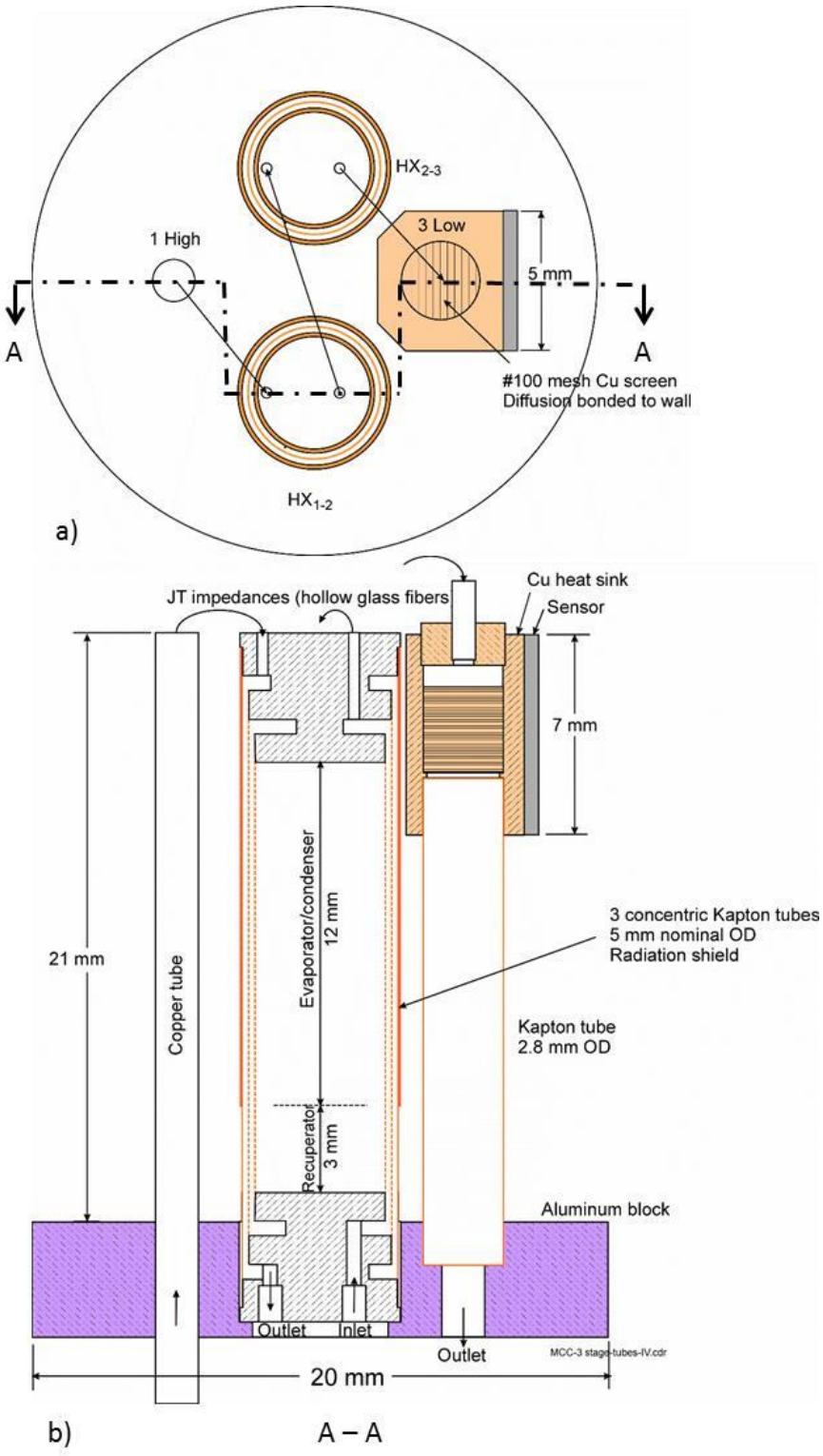

Figure 4.1: Top view and cross-section of a three stage cascaded coldstage. For the two stage coldstage presented in this chapter the stage 2-3 heat exchanger is removed and the stage two JT fiber connects the stage 1-2 heat exchanger to the evaporator block.

The tube-in-tube heat exchanger consists of three concentric Kapton tubes mounted to precision machined aluminum end plugs via epoxy. The end plugs allow simple fluidic access to the two annular channels formed by the three concentric Kapton tubes. The inner tube is 15 mm long with a 5.125 mm ID and 5.2 mm OD. The middle tube is slightly longer to allow coupling to the aluminum end plugs with a 5.45 mm ID and a 5.5 mm OD. The outer tube is slightly longer than the middle tube for coupling to the end plug with a 5.825 ID and a 5.9 OD. The dimensions of the tubes are summarized in Table 4.1. The void inside the inner tube contains air at 0.1 MPa. The gap between the inner tube and the middle tube is 100 µm and is the high pressure channel for the second stage. The gap between the middle tube and outer tube is 125 µm and is the low pressure channel for the first stage. The inner channel must be the high pressure channel to avoid pinching due to the collapse of the middle tube if the outer channel were the high pressure channel. The inner tube must be strengthened to withstand the pressure difference from the high pressure channel to the air-filled void inside the inner tube. A simple vacuum study was run on the inner tube. Vacuum was pulled on the inner tube void with the tube in atmosphere to see what pressure difference caused the tube to collapse. The inner tube collapses with a pressure difference of less than0.01 MPa. To strengthen the inner tube a rigid tube insert was designed and 3D printed out of ABS plastic. The 3D printed tube insert is a tubular design with a tooth pattern on one end intended to minimize any thermal conduction paths. Each insert is 5 mm long to allow for varied heat exchanger lengths. The design is conservative with a wall thickness of 1 mm. Basic mechanical analysis suggests a minimum wall thickness of 0.25 mm is required to withstand crushing under a 0.4:0.1 MPa pressure difference. Figure 4.2 shows all the components used to make one Kapton tube-in-tube heat exchanger. The components shown are longer than the intended 15 mm inner tube length. The fully fabricated heat exchanger uses the correct dimensions as shown in Figure 4.1.

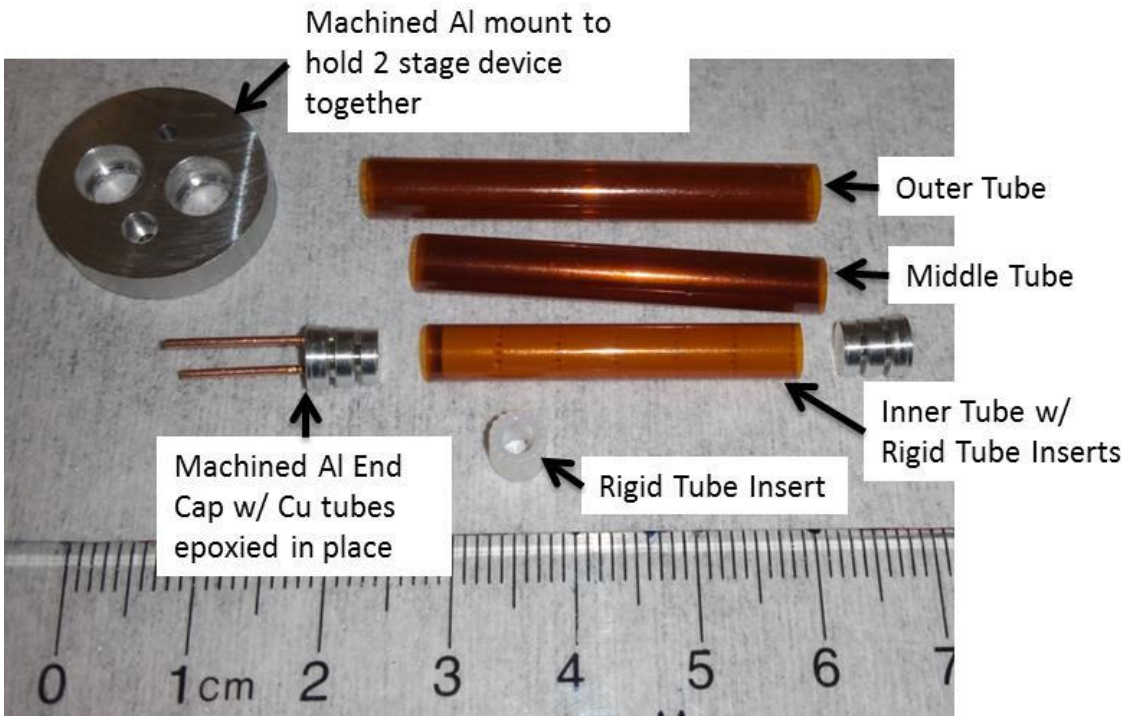

Figure 4.2: All components used for one tube-in-tube heat exchanger.

Table 4.1: Dimensions of the Kapton tubes used for the tube-in-tube heat exchanger.

	Outer Diameter (mm)	Wall Thickness (µm)
Inner Tube	5.2	75
Middle Tube	5.5	50
Outer Tube	5.9	75

The heat exchanger acts as both the isothermal heat exchanger required to precool the second stage and the inter-stage recuperative heat exchanger as shown in the thermal design in Figure 1.20. The required heat exchanger area for the isothermal portion of the heat exchanger is calculated using a basic thermal resistance model [38]

$$\Delta T = \frac{\dot{Q}}{h_{eff}\, A} \tag{4.1}$$

$$h_{eff} = \frac{1}{\frac{1}{h_{kapton}} + \frac{1}{h_{evap}} + \frac{1}{h_{cond}}} \tag{4.2}$$

where ΔT is the temperature difference between the high pressure butane and low pressure isobutane, $\dot{Q}$ is the heat flow across the heat exchanger, A is the total heat exchange area, h_{eff} is the effective heat transfer coefficient that takes into account the thermal resistance of the Kapton tube (h_{kapton}), the two phase evaporation of isobutane in the low pressure channel (h_{evap}), and the two phase condensation of propane in the high pressure channel (h_{cond}). The evaporative heat transfer coefficient for isobutane is estimated by Dr. R. Radebaugh to be 3200 W/m^2-K using the correlation developed by Tu and Hrnjak [42] for two phase evaporative heat transfer of R134a. The same correlation is used to estimate the heat transfer coefficient for two phase condensation of propane to be 4000 W/m^2-K. The calculation is presented in Appendix C. The heat transfer coefficients are assumed to be constant for an average vapor quality of 0.5 through the entire length of the isothermal heat exchanger. It is assumed two phase evaporation and condensation behave similarly meaning the evaporative heat transfer coefficient is the same as the condensation heat transfer coefficient. The heat transfer coefficient for conduction through the Kapton tube is found to be 3600 W/m^2-K by normalizing the thermal conductivity of Kapton to the wall thickness of the middle tube. Considering a temperature difference between the two channels of 2 K and a heat flow of 570 mW an isothermal heat exchange area of 2.5 cm^2 is found corresponding to a length of 12 mm.

In the recuperative portion of the heat exchanger no evaporation or condensation occurs and the heat transfer coefficients are those for the refrigerants flowing through a thin annular gap in vapor phase at 0.1 MPa for isobutane and 0.4 MPa for propane. The recuperative portion of the heat exchanger is assumed to have purely single phase vapor flow in both channels where for an annular channel [38]

$$h = \frac{Nu\ k}{t_g} \tag{4.3}$$

$$t_g = D_o - D_i \tag{4.4}$$

where h is the heat transfer coefficient, Nu is the Nusselt number, k is the thermal conductivity of the vapor refrigerant, t_g is the annular gap, and D_o and D_i are the outer and inner diameters of the annular gap. For $D_i/D_o \cong 1, Nu = 4.86$ [38]. The thermal conductivity for isobutane and propane are 14.343 mW/m-K and 15.65 mW/m-K respectively. The heat transfer coefficients are calculated where $h_{propane}$ is 1100 W/m2-K and $h_{isobutane}$ is 880 W/m^2-K. Using equation 4.1 and 4.2 where h_{evap} is replaced with $h_{isobutane}$ and h_{cond} is replaced with $h_{propane}$ and considering a temperature difference between the two channels of 5 K and a heat flow of 133 mW a recuperative heat exchange area of 0.6 cm^2 is found corresponding to a length of 3 mm. The total heat exchanger length is 15 mm. Heat exchange at the aluminum end plug is not considered.

From chapter 1.2 the gross refrigeration power of a JT refrigeration cycle is [8]

$$\dot{Q}_r = \dot{m}(\Delta h|_T)_{min} \tag{1.1}$$

where $\dot{Q}_r$ is the ideal gross refrigeration power, $\dot{m}$ is the molar flow rate of the refrigerant, and $(\Delta h|_T)_{min}$ is the minimum enthalpy difference between the high and low pressure states of the refrigerant over the temperature range of cooling. This design is assumed to operate without recuperative heat exchange for design purposes even though there is some inter-stage recuperative heat exchange. Assume a recuperative heat exchanger ineffectiveness of 1 (meaning no recuperative heat exchange) the first stage using isobutane is found to operate at 81% of ideal and the second stage using propane is found to operate at 89% of ideal [8], [30]. Isobutane has a minimum enthalpy difference of 19.54 kJ/mol over the temperature range of operation and propane has a minimum enthalpy difference of 17.42 kJ/mol over the temperature range of operation. A flow rate of 51 sccm is found for the first stage using isobutane considering 700 mW of required heat lift at the heat exchanger. A flow rate of 48 sccm is found for the second stage using propane considering 500 mW of designed

heat lift at the evaporator. The heat leak into the evaporator and heat exchanger are estimated to be less than 10 mW when proper radiation shielding is used and the device is run in vacuum.

The length and inner diameter of the capillaries are determined by consideration of the laminar two phase flow undergoing adiabatic expansion through a circular tube as expressed by equation 3.1 [8]

$$L = \frac{\pi d^4}{128\dot{n}} \frac{1}{\int \frac{D_{m,avg}}{\mu_{avg}} dP} \tag{3.1}$$

where L is the length of the capillary, d is the inner diameter of the capillary, $\dot{n}$ is the mass flow rate of the refrigerant, P is the pressure of the fluid, and from chapter 2.4 the Dukler averages of density and viscosity for two phase flow are [39]

$$D_{m,avg} = \frac{1}{\frac{x}{D_{m,v}} + \frac{1-x}{D_{m,l}}} \tag{2.7}$$

$$\mu_{avg} = D_{m,avg}\left(\frac{x\mu_v}{D_{m,v}} + \frac{(1-x)\mu_l}{D_{m,l}}\right) \tag{2.8}$$

where x is the quality of the two phase fluid at a given pressure, $D_{m,v}$ and $D_{m,l}$ are the molar densities of the vapor and liquid portions of the fluid respectively, and μ_v and μ_l are the viscosities of the vapor and liquid portions of the fluid respectively. The integral is evaluated via tabular integration using fluid properties from the NIST REFPROP v. 9.1 program [40]. The properties used are tabulated in Appendix B. A capillary length of 56 mm and ID of 50 µm is found for a desired flow rate of 51 sccm using isobutane as the refrigerant operating at a 0.4:0.1 MPa pressure ratio. A capillary length of 75 mm and ID of 50 µm is found for a desired flow rate of 48 sccm using propane as the refrigerant operating at a 0.4:0.1 MPa pressure ratio. Because of the large channel geometries outside the JT restrictions when compared to the MEMS based coldstage presented in chapter 2 the pressure drop outside the JT restrictions is

assumed to be negligible. Figure 4.3 shows the fully fabricated coldstage with the locations of the high and low pressure sides of the JT restrictions marked.

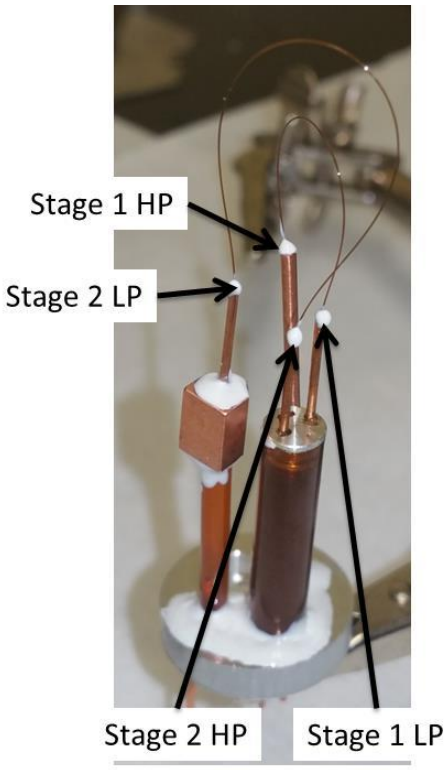

Figure 4.3: Fully fabricated two stage cascaded coldstage with locations of high and low pressure sides of both JT restrictions marked.

4.3 Test Setup

Figure 4.4 shows the schematic of the test setup used to test and characterize the coldstage. The coldstage is run in an open loop configuration where high pressure refrigerant is supplied by high pressure cylinders and the outlet of both stages is vented to atmosphere. Ice packs are used to precool the incoming high pressure isobutane to 290 K where it liquefies at 0.31 MPa. The precooling is necessary because the isobutane cylinder used was not able to supply liquid isobutane at room temperature and 0.35 MPa. Two 7 µm pore size particulate filters are placed upstream of both stages of the coldstage to ensure no particulate contamination or clogging. Any water vapor is removed from the second stage propane with a molecular sieve packed with Drierite desiccant to avoid ice buildup in the

lines when below freezing temperatures. Temperature sensors are placed on the heat exchanger and the second stage evaporator block. A resistive heater is placed on the second stage evaporator block for calculating the natural heat leak into the evaporator and the net refrigeration power available during steady state operation. The voltage across and the current through the resistive heater are measured to calculate the heater power dissipation to avoid any temperature dependence of resistance. The resistive heater consists of a 100 Ω 1 W resistor epoxied to a 0.5 mm thick copper sheet with thermally conductive silver epoxy. The copper sheet allows for a flat mounting surface for ease of mounting to the evaporator block. Pressure sensors are connected to both high pressure refrigerant lines upstream of the coldstage. Because only one mass flow meter is available only the second stage flow rate is measured. The coldstage is mounted to a vacuum flange liquid feedthrough to allow the coldstage to be operated in a vacuum environment. Figure 4.5 shows the coldstage mounted to the liquid feedthrough with the locations of the temperature sensors and resistive heater. The temperature sensors and resistive heater are mounted with double sided graphite tape to ensure good thermal contact. Figure 4.6 shows the coldstage fully mounted into the vacuum chamber for testing.

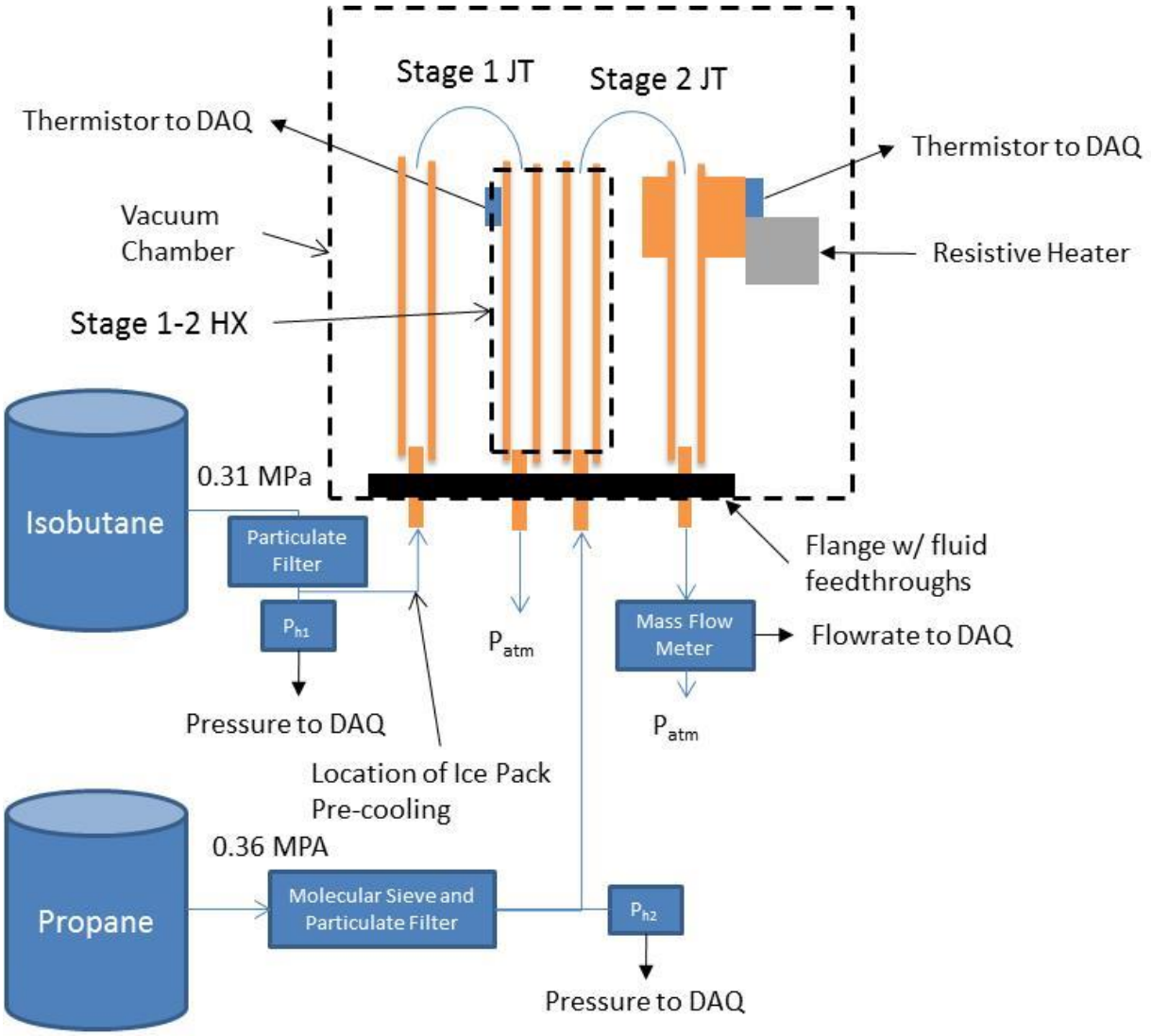

Figure 4.4: Test setup schematic for the two stage cascaded coldstage when run in an open loop configuration. Refrigerant is supplied directly from high pressure refrigerant cylinders and vented to atmosphere after exiting the coldstage.

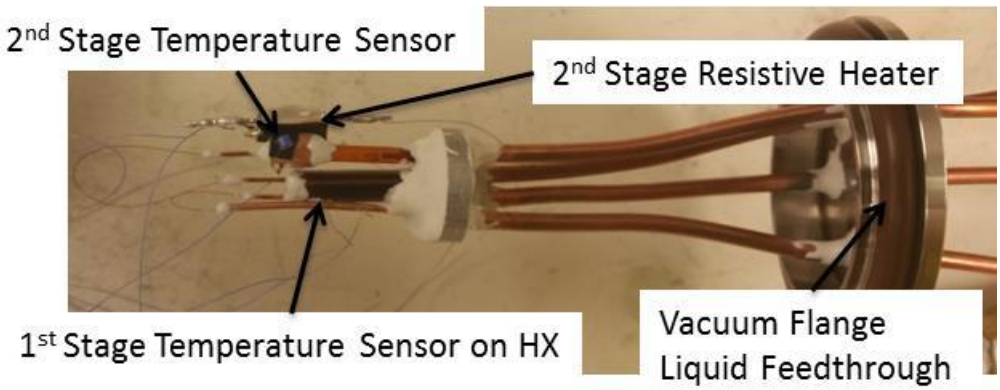

Figure 4.5: Two stage cascaded coldstage mounted to vacuum liquid feedthrough with locations of temperature sensors and resistive heater indicated.

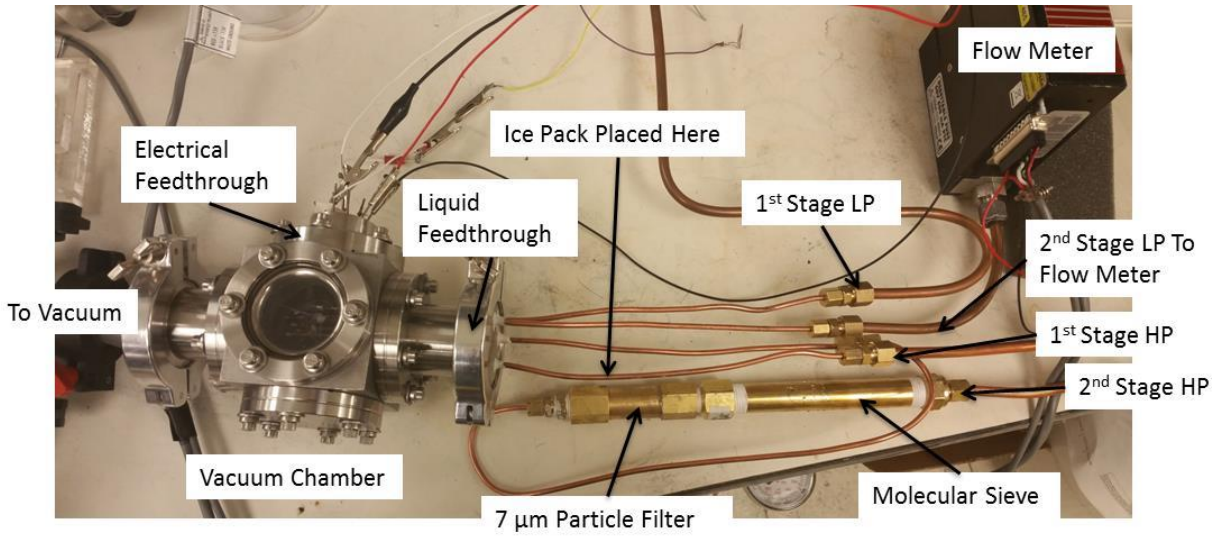

Figure 4.6: Two stage cascaded coldstage fully mounted into the vacuum chamber with external fluidic connections made.

4.4 Test Results

The test begins by pulling vacuum on the refrigerant lines to remove as much air and water vapor as possible. However due to the large internal volume of the test setup lines and the numerous fixtures required for all fluidic connections the refrigerant lines do not hold good vacuum. Because the lines cannot hold good vacuum both stages of the coldstage are run through a bleed through process for 30 to 60 minutes. In the bleed through process the refrigerants are allowed to flow through the coldstage form high pressure side to low pressure side to vent in vapor phase to displace any air and water vapor remaining in the lines. During the bleed through process the vacuum chamber is pumped

down to 5 x 10^{-5} Torr to ensure good insulation of the coldstage. Once the bleed through process is finished and the chamber is pumped to vacuum the cooling test begins. Both refrigerants are brought up to pressure and the coldstage is allowed to reach steady state. Figure 4.7 shows the cool down behavior and steady state operation of the two stage coldstage. In this test both refrigerants are brought to pressure at ~4900 seconds. The heat exchanger temperature (noted here as T_Stage 1) quickly reaches its expected steady state operating temperature of 261 K. Once the heat exchanger reaches 261 K and begins to precool and liquefy the propane in the second stage there is an increase in the second stage flow rate and cooling is seen. The second stage eventually reaches a steady state operating temperature of 228 K as expected. When the coldstage reaches the ultimate temperature of 228 K (the saturation temperature of propane at 0.082 MPa) small droplets of liquid propane condense in the evaporator's small mesh crevices. This leads to a brief drop in mass outflow at ~5450 s. Once all available crevices are filled the flow rate increases back to a steady state average of ~20 sccm. The slower rate of cooling of the second stage evaporator is caused by two factors first the evaporator has a larger thermal mass than the heat exchanger because of the large copper volume and the large resistive heater mounted to the evaporator, and second the second stage has a significantly lower flow rate than the designed value of 48 sccm reducing the available refrigeration power. The latter will be discussed in the chapter 4.6. A separate test was run with the mass flow meter connected to the first stage to confirm it is operating as designed with a steady state flow rate average of ~48 sccm much closer to the designed target of 51 sccm.

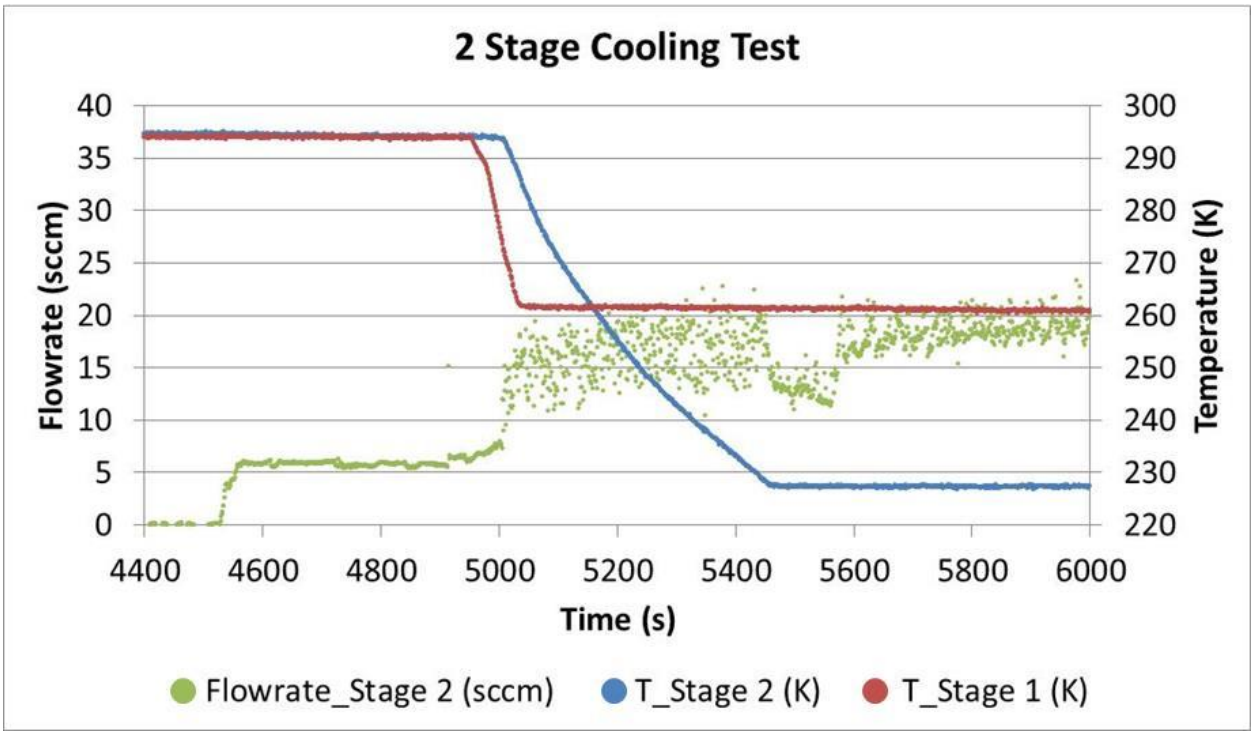

Figure 4.7: Cooldown behavior of the two stage cascaded coldstage with the out flow of the second stage (Flow rate_Stage 2), the temperatures of the stage 2 evaporator (T_Stage 2) and the stage 1-2 heat exchanger (T_Stage 1) measured.

Using the same test setup the natural heat leak into the second stage evaporator was estimated. To make this estimation several warm up curves were measured. For each warm up curve the coldstage is cooled down to its ultimate temperature of 228 K. Once the evaporator reaches steady state the second stage propane flow is stopped by venting the high pressure propane line. Once the flow meter reads zero flow the resistive heater is set to a specific power input and the temperature rise over time is measured. Figure 4.8 shows the temperature rise of the second stage evaporator for heater powers from 0 mW to 292 mW with no refrigeration applied.

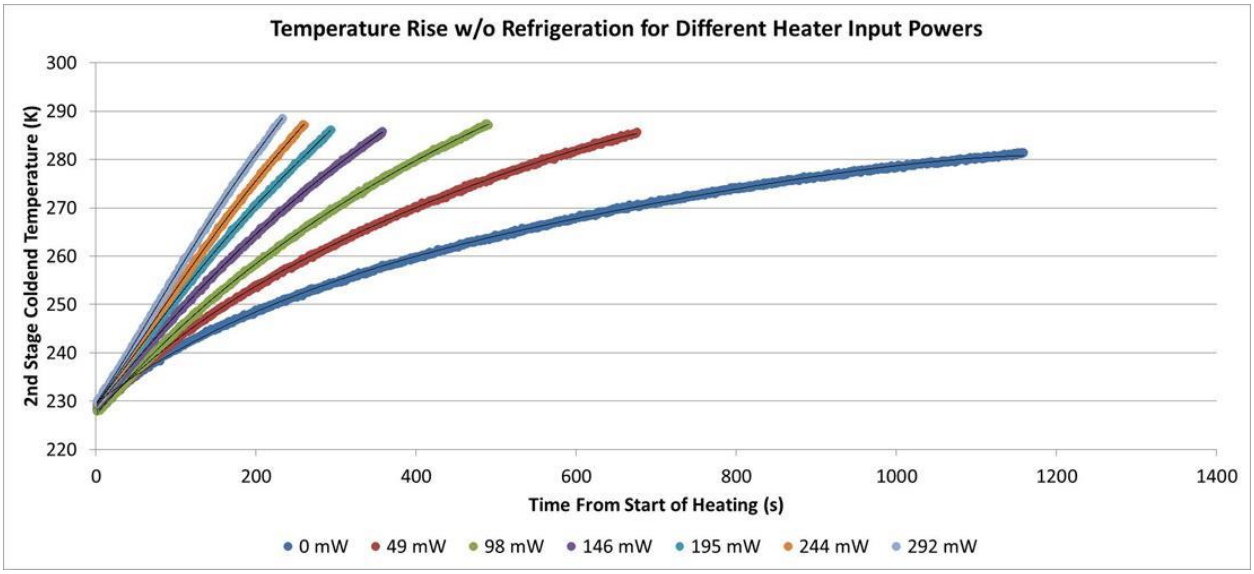

Figure 4.8: Temperature rise of the second stage evaporator over time without active refrigeration for various heater input powers.

The definition of specific heat is [43]

$$Q = C_{pT}\Delta T \tag{4.3}$$

where Q is the energy required to increase the temperature of a material with specific heat at constant pressure and temperature C_{pT} an amount of ΔT. Taking the time derivative of equation 4.3 yields

$$\frac{dQ}{dt} = C_{pT}\frac{dT}{dt} \tag{4.4}$$

where $\frac{dQ}{dt}$ an applied heat load and $\frac{dT}{dt}$ is the temperature rise rate. Equasion 4.4 reveals a linear relationship between an applied heat load and the temperature rise rate for a constant temperature and pressure of the evaporator.

A forth order polynomial is fit to each temperature rise curve in Figure 4.8. This polynomial fit is used to estimate the temperature rise rate at a specific temperature for each heater input power. Figure 4.9 shows the heater input power as a function of temperature rise rate for specific evaporator temperatures. A linear fit is applied to each curve. Extrapolating each linear fit to a temperature rise rate of zero gives a negative heater input power. The negative heater input power is the refrigeration power

that must be supplied to maintain zero temperature change for a specific evaporator temperature. This means all refrigeration power is being used to overcome the natural heat leak into the evaporator. This negative input power is the estimate for natural heat leak into the evaporator at specific evaporator temperatures. The natural heat leak into the evaporator for specific evaporator temperatures is plotted in Figure 4.10 with estimates for heat leak due to radiation assuming an emissivity of the dull copper evaporator and dull silver epoxied resistive heater of 1 and 0.7. In order to minimize the radiative heat leak proper radiation shielding should be applied around the evaporator or the evaporator should be coated in a low emissivity coating like chromium.

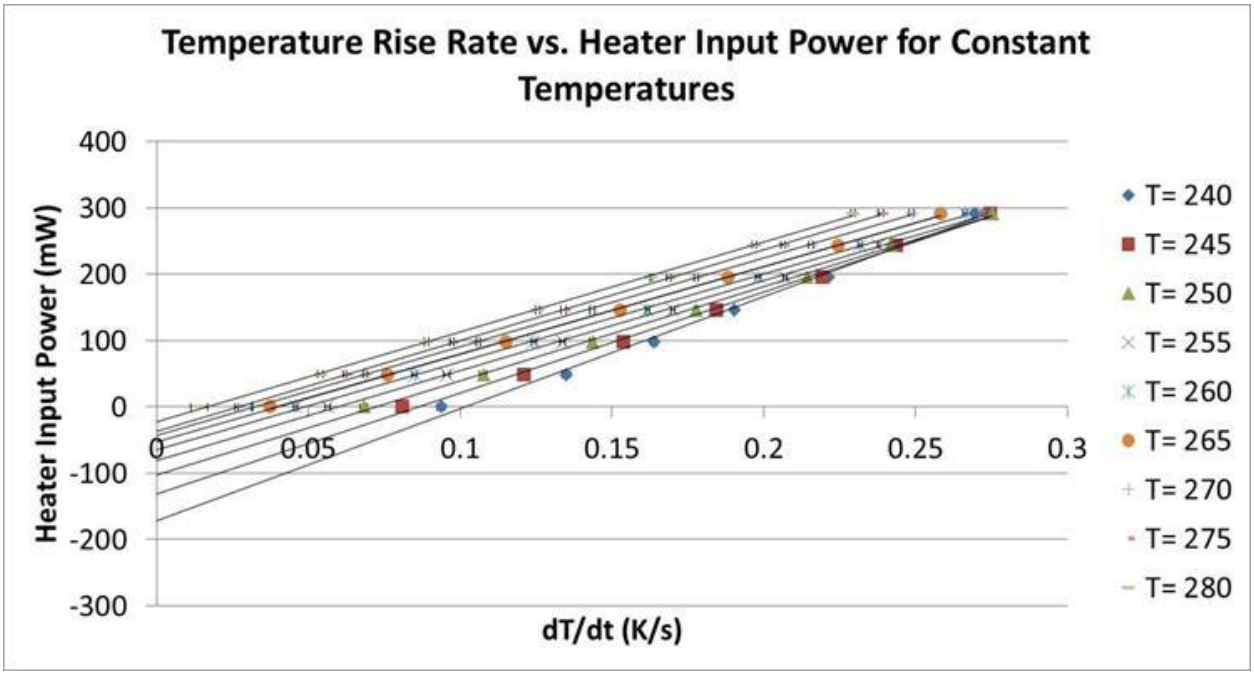

Figure 4.9: Temperature rise rate for specific evaporator temperatures and heater input powers. Linear trend lines are fit to each curve. The extrapolated y intercept is the natural heat leak into the system at specific evaporator temperatures.

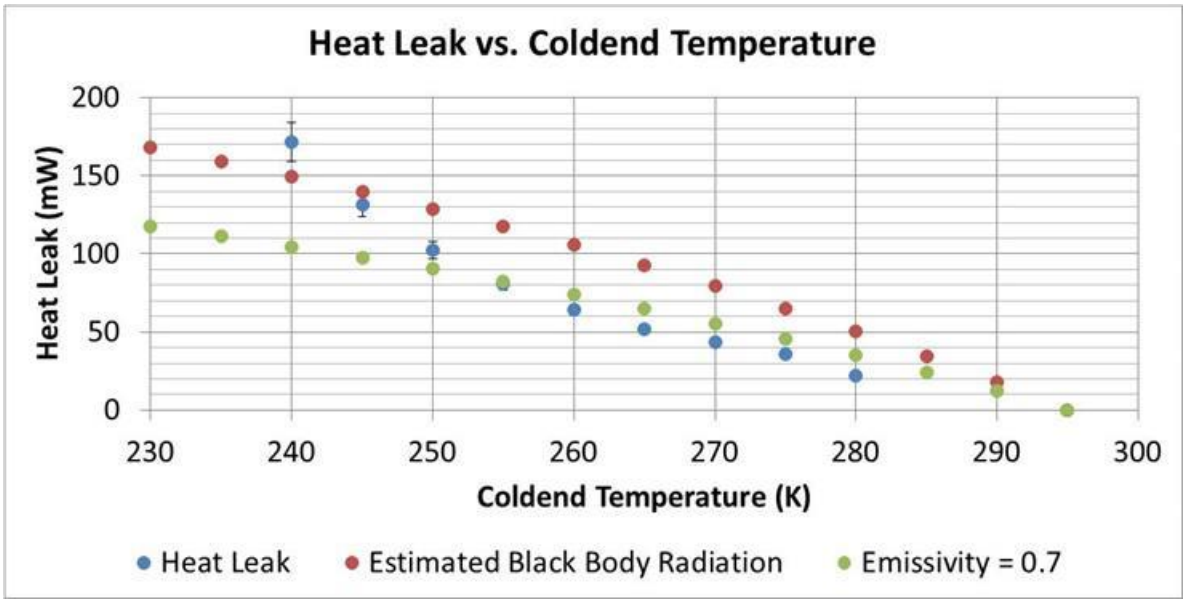

Figure 4.10: Natural heat leak into the evaporator for specific evaporator temperatures and estimated radiation heat leak considering an emissivity of 1 and 0.7.

A power dissipation test is run to determine the net refrigeration capacity of the coldstage at different evaporator temperatures. For this test the coldstage is cooled to its ultimate temperature of 228 K. Once the coldstage reaches steady state operation the resistive heater is turned on. Unlike the heat leak test the second stage of the coldstage remains operational providing refrigeration power to the evaporator. The resistive heater applies a heat load and the evaporator temperature is allowed to reach steady state before increasing the heater input power. Figure 4.11 shows the evaporator temperature as a function of heater input power. This test shows the net refrigeration power of the coldstage is 150 mW at the ultimate temperature of 228 K. This is lower than the designed net refrigeration power of 500 mW. The designed refrigeration power assumes minimal radiation heat leak of less than 10 mW. From the heat leak tests it is shown our radiation heat leak is closer to 150 mW. The designed flow rate for the second stage to provide 510 mW of gross refrigeration is 48 sccm. The actual flow rate is much lower at 20 sccm. A flow rate of 20 sccm corresponds to a gross refrigeration capacity of 212 mW.

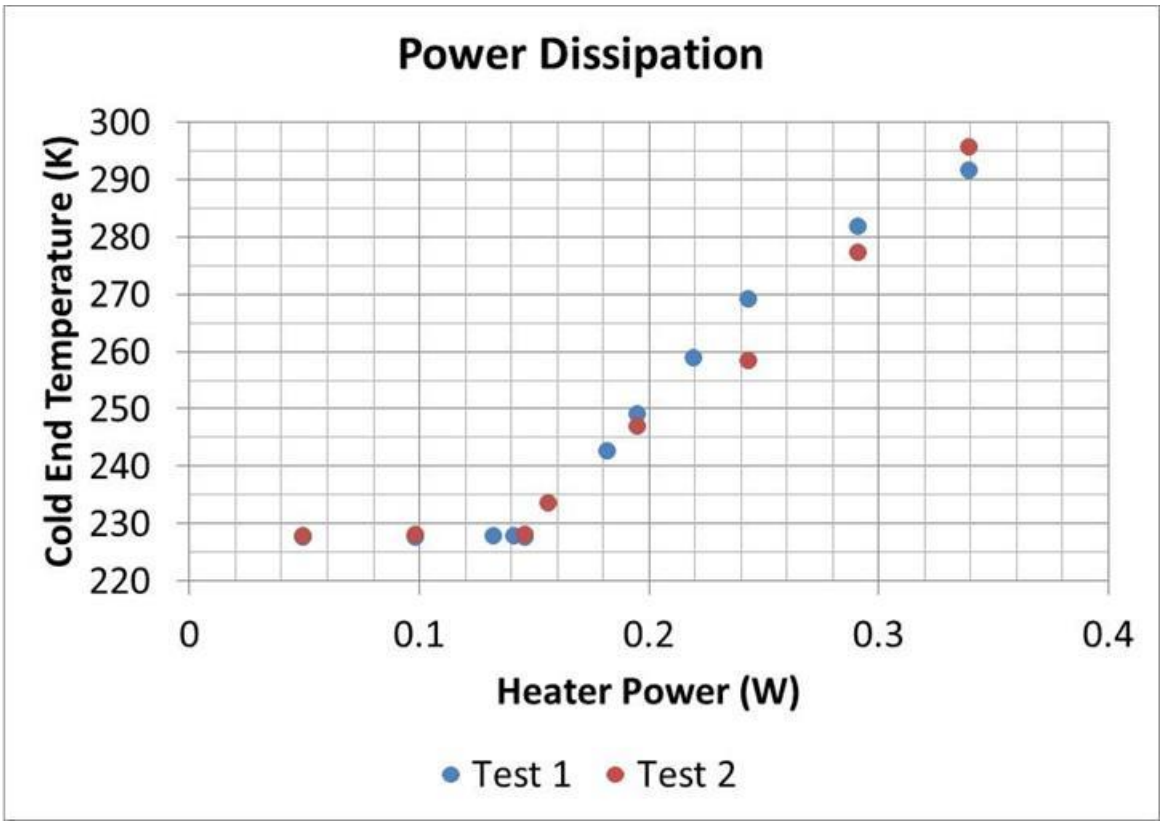

Figure 4.11: Evaporator temperature for specific heater input powers during normal coldstage operation.

4.5 Characterization of Gross Refrigeration Power, Coefficient of Performance (COP), and Efficiency of the Coldstage

From chapter 2.4 the net refrigeration power available at the cold end of the coldstage is

$$\dot{Q}_{net} = \dot{Q}_r - \dot{Q}_{cond} - \dot{Q}_{conv} - \dot{Q}_{rad} - \dot{Q}_{\Delta P} \tag{2.1}$$

where $\dot{Q}_{net}$ is the net refrigeration power, $\dot{Q}_r$ is the gross refrigeration power available from the JT expansion of the refrigerant, $\dot{Q}_{\Delta P}$ is any loss from pressure drop through the micro-channels outside the JT restriction, and $\dot{Q}_{cond}$, $\dot{Q}_{conv}$, and $\dot{Q}_{rad}$ are the heat leak into the cold end of the coldstage by conduction, convection, and radiation respectively. For the two stage coldstage there is no significant pressure loss, all of the conduction, convection, and radiation terms are combined into one natural heat leak term, and a load term is added to include the resistive heater giving

$$\dot{Q}_{net} = \dot{Q}_r - \dot{Q}_{leak} - \dot{Q}_{load} \tag{4.5}$$

where $\dot{Q}_{leak}$ is the natural heat leak and $\dot{Q}_{load}$ is the resistive heater input power.

The coldstage is assumed to be in thermodynamic equilibrium when the temperature of the evaporator is above the ultimate temperature of 228 K. In this scenario there is no available net refrigeration power meaning the gross refrigeration power is equal to the sum of the heat leak and the applied heater load. Using the power dissipation data (Figure 4.11) for all points T > 228 K and interpolating the heat leak at each of these temperatures from the heat leak data (Figure 4.10) a gross refrigeration power of 312 ± 14 mW is estimated. It is therefore reasonable to have an available gross refrigeration of 312 mW considering for a flow rate of 20 sccm of propane the gross refrigeration power is estimated to be 212 mW from equation 1.1.

The coefficient of performance (COP) can be calculated for the coldstage assuming ideal compression of the refrigerants. The COP for any refrigeration cycle is [43]

$$COP = \frac{\dot{Q}_{ref}}{\dot{Q}_{in}} \tag{4.6}$$

where $\dot{Q}_{ref}$ is the heat lifted by the refrigerator at the low temperature and $\dot{Q}_{in}$ is the power input into the system to compress the refrigerant.

The ideal reversible compressor input power is [43]

$$\dot{Q}_{comp} = \dot{m}\Delta G \tag{4.7}$$

Where $\dot{Q}_{comp}$ is the ideal compressor input power, $\dot{m}$ is the mas flow rate, and ΔG is the Gibbs energy of formation for an ideal gas [43]

$$\Delta G = \Delta h - T\Delta s \tag{4.8}$$

where Δh is the change in enthalpy from the low pressure state to the high pressure state, Δs is the entropy change from the low pressure state to the high pressure state, and T is the temperature at which the compression occurs.

The two stage coldstage can provide 150 mW of net refrigeration at 228 K with the first stage operating at a 0.35:0.082 MPa pressure ratio and a flow rate of 48 sccm and the second stage operating at a 0.35:0.082 MPa pressure ratio and a flow rate of 20 sccm. Using fluid properties from the NIST REFPROP v. 9.1 program [40] the ideal compressor input power for the isobutane stage is 89.2 mW and the ideal compressor input power for the propane stage is 51.9 mW. This gives a total ideal compressor input power of 141.1 mW. Equation 4.6 gives a COP of 1.06.

The ideal reversible Carnot COP for any refrigeration cycle is [43]

$$COP_{Carnot} = \frac{1}{\frac{T_h}{T_l} - 1} \tag{4.9}$$

where T_h is the hot temperature of the refrigeration cycle and T_l is the cold temperature of the refrigeration cycle. For the two stage coldstage the hot temperature is 295 K and the cold temperature is 228 K. This gives an ideal Carnot COP of 3.4. With ideal compression of the refrigerants the two stage coldstage has 26.6% efficiency when compared to an ideal Carnot refrigeration cycle. The efficient will decrease when integrated with real compressors. The efficiency will increase with improved radiation shielding to limit heat leak and with optimization of the heat exchanger to ensure designed operation.

4.6 Investigation of Second Stage Low Flow Rate

Noted in chapter 4.4 the flow rate of the second stage is 20 sccm. This is significantly lower than the targeted design value of 48 sccm. Two possible explanations were investigated. First the JT restriction may be more restrictive in practical implementation than in design. Second the stage 1-2 heat exchanger is not capable of precooling all of the propane to a liquid state. If a non-zero amount of vapor

propane is entering the second stage JT restriction the flow rate will drop significantly. Vapor propane is measured to flow through the JT restriction at 6 sccm when not precooled by the first stage. Fully developed 2 phase expansion through the JT restriction is estimated to be 48 sccm. In this case it is assumed 100% liquid propane is entering the JT restriction. This leads to the supposition when the propane entering the JT restriction is less than 100% liquid the flow through the JT restriction will decrease.

To investigate the first possible issue of the JT restriction being more restrictive in implementation than in design, the second stage is run with isobutane. Isobutane liquefies at 0.3 MPa and 290 K requiring no precooling from the first stage and only slight precooling from icepacks placed on the refrigerant lines outside the vacuum chamber. The expected flow rate of isobutane through the second stage JT restriction is 40 sccm. Figure 4.12 shows the schematic of the two stage coldstage with isobutane supplied to the second stage. For this test the first stage of the coldstage is not used. The test results are shown in Figure 4.13. When Isobutane is expanded across the second stage JT restriction the flow rate is 36 sccm and the evaporator temperature is 258 K. The second stage is operating at 90% design with isobutane but only at 42% design with propane precooled to 261 K by the first stage as shown in Figure 4.7. This indicates the second stage JT restriction is as restrictive as designed. The discrepancy in the propane flow rate is most likely due to inefficient precooling in the heat exchanger.

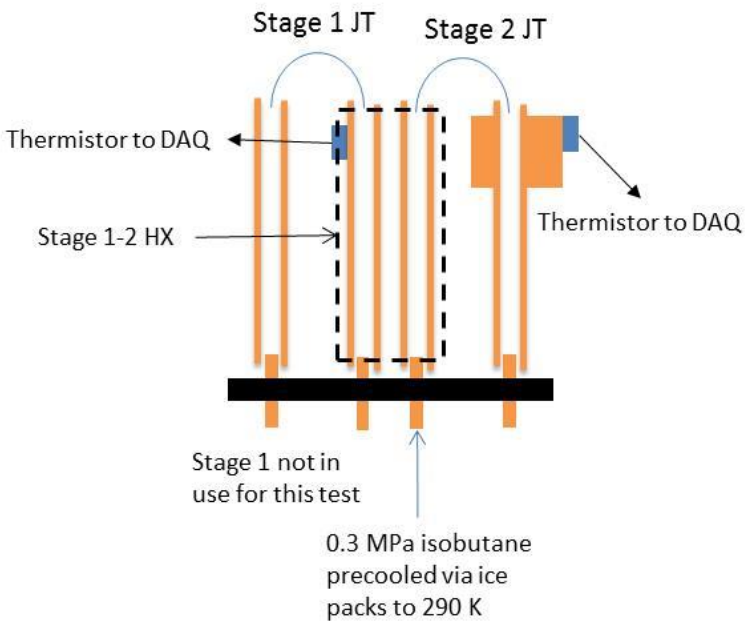

Figure 4.12: Schematic of test configuration for the second stage isobutane test.

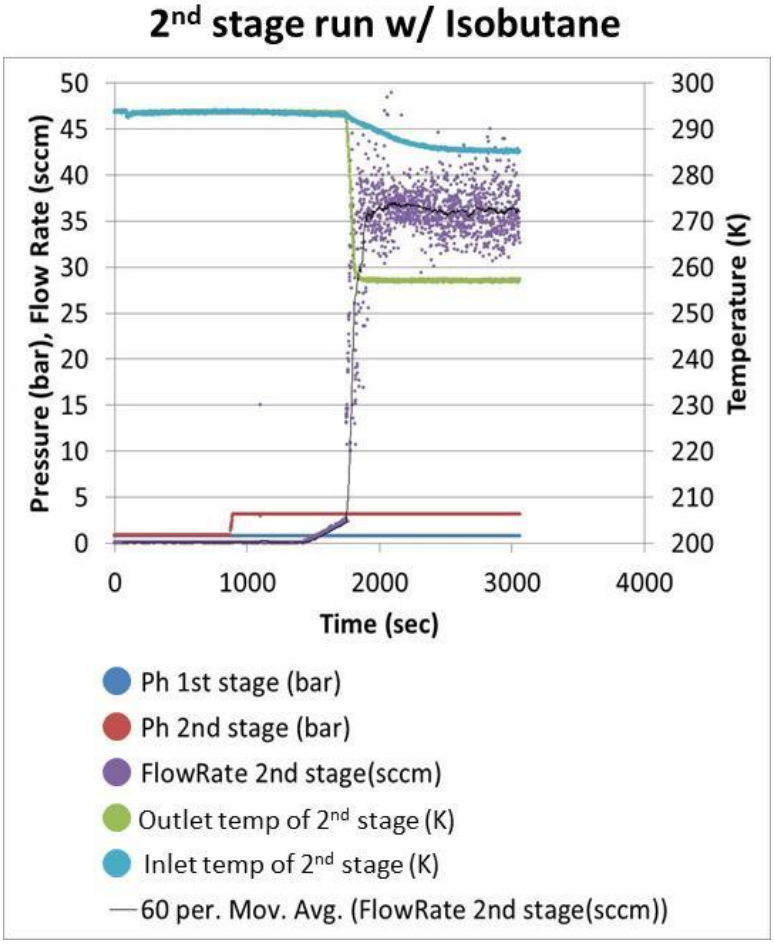

Figure 4.13: Second stage isobutane test indicates second stage JT restriction is as restrictive as designed. A flow rate of 36 sccm is measured and is 90% of the designed 40 sccm. The evaporator reaches 258 K as expected.

The heat exchanger was designed to transfer all 700 mW of available refrigeration power from the first stage to the second stage. If this is the case the temperature measured at the heat exchanger first stage channel inlet should be 261 K and the outlet should be close to room temperature (295 K). If the heat exchanger outlet temperature measures lower than 295 K then all the available refrigeration power is not being transferred to the propane in the second stage. This will cause less than 100% liquid propane to enter the second stage JT restriction significantly reducing flow rate. To investigate the heat exchanger, the second stage temperature sensor was moved to the first stage outlet line from the heat exchanger. Figure 4.14 shows the schematic for the heat exchanger investigation test. In this test the coldstage is run as normal with isobutane in the first stage and propane in the second stage. The test

results are shown in Figure 4.15. It is shown the temperature of the heat exchanger outlet is 289 K at the end of the test. This is the steady temperature without the coldstage running and ice packs precooling the first stage lines. Due to the nature of the test setup all the inlet and outlet lines are cooled by the ice packs. During coldstage operation the heat exchanger outlet temperature is seen to decrease to 283 K. The 6 K temperature drop indicates there is some liquid isobutane exiting the first stage channel of the heat exchanger. It is believed the heat exchanger cannot utilize all the refrigeration power form the first stage precool and liquefy the second stage propane.

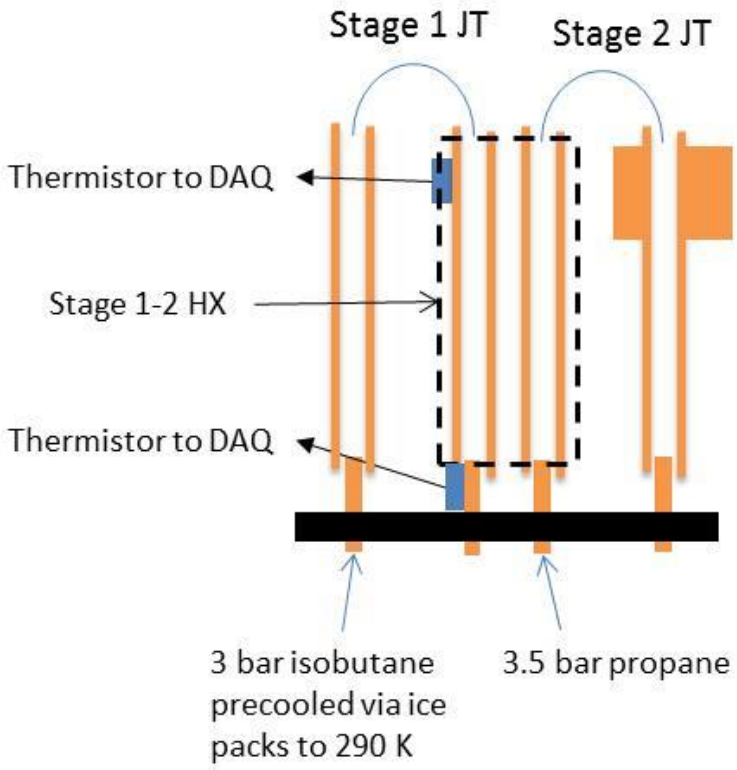

Figure 4.14: Schematic indicating the location of the temperature sensors used to investigate the heat exchanger performance.

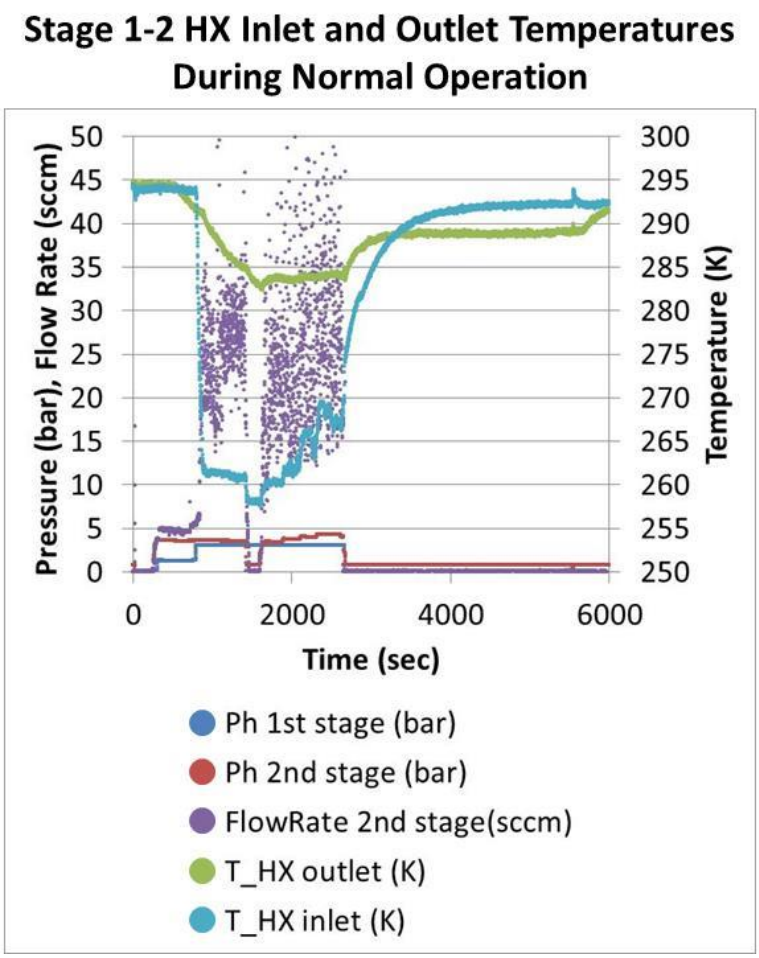

Figure 4.15: Inlet and outlet temperatures of the stage 1-2 heat exchanger during normal coldstage operation. The significant decrease in heat exchanger outlet temperature indicates not all available refrigeration power is utilized to precool the second stage propane.

Chapter 5 investigates the design, fabrication, and characterization of a three stage coldstage. As part of this study the stage 1-2 heat exchanger length was increased for 15 mm to 30 mm. With more heat exchange area the second stage flow rate is shown to increase from 20 sccm with the 15 mm heat exchanger to 43 sccm with the 30 mm heat exchanger. The second stage now operates at 90% of design with the longer heat exchanger. This indicates the estimation of the total heat transfer coefficient for the original heat exchanger design was too high. A copper mesh based heat exchanger design presented in the future works portion of chapter 6 will help alleviate this issue by providing significantly more surface area for evaporation and condensation.

4.7 Summary of Design Criteria, Critical Dimensions, and Coldstage Performance

This section provides a summary of the key design and performance criteria. Table 4.2 provides the design criteria and physical dimensions used to make the three stage coldstage. Table 4.3 provides a summary of the coldstage performance.

Table 4.2: Summary of Two Stage Coldstage Design Criteria and Critical Dimensions.

JT Restrictions			
	Stage 1	**Stage 2**	
Flow Rate (sccm)	51	48	
Inner Diameter (μm)	50	50	
Length (mm)	56	74	
Refrigerant	Isobutane	Propane	
Pressure Ratio (Mpa)	0.35:0.1	0.4:0.1	
Heat Exchanger			
	Stage 1-2		
Temperature (K)	261		
Total Heat Transfer (mW)	700		
Length (mm)	15*		
Heat Exchanger Tubes			
	Inner	**Middle**	**Outer**
Outer Diameter (mm)	5.2	5.5	5.9
Wall Thickness (μm)	75	50	75
Evaporator Block			
Width (mm) (square)	5		
Length (mm)	7		
Bore Diameter (mm)	3		
Mesh Size	#100		
Temperature (K)	231		
Net Refrigeration Power (mW)	500		
Kapton Tube for Thermal Standoff of Evaporator			
Length (mm)	20		
Outer Diameter (mm)	2.8		
Wall Thickness (μm)	100		

* Length needs to be increased to reach designed performance.

Table 4.3: Summary of Two Stage Coldstage Steady State Performance.

	stage 1	Stage 2	Coldstage
Pressure Ratio (Mpa	0.3:0.1*	0.4:0.1	NA
Flow Rate (sccm)	48	43	NA
Temperature (K)	261	228	193
Net Refrigeration Power (mW)	NA	150	150
Gross Refrigeration Power(mW)	NA	NA	312
COP	NA	NA	1.06
Efficiency (% Carnot)	NA	NA	26.6%

NA = not applicable or not measured. * Icepack precooling used to liquefy isobutane at 290 K.

4.8 Summary

This chapter presents the successful design, fabrication, and characterization of a two stage coldstage for low pressure ratio (0.4:0.1 MPa) refrigerants. The coldstage consists of two separate single component refrigerant JT refrigeration cycles where one is used to precool the other. The JT restrictions are fabricated out of 50 µm ID 150 µm OD glass capillaries sheathed in Kapton. The inter-stage heat exchanger is a Kapton tube-in-tube design. The ultimate temperature of the coldstage is 228 K. At 228 K the coldstage can lift 150 mW of net refrigeration. There is a significant discrepancy between the measured net refrigeration capacity and the designed target of 500 mW. This is due to larger than estimated radiation heat leak from the lack of radiation shielding and a significant decrease in the second stage flow rate due to ineffective heat exchange between the two stages. Chapter 5 shows increasing the total heat exchange area solves the low flow rate problem. The COP of the coldstage when considering ideal compression of the refrigerants is 1.06. This is 26.6% of the fully reversible Carnot COP of 3.4. Chapter 5 further develops this coldstage design into a three stage cascaded coldstage to reach cryogenic temperatures of 193 K.

Chapter 5: Low Pressure Ratio Three Stage Cascaded Glass Capillary Coldstage

5.1 Motivation and Summary

The goal of this study is to apply the glass capillary coldstage design presented in chapters 3 and 4 to a three stage cascaded coldstage. The coldstage is designed to cool to 195 K with a heat lift of 350 mW at the evaporator of the third stage. The coldstage presented here is based on the theoretical design presented by Radebaugh et al. [8], [30] and elaborated on in chapter 1.4. The thermal resistance model of a three stage coldstage is shown in Figure 1.20. The coldstage is designed to work with isobutane at a 0.4:0.1 MPa pressure ratio as the first stage refrigerant to precool the second stage to 261 K with a heat lift of 700 mW at the stage 1-2 heat exchanger and flow rate of 51 sccm. The second stage uses propane at a 0.4:0.1 MPa pressure ratio to precool the third stage to 231 K with a heat lift of 660 mW at the stage 2-3 heat exchanger and a flow rate of 48 sccm. The third stage uses R116 at a 0.5:0.1 MPa pressure ratio to cool the third stage evaporator to 195 K with a heat lift of 350 mW and a flow rate of 45 sccm. The length of the stage 1-2 heat exchanger is increased from design in order to provide more heat exchange area. This change is expected to increase the flow rate of the second stage from 15 sccm as shown in chapter 4 to 48 sccm the designed value for 660 mW of heat lift at the stage 2-3 heat exchanger. Due to lack of materials and project schedule the stage 2-3 heat exchanger remains the originally designed length. This leads to a lower than designed flow rate for the third stage and a lower gross refrigeration power from design. The coldstage presented here successfully cools to 193 K with a net refrigeration power of 15 mW. The net refrigeration power is lower than the designed value of 350 mW because of significant radiation heat leak due to lack of radiation shielding and ineffective heat transfer in the stage 2-3 heat exchanger. The coldstage has a coefficient of performance (COP) of 0.061 when considering ideal reversible compression of the refrigerants. The coldstage operates at 3.2% of the ideal Carnot COP. The efficiency of the JT cycle will decrease when the coldstage is practically

integrated with compressors to form a closed system. The efficiency will increase when measures are taken to reduce natural heat leak and the heat exchanger design is optimized.

5.2 Design and Fabrication

The three stage coldstage presented here is based on the thermodynamic design presented in chapter 1.4 and Figure 1.20. The coldstage consists of three single component JT refrigeration cycles. The first stage is used to precool and liquefy the high pressure refrigerant in the second stage and the second stage is used to precool and liquefy the high pressure refrigerant in the third stage. The precooling is accomplished via two tube-in-tube heat exchangers. A top view and cross-section of the coldstage is shown in Figure 5.1. The first stage JT restriction is a 56 mm long 50 µm inner diameter (ID) 150 µm outer diameter (OD) glass capillary sheathed in Kapton. The high pressure inlet of the capillary restriction is epoxied to a 36 mm long 0.813 mm (0.032 in) ID 1.32 mm (0.052 in) OD copper tube. The copper tube maintains room temperature and allows the high pressure isobutane to liquefy at 0.35 MPa and 295 K. The copper tube is mounted to an aluminum fixture designed to accept all components of the coldstage and provide simple fluidic connection on the backside. The first stage glass capillary JT restriction is bent 180^{o} and the low pressure outlet is epoxied to the inlet to the first stage channel of the stage 1-2 heat exchanger. The heat exchanger is also mounted to the aluminum fixture. The second stage JT restriction is a 74 mm long 50 µm ID 150 µm OD glass capillary sheathed in Kapton. The high pressure inlet of the capillary restriction is epoxied to the outlet of the second stage channel of the stage 1-2 heat exchanger. The second stage glass capillary JT restriction is bent 180^{o} and the low pressure outlet is epoxied to the inlet of the second stage channel of the stage 2-3 heat exchanger. The third stage JT restriction is a 55 mm long 50 µm ID 150 µm OD glass capillary sheathed in Kapton. The high pressure inlet of the capillary restriction is epoxied to the outlet of the third stage channel of the stage 2-3 heat exchanger. The third stage glass capillary JT restriction is bent 180^{o} and the low pressure outlet is epoxied to the inlet of the third stage evaporator block. The copper evaporator block consists of a

bored out copper block packed with #100 copper mesh. The mesh is diffusion bonded in place. The copper block is caped with a small copper disk and copper tube to accept the third stage capillary fiber. The evaporator block is thermally isolated from the aluminum mounting fixture with a 20 mm length of 2.8 mm OD Kapton tubing.

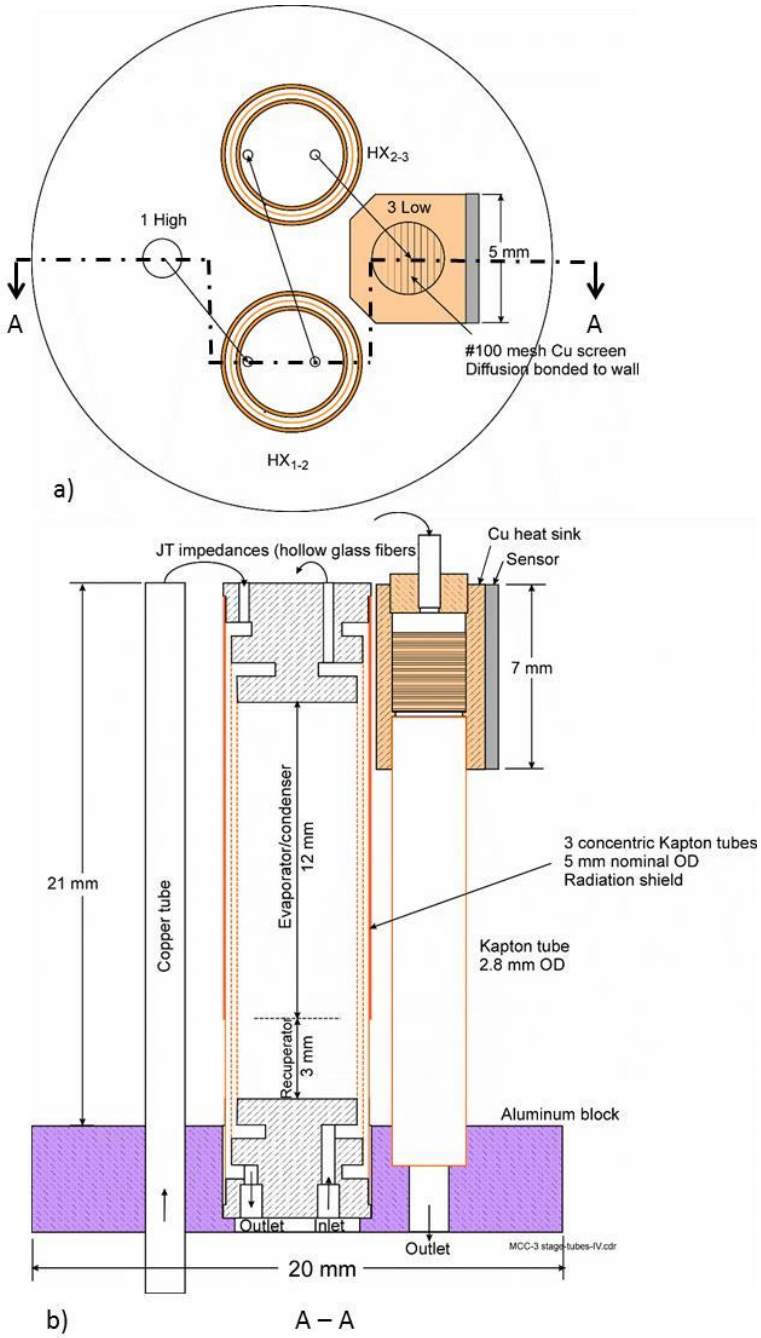

Figure 5.1: a) Top view and b) cross-section of the three stage cascaded coldstage design.

The heat exchangers used for the three stage coldstage are the same design as the heat exchanger presented in chapter 4.2. Because the performance of the stage 1-2 heat exchanger of the two stage coldstage was found to be poor in chapter 4.6, the length of the stage 1-2 heat exchanger was increased from 15 mm to 30 mm allowing for more heat transfer area. The stage 2-3 heat exchanger remains the originally designed 15 mm because of lack of materials and project schedule limitations. It is expected the stage three flow rate will be lower than design and provide reduced refrigeration capacity.

From chapter 1.2 the gross refrigeration power of a JT refrigeration cycle is [8]

$$\dot{Q}_r = \dot{m}(\Delta h|_T)_{min} \tag{1.1}$$

where $\dot{Q}_r$ is the ideal gross refrigeration power, $\dot{m}$ is the molar flow rate of the refrigerant, and $(\Delta h|_T)_{min}$ is the minimum enthalpy difference between the high and low pressure states of the refrigerant over the temperature range of cooling. This design is assumed to operate without recuperative heat exchange for design purposes even though there is some inter-stage recuperative heat exchange. Assuming a recuperative heat exchanger ineffectiveness of 1 (meaning no recuperative heat exchange) the first stage using isobutane is found to operate at 81% of ideal, the second stage using propane is found to operate at 89% of ideal, and the third stage using R116 is found to operate at 77% of ideal [8], [30]. Isobutane has a minimum enthalpy difference of 19.54 kJ/mol over the first stage temperature range of operation (300 – 261 K), propane has a minimum enthalpy difference of 17.42 kJ/mol over the second stage temperature range of operation (261 – 231 K), and R116 has a minimum enthalpy difference of 14.38 kJ/mol over the third stage temperature range of operation (231 – 195 K). A flow rate of 51 sccm is found for the first stage using isobutane considering 700 mW of required heat lift at the stage 1-2 heat exchanger. A flow rate of 48 sccm is found for the second stage using propane considering 660 mW of designed heat lift at the stage 2-3 heat exchanger. A flow rate of 45 sccm is found for the third stage using R116 considering 350 mW of designed heat lift at the evaporator. The

heat leak into the evaporator and heat exchangers are estimated to be less than 10 mW when proper radiation shielding is used and the device is run in vacuum.

The required length and inner diameter of the capillaries are determined by considering laminar two phase flow undergoing adiabatic expansion through a circular tube as expressed by equation 3.1 [8]

$$L = \frac{\pi d^4}{128\dot{n}} \frac{1}{\int \frac{D_{m,avg}}{\mu_{avg}} dP} \tag{3.1}$$

where L is the length of the capillary, d is the inner diameter of the capillary, $\dot{n}$ is the mass flow rate of the refrigerant, P is the pressure of the fluid, and from chapter 2.4 the Dukler averages of density and viscosity for two phase flow are [39]

$$D_{m,avg} = \frac{1}{\frac{x}{D_{m,v}} + \frac{1-x}{D_{m,l}}} \tag{2.7}$$

$$\mu_{avg} = D_{m,avg}\left(\frac{x\mu_v}{D_{m,v}} + \frac{(1-x)\mu_l}{D_{m,l}}\right) \tag{2.8}$$

where x is the quality of the two phase fluid at a given pressure, $D_{m,v}$ and $D_{m,l}$are the molar densities of the vapor and liquid portions of the fluid respectively, and μ_v and μ_l are the viscosities of the vapor and liquid portions of the fluid respectively. The integral is evaluated via tabular integration using fluid properties from the NIST REFPROP v. 9.1 program [40]. The properties used are tabulated in Appendix B. A capillary length of 56 mm and ID of 50 µm is found for a desired flow rate of 51 sccm using isobutane as the refrigerant operating at a 0.4:0.1 MPa pressure ratio. A capillary length of 75 mm and ID of 50 µm is found for a desired flow rate of 48 sccm using propane as the refrigerant operating at a 0.4:0.1 MPa pressure ratio. A capillary length of 55 mm and ID of 50 µm is found for a desired flow rate of 45 sccm using R116 as the refrigerant operating at a 0.5:0.1 MPa pressure ratio. Because of the large channel geometries outside the JT restrictions when compared to the MEMS based coldstage presented in

chapter 2 the pressure drop outside the JT restrictions is assumed to be negligible. Figure 5.2 shows the fully fabricated coldstage with the locations of the heat exchangers and evaporator marked.

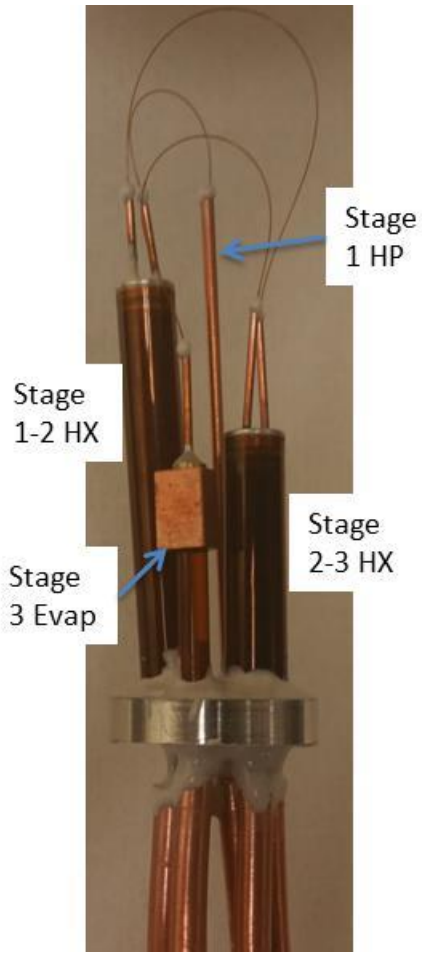

Figure 5.2: Fully Fabricated three stage coldstage with locations of the heat exchangers, third stage evaporator, and first stage high pressure tube marked.

5.3 Test Setup

The coldstage is run in an open loop configuration where high pressure refrigerant is supplied to each stage from a high pressure refrigerant cylinder and the outlet of each stage is vented to atmosphere. Ice packs are used on the first stage high pressure line to precool the incoming high pressure isobutane to 290 K where it liquefies at 0.31 MPa. The precooling is necessary because the isobutane cylinder used was not able to supply liquid isobutane at room temperature and 0.35 MPa. Figure 5.3 shows the schematic of the coldstage in the test setup. The vacuum chamber has enough

electrical feed through lines for two temperature sensors and one resistive heater. The resistive heater and one temperature sensor are mounted to the third stage evaporator. The second temperature sensor is mounted to the cold end of the stage 2-3 heat exchanger. The heater and temperature sensors are secured in place with double sided graphite tape to ensure good thermal contact. The temperature of the stage 1-2 heat exchanger is not measured. Figure 5.4 shows the coldstage mounted to the liquid feedthrough and the locations of the heater and temperature sensors.

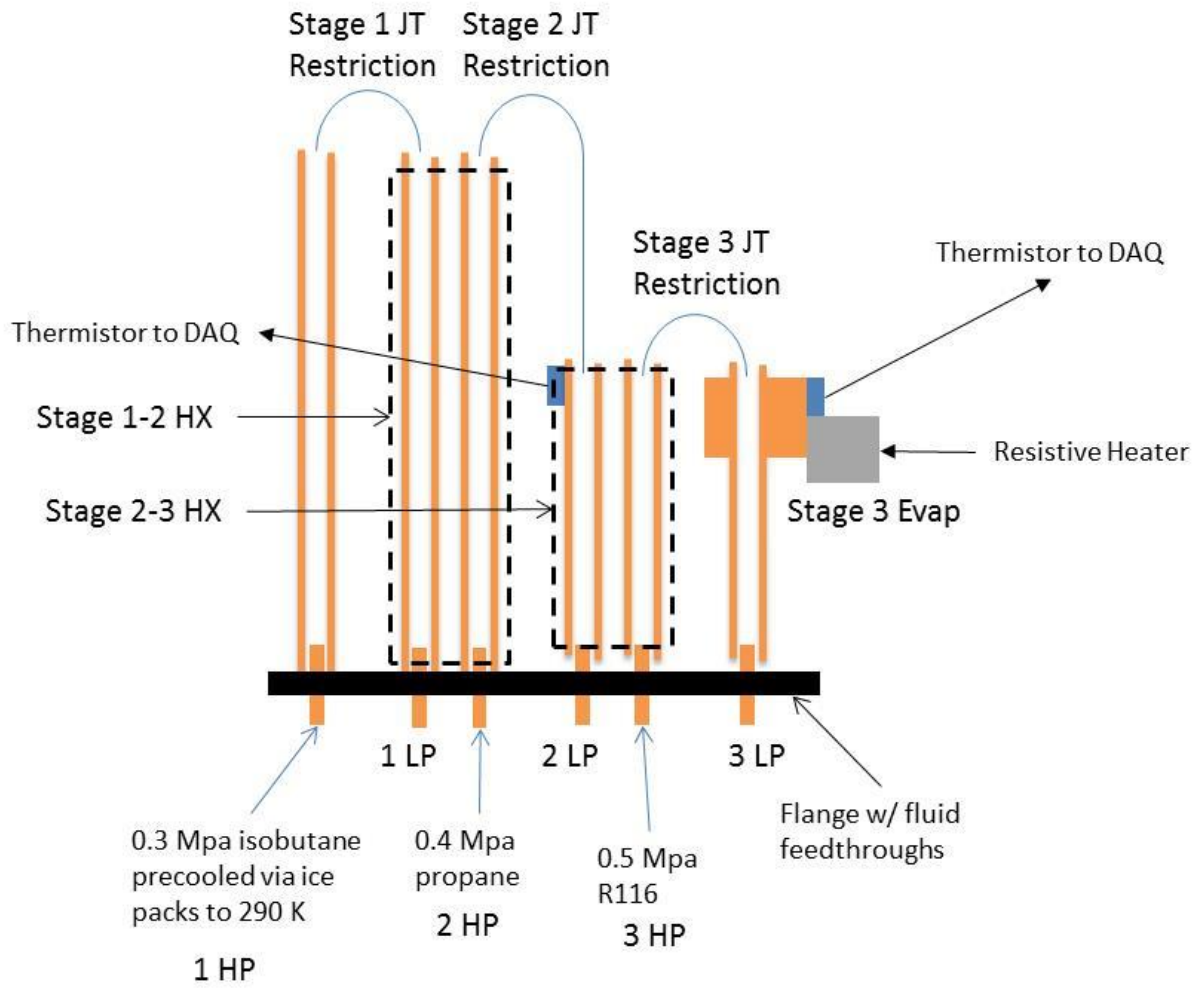

Figure 5.3: Schematic of the three stage coldstage with locations of the temperature sensors and heater noted.

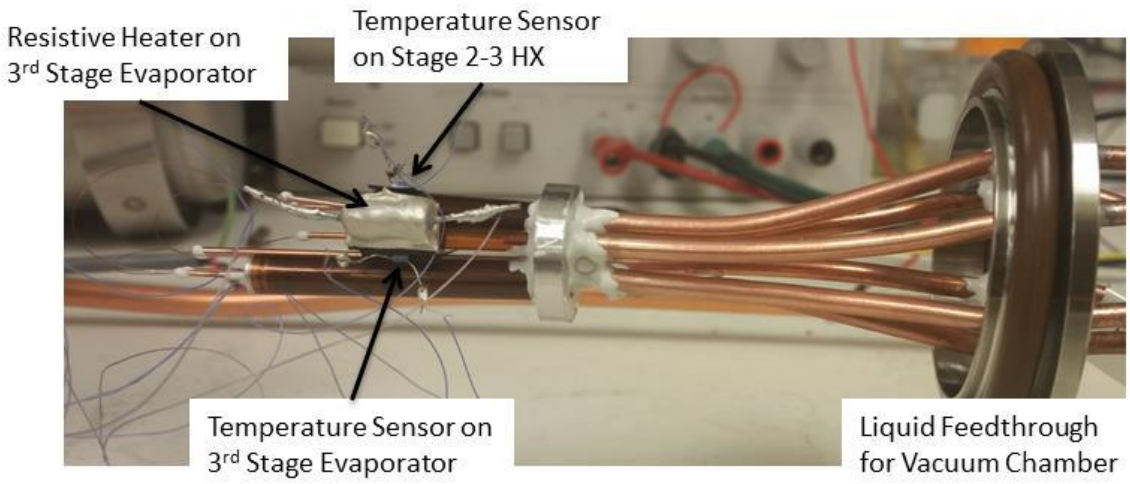

Figure 5.4: Three stage coldstage mounted to the vacuum flange liquid feedthrough with locations of the temperature sensors and heater noted.

The schematic for the high pressure lines upstream of the coldstage is shown in Figure 5.5. Each high pressure line has an individual pressure transducer allowing independent measurement. Each high pressure line has a molecular sieve and particulate filter before entering the coldstage. The molecular sieves ensure no water vapor enters the coldstage eliminating any possible ice buildup inside the coldstage channels. The particulate filters have a 20 µm pore size to stop any particulate contamination. Finally each high pressure line is connected to a vacuum and vent line via a needle valve. The vacuum/vent line allows vacuum to be pulled one each high pressure line before the coldstage is run to eliminate as much trapped air and water vapor in the system as possible. The same line is used to vent the high pressure lines either during or after the test.

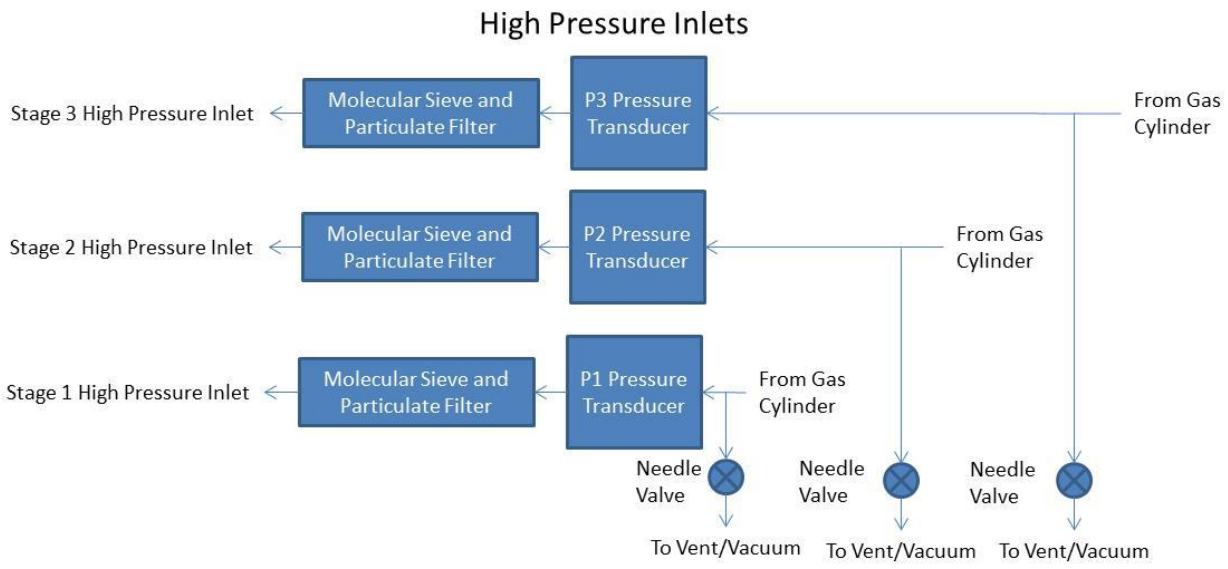

Figure 5.5: Schematic of the configuration of the high pressure lines upstream of the coldstage.

The test setup for the two stage coldstage in chapter 4.3 has the second stage outlet directly connected to the mass flowmeter. The first stage flow rate could not be measured without stopping the test and rearranging the test setup. This caused significant difficulty when diagnosing problems with the coldstage operation. To alleviate this issue a three way valve manifold was implemented. The use of 3 three way valves allows for any stage outlet to be directed through the flowmeter without stopping operation. The schematic for the low pressure outlet lines of the test setup is shown in Figure 5.6. A pressure transducer with a digital readout is used to monitor the outlet pressure of all three stages before the outlet of the test setup to the lab vent. In normal operation this pressure should read atmospheric pressure. The physical test setup is shown in Figure 5.7.

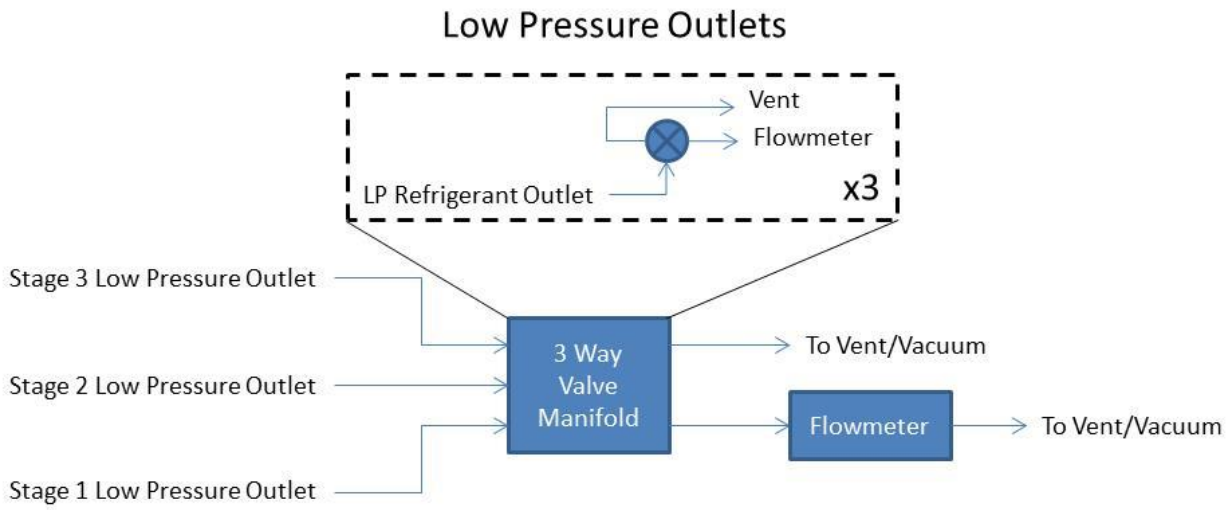

Figure 5.6: Schematic of the three way valve manifold used to direct the outflow of each stage through the flowmeter or directly to vent.

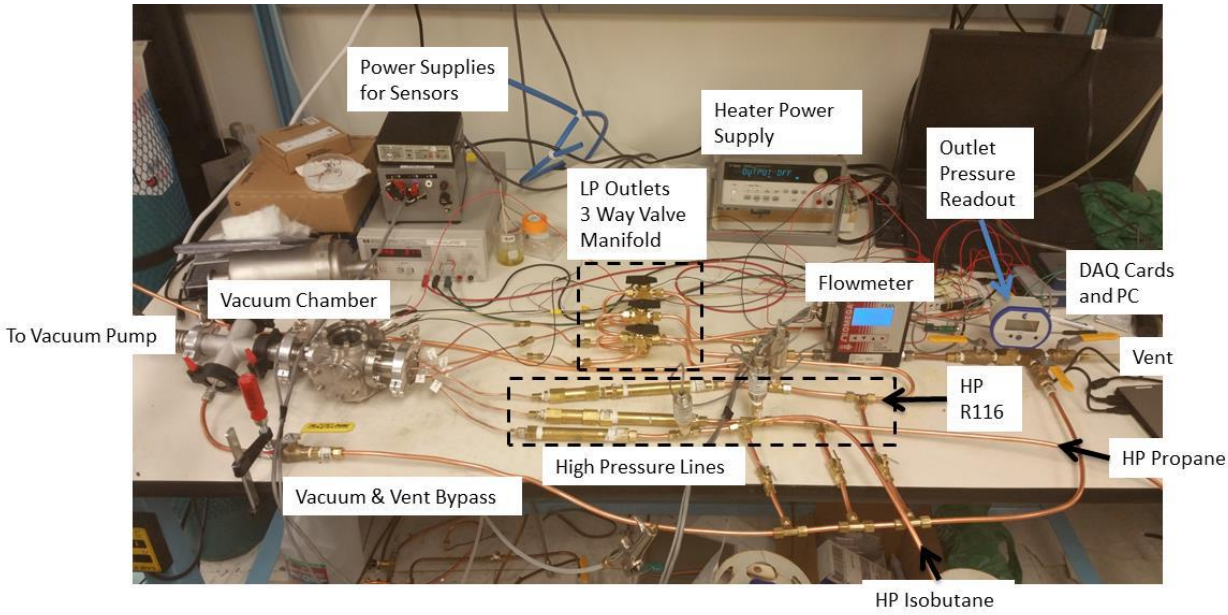

Figure 5.7: The physical test setup used to run the three stage coldstage with important features marked.

5.4 Test Results

The test begins by pulling vacuum on the refrigerant lines to remove as much air as possible. However due to the large internal volume of the test setup lines and the numerous fixtures required the refrigerant lines do not hold good vacuum. Because the lines cannot hold good vacuum all three stages of the coldstage are run through a bleed through process for 30 to 60 minutes. In the bleed through

process the refrigerants are allowed to flow through the coldstage form high pressure side to low pressure side to vent in vapor phase. The refrigerant should displace any air and water vapor remaining in the lines. During the bleed through process the vacuum chamber is pumped down to 5 x 10^{-5} Torr to ensure good insulation of the coldstage. Once the bleed through process is finished and the chamber is pumped to vacuum the cooling test begins. All three refrigerants are brought up to pressure and the coldstage is allowed to reach steady state. Figure 5.8 shows the cool down behavior of the three stage coldstage. The test begins with the bleed through process and evacuation of the vacuum chamber. All three stages are brought up to their operational pressure (Isobutane: 0.3 MPa, Propane: 0.4 MPa, R116: 0.5 MPa) at approximately 4700 s. the flow rate of the first stage is seen to increase when liquid isobutane reaches the JT restriction indicating cooling at the stage 1-2 heat exchanger. The stage 2-3 heat exchanger is seen to quickly cool to 238 K shortly after the increase in the first stage flow rate. The third stage evaporator slowly decreases in temperature reaching a steady state of 193 K. The third stage evaporator has a longer cool down time because of the larger thermal mass of the evaporator and resistive heater when compared to the stage 1-2 heat exchanger and stage 2-3 heat exchanger. The flow rate for the third stage is also significantly lower than design reducing the available refrigeration power at the third stage evaporator. Once the coldstage reaches steady operation the flow rates of all three stages are measured. The first stage has a steady state flow rate of 48 sccm close to the designed value of 51 sccm. The second stage has a steady state flow rate of 43 sccm close to the designed value of 48 sccm. The third stage has a steady state flow rate of 15 sccm significantly reduced from the designed value of 45 sccm. This discrepancy is discussed in chapter 5.5.

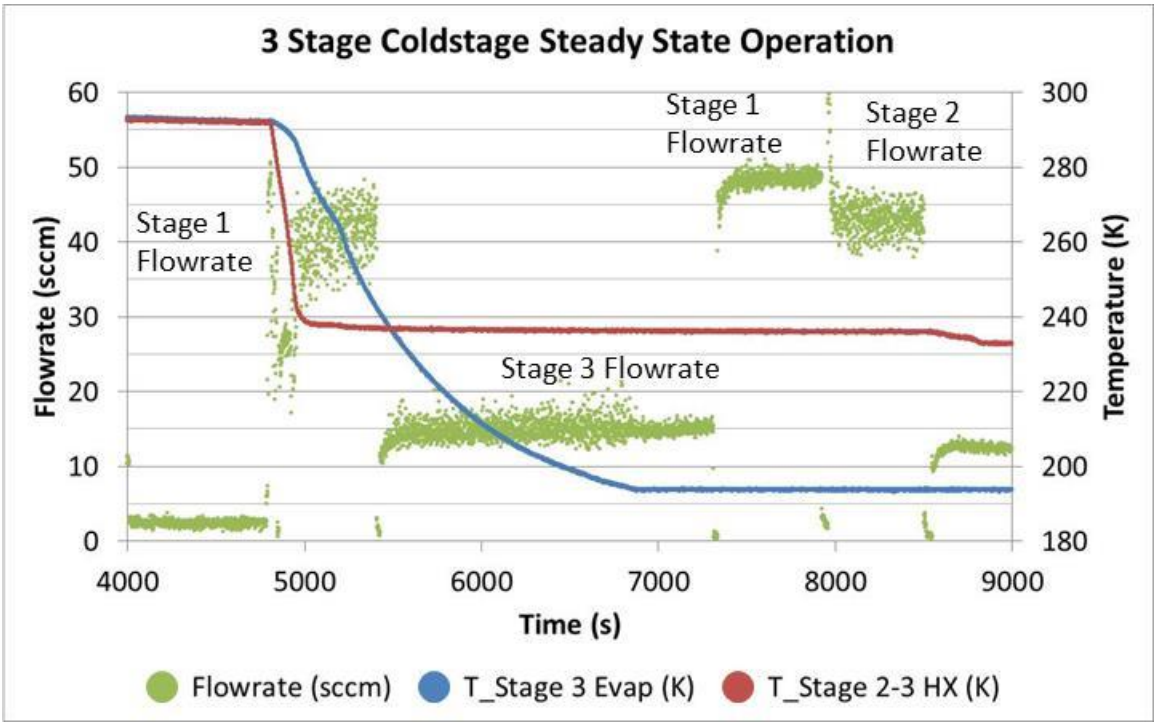

Figure 5.8: Cool down behavior and steady state operation of the three stage coldstage.

The natural heat leak into the coldstage was estimated through the analysis of several warm up curves. For each curve the coldstage is cooled down to the ultimate temperature of 193 K. Once the coldstage reaches steady state the R116 flow is shut off by venting the third stage high pressure lines. When the flowmeter measuring the third stage flow rate reads zero the heater is powered on. Each warm up curve has a different input power. The evaporator is allowed to warm up to around 290 K. The third stage is re-pressurized and the process is repeated with a new heater input power. Figure 5.9 shows the temperature rise behavior of the third stage evaporator without any refrigeration and various heater input powers. At time zero the heater is turned on.

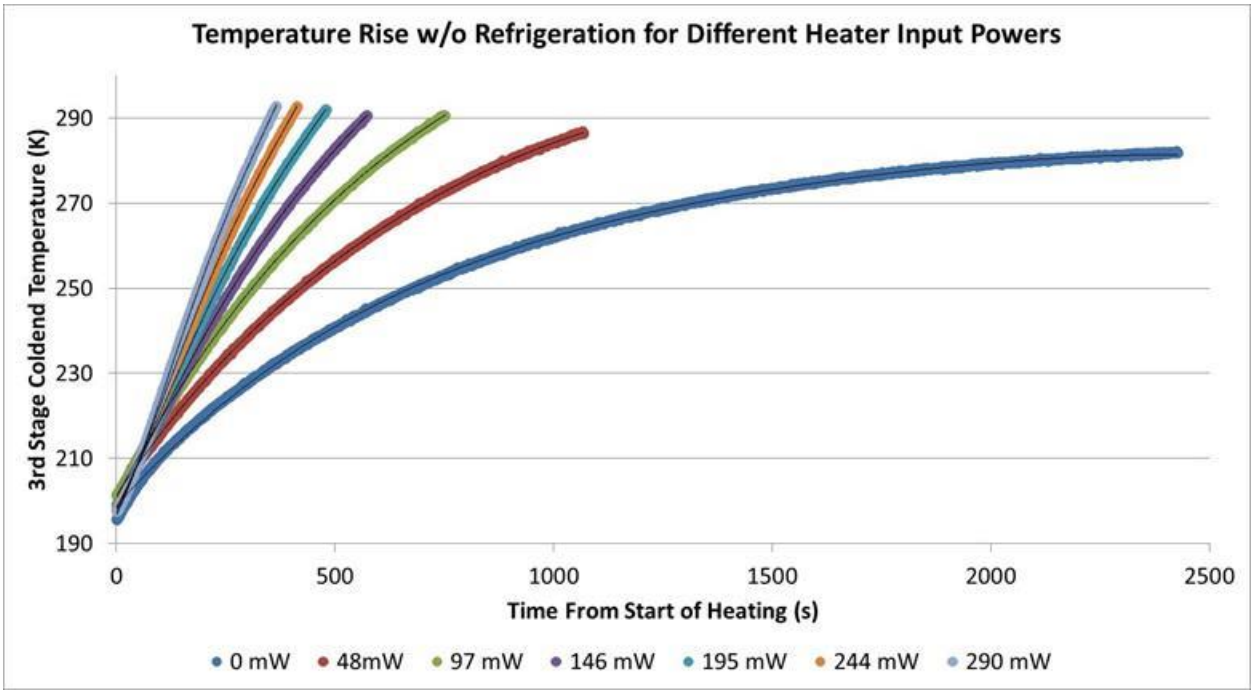

Figure 5.9: Worm up curves for the third stage evaporator without any refrigeration applied for various heater input powers.

From chapter 4.4 the definition of specific heat is [43]

$$Q = C_{pT}\Delta T \tag{4.3}$$

where Q is the energy required to increase the temperature of a material with specific heat at constant pressure and temperature C_{pT} an amount of ΔT. Taking the time derivative of equation 4.3 yields

$$\frac{dQ}{dt} = C_{pT}\frac{dT}{dt} \tag{4.4}$$

where $\frac{dQ}{dt}$ an applied heat load and $\frac{dT}{dt}$ is the temperature rise rate. Equasion 4.4 reveals a linear relationship between an applied heat load and the temperature rise rate for a constant temperature and pressure of the evaporator.

A forth order polynomial is fit to each temperature rise curve in Figure 5.9. This polynomial fit is used to estimate the temperature rise rate at a specific temperature for each heater input power. Figure 5.10 shows the heater input power as a function of temperature rise rate for specific evaporator

temperatures. A linear fit is applied to each curve. Extrapolating each linear fit to a temperature rise rate of zero gives a negative heater input power. The negative heater input power is the refrigeration power that must be supplied to maintain zero temperature change for a specific evaporator temperature. This means all refrigeration power is being used to overcome the natural heat leak into the evaporator. This negative input power is the estimate for natural heat leak into the evaporator at specific evaporator temperatures. The natural heat leak into the evaporator for specific evaporator temperatures is plotted in Figure 5.11 with estimates for heat leak from radiation and conduction through the Kapton thermal standoff with emissivity of 1 and 0.5. Note the T=200 data does not have a good linear fit. This is believed to be due to the T=200 data is derived from data points at the extreme end of the warm up data set used for the 4th order polynomial fit. The heat leak for an evaporator temperature of 200 K in Figure 5.11 should be considered inaccurate and is not included in any further coldstage analysis.

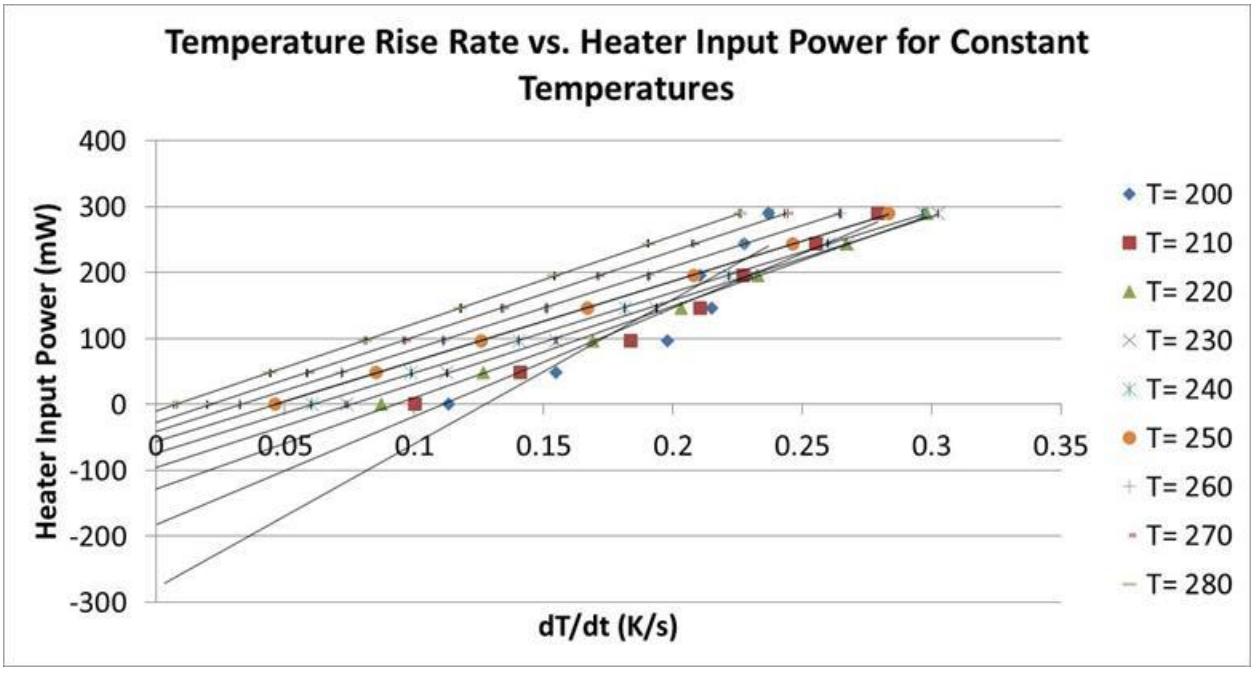

Figure 5.10: Temperature rise rate for specific evaporator temperatures and heater input powers. Linear trend lines are fit to each curve. The extrapolated y intercept is the natural heat leak into the system at specific evaporator temperatures.

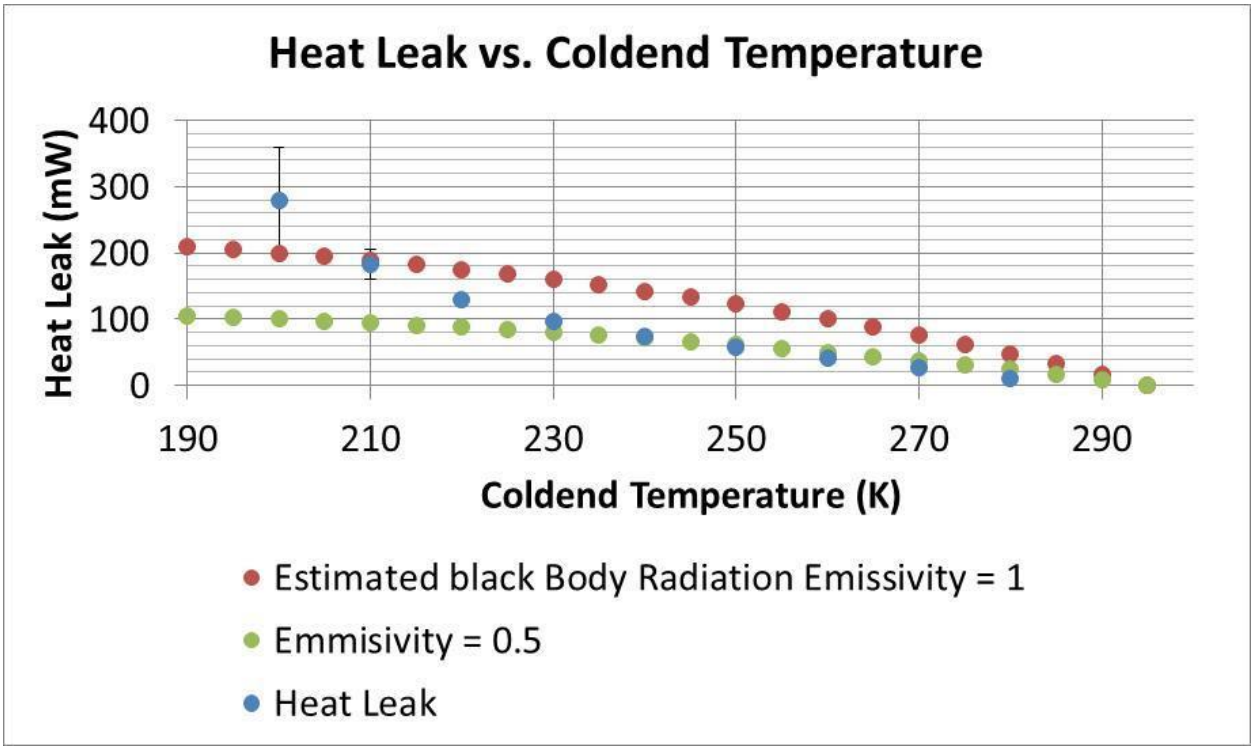

Figure 5.11: Natural heat leak into the evaporator for specific evaporator temperatures and estimated radiation heat leak considering an emissivity of 1 and 0.5.

A power dissipation test is run on the coldstage. For this test the coldstage is cooled to the ultimate temperature of 193 K and allowed to reach steady state operation. Once the coldstage is stable the resistive heater is turned on to provide a heat load. The evaporator temperature is allowed to reach a new steady state temperature before applying a new input power. Figure 5.12 shows the third stage evaporator temperature for various heater input powers. The coldstage is able to provide 15 mW of refrigeration power at the ultimate temperature of 193 K. When above 15 mW of heater input power the temperature of the evaporator increases to balance the gross refrigeration power with the heater input power and heat leak. With constant gross refrigeration available, when the heater input power increases the evaporator temperature must increase to decrease the natural heat leak. The coldstage is designed to provide 350 mW of refrigeration at 295 K. The coldstage has a much lower heat lift of 15 mW. This decrease is in part due to a larger radiative heat leak than designed and a much lower flow rate of the third stage due to ineffective heat exchange in the stage 2-3 heat exchanger.

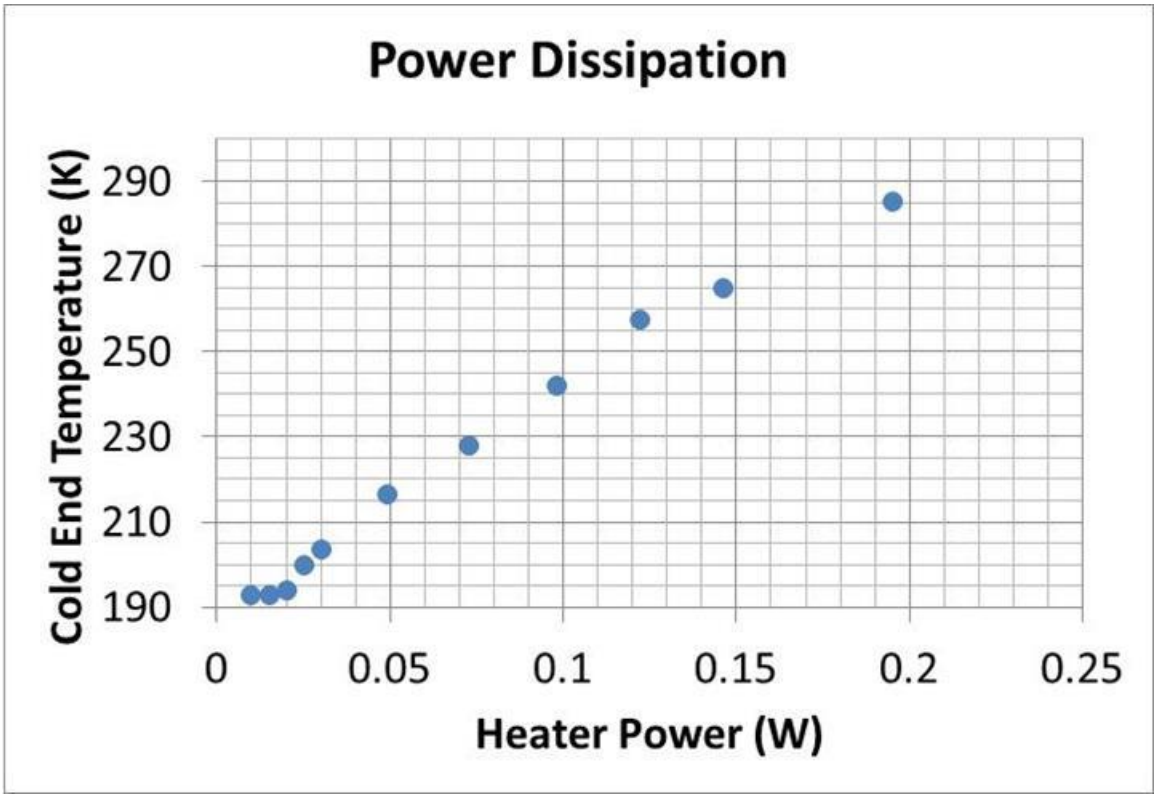

Figure 5.12: Evaporator temperature for specific heater input powers during normal coldstage operation.

5.5 Confirmation of Heat Exchanger Ineffectiveness

The low flow rate of the second stage of the two stage coldstage is investigated in chapter 4.6. From this investigation it is found the heat exchange of the stage 1-2 heat exchanger is worse than designed. To address this issue the length of the stage 1-2 heat exchanger for the three stage coldstage is increased from 15 mm to 30 mm. The increase in total heat exchange area leads to a flow rate increase from 20 sccm with the shorter 15 mm heat exchanger to 43 sccm with the longer 30 mm heat exchanger. The longer heat exchanger allows the second stage of the three stage coldstage to operate at 90% of the designed 48 sccm. The stage 2-3 heat exchanger uses the original 15 mm design because of lack of materials and project schedule limitations. This leads to a lower third stage flow rate. The third stage operates at a flow rate of 15 sccm much lower than the designed value of 45 sccm. This study confirms the estimate for the net heat transfer coefficient for our design was too high. A more conservative heat exchanger design is presented in the future work section of chapter 6. This design

proposes the use of a hollow copper block packed with copper mesh similar to the evaporator block to form a counter flow heat exchanger.

5.6 Characterization of Gross Refrigeration Power, Coefficient of Performance (COP), and Efficiency of the Coldstage

From chapter 4.5 the net refrigeration of the coldstage is

$$\dot{Q}_{net} = \dot{Q}_r - \dot{Q}_{leak} - \dot{Q}_{load} \tag{4.5}$$

where $\dot{Q}_{net}$ is the net refrigeration power, $\dot{Q}_r$ is the gross refrigeration power available from the JT expansion of the refrigerant $\dot{Q}_{leak}$ is the natural heat leak and $\dot{Q}_{load}$ is the resistive heater input power.

The coldstage is assumed to be in thermodynamic equilibrium when the temperature of the evaporator is above the ultimate temperature of 193 K. In this scenario there is no available net refrigeration power meaning the gross refrigeration power is equal to the sum of the heat leak and the applied heater load. Using the power dissipation data (Figure 5.12) for all points T > 210 K and interpolating the heat leak at each of these temperatures from the heat leak data (Figure 5.11) a gross refrigeration power of 178 ± 12 mW is estimated. It is therefore reasonable to have an available gross refrigeration of 178 mW considering for a flow rate of 15 sccm of R116 the gross refrigeration power is estimated to be 109 mW from equation 1.1. Note temperatures below 210 K were not considered because the heat leak estimate for T = 200 K is inaccurate.

From chapter 4.5 the COP for any refrigeration cycle is [43]

$$COP = \frac{\dot{Q}_{ref}}{\dot{Q}_{in}} \tag{4.6}$$

where $\dot{Q}_{ref}$ is the heat lifted by the refrigerator at the low temperature and $\dot{Q}_{in}$ is the power input into the system to compress the refrigerant. The ideal compressor input power is [43]

$$\dot{Q}_{comp} = \dot{m}\Delta G \tag{4.7}$$

Where $\dot{Q}_{comp}$ is the ideal compressor input power, $\dot{m}$ is the mas flow rate, and ΔG is the Gibbs energy of formation for an ideal gas where [43]

$$\Delta G = \Delta h - T\Delta s \tag{4.8}$$

where Δh is the change in enthalpy from the low pressure state to the high pressure state, Δs is the entropy change from the low pressure state to the high pressure state, and T is the temperature at which the compression occurs.

The three stage coldstage can provide 15 mW of net refrigeration at 193 K. The first stage operates at a 0.35:0.082 MPa pressure ratio and a flow rate of 48 sccm using isobutane. The second stage operates at a 0.4:0.082 MPa pressure ratio and a flow rate of 43 sccm using propane. The third stage operates at a 0.5:0.082 MPa pressure ratio and a flow rate of 15 sccm using R116. Using fluid properties from the NIST REFPROP v. 9.1 program [40] the ideal compressor input powers for the isobutane, propane, and R116 stages are 89.2 mW, 111.6 mW, and 44.5 mW respectively. This gives a total ideal compressor input power of 245.3 mW. Equation 4.6 gives a COP of 0.06.

From chapter 4.5 the ideal reversible Carnot COP for any refrigeration cycle is [43]

$$COP_{Carnot} = \frac{1}{\frac{T_h}{T_l} - 1} \tag{4.9}$$

where T_h is the hot temperature of the refrigeration cycle and T_l is the cold temperature of the refrigeration cycle. For the three stage coldstage the hot temperature is 295 K and the cold temperature is 193 K. This gives an ideal Carnot COP of 1.9. With ideal compression of the refrigerants the three stage coldstage has 3.2% efficiency when compared to an ideal Carnot refrigeration cycle. The efficient will decrease when integrated with real compressors. The efficiency will increase with improved radiation shielding to limit heat leak and with optimization of the heat exchanger to ensure designed operation.

5.7 Summary of Design Criteria, Critical Dimensions, and Coldstage Performance

This section provides a summary of the key design and performance criteria. Table 5.1 provides the design criteria and physical dimensions used to make the three stage coldstage. Table 5.2 provides a summary of the coldstage performance.

Table 5.1: Summary of Three Stage Coldstage Design Criteria and Critical Dimensions.

JT Restrictions			
	Stage 1	**Stage 2**	**Stage 3**
Refrigerant	Isobutane	Propane	R116
Flow Rate (sccm)	51	48	45
Pressure Ratio (MPa)	0.35:0.1	0.4:0.1	0.5:0.1
Inner Diameter (µm)	50	50	50
Length (mm)	56	74	55
Heat Exchangers			
	Stage 1-2	**Stage 2-3**	
Temperature (K)	261	231	
Total Heat Transfer (mW)	700	660	
Length (mm)	30	15*	
Heat Exchanger Tubes			
	Inner	**Middle**	**Outer**
Outer Diameter (mm)	5.2	5.5	5.9
Wall Thickness (µm)	75	50	75
Evaporator Block			
Width (mm) (square)	5		
Length (mm)	7		
Bore Diameter (mm)	3		
Mesh Size	#100		
Temperature (K)	193		
Net Refrigeration Power (mW)	350		
Kapton Tube for Evaporator Thermal Standoff			
Length (mm)	20		
Outer Diameter (mm)	2.8		
Wall Thickness (µm)	100		

* Length needs to be increased to reach designed performance.

Table 5.2: Summary of Three Stage Coldstage Steady State Performance.

	Stage 1	Stage 2	Stage 3	Coldstage
Pressure Ratio (Mpa	0.3:0.1*	0.4:0.1	0.5:0.1	NA
Flow Rate (sccm)	48	43	15	NA
Temperature (K)	261	231	193	193
Net Refrigeration Power (mW)	NA	NA	15	15
Gross Refrigeration Power (mW)	NA	NA	178	178
COP	NA	NA	NA	0.06
Efficiency (% Carnot)	NA	NA	NA	3.2%

NA = not applicable or not measured. * Icepack precooling used to liquefy isobutane at 290 K.

5.8 Summary

This chapter presents the successful design, fabrication, and characterization of a three stage coldstage for low pressure ratio (0.5:0.1 MPa) refrigerants. The coldstage consists of three separate single component refrigerant JT refrigeration cycles. Each self-contained JT cycle is used to precool the high pressure refrigerant of the subsequent cycle. The JT restrictions are fabricated out of 50 µm ID 150 µm OD glass capillaries sheathed in Kapton. The inter-stage heat exchangers are a Kapton tube-in-tube design. The ultimate temperature of the coldstage is 193 K. At 193 K the coldstage can lift 15 mW of net refrigeration. There is a significant discrepancy between the measured net refrigeration capacity and the designed target of 350 mW. This is due to larger than estimated radiation heat leak from the lack of radiation shielding and a significant decrease in the third stage flow rate due to ineffective heat exchange between the second and third stages. The heat transfer coefficient used to design and estimate the heat exchanger performance was too large. This leads to a heat exchanger design with too little heat exchange area. The heat exchange area problem is investigated in chapter 4.6 and confirmed in chapter 5.5. A more conservative heat exchanger design is presented in the future work section of chapter 6. The COP of the coldstage when considering ideal compression of the refrigerants is 0.06. This is 3.2% of the fully reversible Carnot COP of 1.9.

Chapter 6: Conclusion and Future Work

6.1 Conclusion

Cascading multiple self-contained Joule-Thomson (JT) refrigeration cycles allows for a dramatic reduction in required pressure ratios when using single component refrigerants to cool to cryogenic temperatures. Single stage coldstages require pressure ratios greater than 8:0.1 MPa to reach cryogenic temperatures when operated with single component refrigerants such as nitrogen and oxygen. For a cascaded coldstage each self-contained single stage JT cycle is used to precool the following stage. This precooling allows the next stage refrigerant to liquefy at a low pressure and the low temperature of the preceding stage. This work focuses on refrigerants designed to operate at a 0.4:0.1 pressure ratio. Using single component refrigerants eliminates any flow stratification problems as identified with mixed refrigerants operating at low pressure ratios [29]. Low pressure ratio single component refrigerants have an order of magnitude larger specific refrigeration capacity but a smaller temperature range of cooling when compared to low pressure ratio mixed refrigerants. Cascading several single component refrigerant JT cycles allows for a larger temperature range of cooling. A cascaded design has higher specific refrigeration capacity when compared to a single stage mixed refrigerant JT cycle operation over the same temperature range [8]. This allows cascaded coldstages to be run at lower flow rates to accomplish the same heat lift as a single stage mixed refrigerant coldstage. The cascaded approach to coldstage design using single component refrigerants reduces the pressure ratios and flow rates demanded from the compression mechanism. This significantly expands the design space for future micro-compressor research and development.

This thesis presents the design, fabrication, and characterization of several coldstages intended to study a low pressure ratio three stage cascaded JT cryogenic cooler. The three stage coldstage investigated uses a unique approach to cascade the three stages together. This approach eliminates the use of intra-stage recuperative heat exchangers. The removal of the recuperative heat exchangers

decreased the coldstage to ~75% of ideal efficiency [8], [30]. In contrast a mixed refrigerant coldstage operating between 300 – 150 K requires a recuperative heat exchanger with heat exchange efficiency of greater than 90 % to not lose all available refrigeration capacity to heat exchanger ineffectiveness [8]. Removing the recuperative heat exchangers allows for a simplified design for micro fabrication. The design removes the need for complicated vertical connections between multiple device layers and allows for a coldstage containing any number of stages to be fabricated using only two stacked channel layers.

A planar polyimide based micro-fabricated coldstage is presented (chapter 2) based on the fabrication process developed by Wang et al. [26]–[28], [36], [37]. The coldstage is designed to investigate the feasibility of the fabrication techniques when applied to the relative large device size of the first stage of a cascaded coldstage. The large size of the coldstage is driven by the size of the cold end required for efficient heat exchange to a theoretical second stage. The coldstage is designed to use Isobutane as the refrigerant at a 0.4:0.1 MPa pressure ratio to cool from 295 K to 261 K with a net refrigeration power of 100 mW. A gross refrigeration power of 110 mW is estimated for a net refrigeration power of 100 mW when considering lack of a recuperative heat exchanger, and expected heat leak form conduction and radiation when run in a vacuum environment. Major fabrication issues include copper-polyimide interactions, step coverage of evaporated copper, polyimide-polyimide adhesion, electroplating uniformity, and chemical compatibility. Several solutions and best practices are presented. However the best coldstage fabricated had partial delamination of the posts supporting the JT restriction. Because the JT restriction was not fully supported it could not provide the required pressure drop. To solve this, the coldstage was run in a high pressure environment to squeeze the JT restriction into the correct shape. When tested in the hyperbaric chamber the coldstage cooled to a temperature of 280 K with a flow rate of 10 sccm at a 0.4:0.082 MPa pressure ratio. Due to increased convective heat leak form running the coldstage in a high pressure environment, the coldstage reaches

thermodynamic equilibrium at 280 K. This is higher than the designed target of 261 K. The benefits of micro-fabrication are important for coldstage miniaturization and mass production. However the long design cycle and low process yield are not conducive to rapid prototyping. A faster and more reliable fabrication technique using glass capillaries and hand assembly is identified.

A glass capillary macro-scale hand assembled approach is identified as a relatively reliable and fast fabrication approach when compared to the polyimide based micro-fabrication approach. A coldstage consisting of a 32 mm long 25 um inner diameter (ID) 150 um outer diameter (OD) glass capillary restriction and copper mesh based evaporator is presented (chapter 3). The coldstage is capable of running with low pressure (0.25 MPa) and low flow rate (3 sccm) when connected directly to a high pressure n-butane cylinder. Evaporator temperatures of 268 K and 283 K are reached when the coldstage is run in vacuum and atmosphere respectively. The coldstage was integrated with a mini-compressor and able to cool to 288 K in atmospheric conditions with pulsatile flow. The pulsatile flow was due to a flow rate mismatch between the compressor and coldstage. Because the compressor supply flow rate was 2 sccm and the coldstage operational flow rate was 3 sccm the high side pressure would fluctuate around the saturation pressure of n-butane.

The successful design, fabrication, and characterization of a two stage coldstage for low pressure ratio (0.4:0.1 MPa) refrigerants is presented (chapter 4). The coldstage consists of two separate single component refrigerant JT refrigeration cycles where one is used to precool the other. The JT restrictions are fabricated out of 50 µm ID 150 µm OD glass capillaries sheathed in Kapton. The inter-stage heat exchanger is a Kapton tube-in-tube design. The ultimate temperature of the coldstage is 228 K. At 228 K the coldstage can provide 150 mW of net refrigeration. There is a significant discrepancy between the measured net refrigeration capacity and the designed target of 500 mW. This is due to larger than estimated radiation heat leak from the lack of radiation shielding and a significant decrease

in the second stage flow rate due to ineffective heat exchange between the two stages. The heat exchanger is found to not have enough heat exchange area to adequately lift all the heat from the second stage refrigerant and provide 100% liquid refrigerant. This indicates the heat transfer estimate used was too optimistic. Future design requires a more conservative heat exchanger design. The coefficient of performance (COP) of the coldstage when considering ideal compression of the refrigerants is 1.06. This is 26.6% of the fully reversible Carnot COP of 3.4. The efficiency of the coldstage can be increased through the implementation of proper radiation shielding to reduce the natural heat leak in to the cold end, and further optimization of the heat exchanger. The efficiency of a fully closed JT refrigeration cycle will decrease when the coldstage is practically integrated with mini or micro-compressors due to the inefficiency of the compression mechanism.

The successful design, fabrication, and characterization of a three stage coldstage for low pressure ratio (0.5:0.1 MPa) refrigerants is presented (chapter 5). The coldstage consists of three separate single component refrigerant JT refrigeration cycles. Each self-contained JT cycle is used to precool the high pressure refrigerant of the subsequent cycle. The JT restrictions are fabricated out of 50 µm ID 150 µm OD glass capillaries sheathed in Kapton. The inter-stage heat exchangers are a Kapton tube-in-tube design. The ultimate temperature of the coldstage is 193 K. At 193 K the coldstage can lift 15 mW of net refrigeration. There is a significant discrepancy between the measured net refrigeration capacity and the designed target of 350 mW. This is due to larger than estimated radiation heat leak from the lack of radiation shielding and a significant decrease in the third stage flow rate due to ineffective heat exchange between the second and third stages. The stage 1-2 heat exchanger is increased in length from 15 mm as designed to 30 mm. This change is made to investigate the ineffectiveness of the heat exchanger identified in the two stage coldstage study. The increase in heat exchange area successfully allowed for adequate heat lift from the second stage increasing the second stage flow rate from 20 sccm for the shorter heat exchanger to 43 sccm for the longer heat exchanger.

The higher flow rate is 90% of the designed target of 48 sccm. This study confirms the heat transfer coefficient estimate used was too optimistic and a more conservative heat exchanger design is needed. The short 15 mm stage 2-3 heat exchanger exhibits the same low flow characteristics as the short 15 mm stage 1-2 heat exchanger used for the two stage coldstage further confirming the inaccuracy of the heat transfer coefficient estimate. The COP of the coldstage when considering ideal compression of the refrigerants is 0.06. This is 3.2% of the fully reversible Carnot COP of 1.9. The efficiency of the coldstage can be increased through the implementation of proper radiation shielding to reduce the natural heat leak in to the cold end, and further optimization of the heat exchanger. The efficiency of a fully closed JT refrigeration cycle will decrease when the coldstage is practically implemented with a mini or micro-compressor due to the inefficiency of the compression mechanism.

Major accomplishments of this thesis are summarized as follows:

(1) Development of a three stage cascaded Joule-Thomson cryogenic coldstage for use with low pressure ratio refrigerants (0.5:0.1 MPa). The coldstage is capable of cooling to an ultimate temperature of 193 K with a measured net refrigeration power of 15 mW.
(2) Development of a two stage cascaded Joule-Thomson cryogenic coldstage for use with low pressure ratio refrigerants (0.4:0.1 MPa). The coldstage is capable of cooling to an ultimate temperature of 228 K with a measured net refrigeration power of 150 mW.
(3) Identified a major problem of insufficient heat exchange at the inter-stage heat exchangers of a cascaded coldstage that leads to a significant decrease in coldstage performance from design.
(4) Development of a glass capillary macro-scale fabrication approach for rapid prototyping of low pressure ratio single stage and multi-stage cascaded Joule-Thomson based coldstages.

(5) Successful integration of a low flow rate low pressure ratio glass capillary based single stage coldstage with a PZT driven silicon chip based membrane mini-compressor.

(6) Identified a micro-fabricated polyimide based three stage cascaded Joule-Thomson coldstage design which leverages the lack of the need of intra-stage recuperative heat exchangers to simplify coldstage layout and fabrication process.

(7) Identified, solved, and implemented several best practices for several processing challenges with the polyimide and coper micro-fabrication technique developed in previous works.

6.2 Future Work

A major issue identified in this thesis is the effective heat exchange between each stage of a cascaded JT coldstage. If the heat lift is insufficient to pre-cool the required volume of liquid refrigerant in the subsequent stage the flow rate and thus the available refrigeration power of the pre-cooled stage will be dramatically reduced. When this issue is compounded across multiple cascaded stages, the available refrigeration power of the final stage can become insignificant or the final stage will not function altogether. To prevent this scenario a conservative inter-stage heat exchanger must be designed. Figure 6.1 shows a top view and cross-section of a three stage coldstage with a new inter-stage heat exchanger design. This design replaces the 12 mm long Kapton tube-in-tube isothermal portion of the heat exchanger with a copper end plug where each channel has a section packed with #100 copper mesh and diffusion bonded in place. The copper mesh provides an order of magnitude higher surface area for heat exchange. This design assumes the entire copper end plug and mesh are isothermal at the cold temperature of the heat exchanger. Because of the increased surface area of heat exchange the design presented is very conservative and should ensure the required heat lift occurs at the heat exchanger.

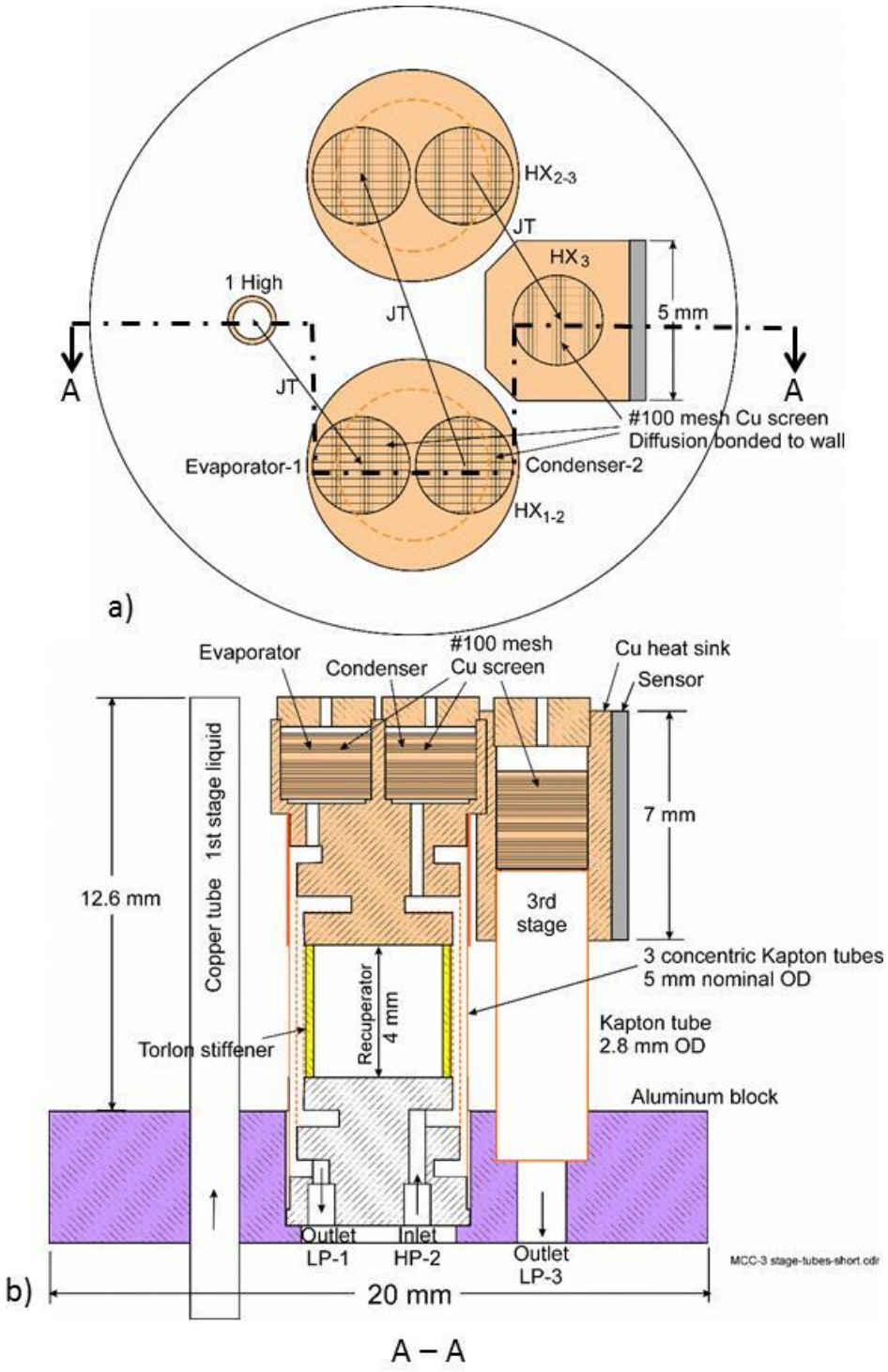

Figure 6.1: a) Top view and b) cross-section of the three stage cascaded coldstage design with copper mesh based isothermal heat exchangers.

The hand assembled glass capillary macro-fabrication approach developed in this thesis is an excellent approach for rapid prototyping of small quantities of coldstages with varied design criteria.

This approach is conducive to a research environment but may be difficult to practically implement on a mass fabrication scale. Further development of micro-fabrication processes for microfluidic devices with internal pressures of up to 1 MPa is needed. The polyimide approach developed by Wang et al. [26]–[28], [36], [37] has been shown to withstand internal pressures up to 1 MPa [28] with proper intra-channel post design. However when implemented in this thesis many challenges were encountered and quality post adhesion was not accomplished. As a result the JT restriction was not well controlled. Further simplification of the fabrication process presented in chapter 2.5 is needed to ensure high process yield. This process may be simplified by starting with copper clad polyimide, patterning the copper into the desired micro-channel structure, and over-coating the copper with more polyimide as shown in Figure 6.2. This approach could turn a 13+ step process into a process with as few as 3 or 4 processes. Even with process simplification quality JT restriction control may remain difficult with a polymer based micro fluidic structure. The major problem with polymer based microfluidics for high internal pressure applications is the ability to precisely control the microfluidic channel thickness. When a polymer based fabrication approach is applied to a JT coldstage the JT restriction will deform under high internal pressure. Because the JT restriction is dependent on the gap thickness cubed, any small variation in the gap thickness can cause a large change to the behavior of the JT restriction. A more ridged material such as glass may prove to be a better material for the fabrication of the coldstage. The three glass wafer stack approach developed by brake et al. [19], [20] has been shown to withstand internal pressures greater than 8 MPa. However the thermal characteristics of the structural material need to be considered. By implementing a stiffer material additional heat leak via conduction and radiation may be introduced. A thorough analysis of the materials used to fabricate future coldstages based on mechanical design, thermal design, ease of fabrication, and quantity of fabrication is needed.

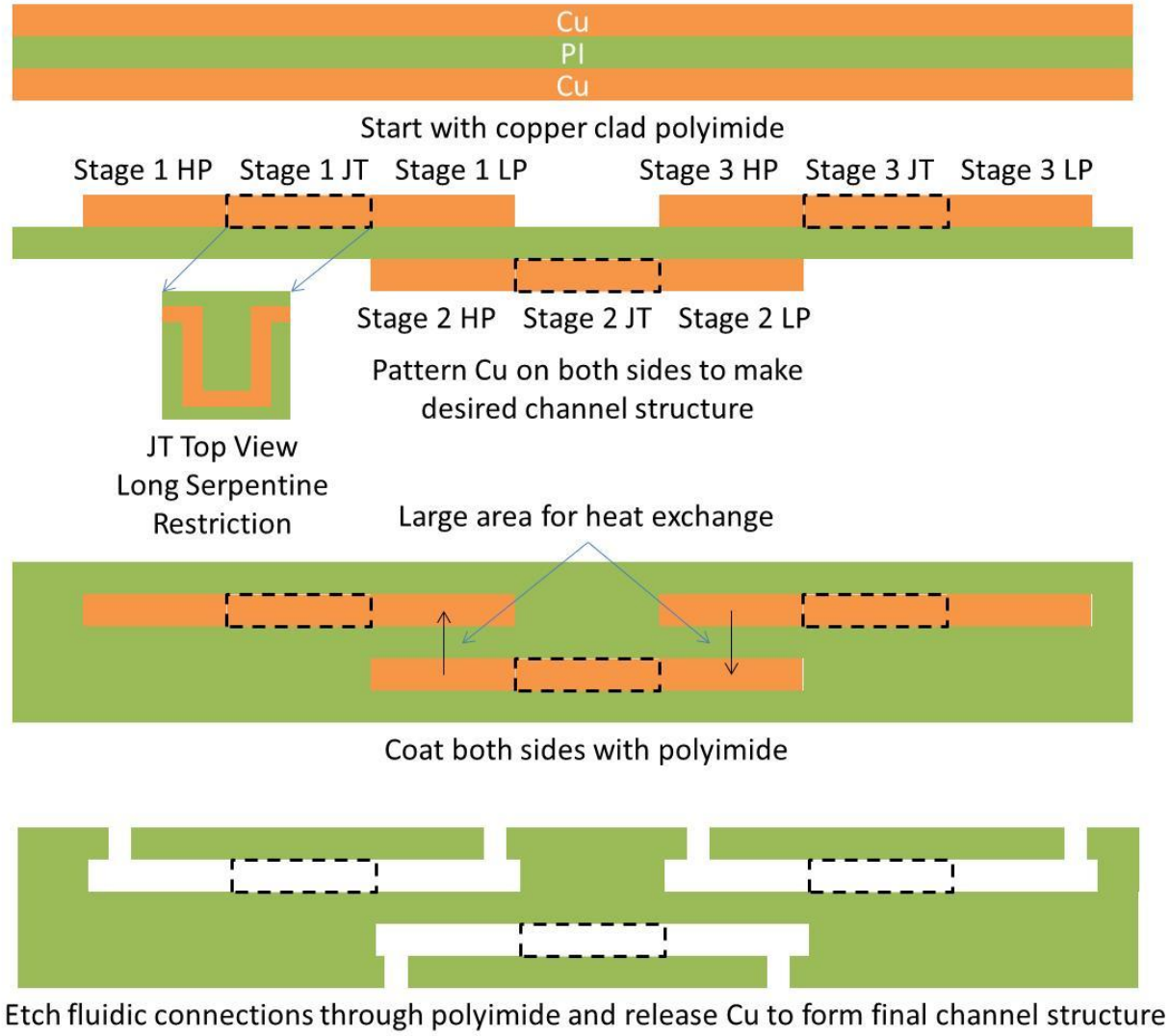

Figure 6.2: Basic fabrication approach for a three stage coldstage starting with copper clad polyimide. Processing is significantly simplified from the design presented in chapter 2.5.

References

[1] R. Radebaugh, “Cryocoolers: the state of the art and recent developments.,” *J. Phys. Condens. Matter*, vol. 21, no. 16, p. 164219, 2009.

[2] R. Lewis, Y. Wang, J. Cooper, M. M. Lin, V. M. Bright, Y. C. Lee, P. E. Bradley, R. Radebaugh, and M. L. Huber, “Micro Cryogenic Coolers for IR Imaging,” in *SPIE Defense, Security, and Sensing*, 2011, vol. 8012, p. 80122H–1–80122H–9.

[3] J. S. Yoon, J. W. Choi, and M. S. Kim, “Computational and experimental investigation on the performance characteristics of the micro gas compressor,” *Microelectron. Eng.*, vol. 86, no. 10, pp. 1975–1982, 2009.

[4] R. Lewis, C. J. Coolidge, P. J. Schroeder, V. M. Bright, and Y. C. Lee, “Fabrication, assembly, and testing of a MEMS-enabled micro gas compressor for a 4:1 pressure ratio,” *Sensors Actuators A Phys.*, vol. 190, pp. 84–89, Feb. 2013.

[5] R. Lewis and M. Huber, “Demonstration of an Integrated Micro Cryogenic Cooler and Minature Comressor for Cooling to 200 K,” pp. 1–6, 2011.

[6] M. Q. Gong, J. F. Wu, B. Yan, X. Zou, X. R. Zhuang, and Q. G. Hu, “Study on a miniature mixed-gases joule-thomson cooler driven by an oil-lubricated mini-compressor for 120 K temperature ranges,” *Phys. Procedia*, vol. 67, pp. 405–410, 2015.

[7] R. Radebaugh, “Microscale Heat Transfer At Low Temperatures,” in *Microscale Heat Transfer Fundamentals and Applications*, Springer, 2005, pp. 93–124.

[8] R. Radebaugh, P. Bradley, C. Coolidge, R. Lewis, and Y. C. Lee, “Design and Analysis of a 150 K Cascade Joule-Thomson Microcooler,” in *Cryocoolers*, 2014, vol. 18, pp. 377–388.

[9] J. S. Yoon, J. W. Choi, M. S. Kim, Y.-E. Yoo, and D.-S. Choi, “Studies on the performance characteristics and improvements of the piezoelectrically-driven micro gas compressors,” *Microelectron. Eng.*, vol. 86, no. 11, pp. 2297–2304, Nov. 2009.

[10] “Rix Industries SA-6 Compressor,” 2017. [Online]. Available: http://www.rixindustries.com/industrial-compressors/sa-6g%0A.

[11] “Rix Industries Microboost Compressor,” 2017. [Online]. Available: http://www.rixindustries.com/industrial-compressors/microboost%0A.

[12] “Aspen Mini-Compressor,” 2017. [Online]. Available: http://www.aspencompressor.com/Download Pdf/14-24-000XBrochure.pdf.

[13] L.-A. Liew, C. Lin, C. J. Coolidge, R. Lewis, and Y. C. Lee, “Silicon Chip-based Compressor for Joule-Thomson Micro-coolers Operating at 2:1 Pressure Ratio,” unpublished.

[14] W. A. Little, “Microminiature refrigeration,” *Rev. Sci. Instrum.*, vol. 55 (5), no. 1984, pp. 661–680, 1984.

[15] S. Garvey, S. Logan, R. Rowe, and W. A. Little, “Performance characteristics of a low-flow rate 25 mW, LN2 Joule-Thomson refrigerator fabricated by photolithographic means,” *Appl. Phys. Lett.*, vol. 42, no. 12, pp. 1048–1050, 1983.

[16] W. A. Little, “Microminiature refrigeration,” *AIP Conf. Proc.*, vol. 985, no. 2008, pp. 597–605, 2008.

[17] “MMR Technologies Joule Thomson Temperature Stages,” 2017. [Online]. Available: http://www.mmr-tech.com/PDFs/jThomson.pdf%0A.

[18] “Kryoz CryoLab MSG 75,” 2017. [Online]. Available: http://kryoz.nl/portfolio-item/cryolab-

msg/%0A.

[19] H. J. M. Brake and H. Rogalla, “All-Micromachined Joule-Thomson Cold Stage,” in *International Cryocooler Conference*, 2007, pp. 437–441.

[20] H. J. M. Ter Brake, J. F. Burger, H. J. Holland, and P. P. P. M. Lerou, “Micromachined cryogenic coolers for cooling low-temperature detectors and electronics,” *Proc. IEEE Sensors*, pp. 1352–1355, 2008.

[21] A. Widyaparaga, M. Kuwamoto, N. Sakoda, M. Kohno, and Y. Takata, “Theoretical and Experimental Study of a Flexible Wiretype Joule–Thomson Microrefrigerator for Use in Cryosurgery,” *J. Heat Transfer*, vol. 134, no. 2, pp. 20903-1-20903–7, 2012.

[22] A. Widyaparaga, M. Kuwamoto, A. Tanabe, N. Sakoda, H. Kubota, M. Kohno, and Y. Takata, “Study on a wire-type Joule Thomson microcooler with a concentric heat exchanger,” *Appl. Therm. Eng.*, vol. 30, no. 16, pp. 2563–2573, 2010.

[23] “Le Thenika Self Regulated Joule Thomson Cooler,” 2017. [Online]. Available: http://cryocoolers.eu/wp-content/uploads/2016/01/self-regulating-JT-cryogenic-cooler.pdf%0A.

[24] “Le Tehnika Dual Flow Joule Thomson Cooler,” 2017. [Online]. Available: http://cryocoolers.eu/wp-content/uploads/2016/04/Epp-JTDB-520-L55-5W-v1.pdf%0A.

[25] M. H. Lin, P. E. Bradley, H. J. Wu, J. C. Booth, R. Radebaugh, and Y. C. Lee, “Design, fabrication, and assembly of a hollow-core fiber-based micro cryogenic cooler,” *TRANSDUCERS 2009 - 15th Int. Conf. Solid-State Sensors, Actuators Microsystems*, pp. 1114–1117, 2009.

[26] Y. D. Wang, R. Lewis, M. H. Lin, R. Radebaugh, and Y. C. Lee, “Wafer-level processing for polymer-based planar micro cryogenic coolers,” *Proc. IEEE Int. Conf. Micro Electro Mech. Syst.*, no.

February, pp. 341–344, 2012.

[27] Y. Wang, R. Lewis, M. M. H. Lin, R. Radebaugh, and Y. C. Lee, “The development of polymer-based planar microcryogenic coolers,” *J. Microelectromechanical Syst.*, vol. 22, no. 1, pp. 244–252, 2013.

[28] Y. Wang and R. Lewis, “A monolithic polyimide micro cryogenic cooler,” in *Solid-State Sensors, Actuators and Microsystems (TRANSDUCERS & EUROSENSORS XXVII)*, 2013, no. June, pp. 1903–1906.

[29] R. Lewis, Y. Wang, H. Schneider, Y. C. Lee, and R. Radebaugh, “Study of mixed refrigerant undergoing pulsating flow in micro coolers with pre-cooling,” *Cryogenics (Guildf).*, vol. 57, pp. 140–149, 2013.

[30] R. Radebaugh, “Thermodynamic analysis of cascade microcryocoolers with low pressure ratios,” in *Advances in Cryogenic Engineering*, 2014, vol. 132, pp. 132–141.

[31] H. S. Cao, A. V. Mudaliar, J. H. Derking, P. P. P. M. Lerou, H. J. Holland, D. R. Zalewski, S. Vanapalli, and H. J. M. Ter Brake, “Design and optimization of a two-stage 28 K Joule-Thomson microcooler,” *Cryogenics (Guildf).*, vol. 52, no. 1, pp. 51–57, 2012.

[32] H. S. Cao, H. J. Holland, C. H. Vermeer, S. Vanapalli, P. P. P. M. Lerou, M. Blom, and H. J. M. Ter Brake, “Characterization of a two-stage 30 K Joule–Thomson microcooler,” *J. Micromechanics Microengineering*, vol. 23, no. 6, p. 65022, 2013.

[33] H. S. Cao, S. Vanapalli, H. J. Holland, C. H. Vermeer, and H. J. M. ter Brake, “A micromachined Joule–Thomson cryogenic cooler with parallel two-stage expansion,” *Int. J. Refrig.*, vol. 69, pp. 222–231, 2016.

[34] H. S. Cao, S. Vanapalli, H. J. Holland, C. H. Vermeer, and H. J. M. Ter Brake, “Characterization of a thermoelectric/Joule-Thomson hybrid microcooler,” *Cryogenics (Guildf).*, vol. 77, pp. 36–42, 2016.

[35] M.-H. Lin, P. E. Bradley, M. L. Huber, R. Lewis, R. Radebaugh, and Y. C. Lee, “Mixed refrigerants for a glass capillary micro cryogenic cooler,” *Cryogenics (Guildf).*, vol. 50, no. 8, pp. 439–442, Aug. 2010.

[36] Y. Wang, M. Lin, R. Lewis, Y. Yan, R. Radebaugh, P. Bradley, and Y. C. Lee, “A Polyimide Micro Heat Exchanger with a Suspended 3D Parallel Channel Structure for Cryogenic Application,” in *ASME 2011 International Mechanical Engineering Congress & Exposition (IMECE2011), November 11-17, 2011, Denver, Colorado, USA*, p. 1–6 Paper# 62513.

[37] B. Shaoi, L. Wang, J. Li, and Z. Sun, “Application of thermal resistance network model in optimization design of micro-channel cooling heat sink,” *Int. J. Numer. Methods Heat Fluid Flow*, vol. 19, no. 3/4, pp. 535–545, 2009.

[38] Y. A. Cengel, *Heat And Mass Transcer: A Practical Approach*, 3rd Editio. New York, NY: McGraw-Hill, 2007.

[39] A. E. Dukler, M. Wicks, and R. G. Cleveland, “Frictional pressure drop in two-phase flow. Part-A: A comparison of existing correlations for pressure loss and holdups, and Part-B: An approach through similarity analysis,” *AIChE J.*, vol. 10, no. 1, pp. 38–51, 1964.

[40] M. National Institute of Standards and Technology, Gaithersberg, “NIST Reference Fluid Thermodynamic and Transport Properties Database (REFPROP): Version 9.1.” 2016.

[41] M. K. Ghosh and K. L. Mittal, Eds., *Polyimide Fundamentals and Applications*. New York, NY: Marcel Dekker, Inc., 1996.

[42] X. Tu and P. S. Hrnjak, “Flow and Heat Transfer in Microchannels 30 to 300 Microns in Hydraulic Diameter,” *Air Cond. Refrig. Center. Coll. Eng. Univ. Illinois Urbana-Champaign.*, vol. 61801, no. 217, 2004.

[43] Y. A. Cengel and M. A. Boles, *Thermodynamcs: An Engineering Approach*, 6th Editio. New York, NY: McGraw-Hill, 2008.

Appendix A: List of Publications Related to This Thesis

[1] R. Lewis, **C. J. Coolidge**, P. J. Schroeder, V. M. Bright, and Y. C. Lee, "Fabrication, assembly, and testing of a MEMS-enabled micro gas compressor for a 4:1 pressure ratio," *Sensors Actuators A Phys.*, vol. 190, pp. 84–89, Feb. 2013.

[2] R. Radebaugh, P. Bradley, **C. Coolidge**, R. Lewis, and Y. C. Lee, "Design and Analysis of a 150 K Cascade Joule-Thomson Microcooler," in *Cryocoolers*, 2014, vol. 18, pp. 377–388.

[3] R. Lewis, S. Xu, L. A. Liew, **C. Coolidge**, R. Yang, and Y. C. Lee, "Thin Flexible Thermal Ground Planes: Fabrication and Scaling Characterization," *J. Microelectromechanical Syst.*, vol. 24, no. 6, pp. 2040–2048, 2015.

[4] R. Lewis, Y. Wang, P. Schroeder, **C. Coolidge**, R. Radebaugh, and Y. C. Lee, "Micro Cryogenic Coolers With Mixed Refrigerants," in *Volume 1: Advanced Packaging; Emerging Technologies; Modeling and Simulation; Multi-Physics Based Reliability; MEMS and NEMS; Materials and Processes*, 2013, p. V001T06A005.

Future Publications

[5] **C. Coolidge**, R. Radebaugh, R. Lewis, L. Liew, and Y. C. Lee, "Low Pressure Ratio Three Stage Cascaded Joule-Thomson Cryogenic Cooler." Unpublished, In Preparation for *Cryogenics*

[6] **C. Coolidge**, R. Radebaugh, R. Lewis, L. Liew, P. E. Bradley, and Y. C. Lee, "The Development of a Polyimide Based Joule-Thomson Coldstage For Low Pressure Ratio Single Refrigerants." Unpublished, In Preparation for *IEEE/ASME J. of MEMS*

[7] **C. Coolidge**, L. Liew, R. Radebaugh, R. Lewis, and Y. C. Lee, "Glass Capillary Based Joule-Thomson Coldstage for Low Pressure and Low Flow Rate Applications." Unpublished, In Preparation for *J. of MEMS* or *J. of Micromechanics and Microengineering*

[8] L.-A. Liew, C. Lin, **C. J. Coolidge**, R. Lewis, and Y. C. Lee, "Silicon Chip-based Compressor for Joule-Thomson Micro-coolers Operating at 2:1 Pressure Ratio." Unpublished, In Preparation for *J. of MEMS* or *J. of Micromechanics and Microengineering*

Appendix B: Fluid Properties from the NIST REFPROP Program

The following tables contain the fluid properties used to calculate the two phase expansion for n-butane, isobutane, propane, and R116

Table B-1: n-Butane properties used for two phase expansion across JT restriction

Pressure (Mpa)	Temperature (K)	Quality	Liquid Density (kmol/m^3)	Vapor Density (kmol/m^3)	Liquid Viscosity (µPa-s)	Vapor Viscosity (µPa-s)
0.1	272.31	0.2545	10.351	0.046045	204.22	6.748
0.11	274.84	0.22905	10.304	0.050332	199.03	6.8094
0.12	277.2	0.2036	10.26	0.054598	194.35	6.8668
0.13	279.4	0.17815	10.219	0.058845	190.1	6.9207
0.14	281.48	0.1527	10.18	0.063077	186.21	6.9716
0.15	283.45	0.12725	10.142	0.067294	182.62	7.02
0.16	285.32	0.1018	10.107	0.071499	179.29	7.0661
0.17	287.1	0.07635	10.072	0.075693	176.19	7.1102
0.18	288.8	0.0509	10.04	0.079877	173.3	7.1525
0.19	290.43	0.02545	10.008	0.084052	170.58	7.1933
0.2	291.99	0	9.9774	0.08822	168.02	7.2325

Table B-2: Isobutane properties used for two phase expansion across JT restriction

Pressure (Mpa)	Temperature (K)	Quality	Liquid Density (kmol/m^3)	Vapor Density (kmol/m^3)	Liquid Viscosity (µPa-s)	Vapor Viscosity (µPa-s)
0.1	261.07	0.2484	10.223	0.048038	228.69	6.571
0.11	263.52	0.23484	10.176	0.052508	222.09	6.6302
0.12	265.8	0.22199	10.132	0.056955	216.18	6.6855
0.13	267.95	0.20975	10.091	0.061383	210.83	6.7375
0.14	269.97	0.19805	10.051	0.065794	205.95	6.7865
0.15	271.88	0.18682	10.014	0.070191	201.47	6.8331
0.16	273.69	0.17599	9.9782	0.074574	197.34	6.8775
0.17	275.42	0.16554	9.9439	0.078947	193.51	6.9199
0.18	277.08	0.15542	9.9109	0.083308	189.93	6.9605
0.19	278.66	0.1456	9.8792	0.087661	186.59	6.9997
0.2	280.19	0.13605	9.8485	0.092006	183.45	7.0374
0.21	281.65	0.12675	9.8189	0.096345	180.5	7.0738
0.22	283.06	0.11768	9.7901	0.10068	177.71	7.1091
0.23	284.43	0.10881	9.7622	0.105	175.07	7.1433
0.24	285.75	0.10014	9.7351	0.10933	172.56	7.1765
0.25	287.03	0.091647	9.7087	0.11364	170.17	7.2088
0.26	288.27	0.08332	9.683	0.11796	167.9	7.2403
0.27	289.48	0.075148	9.6579	0.12227	165.73	7.2711
0.28	290.65	0.067119	9.6334	0.12658	163.65	7.3011
0.29	291.79	0.059225	9.6094	0.13089	161.66	7.3304
0.3	292.91	0.051458	9.586	0.1352	159.75	7.3591
0.31	293.99	0.043809	9.563	0.1395	157.92	7.3873
0.32	295.05	0.036272	9.5405	0.14381	156.15	7.4149
0.33	296.08	0.028839	9.5184	0.14811	154.45	7.442
0.34	297.1	0.021506	9.4967	0.15242	152.81	7.4686
0.35	298.08	0.014266	9.4754	0.15672	151.23	7.4947
0.36	299.05	0.007115	9.4545	0.16103	149.7	7.5204

0.37	300	4.81E-05	9.4339	0.16534	148.22	7.5458
0.38	300	0	9.4342	NA	148.24	NA
0.39	300	0	9.4346	NA	148.27	NA
0.4	300	0	9.4351	NA	148.3	NA

Table B-3: Propane properties used for two phase expansion across JT restriction

Pressure (Mpa)	Temperature (K)	Quality	Liquid Density (kmol/m^3)	Vapor Density (kmol/m^3)	Liquid Viscosity (µPa-s)	Vapor Viscosity (µPa-s)
0.1	230.74	0.16545	13.181	0.054127	197.89	6.301
0.11	232.92	0.15477	13.124	0.059142	193.06	6.357
0.12	234.94	0.14466	13.07	0.06413	188.7	6.4093
0.13	236.85	0.13506	13.02	0.069093	184.73	6.4583
0.14	238.64	0.1259	12.972	0.074034	181.09	6.5047
0.15	240.33	0.11712	12.926	0.078957	177.73	6.5487
0.16	241.94	0.10867	12.883	0.083862	174.62	6.5906
0.17	243.48	0.10053	12.841	0.088752	171.71	6.6307
0.18	244.94	0.092658	12.801	0.093628	168.99	6.6691
0.19	246.35	0.08503	12.763	0.098491	166.43	6.7061
0.2	247.7	0.077623	12.726	0.10334	164.02	6.7417
0.21	249	0.070419	12.69	0.10819	161.75	6.776
0.22	250.25	0.0634	12.655	0.11302	159.59	6.8093
0.23	251.46	0.056551	12.621	0.11784	157.53	6.8416
0.24	252.63	0.04986	12.588	0.12266	155.58	6.8729
0.25	253.77	0.043314	12.556	0.12747	153.72	6.9033
0.26	254.87	0.036904	12.525	0.13227	151.93	6.933
0.27	255.94	0.03062	12.495	0.13707	150.22	6.9619
0.28	256.98	0.024453	12.465	0.14187	148.58	6.9902
0.29	257.99	0.018397	12.436	0.14666	147.01	7.0177
0.3	258.97	0.012443	12.408	0.15144	145.49	7.0447
0.31	259.94	0.006587	12.38	0.15623	144.04	7.0711
0.32	260.87	0.000822	12.353	0.16101	142.63	7.097
0.33	261	0	12.327	NA	141.27	NA
0.34	261	0	12.3	NA	139.95	NA
0.35	261	0	12.275	NA	138.68	NA

Table B-4: R116 properties used for two phase expansion across JT restriction

Pressure (Mpa)	Temperature (K)	Quality	Liquid Density ($kmol/m^3$)	Vapor Density ($kmol/m^3$)	Liquid Viscosity (µPa-s)	Vapor Viscosity (µPa-s)
0.12	198.27	0.26945	11.525	0.076694	379.95	9.1577
0.13	199.83	0.25812	11.475	0.082694	370.41	9.2239
0.14	201.3	0.24729	11.426	0.088676	361.71	9.2865
0.15	202.69	0.23689	11.38	0.094641	353.72	9.3458
0.16	204.01	0.22687	11.337	0.10059	346.34	9.4023
0.17	205.27	0.21719	11.294	0.10653	339.49	9.4563
0.18	206.47	0.20782	11.254	0.11246	333.1	9.5082
0.19	207.62	0.19873	11.215	0.11838	327.12	9.558
0.2	208.73	0.18988	11.177	0.1243	321.5	9.6061
0.21	209.8	0.18126	11.141	0.13021	316.2	9.6526
0.22	210.83	0.17286	11.105	0.13611	311.19	9.6977
0.23	211.82	0.16464	11.071	0.14201	306.44	9.7414
0.24	212.78	0.15661	11.037	0.14791	301.92	9.784
0.25	213.71	0.14873	11.005	0.1538	297.62	9.8254
0.26	214.61	0.14101	10.973	0.15969	293.52	9.8658
0.27	215.49	0.13343	10.942	0.16559	289.6	9.9053
0.28	216.34	0.12598	10.911	0.17148	285.85	9.9439
0.29	217.17	0.11865	10.882	0.17738	282.24	9.9817
0.3	217.98	0.11144	10.853	0.18327	278.78	10.019
0.31	218.77	0.10433	10.824	0.18917	275.46	10.055
0.32	219.54	0.097329	10.796	0.19507	272.25	10.091
0.33	220.29	0.090421	10.769	0.20098	269.16	10.126
0.34	221.02	0.083601	10.742	0.20689	266.17	10.16
0.35	221.74	0.076867	10.715	0.2128	263.29	10.195
0.36	222.45	0.070211	10.689	0.21871	260.49	10.228
0.37	223.13	0.063631	10.664	0.22464	257.79	10.261
0.38	223.81	0.057122	10.639	0.23056	255.17	10.294

0.39	224.47	0.050681	10.614	0.2365	252.63	10.326
0.4	225.12	0.044303	10.589	0.24243	250.16	10.358
0.41	225.76	0.037986	10.565	0.24838	247.76	10.389
0.42	226.38	0.031726	10.541	0.25433	245.42	10.421
0.43	227	0.025521	10.518	0.26029	243.15	10.451
0.44	227.6	0.019367	10.495	0.26626	240.94	10.482
0.45	228.19	0.013263	10.472	0.27223	238.79	10.512
0.46	228.78	0.007206	10.449	0.27821	236.69	10.542
0.47	229.35	0.001193	10.427	0.2842	234.64	10.572

Appendix C: Calculation of Kapton Tube-In-Tube Heat Exchanger

The following calculations were run by Dr. Ray Radebaugh to calculate the heat exchange area required for the inter-stage Kapton tube-in-tube heat exchangers using the correlation developed by Tu and Hrnjak [42].

Evaporation heat transfer in microchannels based on Tu and Hrnjak correlation										
X. Tu and P.S. Hrnjak, "Flow and heat transfer in microchannels 30 to 300 microns in hydraulic diamter," ACRC CR-53, January 2004, University of Illinois										
Dryout parameter: $U_{LS} = G(1-x)/\rho_l$										
	G=mass flux; x=quality; ρ_l = liquid density									
Valid for R134a at 25 °C										
For $U_{LS} \geq 0.039$:										
$h_{tp} = 0.985*\phi_l^{1.719}*h_l + h_{pb}$										
	$\phi_l^2 = 1 + C/X + 1/X^2$									
		X = Martinelli parameter = $[(dP/dz)F_l/(dP/dz)F_v]^{1/2}$								
			$(dP/dz)F_l = f_l(1/D_h)[(G^2(1-x)^2/2\rho_l]$							
			$(dP/dz)F_v = f_v(1/D_h)[(G^2x^2/2\rho_v]$							
				f = Darcy friction factor = 4*Fanning friction factor						
				D_h = hydraulic diameter						
		$C = 1.279x10^{-9}\lambda^{-1.96}\psi Re_{lo}^{0.40}$			$We_{GS} \leq 11.0We_{LS}^{0.14}$		We_{GS} = Weber # = $U_{GS}^2 D_h \rho_v/\sigma$			
		$C = 1.386x10^{-4}\lambda^{-0.65}\psi^{0.2}Re_{lo}^{0.52}$			$We_{GS} > 11.0We_{LS}^{0.14}$		$We_{LS} = U_{LS}^2 D_h \rho_l/\sigma$			
			$\lambda = kT_g/h$	2.2334E+28		$\psi = \mu_l U_B/\sigma$	0.00011084		C=	4.9047E-69
			$k = 5.670x10^{-8}$ W/(m^2-K^4)			μ_l = liquid viscosity				
			$h = 6.6261x10^{-34}$ m^2-kg/s			U_B = bubble velocity = $1.2(U_{GS} + U_{LS})$				
						σ = surface tension (N/m)				
	h_{pb} = Groenflo correlation = $h_0 F_{PF} (q/q_0)^{nf} (Ra/Ra_0)^{0.133}$									
		$F_{PF} = 1.2P_r^{0.27} + 2.5P_r$		h_0 = 4,500 W/m^2-K						
		$nf = 0.9 - 0.3P_r^{0.3}$		q_0 = 20,000 W/m^2						
		$P_r = P/P_{crit}$		Ra_0 = 0.40 μm						
	$h_l = k_l Nu/2t_g$	9240								
For $U_{LS} < 0.039$										
$h_{tp} = 18.42Co^{1.356}\phi_{l,x=crit}^{1.719}h_l + [(x - x_{crit})/(1 - x_{crit})]h_v$										
	$Co = [(1 - x)/x]^{0.8}(\rho_v/\rho_l)^{0.5}$									

Figure C-1: Correlation equations for two-phase evaporative heat transfer used by Dr. Ray Radebaugh from Tu and Hrnjak [42].

Table C-1: Properties of isobutane used in the two-phase heat transfer coefficient calculations.

Inputs:			
Molecular weight	kg/mol	M	0.058122
Vapor density	(kg/m^3)	ρ_v	2.792
Liquid density	(kg/m^3)	ρ_L	594.19
Heat flux	(W/m^2)	q	1.00E+04
Flow rate	mol/s	n	2.03E-05
Latent heat	(J/kg)	h_{fg}	3.65E+05
Vapor therm cond	(W/m-K)	k_v	1.32E-02
Liquid therm cond	(W/m-K)	k_L	1.03E-01
Nusselt number		Nu	5.00E+00
Gap thickness	(m)	t_g	1.00E-05
Width	(m)	w	5.00E-03
Length	(m)	L	8.00E-03
vapor viscosity	Pa-s	μv	7.31E-06
Liquid viscosity	Pa-s	μL	4.47E-05
vapor specific heat	(J/kg-K)	Cpv	1.54E+03
liquid specific heat	(J/kg-K)	CpL	2.22E+03
Liquid Prandlt number		PrL	4.91E+00
Surface tension	(N/m)	σ	0.01448
Critical quality		xcrit	2.00E-01

Calculations:			
Liquid heat transfer	(W/m^2-K)	h_l	25750
Mass flux	(kg/m^2-s)	G	23.597532
Vapor molar density	(mol/m^3)	Dmv	48.03688793
Liquid molar density	(mol/m^3)	DmL	10223.1513
Liquid Reynolds #		ReL	10.55581839
Boiling number		Bo	0.6458
Weber number (liq)		We	0.001294402
Flow parameter		C	
Gas heat transfer	(W/m^2-K)	h_g	3292.5

Table C-2: Calculated two-phase heat transfer coefficient for isobutane with varied quality in a 100 μm gap.

Quality	Dryout Parameter	Martinelli #				Two Phase Heat Transfer Coefficient
x	U_{LS}	*Co*	X^2	ϕ^2	$\phi^{1.719}$	h_{tp} (W/m^2-s)
0.000001	0.039714	4325.085	2.8731E+10	1	1	1.09104E+11
0.05	0.037728	0.722766	10.3720778	1.096413	1.082325	823960.7651
0.1	0.035742	0.397548	2.32725291	1.429691	1.359661	366196.6325
0.15	0.033757	0.274573	0.92260095	2.083892	1.879634	221741.458
0.2	0.031771	0.207799	0.45970428	3.175311	2.699513	152108.8816
0.25	0.029785	0.165079	0.25858366	4.86722	3.896889	111538.0429
0.3	0.0278	0.135013	0.15642715	7.392752	5.581345	85177.44957
0.35	0.025814	0.112479	0.09909442	11.09139	7.909796	66790.71937
0.4	0.023828	0.094813	0.06464591	16.46888	11.11022	53311.56826
0.45	0.021843	0.080485	0.04291992	24.2992	15.52088	43060.9401
0.5	0.019857	0.068548	0.02873152	35.80498	21.6578	35044.27675
0.55	0.017871	0.058381	0.0192335	52.99263	30.33634	28636.11503
0.6	0.015886	0.049559	0.01276956	#VALUE!	#VALUE!	23424.15489
0.65	0.0139	0.041775	0.00833044	#VALUE!	#VALUE!	19126.17382
0.7	0.011914	0.034803	0.00527722	190.4938	91.10823	15543.05243
0.75	0.009928	0.028464	0.00319239	1149.537	427.0902	12530.95299
0.8	0.007943	0.022612	0.00179572	1114.741	415.9548	9984.309782
0.85	0.005957	0.017113	0.00089475	1644.552	581.0223	7825.426777
0.9	0.003971	0.01182	0.00035471	3446.673	1097.477	5998.948337
0.95	0.001986	0.006501	7.9589E-05	13623.64	3576.225	4472.989271
0.999999	3.97E-08	1.09E-06	2.8732E-14	3.48E+13	4.36E+11	3292.506361

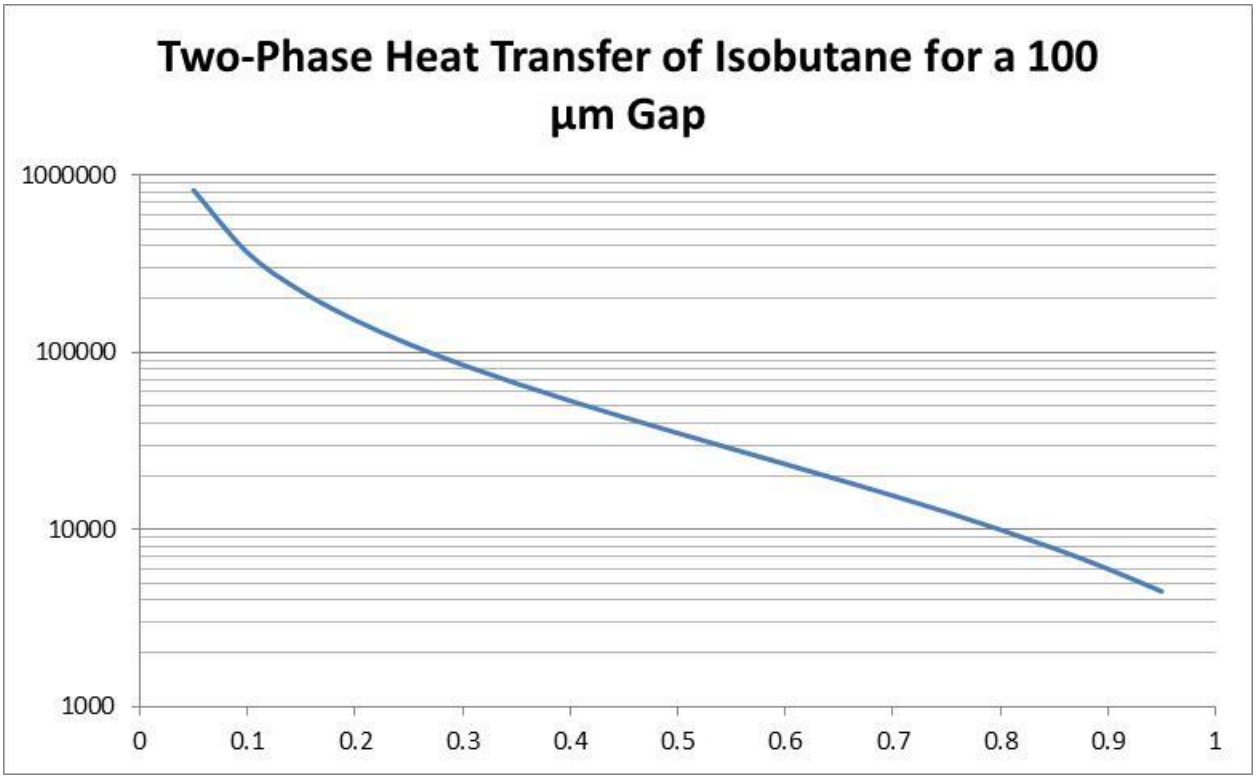

Figure C-2: Plot of the two-phase heat transfer coefficient for isobutane as a function of quality in a 100 µm gap.

Table C-3: Calculated two-phase heat transfer coefficient for isobutane of quality 0.5 with varied gap thickness.

Gap Thickness	Mass Flux	Dryout Parameter	Martinelli #				Two Phase Heat Transfer Coefficient
t_g (m)	G	U_{LS}	*Co*	X^2	ϕ^2	$\phi^{1.719}$	h_{tp} (W/m^2-s)
5.00E-06	4.72E+01	3.97E-02	6.85E-02	2.87E-02	3.58E+01	2.17E+01	7.01E+04
1.00E-05	2.36E+01	1.99E-02	6.85E-02	2.87E-02	3.58E+01	2.17E+01	3.50E+04
1.50E-05	1.57E+01	1.32E-02	6.85E-02	2.87E-02	3.58E+01	2.17E+01	2.34E+04
2.00E-05	1.18E+01	9.93E-03	6.85E-02	2.87E-02	3.58E+01	2.17E+01	1.75E+04
2.50E-05	9.44E+00	7.94E-03	6.85E-02	2.87E-02	3.58E+01	2.17E+01	1.40E+04
3.00E-05	7.87E+00	6.62E-03	6.85E-02	2.87E-02	3.58E+01	2.17E+01	1.17E+04
3.50E-05	6.74E+00	5.67E-03	6.85E-02	2.87E-02	3.58E+01	2.17E+01	1.00E+04
4.00E-05	5.90E+00	4.96E-03	6.85E-02	2.87E-02	3.58E+01	2.17E+01	8.76E+03
4.50E-05	5.24E+00	4.41E-03	6.85E-02	2.87E-02	3.58E+01	2.17E+01	7.79E+03
5.00E-05	4.72E+00	3.97E-03	6.85E-02	2.87E-02	3.58E+01	2.17E+01	7.01E+03
5.50E-05	4.29E+00	3.61E-03	6.85E-02	2.87E-02	3.58E+01	2.17E+01	6.37E+03
6.00E-05	3.93E+00	3.31E-03	6.85E-02	2.87E-02	3.58E+01	2.17E+01	5.84E+03
6.50E-05	3.63E+00	3.05E-03	6.85E-02	2.87E-02	3.58E+01	2.17E+01	5.39E+03
7.00E-05	3.37E+00	2.84E-03	6.85E-02	2.87E-02	3.58E+01	2.17E+01	5.01E+03
7.50E-05	3.15E+00	2.65E-03	6.85E-02	2.87E-02	3.58E+01	2.17E+01	4.67E+03
8.00E-05	2.95E+00	2.48E-03	6.85E-02	2.87E-02	3.58E+01	2.17E+01	4.38E+03
8.50E-05	2.78E+00	2.34E-03	6.85E-02	2.87E-02	3.58E+01	2.17E+01	4.12E+03
9.00E-05	2.62E+00	2.21E-03	6.85E-02	2.87E-02	3.58E+01	2.17E+01	3.89E+03
9.50E-05	2.48E+00	2.09E-03	6.85E-02	2.87E-02	3.58E+01	2.17E+01	3.69E+03
1.00E-04	2.36E+00	1.99E-03	6.85E-02	2.87E-02	3.58E+01	2.17E+01	3.50E+03
1.05E-04	2.25E+00	1.89E-03	6.85E-02	2.87E-02	3.58E+01	2.17E+01	3.34E+03
1.10E-04	2.15E+00	1.81E-03	6.85E-02	2.87E-02	7.56E+01	4.12E+01	3.19E+03
1.15E-04	2.05E+00	1.73E-03	6.85E-02	2.87E-02	7.06E+01	3.88E+01	3.05E+03
1.20E-04	1.97E+00	1.65E-03	6.85E-02	2.87E-02	3.58E+01	2.17E+01	2.92E+03
1.25E-04	1.89E+00	1.59E-03	6.85E-02	2.87E-02	3.58E+01	2.17E+01	2.80E+03
1.30E-04	1.82E+00	1.53E-03	6.85E-02	2.87E-02	3.58E+01	2.17E+01	2.70E+03
1.35E-04	1.75E+00	1.47E-03	6.85E-02	2.87E-02	3.58E+01	2.17E+01	2.60E+03
1.40E-04	1.69E+00	1.42E-03	6.85E-02	2.87E-02	3.58E+01	2.17E+01	2.50E+03
1.45E-04	1.63E+00	1.37E-03	6.85E-02	2.87E-02	5.57E+01	3.17E+01	2.42E+03
1.50E-04	1.57E+00	1.32E-03	6.85E-02	2.87E-02	5.44E+01	3.10E+01	2.34E+03

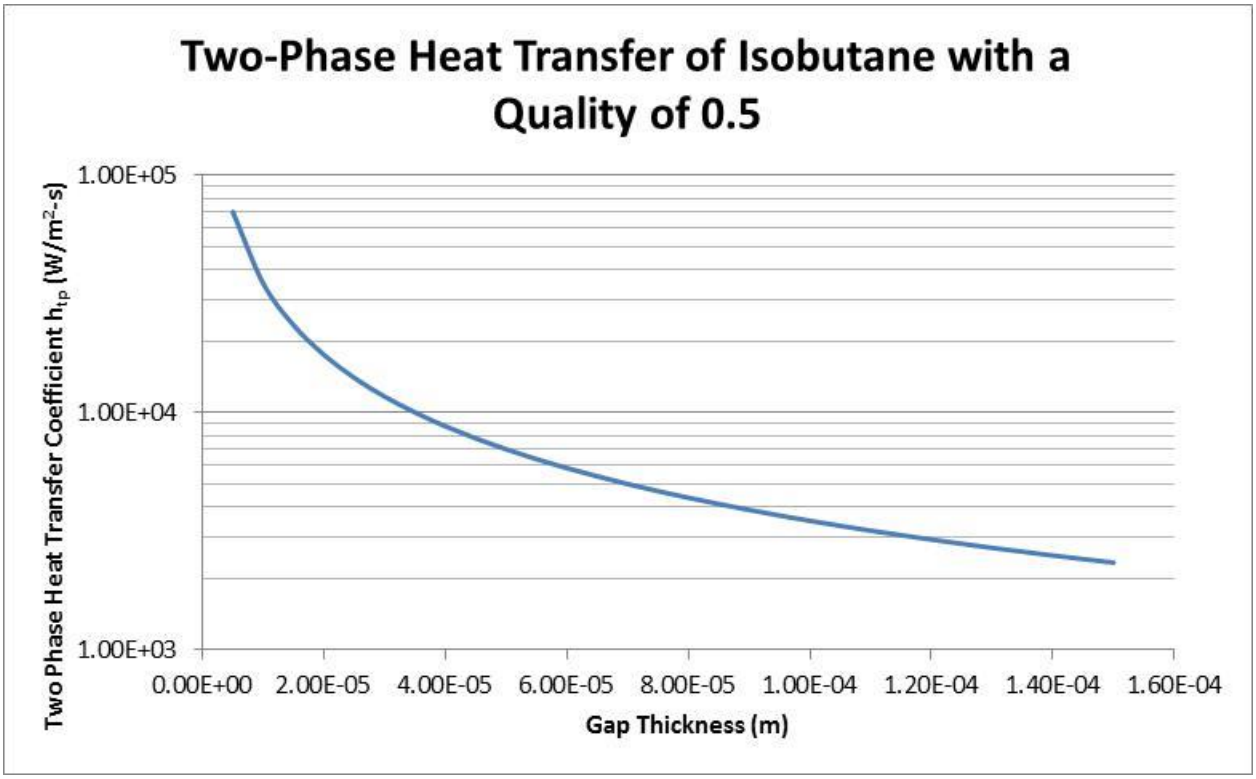

Figure C-3: Plot of the two-phase heat transfer coefficient for isobutane of quality 0.5 as a function of gap thickness.

Table C-4: Properties of propane used in the two-phase heat transfer coefficient calculations.

Inputs:			
Molecular weight	kg/mol	M	0.044096
Vapor density	(kg/m^3)	ρ_v	2.3868
Liquid density	(kg/m^3)	ρ_L	581.23
Heat flux	(W/m^2)	q	1.00E+04
Flow rate	mol/s	n	2.03E-05
Latent heat	(J/kg)	h_{fg}	4.26E+05
Vapor therm cond	(W/m-K)	k_v	1.15E-02
Liquid therm cond	(W/m-K)	k_L	1.29E-01
Nusselt number		Nu	5.00E+00
Gap thickness	(m)	t_g	1.00E-04
Width	(m)	w	5.00E-03
Length	(m)	L	8.00E-03
vapor viscosity	Pa-s	μv	6.30E-06
Liquid viscosity	Pa-s	μL	1.98E-04
vapor specific heat	(J/kg-K)	Cpv	1.44E+03
liquid specific heat	(J/kg-K)	CpL	2.24E+03
Liquid Prandlt number		PrL	3.43E+00
Surface tension	(N/m)	σ	0.015712
Critical quality		xcrit	2.00E-01
Calculations:			
Liquid heat transfer	(W/m^2-K)	h_l	9240
Mass flux	(kg/m^2-s)	G	5.115136
Vapor molar density	(mol/m^3)	Dmv	54.12735849
Liquid molar density	(mol/m^3)	DmL	13181.01415
Liquid Reynolds #		ReL	1.809386629
Boiling number		Bo	0.120101808
Weber number (liq)		We	0.000200555
Gas heat transfer	(W/m^2-K)	h_g	824.4285714

Table C-5: Calculated two-phase heat transfer coefficient for propane with varied quality in a 100 µm gap.

Quality	Dryout Parameter	Martinelli #				Two Phase Heat Transfer Coefficient
x	U_{LS}	*Co*	X^2	ϕ^2	$\phi^{1.719}$	h_{tp} (W/m^2-s)
0.000001	3.08E-03	4.04E+03	1.29E+11	1.00E+00	1.00E+00	1.25E+10
0.05	2.93E-03	6.76E-01	4.66E+01	1.02E+00	1.02E+00	9.45E+04
0.1	2.77E-03	3.72E-01	1.04E+01	1.10E+00	1.08E+00	4.20E+04
0.15	2.62E-03	2.57E-01	4.14E+00	1.24E+00	1.20E+00	2.54E+04
0.2	2.46E-03	1.94E-01	2.06E+00	1.48E+00	1.40E+00	1.74E+04
0.25	2.31E-03	1.54E-01	1.16E+00	1.86E+00	1.71E+00	1.28E+04
0.3	2.16E-03	1.26E-01	7.02E-01	2.42E+00	2.14E+00	9.75E+03
0.35	2.00E-03	1.05E-01	4.45E-01	3.25E+00	2.75E+00	7.64E+03
0.4	1.85E-03	8.86E-02	2.90E-01	4.45E+00	3.61E+00	6.09E+03
0.45	1.69E-03	7.52E-02	1.93E-01	6.19E+00	4.79E+00	4.91E+03
0.5	1.54E-03	6.41E-02	1.29E-01	8.75E+00	6.45E+00	3.98E+03
0.55	1.39E-03	5.46E-02	8.63E-02	1.26E+01	8.82E+00	3.24E+03
0.6	1.23E-03	4.63E-02	5.73E-02	1.84E+01	1.22E+01	2.64E+03
0.65	1.08E-03	3.91E-02	3.74E-02	2.77E+01	1.74E+01	2.14E+03
0.7	9.24E-04	3.25E-02	2.37E-02	4.32E+01	2.55E+01	1.73E+03
0.75	7.70E-04	2.66E-02	1.43E-02	7.08E+01	3.89E+01	1.38E+03
0.8	6.16E-04	2.11E-02	8.06E-03	1.25E+02	6.35E+01	1.08E+03
0.85	4.62E-04	1.60E-02	4.02E-03	2.50E+02	1.15E+02	8.25E+02
0.9	3.08E-04	1.10E-02	1.59E-03	6.29E+02	2.54E+02	6.10E+02
0.95	1.54E-04	6.08E-03	3.57E-04	2.80E+03	9.18E+02	4.29E+02
0.999999	3.08E-09	1.02E-06	1.29E-13	7.75E+12	1.20E+11	2.89E+02

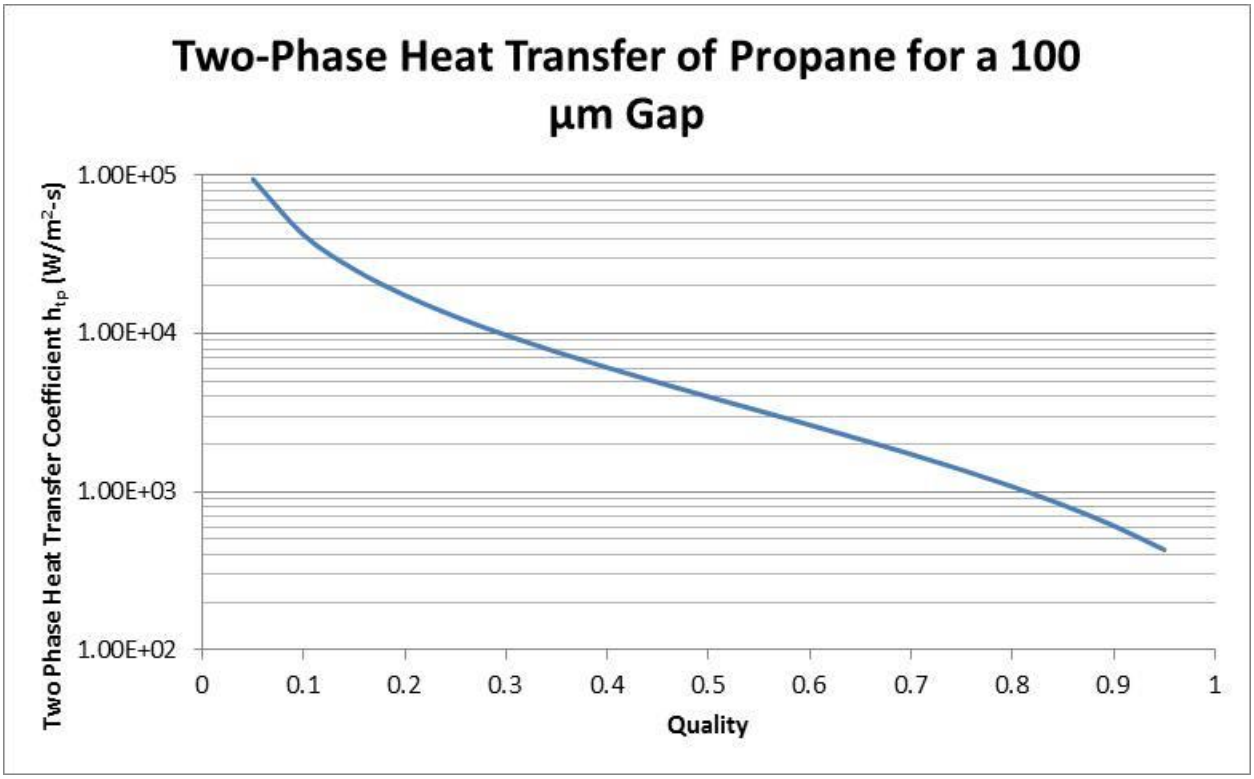

Figure C-4: Plot of the two-phase heat transfer coefficient for propane as a function of quality in a 100 µm gap.

Table C-6: Calculated two-phase heat transfer coefficient for propane of quality 0.5 with varied gap thickness.

Gap Thickness	Mass Flux	Dryout Parameter	Martinelli #				Two Phase Heat Transfer Coefficient
t_g (m)	G	U_{LS}	*Co*	X^2	ϕ^2	$\phi^{1.719}$	h_{tp} (W/m^2-s)
5.00E-06	3.58E+01	3.08E-02	6.41E-02	1.29E-01	8.75E+00	6.45E+00	7.97E+04
1.00E-05	1.79E+01	1.54E-02	6.41E-02	1.29E-01	8.75E+00	6.45E+00	3.98E+04
1.50E-05	1.19E+01	1.03E-02	6.41E-02	1.29E-01	8.75E+00	6.45E+00	2.66E+04
2.00E-05	8.95E+00	7.70E-03	6.41E-02	1.29E-01	8.75E+00	6.45E+00	1.99E+04
2.50E-05	7.16E+00	6.16E-03	6.41E-02	1.29E-01	8.75E+00	6.45E+00	1.59E+04
3.00E-05	5.97E+00	5.13E-03	6.41E-02	1.29E-01	8.75E+00	6.45E+00	1.33E+04
3.50E-05	5.12E+00	4.40E-03	6.41E-02	1.29E-01	8.75E+00	6.45E+00	1.14E+04
4.00E-05	4.48E+00	3.85E-03	6.41E-02	1.29E-01	8.75E+00	6.45E+00	9.96E+03
4.50E-05	3.98E+00	3.42E-03	6.41E-02	1.29E-01	8.75E+00	6.45E+00	8.85E+03
5.00E-05	3.58E+00	3.08E-03	6.41E-02	1.29E-01	8.75E+00	6.45E+00	7.97E+03
5.50E-05	3.26E+00	2.80E-03	6.41E-02	1.29E-01	8.75E+00	6.45E+00	7.24E+03
6.00E-05	2.98E+00	2.57E-03	6.41E-02	1.29E-01	8.75E+00	6.45E+00	6.64E+03
6.50E-05	2.75E+00	2.37E-03	6.41E-02	1.29E-01	8.75E+00	6.45E+00	6.13E+03
7.00E-05	2.56E+00	2.20E-03	6.41E-02	1.29E-01	8.75E+00	6.45E+00	5.69E+03
7.50E-05	2.39E+00	2.05E-03	6.41E-02	1.29E-01	8.75E+00	6.45E+00	5.31E+03
8.00E-05	2.24E+00	1.93E-03	6.41E-02	1.29E-01	8.75E+00	6.45E+00	4.98E+03
8.50E-05	2.11E+00	1.81E-03	6.41E-02	1.29E-01	8.75E+00	6.45E+00	4.69E+03
9.00E-05	1.99E+00	1.71E-03	6.41E-02	1.29E-01	8.75E+00	6.45E+00	4.43E+03
9.50E-05	1.88E+00	1.62E-03	6.41E-02	1.29E-01	8.75E+00	6.45E+00	4.19E+03
1.00E-04	1.79E+00	1.54E-03	6.41E-02	1.29E-01	8.75E+00	6.45E+00	3.98E+03
1.05E-04	1.71E+00	1.47E-03	6.41E-02	1.29E-01	8.75E+00	6.45E+00	3.79E+03
1.10E-04	1.63E+00	1.40E-03	6.41E-02	1.29E-01	2.30E+01	1.48E+01	3.62E+03
1.15E-04	1.56E+00	1.34E-03	6.41E-02	1.29E-01	2.12E+01	1.38E+01	3.46E+03
1.20E-04	1.49E+00	1.28E-03	6.41E-02	1.29E-01	8.75E+00	6.45E+00	3.32E+03
1.25E-04	1.43E+00	1.23E-03	6.41E-02	1.29E-01	8.75E+00	6.45E+00	3.19E+03
1.30E-04	1.38E+00	1.18E-03	6.41E-02	1.29E-01	8.75E+00	6.45E+00	3.06E+03
1.35E-04	1.33E+00	1.14E-03	6.41E-02	1.29E-01	8.75E+00	6.45E+00	2.95E+03
1.40E-04	1.28E+00	1.10E-03	6.41E-02	1.29E-01	8.75E+00	6.45E+00	2.85E+03
1.45E-04	1.23E+00	1.06E-03	6.41E-02	1.29E-01	1.59E+01	1.08E+01	2.75E+03
1.50E-04	1.19E+00	1.03E-03	6.41E-02	1.29E-01	1.54E+01	1.05E+01	2.66E+03

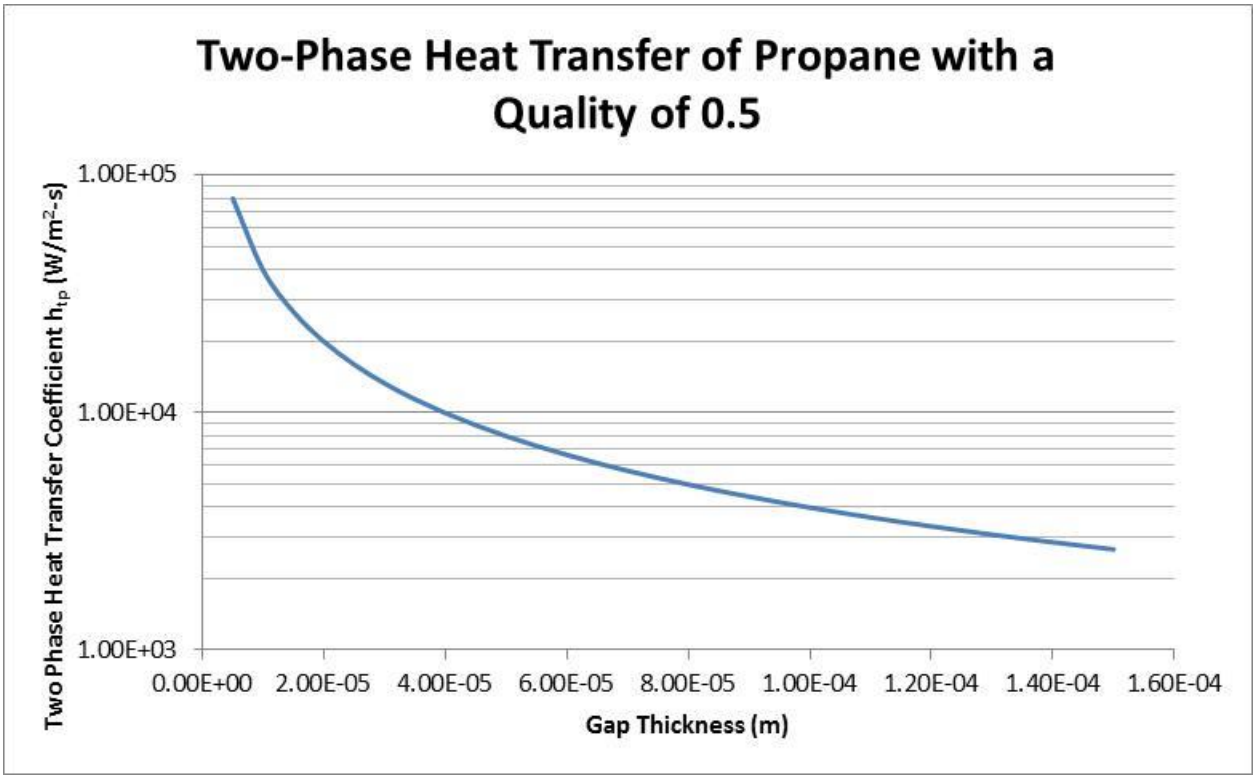

Figure C-5: Plot of the two-phase heat transfer coefficient for propane of quality 0.5 as a function of gap thickness.

Table C-7: Properties of R116 used in the two-phase heat transfer coefficient calculations.

Inputs:			
Molecular weight	kg/mol	M	0.13801
Vapor density	(kg/m^3)	ρ_v	8.9191
Liquid density	(kg/m^3)	ρ_L	1606
Heat flux	(W/m^2)	q	1.00E+04
Flow rate	mol/s	n	2.03E-05
Latent heat	(J/kg)	h_{fg}	1.17E+05
Vapor therm cond	(W/m-K)	k_v	5.39E-03
Liquid therm cond	(W/m-K)	k_L	7.69E-02
Nusselt number		Nu	5.00E+00
Gap thickness	(m)	t_g	1.00E-05
Width	(m)	w	5.00E-03
Length	(m)	L	8.00E-03
vapor viscosity	Pa-s	μv	9.01E-06
Liquid viscosity	Pa-s	μL	4.02E-04
vapor specific heat	(J/kg-K)	Cpv	6.13E+02
liquid specific heat	(J/kg-K)	CpL	9.41E+02
Liquid Prandlt number		PrL	4.92E+00
Surface tension	(N/m)	σ	0.011085
Critical quality		xcrit	2.00E-01
Calculations:			
Liquid heat transfer	(W/m^2-K)	h_l	19223.5
Mass flux	(kg/m^2-s)	G	56.03206
Vapor molar density	(mol/m^3)	Dmv	64.62647634
Liquid molar density	(mol/m^3)	DmL	11636.83791
Liquid Reynolds #		ReL	2.785932132
Boiling number		Bo	4.785383893
Weber number (liq)		We	0.003527134
Flow parameter		C	
Gas heat transfer	(W/m^2-K)	h_g	1347.6

Table C-8: Calculated two-phase heat transfer coefficient for R116 with varied quality in a 100 µm gap.

Quality	Dryout Parameter	Martinelli #				Two Phase Heat Transfer Coefficient
x	U_{LS}	*Co*	X^2	ϕ^2	$\phi^{1.719}$	h_{tp} (W/m^2-s)
0.000001	0.034889	4702.052	2.479E+11	1	1	91223674790
0.05	0.033145	0.785761	89.4904806	1.011174	1.009597	689192.8263
0.1	0.0314	0.432197	20.0795815	1.049802	1.042658	306359.6618
0.15	0.029656	0.298504	7.96021819	1.125625	1.107064	185490.0996
0.2	0.027911	0.22591	3.96633709	1.252122	1.213186	127181.1403
0.25	0.026167	0.179467	2.23106461	1.448217	1.37479	93171.25475
0.3	0.024422	0.146781	1.34965637	1.740929	1.610465	71042.82669
0.35	0.022678	0.122282	0.85498848	2.169606	1.945895	55581.49786
0.4	0.020934	0.103077	0.55776615	2.792866	2.417576	44223.48962
0.45	0.019189	0.0875	0.37031388	3.700412	3.079009	35564.91106
0.5	0.017445	0.074523	0.24789607	5.033949	4.01135	28774.19313
0.55	0.0157	0.06347	0.16594695	7.026022	5.342528	23328.37413
0.6	0.013956	0.053878	0.11017603	#VALUE!	#VALUE!	18882.7221
0.65	0.012211	0.045416	0.07187519	#VALUE!	#VALUE!	15201.26544
0.7	0.010467	0.037836	0.04553193	22.96261	14.7842	12117.51659
0.75	0.008722	0.030945	0.02754401	712.5375	283.1315	9511.210101
0.8	0.006978	0.024583	0.0154935	515.6978	214.439	7294.080461
0.85	0.005233	0.018605	0.00771995	555.6807	228.6532	5401.164527
0.9	0.003489	0.01285	0.00306045	834.1738	324.2052	3786.178396
0.95	0.001744	0.007068	0.00068669	2312.549	778.8184	2422.462252
0.999999	3.49E-08	1.18E-06	2.479E-13	4.03E+12	6.83E+10	1347.607076

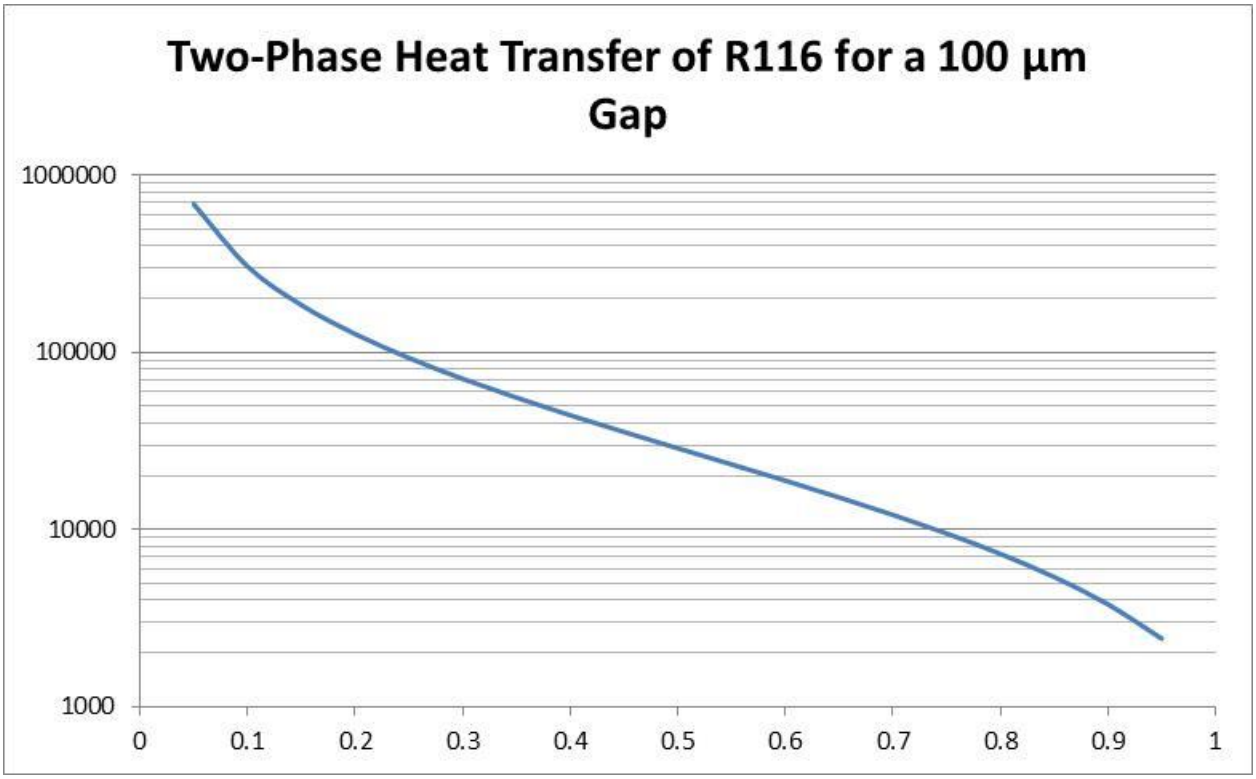

Figure C-6: Plot of the two-phase heat transfer coefficient for R116 as a function of quality in a 100 µm gap.

Table C-9: Calculated two-phase heat transfer coefficient for R116 of quality 0.5 with varied gap thickness.

Gap Thickness	Mass Flux	Dryout Parameter	Martinelli #				Two Phase Heat Transfer Coefficient
t_g (m)	G	U_{LS}	*Co*	X^2	ϕ^2	$\phi^{1.719}$	h_{tp} (W/m^2-s)
5.00E-06	1.12E+02	3.49E-02	7.45E-02	2.48E-01	5.03E+00	4.01E+00	5.75E+04
1.00E-05	5.60E+01	1.74E-02	7.45E-02	2.48E-01	5.03E+00	4.01E+00	2.88E+04
1.50E-05	3.74E+01	1.16E-02	7.45E-02	2.48E-01	5.03E+00	4.01E+00	1.92E+04
2.00E-05	2.80E+01	8.72E-03	7.45E-02	2.48E-01	5.03E+00	4.01E+00	1.44E+04
2.50E-05	2.24E+01	6.98E-03	7.45E-02	2.48E-01	5.03E+00	4.01E+00	1.15E+04
3.00E-05	1.87E+01	5.81E-03	7.45E-02	2.48E-01	5.03E+00	4.01E+00	9.59E+03
3.50E-05	1.60E+01	4.98E-03	7.45E-02	2.48E-01	5.03E+00	4.01E+00	8.22E+03
4.00E-05	1.40E+01	4.36E-03	7.45E-02	2.48E-01	5.03E+00	4.01E+00	7.19E+03
4.50E-05	1.25E+01	3.88E-03	7.45E-02	2.48E-01	5.03E+00	4.01E+00	6.39E+03
5.00E-05	1.12E+01	3.49E-03	7.45E-02	2.48E-01	5.03E+00	4.01E+00	5.75E+03
5.50E-05	1.02E+01	3.17E-03	7.45E-02	2.48E-01	5.03E+00	4.01E+00	5.23E+03
6.00E-05	9.34E+00	2.91E-03	7.45E-02	2.48E-01	5.03E+00	4.01E+00	4.80E+03
6.50E-05	8.62E+00	2.68E-03	7.45E-02	2.48E-01	5.03E+00	4.01E+00	4.43E+03
7.00E-05	8.00E+00	2.49E-03	7.45E-02	2.48E-01	5.03E+00	4.01E+00	4.11E+03
7.50E-05	7.47E+00	2.33E-03	7.45E-02	2.48E-01	5.03E+00	4.01E+00	3.84E+03
8.00E-05	7.00E+00	2.18E-03	7.45E-02	2.48E-01	5.03E+00	4.01E+00	3.60E+03
8.50E-05	6.59E+00	2.05E-03	7.45E-02	2.48E-01	5.03E+00	4.01E+00	3.39E+03
9.00E-05	6.23E+00	1.94E-03	7.45E-02	2.48E-01	5.03E+00	4.01E+00	3.20E+03
9.50E-05	5.90E+00	1.84E-03	7.45E-02	2.48E-01	5.03E+00	4.01E+00	3.03E+03
1.00E-04	5.60E+00	1.74E-03	7.45E-02	2.48E-01	5.03E+00	4.01E+00	2.88E+03
1.05E-04	5.34E+00	1.66E-03	7.45E-02	2.48E-01	5.03E+00	4.01E+00	2.74E+03
1.10E-04	5.09E+00	1.59E-03	7.45E-02	2.48E-01	3.72E+01	2.24E+01	2.62E+03
1.15E-04	4.87E+00	1.52E-03	7.45E-02	2.48E-01	3.32E+01	2.03E+01	2.50E+03
1.20E-04	4.67E+00	1.45E-03	7.45E-02	2.48E-01	5.03E+00	4.01E+00	2.40E+03
1.25E-04	4.48E+00	1.40E-03	7.45E-02	2.48E-01	5.03E+00	4.01E+00	2.30E+03
1.30E-04	4.31E+00	1.34E-03	7.45E-02	2.48E-01	5.03E+00	4.01E+00	2.21E+03
1.35E-04	4.15E+00	1.29E-03	7.45E-02	2.48E-01	5.03E+00	4.01E+00	2.13E+03
1.40E-04	4.00E+00	1.25E-03	7.45E-02	2.48E-01	5.03E+00	4.01E+00	2.06E+03
1.45E-04	3.86E+00	1.20E-03	7.45E-02	2.48E-01	2.11E+01	1.38E+01	1.98E+03
1.50E-04	3.74E+00	1.16E-03	7.45E-02	2.48E-01	2.00E+01	1.32E+01	1.92E+03

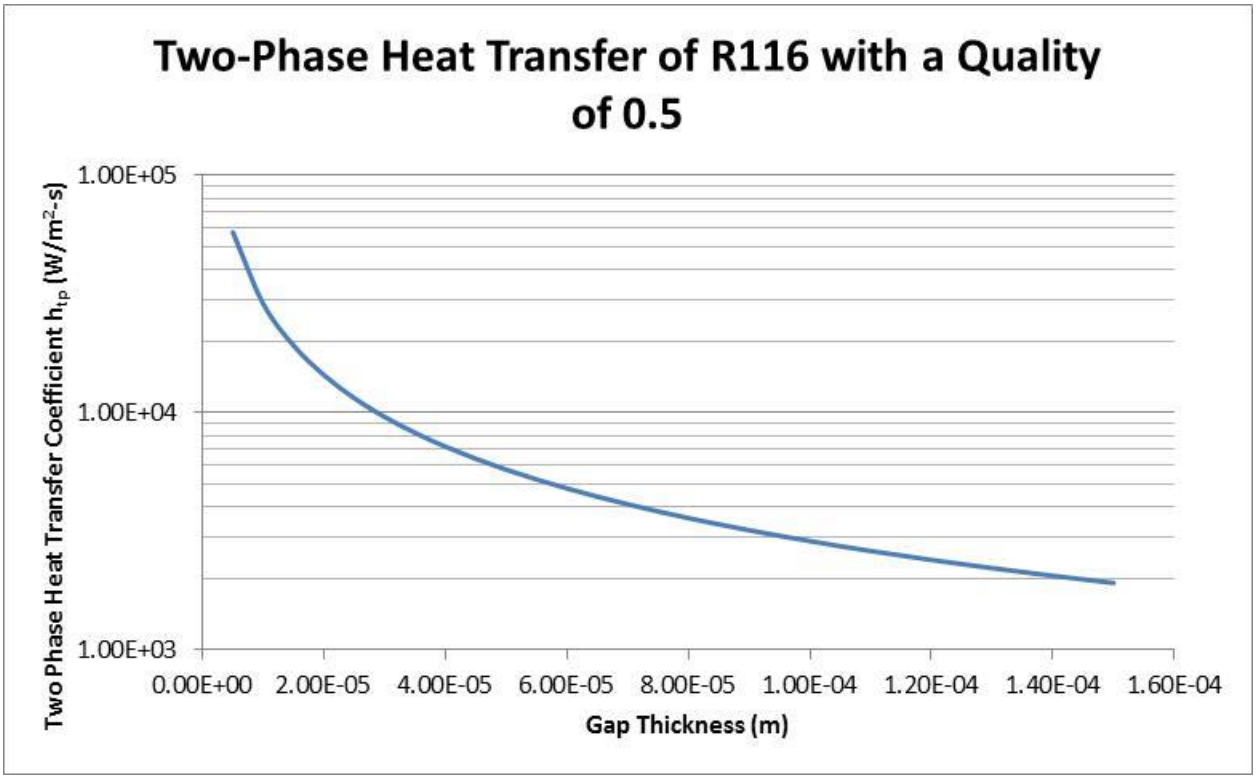

Figure C-7: Plot of the two-phase heat transfer coefficient for R116 of quality 0.5 as a function of gap thickness.

Appendix D: General Processing Parameters for the Polyimide Based Coldstage

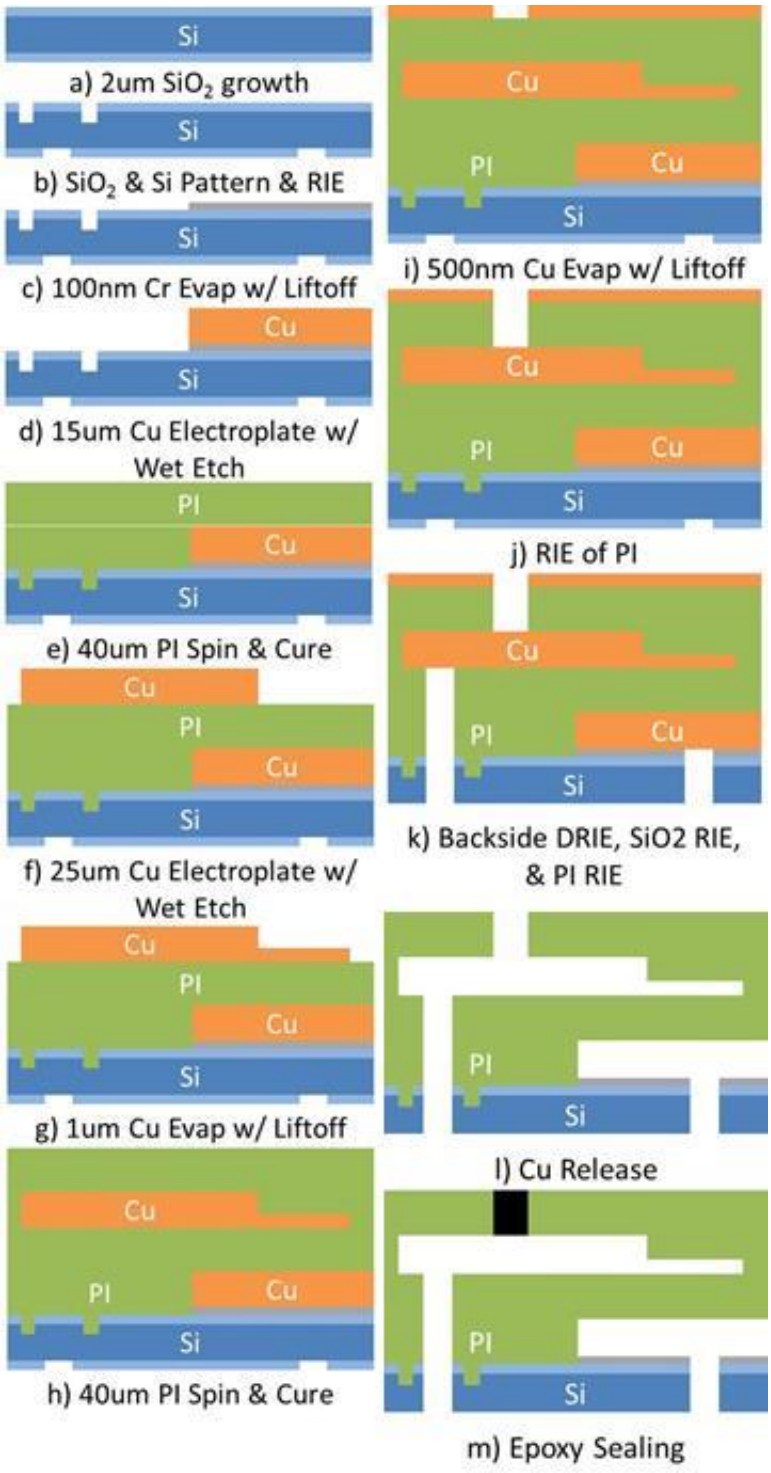

Figure D-1: Fabrication process for the polyimide based single stage coldstage.

Figure D-1 shows the process flow for the fabrication of the polyimide based single stage coldstage. Table D-1 gives a time estimate for a full fabrication run of a coldstage wafer without reworking any process steps. Realistically reworking will be necessary on several process steps and can significantly increases processing time. Detailed processing parameters for critical processing steps follow:

(a) Start with a 3 in 380 μm thick silicon wafer with 2 μm of thermally grown silicon oxides. Pre-oxidized wafers may be purchased from a vendor or a bare silicon wafer can be thermally oxidized in an oxidation furnace via wet oxidation at 1100 ^{o}C for ~8 hours.

(b) The front side and back side oxide is patterned and the front side Si is etched.

1. Pattern both the front and back sides with 10 μm thick photoresist.
2. The oxide is etched in a wet chemical etch of buffered oxide etchant (BOE) for ~ 25 min with an etch rete of ~100 nm/min.
    i. BOE is a hydrofluoric acid (HF) based process. If HF is wished to be avoided, a dry reactive ion etching (RIE) process can be used to etch the front and back side oxide in separate steps. The standard SiO_2 RIE recipe is 4 sccm O_2 +16 sccm CF_4 @ 150 mTorr @ 150 W and produces an etch rate of ~50 nm/min.
3. The photoresist pattern is left on the front side of the wafer and the front side Si is etched an additional 5 μm via RIE. The standard Si RIE recipe is 6 sccm SF6 @ 150 mTorr @ 150 W and produces an etch rate of ~1 μm/min.
4. The photo resist is removed via a standard acetone/IPA solvent spin clean.

(c) A 100 nm Cr layer is deposited and patterned via liftoff.

1. The front side is patterned with a liftoff photoresist (generally a negative photoresist) of thickness >1 μm.
2. A 100 nm thick Cr layer is evaporated via thermal evaporation.

3. The photo resist is removed via an ultrasonic solvent bath to complete the liftoff process.

(d) The first thick copper layer is plated and patterned.

1. The entire front side of the wafer is covered by a 500 nm thick seed layer of Cu. The Cu seed layer is deposited via e-beam evaporation with a 50 nm thick Ti adhesion layer.
2. After the seed layer is evaporated the back side and perimeter of the front side of the wafer are manually masked with blue tape (wafer dicing tape). This masking ensures the electroplating of the subsequent step only occurs on the front of the wafer and eliminates most current concentrations that cause increased plating rates at the perimeter of the wafer.
3. 15 µm of copper is electroplated. Electrical connection is made to the front side of the wafer and the wafer is suspended in an electroplating bath by a slowly oscillating arm. The wafer is plated at a current density of 5 mA/cm^2 (~0.169 A) with a plating rate of ~5 µm/hour.
4. When plating is complete the wafer is rinsed in DI water and the blue tape is removed with acetone and IPA.
5. The wafer is cleaned with a standard acetone/IPA spin clean.
6. The front side of the wafer is patterned with 10 µm thick photoresist.
7. The thick copper layer is etched with a wet chemical etch using copper etchant CE-100. CE-100 has an etch rate of ~1 µm/min. Agitation of the etch bath with a stir bar is recommended for an even etch rate. Frequent visual inspection is recommended to ensure no over-etching.

8. After the etch is finished the wafer is rinsed in DI water and cleaned with a standard acetone/IPA spin clean to remove the photo resist.

(e) The electroplated copper is cleaned using a formic acid process and the first polyimide layer is spun on.

1. The wafer is cleaned on a hotplate with a hood as shown in Figure 2.28.
2. The wafer is heated on the hooded hotplate from room temperature to 200 ^{o}C in a nitrogen environment with nitrogen flow into the hood of 50 sccm.
3. When the wafer is at temperature reduce the nitrogen flow to 20 sccm and increase the nitrogen flow through the formic acid bubbler to 30 sccm.
4. Wait until all visible oxide is removed. This may take several hours.
5. Once all oxide is removed stop the formic acid flow and increase the nitrogen flow to 50 sccm.
6. Turn off the hot plate heater and allow the wafer to cool room temperature in the nitrogen environment.
7. When the wafer is cooled, stop all nitrogen flow and immediately proceed to the next process step to minimize exposure to atmospheric oxygen.
8. The first 40 µm PI layer is spun onto the wafer
    i. VM-651 is mixed with DI water at a ratio of 1:999 (VM-651:DI H_2O) as per the recommended processing procedure
    ii. Start by letting the VM-651 solution sit over the entirety of the wafer for 3 min.
    iii. The solution is spun off the wafer at an rpm of 3000 for 30 sec.
    iv. Immediately coat the wafer on the spinner with PI 2611

a. Note the PI 2611 needs to warm up to room temperature before spinning. It is recommended to remove the PI 2611 from the chemical refrigerator/freezer 1 hour before application.

v. Allow the PI 26 11 to settle on the wafer for ~1 min. the settled amount of PI should be about the size of a quarter (US).

vi. The PI is evenly spread over the surface of the wafer by spinning at 500 rpm for 15 sec followed by spinning at 2400 rpm for 30 sec with a ramp of 1000 rpm/sec

vii. After the spin, soft bake the wafer in a nitrogen environment at 130 ^{o}C for 3 min using a hood setup similar to the one presented in Figure 2.28 with a nitrogen flow of 50 sccm.

a. The soft bake removes the solvent from the spin-on PI but does not cross-link the PI.

viii. The standard spin process should give a PI thickness of 10 µm. Repeat steps iv through vii 4 times to create a 40 µm PI layer.

a. Note layers thicker than 50 µm have significant problems with the final cure (next step). It is recommended to limit the PI thickness to less than 50 µm. If thicker layers are needed it is recommended to perform multiple full cure steps in increments < 50 µm

ix. The PI is cured in a nitrogen environment using a hood setup similar to the one presented in Figure 2.28 with a nitrogen flow of 50 sccm. The cure schedule is run with a programed hot plate and is as follows:

a. Dwell for 5 min with a plate temperature of 130 ^{o}C.

b. Set a temperature ramp rate of 4 ^{o}C/min.

c. Wait for the plate temperature to reach to reach 265 ^{o}C.

d. Dwell for 1.5 hrs.

e. Allow the plate to cool to 200 ^{o}C @ 4 ^{o}C/min.

f. Temperature ramp rate control is turned off and the hotplate is allowed to cool naturally to room temperature.

g. Turn off nitrogen flow and unload wafer.

(f) A 25 µm copper layer is electroplated and patterned following the process steps from section (d)

1. Before the process steps from step (d) are run the PI surface is cleaned

   i. A standard acetone/IPA spin clean is run to remove any organic contamination.

   ii. A standard spin-rinse-dry cycle is run with DI water to remove any particulate contamination

   iii. A dehydration bake is run to remove any water adsorbed in the PI. The wafer is placed on a vacuum hotplate at 115 ^{o}C foe 20 min.

   iv. A plasma clean process is used to clean and activate the PI surface before evaporation of the seed layer. The wafer is placed in a bench-top oxygen RIE. For 5 min. The RIE operates at 100 mTorr, 50 sccm O_2, and 60 W.

   v. Proceed immediately to the seed layer evaporation.

(g) A 1 µm Cu layer is deposited and patterned via liftoff.

1. The front side is patterned with a liftoff photoresist (generally a negative photoresist) of thickness ~10 µm.
2. The cleaning process described in step (f) is repeated

3. A 1 µm thick Cu layer is evaporated via e-beam evaporation with a 50 nm Ti adhesion layer.
    i. The evaporation is run with a 45^{o} angled rotating stage to ensure good step coverage with the thick electroplated Cu.
4. The photo resist is removed via an ultrasonic solvent bath to complete the liftoff process.

(h) The copper is cleaned using a formic acid process and the second 40 µm polyimide layer is spun on following the process described in step (e).

(i) A 500 nm Cu layer is deposited via liftoff as described in step (g) without angled evaporation. This layer acts as a hard mask for the following RIE process.

(j) A front side RIE is used to etch the PI into the coldstage geometry and expose the encapsulated Cu layers with release holes to allow access to the release etchant at the end of the process.

1. The RIE recipe is 10 sccm O_2, 6 sccm CF_4, @ 100 mTorr, and 150 W. The etch rate is 250 – 500 nm/min. The etch rate increases with chamber temperature. The RIE used does not have good thermal control of the chamber. It is recommended to perform short etched of ~30 min with profilometer measurements of the etch depth in-between. Continue etching until the silicon wafer is exposed.

(k) The backside through wafer etch is made with deep reactive ion etching (DRIE)

1. The wafer is mounted to a handle wafer with Crystalbond 555 wafer bonding wax.
    i. The wafer is mounted to the handle wafer so the backside is exposed.
    ii. The handle wader must be a passivated wafer so as to not be etched in the DRIE. Such wafers include silicon with a thick oxide or nitride layer and glass.

iii. The Crystalbond wax is applied to the handle wafer and the front side of the coldstage wafer. The wax is applied manually from the wax stick on a hotplate at 130 ^{o}C.

iv. The wax is degassed in a vacuum oven to remove any trapped air bubbles for 30 min. The oven maintains a wafer temperature of 130 ^{o}C.

v. The two wafers are removed from the vacuum oven and allowed to cool. The waxed sides of the wafers are placed together and the wafer stack is placed back in the vacuum oven for 30 min to allow the wax to reflow and remove any air from the wax bond.

2. A thick > 10 µm layer of photoresist is spun onto the backside of the device wafer and patterned to match the oxide pattern allowing the underlying silicon to be exposed.
3. The wafer is placed in a DRIE and the through wafer etch is made to expose the front side oxide.
    i. The DRIE is run in the NIST cleanroom using their standard silicon DRIE process. The etch rate is ~1 µm/cycle and can vary based on the wafer temperature. Inspection and measurement of the etch depth is recommended every 100 cycles.
4. With the wafer still mounted to the handle wafer and the photoresist remaining on the back side, the front side oxide is etched from the back side to expose the first copper layer and the first polyimide layer via the SiO_2 RIE process described in step (b).

5. With the wafer still mounted to the handle wafer and the photoresist remaining on the back side, the first polyimide layer is etched from the back side to expose the second copper (copper channel) layer using the RIE process described in step (j).
6. The coldstage chips were diced by the DRIE process and are now removed from the handle wafer in an acetone bath. The chips are cleaned with a standard acetone/IPA clean. Further processing is performed individually on each chip.

(l) The copper is released to leave behind a suspended polyimide structure with micro channels.

1. The chip is placed in a heated and stirred bath of CE-100 to release the copper. The bath is heated to 60 ^{o}C on a hotplate with a stir bar. Make sure to cover the beaker so the etchant does not evaporate.
2. The release process takes several days to complete. It is recommended to refresh the copper etchant every 24 – 48 hours.
3. Visual inspection is used to identify the end of the release process.
4. The chip is rinsed in DI water for 24 hours.
5. A critical point dryer is used to make sure there is no stiction occurs.
    i. The chip is rinsed in a methanol bath for 24 hours without being dried from the DI water rinse before the critical point drying process is run.

(m) Finally the top side release holes are sealed.

1. The release holes are capped with small pieces of Kapton tape. The tape must cover the entire release hole.
2. Epoxy is applied to the perimeter of the tape to provide an effective seal.
    i. TorrSeal vacuum epoxy or Stycast 2850 are used as the epoxy.

Table D-1: Estimate of total time required to process one coldstage wafer from start to finish without reworking any process steps.

Process Step	Estimate of number of days to complete
Front side SiOx PR (step b)	1
Backside SiOx PR (step b)	1
Backside SiOx Etch (step b)	1
Cr PR (step c)	1
Cr 100 nm evap (step c)	1
Cu 500 nm Seed Layer (step d)	1
Cu 15 µm Electroplate (step d)	1
Cu PR (step d)	1
Cu Etch (step d)	1
Cu deOx Cleaning (step d)	1
PI 40 µm Spin & Cure (step e)	1
Cu 500 nm Seed Layer (step f)	1
Cu 20 µm Electroplate (step f)	1
Cu PR (step f)	1
Cu Etch (step f)	1
JT PR (step g)	1
JT 1 µm evap (step g)	1
JT Liftoff (step g)	1
Cu deOx Cleaning (step g)	1
PI 40 µm Spin & Cure (step h)	1
Cu PR (step i)	1
Cu 500 nm evap (step i)	1
Cu Liftoff (step i)	1
PI Etch (step j)	2
Handle Wafer Mount (step j)	1
Backside PR (step k)	1
Backside DRIE (step k)	1
Chip Demount	1
Backside RIE of Front Side Ox (step k)	1
Backside RIE of PI (step k)	1
Release (step l)	10
Critical Drying (step l)	1
Release Hole sealing and Tube attachment (step m)	2
Total Days	44
Total Weeks	9